Plasmonic DNA Nanostructures with Tailored Optical Response

Robert Schreiber

München 2013

Datum der mündlichen Prüfung:
28 Mai 2014

Erstgutachter: Prof. Dr. Tim Liedl
Zweitgutachter: Prof. Dr. Alexander Högele

Plasmonic DNA Nanostructures with Tailored Optical Response

Robert Schreiber

Dissertation
durchgeführt an der Fakultät für Physik
der Ludwig-Maximilians-Universität München

vorgelegt von
Robert Schreiber
geboren in Jena

München, den 04.11.2013

Erstgutachter: Prof. Dr. Tim Liedl
Zweitgutachter: Prof. Dr. Alexander Högele

Zusammenfassung

Auch heute noch ist die quantitative und qualitative Strukturierung der nanoskopischen Welt eine große Herausforderung. Die DNA Nanotechnologie beginnt sich hierbei als vielversprechende Methode in der Forschung zu etablieren. In dieser Dissertation wurde gezeigt, dass es möglich ist mit Hilfe von DNA Nanotechnologie komplexe Nanostrukturen mit einzigartigen optischen Eigenschaften selbst-organisierend herzustellen. Hierzu wurden mit Hilfe der DNA-Origami-Methode plasmonische Nanopartikel, Quantenpunkte und fluoreszierende, organische Farbstoffe mit Nanometerpräzision angeordnet und optisch aktive Strukturen mit spezifisch ausgewählten Eigenschaften konstruiert.

Im ersten Teil der Arbeit wurden zuerst DNA Nanostrukturen in definierten geometrischen Formen wie Zylinder, Ringen und Kuboiden synthetisiert und dann mit Gold unspezifisch metallisiert.

Im zweiten Teil wurden chirale plasmonische Strukturen mit kontrollierten optischen Eigenschaften hergestellt. Hierzu wurden Goldnanopartikel mit Hilfe einer DNA-Origami-Struktur präzise in einer Helix angeordnet. Die chirale Struktur zeigte einen Zirkulardichroismus im sichtbaren Bereich des Lichts. Den Wellenlängenbereich und die Stärke des Signals ließen sich durch zusätzliche Metallisierung der Goldnanopartikel kontrollieren.

Im dritten Teil der Dissertation wurde ein schaltbares, zweistufiges, plasmonisches System hergestellt. Hierfür wurden die vorher entwickelten Origamistrukturen mit chiral angeordneten Metallnanopartikeln verwendet, welche dann an einer Oberfläche zueinander ausgerichtet und durch Trocknen und Resuspendieren an der Oberfläche zwischen orthogonaler und paralleler Orientierung hin und her geschaltet wurden. Auf Grund der Chiralität konnte für jede der beiden Orientierungen ein spezifisches Signal des Zirkulardichroismus gemessen werden.

Im abschließenden Projekt dieser Arbeit wurden komplexe hierarchische Planeten-Satelliten-Nanostrukturen hergestellt. Bei diesen Systemen wurden DNA-Origami-Strukturen als Bindungs- und Distanzkontrolle zwischen Planeten und Satelliten benutzt. Als Planeten wurden Metallnanopartikel, Halbleiterelemente oder DNA-Origami-Strukturen verwendet, die von Satelliten aus organischen Farbstoffen oder Metallnanopartikeln mit kontrollierten Abstand, umringt wurden. Die hier entwickelten hierarchische Assemblierungsmethode erwies sich als geeignet optische Interaktionen zwischen Planeten- und Satellitenpartikeln über relativ große (>20 nm) Distanzen zu charakterisieren.

Abstract

The optical properties of the macroscopic world are to some extent determined at the nanometer scale and below. Even today, the quantitative and qualitative structuring of the nanoscopic world is extremely challenging. In this context, DNA nanotechnology seems to establish itself as an inevitable method in research. This thesis shows that it is possible to produce complex pre-designed self-assembled nanostructures with unique optical properties with the aid of DNA nanotechnology. For this purpose plasmonic nanoparticles, semiconductor elements and organic dyes were individually positioned with nanometer precision by the use of the DNA origami method, thereby creating optical structures with specific optical properties.

In the first part of this thesis DNA nanostructures were produced in the desired shape and then metallized non-specifically with gold ions from solution.

In the second part of this thesis, chiral plasmonic structures with controlled optical properties were created. For this purpose, gold nanoparticles were arranged precisely into a helix along a DNA origami scaffold. The chiral structures showed a circular dichroism in the visible range of light. The wavelength range and the intensity of the signal were controlled by an additional metallization process of gold nanoparticles.

In the third part of the thesis a switchable two-state plasmonic system was established. For this, the previously developed origami structures with chiral arrangement of metal nanoparticles were used. The structures were connected to a surface and aligned to each other. By drying and resuspending the surface, the structures could be orientated perpendicular and parallel to the surface. Due to the chirality, a specific signal of the circular dichroism for each of the two orientations was measured.

In the final part, complex hierarchical planet-satellite nanostructures were created. In these systems, DNA origami structures were used to control the distance between planets and satellites. Metal nanoparticles, quantum dots or DNA origami structures were used as planets which were surrounded by satellites of fluorescent organic dyes or metal nanoparticles with controlled inter-particle distances. Further long-range interactions between organic dyes around a planet nanoparticle were investigated.

Contents

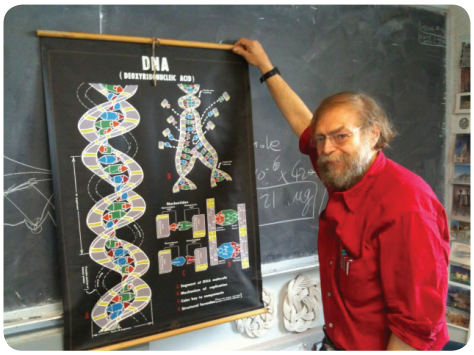

"... they allow us to make something that is not just a long piece of spaghetti ..."

Nadrian C. Seeman about branched DNA molecules (which make DNA nanotechnology so exciting) [1]

Image: Nadrian C. Seeman in front of a vintage poster with the structure of double-stranded DNA and a branched DNA molecule [2]. Reprinted with kind permission from Nadrian C. Seeman.

1 Introduction

Nanotechnology enables the creation of nanoscale objects with macroscale impact. Some of the processes experienced by us every day are controlled by a nanoscale mechanisms. For example, the red colored windows of churches are a result of gold nanoparticles incorporated into the glass. The gold nanoparticles are absorbing most of the visual light except the red light, therefore the window has a reddish look. The color of a butterfly is the result of photonic nanocrystals on the surface of the wings. Furthermore, nanotechnology is involved in anti-reflex coating of glasses, in sunscreens (e.g. zinc oxide nanoparticles), as disinfectants (e.g. silvernanoparticles) in food packaging and clothing. To manipulate the macroscale, nanoscale structures with specific properties are produced with top-down lithography or bottom-up wet chemistry in industry (e.g. for textiles, cosmetics, surface coatings, food industry), in medicine (e.g. for cancer therapy, diagnostics, drug delivery) and in research (e.g. nanorobots, metamaterials, quantum computing). Especially DNA nanotechnology shows an increasing impact in the research fields of nanotechnology [3]. In the field of DNA nanotechnology, DNA is used as a programmable material to arrange nanoparticles through a self-assembly process and to achieve function. The success of DNA nanotechnology is promoted by the readily available DNA oligos and the reliability of the DNA assembly methods.

The field of DNA nanotechnology was established by Nadrian C. Seeman in the early 1980s, when he had the idea to use branched DNA molecules to create three-dimensional lattices constructed from DNA to orientate molecules/proteins of interest for crystallographic studies. During the following ten years Nadrian C. Seeman published various basic studies showing the principles of branched DNA molecules [3, 4]. He published the first structure created with DNA nanotechnology in the early 1990s [5] (see **Figure 1.1**).

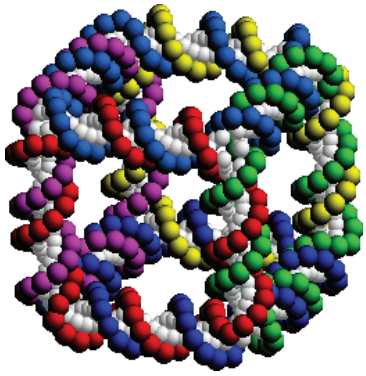

Figure 1.1: Schematic drawing of the first DNA structure created with DNA nanotechnology by Nadrian C. Seeman in 1991. The structure is self-assembled by six single DNA strands. From ref. [5]. Reprinted with permission from Macmillan Publishers Limited.

During the following 15 years many DNA nanostructures (truncated octahedron, buckyballs, tetrahedra and icosahedra) [6-9] and various two-dimensional arrays of DNA tiles [10-14] have been demonstrated. Apart from structural DNA nanotechnology, even programmable DNA tweezers and walkers have been demonstrated [15-18]. These DNA structures were driven by branch migration process and strand displacement using toehold sequences [19]. This process was first demonstrated by Bernard Yurke et al. in 2000 [15].

In 2006, Paul W. K. Rothemund developed the DNA origami technique to create two-dimensional DNA structures of arbitrary shapes [20]. The technique uses a long single-stranded DNA scaffold (around 8000 nucleotides long) which is folded together by multiple smaller single-stranded DNA oligos (around 40 nucleotides long). The DNA origami technique owns the ability to create DNA structure of almost arbitrary shapes. Later, Shawn M. Douglas et al. took this technique a step further and demonstrated assembly of three-dimensional DNA origami structures of programmable shape [21]. The technique is used in all associated publications (P1-P4). Shawn M. Douglas also had great influence on the DNA origami community with creation of the design software "caDNAno" [22], which allows to easily design DNA origami structures without paying attention to the DNA sequence. Further methods to create DNA nanostructures with curved and pre-stressed shapes were developed [23-25], followed by hierarchically assemblies [26,27] and tile assemblies of arbitrary shapes [28, 29].

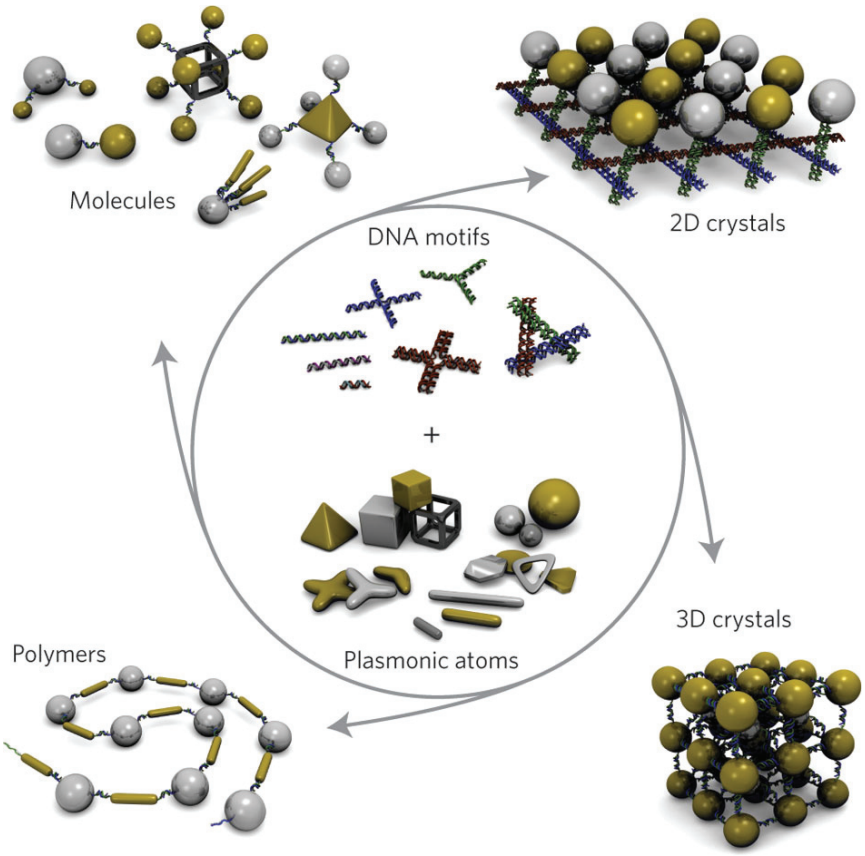

Figure 1.2: Various hierarchical assemblies of plasmonic nanoparticles which can be created with the help of DNA nanotechnology. From ref. [39]. Reprinted with permission from Macmillan Publishers Limited.

The apparent next step in DNA nanotechnology was to modify ssDNA with nanoparticles or functional molecules and arrange these components by means of DNA self-assembly, a process that already started to evolve soon after the assembly power of nucleic acids has been realized [30, 31]. Many groups have been using DNA nanostructures as scaffolds to arrange fluorophores [32], metallic nanoparticles [33-35] (**Figure 1.2**), quantum dots [36], proteins [37] and other bio-molecules [38] in spatially controlled arbitrary arrangements. These approaches have shown that the properties of creating arbitrary shapes can be transferred to new materials which only need to be linked to single-stranded DNA.

As a next step the function was added by controlled assembly of such components with the help of DNA nanotechnology. During the course of my work from 2010 to 2013 outstanding examples of other groups showed how to create nanostructures with functional components using DNA origami scaffolds (e.g. an artificial nanopore [40], a ruler [32], photoluminescence enhancement [41] and chiral plasmonics [42,43]) (see also associated publication P2).

2 Theoretical and Experimental Basics

2.1 Chirality and Circular Dichroism

In general, chirality is the property of an object that is not superposable on its mirror image. Therefore, chirality is a consequence of asymmetry. An object can show chirality in two-dimensions but has a symmetry in the third-dimension (e.g. a two-dimensional spiral). A well-known example for asymmetry in all three dimensions is a helix. Every chiral object has exactly one mirror image (chiral partner), which looks alike the original (see right and left hand of a human) but can have opposite properties as will be shown in the associated publication P2 for a plasmonic helix. In nature, chirality of molecules plays an important role in the molecular interactions as most of the biological molecules are chiral. Chiral partner molecules (enantiomers) could have extremely different impact reaction schemes (e.g. see "Contergan affair"). Therefore the reliable analysis and the exact knowledge of the chirality of molecules is required.

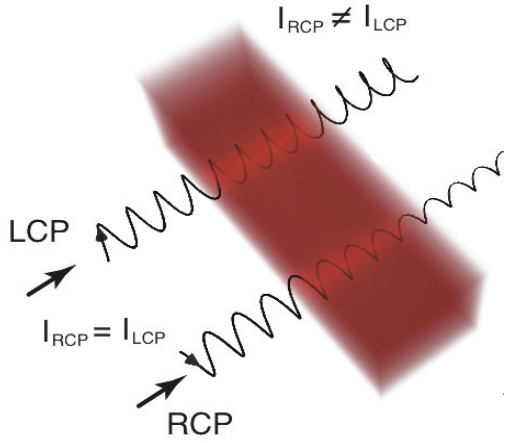

Figure 2.1: The basic principle of a circular dichroism measurement. The absorption of the red-colored material, here for right-handed circular polarized (RCP) light is stronger than for left-handed circular polarized (LCP) light. Printed with kind permission from Anton Kuzyk.

A typical optical phenomenon caused by chiral molecules and other optically active chiral objects is circular dichroism (CD). Here, a chiral molecule or object is preferentially absorbing circular polarized light of one chirality (e.g. right-handed circular polarized light, RCP) at a specific wavelength (**Figure 2.1**). The enantiomer of the molecule or object preferably absorbs light of the inverted chirality (e.g. Left-handed circular polarized light, LCP). The strength of the CD signal is given by the difference between the absorption of the two different chiralities of light passing through the sample.

$$\Delta A = A_{LCP} - A_{RCP}$$

CD is frequently used for the detection of the secondary structure of chiral molecules (e.g. proteins) (**Figure 2.2**). To analyze the chirality of molecules typically a CD spectrometer is used. A standard CD spectrometer uses a Xenon lamp as light source. The light from the Xenon lamp is collimated and sent through a 45° polarizer and passes on to a photo-elastic modulator, which modulates the polarization of the light beam. The polarized light beam passes through the sample cuvette to the detecting photomultiplier. The absorption by the sample is evaluated by comparing it to a reference beam which also hits the photomultiplier.

However, if plasmonic particles are arranged in a chiral fashion a plasmonic CD signal can be achieved. It has been demonstrated by other groups that the chirality of natural molecules such as peptides [44] and double-stranded DNA [45-47] can be used as templates for the growth of chiral metal nanostructures.

In the associated publication P2 a chiral assembly of plasmonic nanoparticles on a DNA origami scaffold is presented. This artificial nanostructure has an optical chirality in the visible range of light (**Figure 2.2**). The CD signal of this structure originates from plasmonic interactions between nanoparticles, which are assembled in a chiral geometry.

It has been shown that bio-molecules of a certain chirality can couple with non chiral metal nanoparticles to generate a CD signal at the plasmonic resonance of the metal nanoparticle [48-50]. This effect will be further illustrated in chapter 7 of this thesis.

2.2 Plasmonic Nanoparticles and Plasmonic Circular Dichroism

The majority of all bio-molecules shows CD in the UV range of light. The CD of bio-molecules is exitonic in nature and originating from interactions of electric and magnetic dipoles within the molecular structure. In contrast to bio-molecules, plasmonic nanoparticles normally have symmetries and are not chiral (**Figure 2.2**). Therefore these particles do not show any CD signal. They have a higher molar extinction ($\varepsilon \sim 10^4$ $(M{\cdot}cm)^{-1}$), which is many magnitudes higher than the one for biological molecules ($\varepsilon \sim 10^8$ $(M{\cdot}cm)^{-1}$). Plasmonic nanoparticles are optically more active in the visible range of light. If plasmonic particles are arranged in a chiral geometry, plasmonic dipole theory predicts the emergence of plasmonic CD signals.

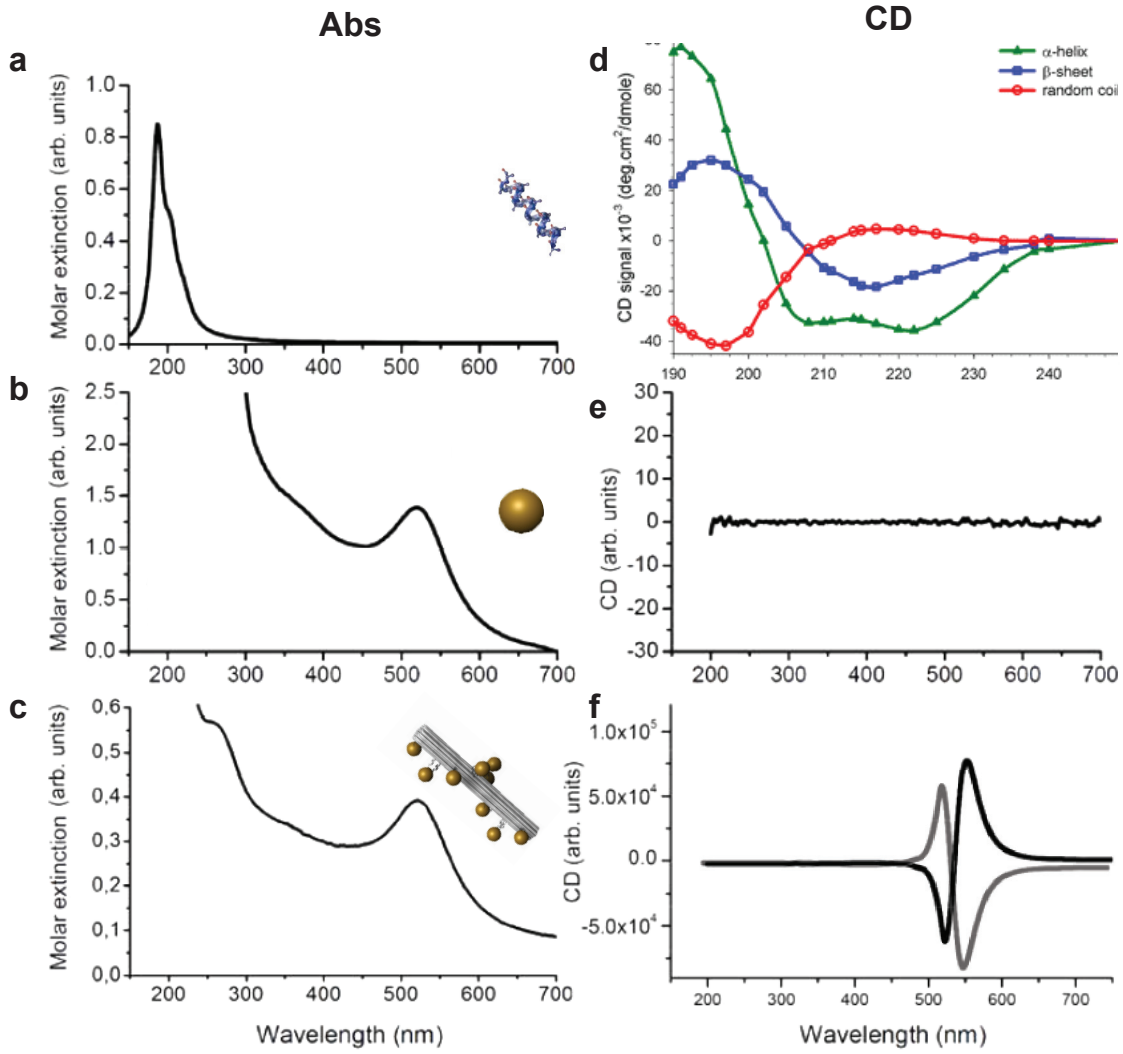

Figure 2.2: Optical properties of proteins, gold nanoparticles and gold nanohelices. **Left**, Absorption spectra of, **a**, a α-helix protein, **b**, a gold nanoparticle, **c**, a chiral array of gold nanoparticles. Reprinted with permission from reference [50]. **Right**, Circular dichroism spectra of, **d**, different secondary structures of proteins. Here the CD signal allows to distinguish between the secondary structures of proteins (α-helix, β-sheet and random coil). The CD signal originates from the peptide ponds excitations of the proteins. Reprinted with permission from reference [51]. **e**, No CD signal for gold nanoparticles. **f**, Plasmonic CD signal for a chiral array of gold nanoparticles (left-handed (grey) and right-handed (black)).

For plasmonic nanoparticles it is possible to couple photons to surface charge densities at the interface of the nanoparticle and the surrounding medium. The resulting collective oscillations of free electrons are called plasmons. The optical response of metal can be described with the Drude-Lorentz-Sommerfeld model [52, 53]. The dielectric response of an electron gas is described by [52]

$$D = \varepsilon_0 E + P = \varepsilon_0(1 + \chi)E = \varepsilon\varepsilon_0 E$$

where D is the electric flux density, E is the external field and P the polarization density. The external field gives rise to the polarization density and the flux density. Further, ε_0 describes the permittivity of the vacuum, χ the electric susceptibility and ε the electric permittivity of the medium. Using the Drude-Lorentz-Sommerfeld model, one can derive a relation for the material permittivity of metal. This model describes the conducting electrons as detached from their ion cores thus forming a free electron gas. Like in an ideal gas, the particles perform movements without interacting with each other. When considering the response to an external oscillatory field, taking a constant damping Γ into account and using the equation of motion for electrons, the material permittivity of metals can be described with

$$\varepsilon(\omega) = 1 - \frac{Ne^2}{\varepsilon_0 m(\omega^2 + i\Gamma\omega)} = 1 - \frac{\omega_p^2}{\omega^2 + i\Gamma\omega}$$

where ω is the angular frequency of the oscillating electric field, N the electron density, e is the electron charge, m is the effective electron mass and ω_p the plasma frequency described by

$$\omega_p^2 = \frac{Ne^2}{\varepsilon_0 m}$$

The free electron scheme can be accuratly used when describing the response for metals with a low number of core electrons [54]. A more sophisticated model is required for gold and silver where core electrons in addition to conduction electrons give a contribution to the optical response.

The material permittivity of metals can also be described with the Drude-Lorentz-Sommerfeld susceptibility $\chi^{DS}(\omega)$

$$\varepsilon(\omega) = 1 + \chi^{DS}(\omega).$$

By including the influence of core electrons which contribute to the optical response, the permittivity equation is described by [55].

$$\varepsilon(\omega) = 1 + \chi^{DS}(\omega) + \chi^{IB}(\omega)$$

where $\chi^{IB}(\omega)$ describes the susceptibility for interband transitions. The equation describes the optical response of metals including polarizability and absorption properties. To describe the optical response of metal nanoparticles analytically, Mie-theory is needed while for particle arrays numerical techniques are required, which will not be discussed here.

An optical response of a nanoparticle can be mediated by the coupling of photons to surface charge

densities at the interface of the NP and the surrounding medium (e.g. between a metal and a dielectric material). These oscillating surface charge densities are called localized surface plasmon resonances. To describe localized surface plasmons one can use quasi-static approximations which requires the nanoparticle to be smaller than the wavelength of the incident light (~1%) [56]. The static polarizability of a spherical nanoparticle is given by

$$\alpha = 4\pi\varepsilon_0 R^3 \frac{\varepsilon_p - \varepsilon_m}{\varepsilon_p + 2\varepsilon_m}$$

where ε_p is the complex permittivity of the nanoparticle and ε_m is the complex permittivity of the surrounding medium. The localized surface plasmons of the nanoparticle show resonance if

$$|\varepsilon_p + 2\varepsilon_m| = \text{minimum}$$

From this equation the resonance condition for a dipole resonance in the quasi-static approximation follows

$$\varepsilon_m(\omega) = -2\varepsilon_p$$

The Drude-Lorentz-Sommerfeld model for the permittivity of metal particles, neglecting the damping effects, can be described by

$$\varepsilon(\omega) \approx 1 - \frac{\omega_p^2}{\omega^2}$$

and using the resonance condition for dipoles in the quasi-static approximation, the dipole resonance of the nanoparticle is then described by

$$\omega_{SP} = 1 - \frac{\omega_p}{\sqrt{1 + 2\varepsilon_p}} .$$

For an increasing particle size the resonance shifts to longer wavelengths which can be observed experimentally and is also predicted by Mie-theory. If the incident light hits the plasmon resonance of the nanoparticle, the energy of the light gets confined inside the nanoparticle. The confinement of the light leads to strong electro-magnetic fields around the particle's surface with a decay to zero within a couple of nanometers from the nanoparticle (depending on the material and size of the nanoparticles). When particles are brought together closely enough, the near-field of the plasmonic nanoparticles are overlapping and the plasmons of the nanoparticles are hybridizing together similarly to the hybridization of atomic orbitals in molecules [57, 58]. A detailed description of the model of interacting dipoles can be found in references [59-61]. The coupling between the nanoparticles also depends on the polarization of the exciting electro-magnetic field [62], which is strongest when the light is polarized along the geometry of the nanoparticle assembly (**Figure 2.3**). If the nanoparticles are assembled in chiral geometry and brought together closely enough, it is possible to generate a plasmonic CD signal [61, 63-65], which originates from the hybridization of plasmons of the nanoparticles in the chiral assembly. Depending on the chiral geometry, preferably only one polarization of light is absorbed by the

hybridized plasmons. The plasmonic CDs of various chiral assemblies were calculated in reference [61], where it is shown that the assembly of plasmonic nanoparticles in a geometry of a helix exhibit the strongest CD signal. The collective plasmonic excitation in a helix can be divided into hybridized plasmons parallel (longitudinal/z-mode) and hybridized plasmons perpendicular (transverse/xy-mode) to the helix axis. These two plasmonic modes have an inverted CD signal to each other with a small red-shift of the resonance wavelength. When superimposing the various signals (CD_z and CD_{xy}), one obtains the bisignated (dip-peak) CD shape of helices dispersed in solution, i.e. illuminated from all sides. Interestingly, such bisignated shapes are also observed from bio-molecules.

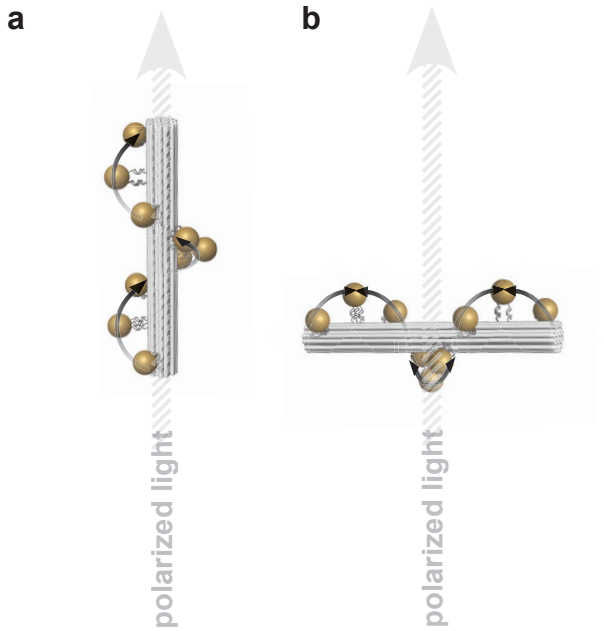

Figure 2.3: The two opposite chiralities in one helical structure (here: for a left-handed nanohelix from associated publication P2). **a**, The left-handed property of a left-handed helix: The incident circular polarized light progresses parallel to helix's axis and "recognizes" a left-handed chirality of the gold particle arrangement (following the black arrows, starting with the first gold particle which gets hit by the wave front). **b**, The right-handed property of a left-handed helix: The incident circular polarized light progresses orthogonal to helix's axis and "recognizes" a right-handed chirality of the gold particle arrangement (following the black arrows, starting with the first gold particle which gets hit by the wave front).

3 DNA Origami-Templated Growth of Arbitrarily Shaped Metal Nanoparticles

Generating metal nanoparticles of arbitrary shape is still highly demanding and of great interest for applications in plasmonics, photonics and electronics. For photonic applications it might be useful to create metallic nanostructures that interact with light. For example, specific nanoparticle shapes like split-ring structures would be useful to create plasmonic resonators and can achieve distinct optical properties like the change of the refractive index. For Raman spectroscopy it would be beneficial to create nanoparticles with spike-like structures that focus the electro-magnetic near-field surrounding the nanoparticle on a single spot. It can be envisioned that metallized hierarchical assemblies of rod shaped nanoparticles could be used as electrical leads that connect logic elements like transistors to self-assembled devices for electronic applications. Furthermore, branched metal nanoparticles with large surfaces can be envisioned to support the energy conservation for solar cells, by extending the wavelength's absorbance range of the device. Already today customized metal nanoparticles are used in industry, e.g. for paints with designed color or heat generation effects.

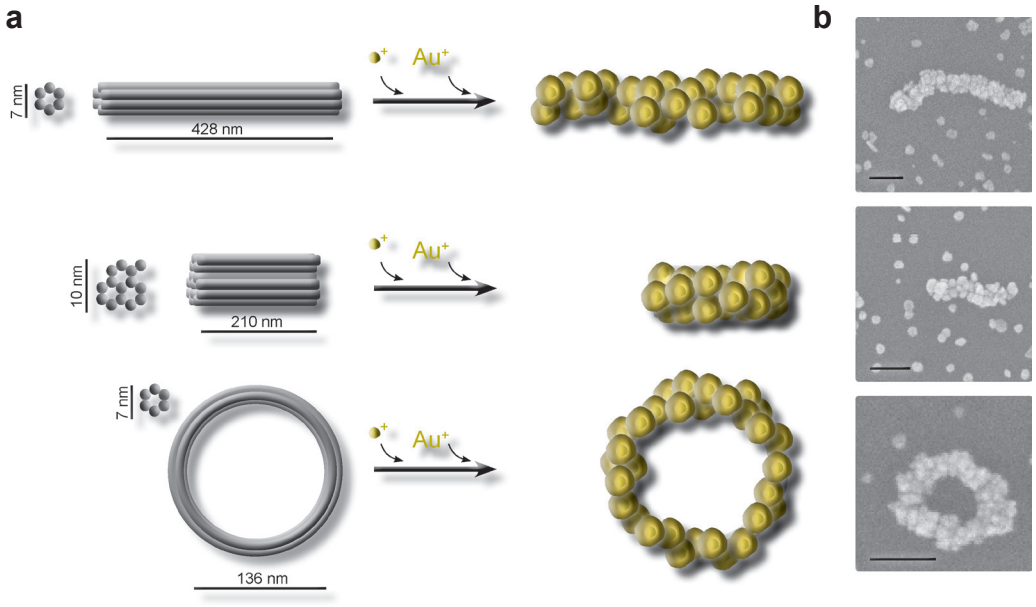

Figure 3.1: a, Schematic drawing of the metallization of various DNA origami structures (6-helix bundle, 14-helix bundle and origami ring structure). **b**, Scanning electron microscopy images of the metallized DNA origami structures. Scale bars, 100 nm.

Using the bottom-up approach the shape of the prospective metal nanoparticle can be influenced by the initiating seed. Recent works have already shown that it is possible to metallize double-stranded DNA as well as other molecules [66-72]. Furthermore, wet chemistry allows to grow metal nanoparticle of various shapes in high quality (e.g. nanorods, nanocubes or tetrapods) [39]. Still arbitrary

control of the shape is missing in these approaches and especially the creation of asymmetric or ring structures was not achieved. Specifically with the DNA origami method we were able to show in the associated publication P1 that it is possible to create arbitrary shaped seeds of DNA nanostructures, which could later be transformed into metal nanoparticles with preferred overall shape (**Figure 3.1**). We used the principle that small positive-charged gold particles (1.4 nm diameter) attach to the highly negative charged backbone of the DNA (each phosphine group of the DNA backbone possess one negative charge at physiological pH values). After covering the origami structures with the positive-charged gold particles, we applied electroless deposition of metal ions from solution. This turned the DNA origami structures into continuously covered metallized objects. We created various metallized shapes such as gold nanorods of different lengths (100 nm, 200 nm and polymers of up to micrometer length), nanodonuts, nanocuboids and nanokites.

A following project was combining the metallization method of the associated publication P1 with a chiral origami structure (cork screw design) and further investigated the creation of chiral metal nanoparticles, which is currently not possible with other methods.

The metallized structures presented in the associated Publication P1 showed a high graininess due to the different orientation of the crystal lattices of the single gold seeds. Susanne Kempter from Tim Liedl's group tried to fuse the gold grains and smoothen the surface by melting of the metallized nanostructures. The melting attempts formed gold blobs out of the metallized nanostructures without preserving their original geometry. Further attempts using click chemistry and Tollen's reagent to produce sophisticated metallized nanostructures were not successful.

3.2 Associated publication P1

DNA Origami-Templated Growth of Arbitrarily Shaped Metal Nanoparticles

by

Robert Schreiber, Susanne Kempter, Stefan Holler, Verena Schüller, Daniel Schiffels, Stephanie S. Simmel, Philipp C. Nickels, and Tim Liedl

published in

Small 2011, 7, 1795-1799

NANO small

Self-Assembly

DNA Origami-Templated Growth of Arbitrarily Shaped Metal Nanoparticles

*Robert Schreiber, Susanne Kempter, Stefan Holler, Verena Schüller, Daniel Schiffels, Stephanie S. Simmel, Philipp C. Nickels, and Tim Liedl**

In self-assembly, the information for the overall shape and functionality of the resulting structure is encoded in its multiple subunits. A promising path to the successful construction of self-assembling objects is DNA nanotechnology, where the hybridization specificity of complementary sequences is employed to create nanoscale objects of defined shapes.[1,2] Driven by the hope to rival conventional top-down lithography methods, a lot of effort went into the spatial arrangement of metal nanoparticles[3–6] and the metallization of individual DNA double strands (dsDNA) or DNA multihelical bundles which were presented as promising scaffolds for nanoelectronic applications.[7–13] However, one reason why metallized DNA structures have yet found little application in nanoelectronics and nanooptics might be the limited control over the final 3D shape of the metallized objects. With the establishment of DNA origami,[14,15] where a long, single-stranded DNA scaffold is folded into shape by the help of hundreds of short staple oligonucleotides, new possibilities for the positioning of nanoparticles in defined confirmations[16–18] and the creation of metallized objects of unprecedented shapes have arisen.[19] Besides the spatial labeling precision which is offered by this technique,[20] DNA origami structures can assemble hierarchically into multimeric architectures with dimensions of several micrometers.[15,21,22] This offers the possibility to create complex and large-scale spatial arrangements of anisotropic optical and electronic components.

Here we show that DNA origami structures can be used to attract and template positively charged gold particles in desired conformations and that by further electroless deposition of metal ions from solution such structures can be converted into continuously metallized objects. In contrast to previous work, where DNA nanostructures were metallized via a glutaraldehyde-based method,[19] we use 1.4 nm gold clusters coated with positively charged amines, which bind to negatively charged DNA origami structures, as seeding sites for the gold cluster growth (**Figure 1**). Such metal-seeded objects can then grow further into continuously metallized objects of arbitrary shapes such as gold nanocuboids, nanodonuts, or polymerized nanorods of micrometer length.

To demonstrate the principle of our strategy, 428 nm-long six-helix bundles[23] were converted into gold nanorods of defined length. First, the DNA objects were assembled in a one-pot reaction where 10 nM of scaffold (p7560 and p8634) is mixed with ≈200 oligonucleotides of 100 nM each in a 1 mM Tris-EDTA buffer and 15 mM $MgCl_2$. After a thermal annealing process, the objects were purified by electrophoresis followed by physical gel extraction. For the metallization process, Au clusters of 1.4 nm diameter covered with positively charged amines (Nanoprobes, USA) are deposited on the negatively charged backbones of the DNA strands of the origami structures. The Au-seeding process of the DNA structures was performed successfully in solution and on two

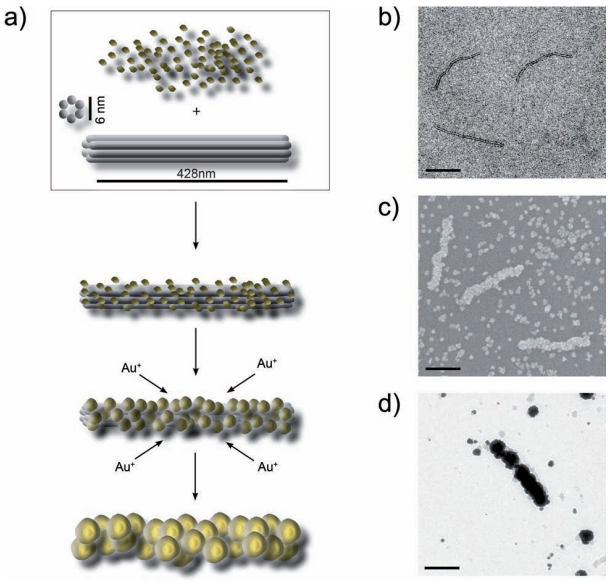

Figure 1. a) Metallization strategy. Positively charged gold clusters cover the negatively charged DNA origami structure. Continuous metallization of such pre-seeded DNA origami structures is achieved by the electroless deposition of gold ions to the electrostatically bound Au clusters (text for details). b) TEM image of native six-helix bundles stained with uranyl acetate. Successful metal deposition results in continuously metallized objects of defined shape and dimensions, which is revealed by SEM (c) and TEM (d). Gold cluster seeding was performed on substrate (c) and in solution (d). Scale bars 200 nm.

R. Schreiber, Dr. S. Kempter, S. Holler, V. Schüller, D. Schiffels, S. S. Simmel, P. C. Nickels, Prof. T. Liedl
Department of Physics and Center for Nanoscience
Ludwig-Maximilians-Universität
Geschwister-Scholl-Platz 1, 80539 München, Germany
E-mail: tim.liedl@lmu.de

DOI: 10.1002/smll.201100465

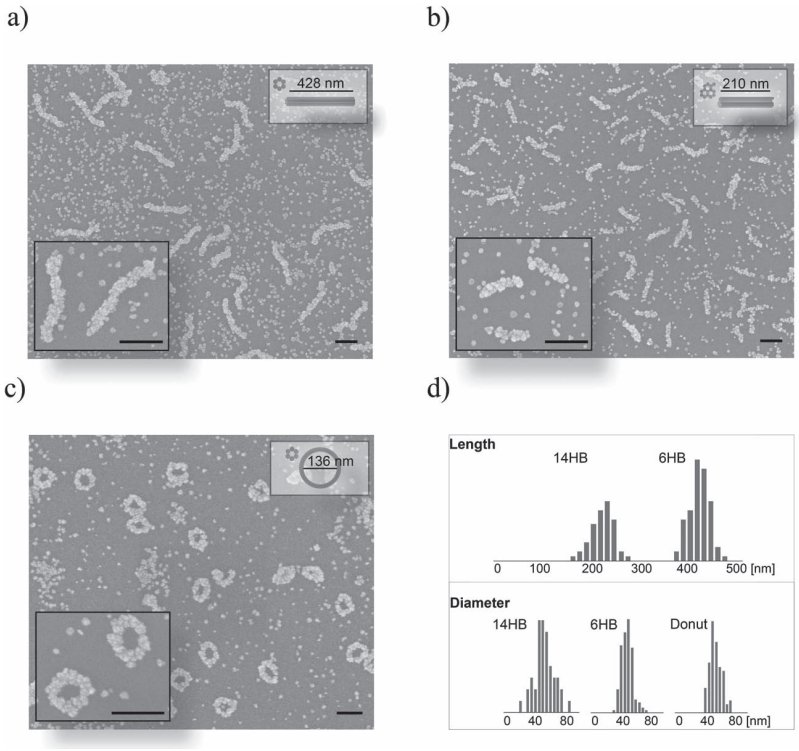

Figure 2. Fidelity of two-step metallization process. a) SEM image of metallized six-helix bundles on a silicon wafer. b) SEM image of metallized 14-helix bundles on a silicon wafer. c) SEM image of metallized nanodonuts on a silicon wafer. d) Contour length distribution of 14-helix bundles (14HB) and six-helix bundles (6HB, top) and distribution of bundle thicknesses for the 14-helix bundles, the six-helix bundles and donut (bottom). $N = 52, 102, 64, 140, 86$, respectively. All scale bars: 200 nm.

different solid substrates: carbon-coated electron microscope grids and silicon wafers with a 20 nm oxide layer. The particles coating the DNA origami structures act as nucleation sites for further metallization by deposition of gold ions (Au^+) from solution to the Au clusters as metallic gold (Au^0). By adjusting the incubation time, the pre-seeded structures can grow into continuously metallized objects of defined shapes with controlled length and diameter (**Figure 2**).

In the following, two Au cluster seeding strategies are described: seeding on substrates and seeding in solution. For the seeding process on substrates, the DNA origami structures are deposited on hydrophilic surfaces, either on plasma-treated carbon grids for later transmission electron microscope (TEM) imaging or on aminosilane-treated Si-wafers for later scanning electron microscope (SEM) imaging. After rinsing with H_2O, the DNA structures are exposed for 1 min to a 150 nM solution of positively charged Au clusters in H_2O followed by another rinsing step. For successful seeding in solution, the aggregation of the negatively charged DNA objects by the positively charged Au clusters poses a severe problem. This can be prevented by the application of a high concentration of positively charged Au clusters during the seeding process. Therefore, a 1 nM solution of DNA origami particles was incubated for 5 min in a 375 nM solution of Au clusters dissolved in water. Interestingly, the DNA objects withstand the lack of stabilizing Mg^{2+} ions in the presence of positively charged Au clusters (Supporting Information (SI), Figure S1). The Au-seeded DNA structures were then deposited on a Si wafer or a carbon-coated grid and were ready for the enhancement process.

For the following gold-enhancement process of the Au-seeded DNA structures we used a commercially available enhancement kit (EM HQ Gold Enhance, Nanoprobes, USA) and followed the suppliers' instructions. We found an incubation time of 30 s to give the best results for our purposes. Shorter enhancement times resulted in lack of growth continuity—EM images reveal separated gold clusters along the origami constructs—while longer enhancement times increase the background and lead to large shapeless gold particles. The objects were analyzed before (uranyl acetate staining, Figure 1,2) and after (no staining, SI, Figure S1) cluster seeding and finally after the enhancement process (no staining, Figure 1) with TEM and SEM. Both methods are complementary in assessing the shapes of the native and the metallized DNA origami structures.

To quantify the growth fidelity and narrow size distribution of particles generated with our strategy, we chose three DNA origami designs for detailed examination: the 428 nm long six-helix bundle, the 210 nm long 14-helix bundle and a nanodonut based on a curved[21] and circularized six-helix bundle with a diameter of 136 nm (Figure 2). Since the particle growth starts from multiple small nucleation sites distributed over the whole structure, a completely smooth surface was not achievable. From the obtained electron microscope images we conclude that the grains growing from the individual nucleation sites touch each other only after a certain growth time. To finally prove the growth continuity of the metalized objects, electrical conductivity measurements are currently underway. We found metallization parameters to routinely obtain structures with an extremely narrow length distribution and feature thicknesses of only 50–60 nm, which is considerably smaller than recently published results on DNA origami metallization.[19] Wide-field images of particles were used to determine the size distribution of the shape-defined metal nanoparticles under a given set of metallization parameters. For the six-helix bundles (Figure 2a), which have a length of 428 nm and a diameter of 6 nm as native DNA objects, we found metallized objects of 438 nm length with an average deviation of 4% or 16 nm. Noteworthy, the maximum observed error is less than 17% or 70 nm. The average diameter of the metallized objects is 56 nm with a mean deviation of 8 nm. For the shorter 14-helix bundles, which are natively 210 nm long and 10 nm wide, we found 221 nm (±14 nm) long metal nanoparticles with a width of 60 nm (±18 nm) (Figure 2b) and the average thickness of the donut ring is 53 nm

NANO small

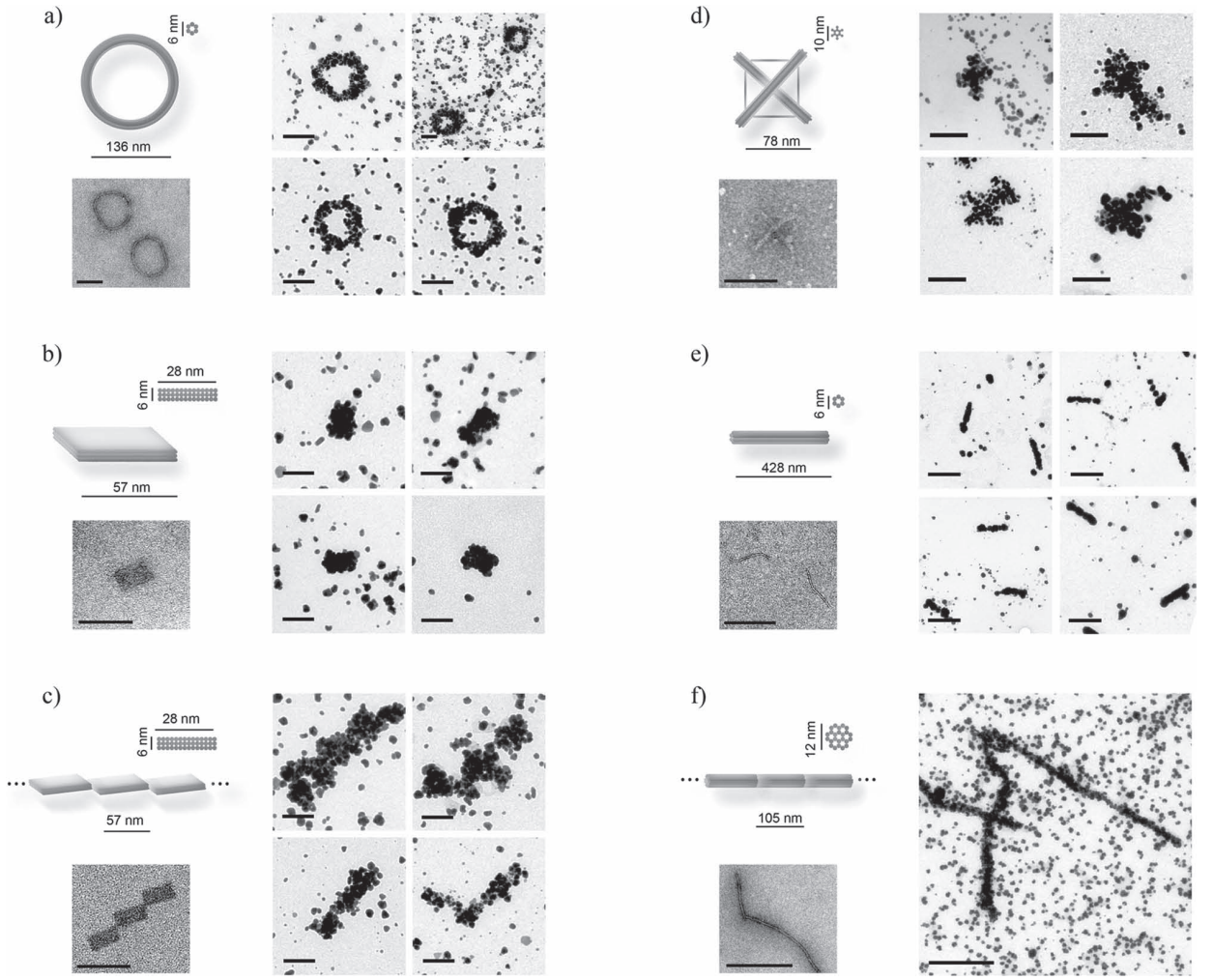

Figure 3. Metallization of arbitrarily shaped DNA origami nanostructures. Computer models, native DNA objects after negative staining with uranyl acetate and metallized objects are shown. a) Six-helix bundle donut. Native dimensions: 136 nm overall diameter, 6 nm strut diameter. b) 14 × 3-helix cuboid. Native dimensions: 60 nm × 30 nm × 6 nm. c) Corner-to-corner multimerized cuboids of (b). d) 12-helix bundle kite. Native strut length: 110 nm, 10 nm height. e) Six-helix bundles seeded in solution. Native dimensions: 428 nm length, 6 nm diameter. f) Multimerized 24-helix bundle. 105 nm monomer length, 12 nm diameter. Scale bars: a,b,c,d): 100 nm, e,f): 500 nm.

(±8 nm) (Figure 2c). By comparing the total volumes of well-defined nanoparticles with the volumes of background particles and particles of undefined shape on Si substrates, we conclude that more than 81% of the deposited material is converted into particles of desired shape and size (SI, Figure S2). Nonetheless, significant amounts of background particles can be found on all substrates. We were able to eliminate the influence of the amount of staple oligonucleotides on the background particle formation as described by Liu et al.[19] by purifying the DNA origami structures through gel electrophoresis. We further tested several methods to completely suppress the formation of background particles on carbon-coated TEM grids, e.g., by varying the concentration of $MgCl_2$ during the washing steps or by passivating the surface with BSA and Tween-20 (SI, Figure S3). None of our attempts yielded consistently better results than those obtained when applying the protocol described in the experimental section. However, the background was reduced considerably by seeding the DNA structures in solution followed by spin filter purification (Figure 1d). In our studies, we optimized the conditions to minimize the formation of background particles on carbon-coated grids and then applied the established protocol without further modification to Si wafers. We therefore believe that optimizing the growth conditions for silicon substrates can lead to further background reduction.

We finally set out to metallize a number of DNA origami objects with a wide variety of shapes and overall length ranging from 60 nm to several micrometers with the method described above. **Figure 3** shows the results for the metallization of DNA shapes as diverse as the six-helix bundles of Figure 1, the DNA nanodonut of Figure 2, a cuboid,[20] corner-to-corner polymerized cuboids, a DNA kite,[24] and a 100 nm-long 24-helix bundle that forms micrometer-long straight polymers. For all structures, the underlying shape is clearly recognizable. The final shape of the metallized DNA origami structure is affected by the development time and

the quantity of gold seeds accessible for the gold enhancement process. For longer development times the pre-defined shapes vanish due to increase of Au^0 deposition on the Au-cluster-seeded DNA structures. Overall, we found the features of our DNA structures to be distinguishable in the metallized version, if the distances between internal DNA struts were greater than 50 nm. It is worth mentioning that the speed of the development process decreases with the number of accessible Au cluster seeds, which in turn depends on the concentration and size of the Au-seeded DNA objects on the substrates.

We have demonstrated a universal strategy for the generation of arbitrarily shaped metal nanoparticles. This is achieved by a two-step procedure where DNA origami objects of defined shapes and dimensions are first incubated with positively charged 1.4 nm gold clusters, which in a second step act as seeds for the electroless deposition of gold ions from solution. We found a narrow size distribution of our continuously metallized structures with a mean deviation of less than 5% for the long axis and 17% for the short axis while only 19% of the material deposited on the substrate is part of unspecifically grown clusters. In general, metallized structures of complex shapes are expected to show unprecedented optical and electronic behavior. Considering the wide variety of shapes and sizes that DNA origami structures can adopt[15,21,22,24–26] we anticipate that DNA-origami-templated metallization will constitute a general path to the generation of complex materials. The possibility to selectively address DNA origami structures with gold nanoparticles and chemical groups[16–18,27,28] will enable the controlled metallization of seeding sites which are arranged in space with nanometer precision.[20,29]

Experimental Section

Annealing Process of DNA Origami Structures: All DNA origami objects were folded and purified according to the same basic protocol with variations in the folding times and the Mg^{2+} concentrations. For each structure, 10 nM of the corresponding scaffold (six-helix bundle, 24-helix bundle, and donut: p7560, cuboid: p8064, 14-helix bundle, and kite: p8634) were mixed with a staple mix containing 100 nM of each staple. The complete folding mixture amounted to 20 μL and contained next to the staple and scaffold strands 5 mM Tris, 1 mM EDTA (pH 8 at room temperature) and the following Mg^{2+} concentrations: 15 mM for the six-helix bundle, the donut, the 14-helix bundle, and the Kite, and 18 mM for the 24-helix bundle and the FRET block. The folding mixture was then exposed to structure-specific thermal annealing ramps. All these ramps started with a heating step to 80 °C for 4 min, followed by cooling to 60 °C at a cooling rate of 1 °C per 4 min. The following cooling from 60 °C to 20 °C was performed at 1 °C per 20 min (14 h) for the six-helix bundles and the donut, at 1 °C per 30 min (20 h) for the FRET block, and at 1 °C per 60 min (40 h) for the 14-helix bundle, the 24-helix bundle, and the kite.

Purification of DNA Origami Structures: DNA origami objects were purified by agarose gel electrophoresis. We ran a 2% agarose gel in 0.5× TBE buffer, soaked in ethidium bromide 5 μM and cut out the favored bands to extract them with Freeze'N'Squeeze spin columns (Bio-Rad, Germany).

Two-Step Metallization with Seeding in Solution: 400 μL H_2O were added to 25 μL DNA origami objects (2 nM in 5 mM Tris, 1 mM EDTA and 18 mM $MgCl_2$) and spun through an Amicon Ultra filter (0.5 mL, 100 K, Millipore, USA) at 16 000 rcf for 5 min in a Biofuge fresco centrifuge (Kendro, Thermo Fisher Scientific Inc., USA). Then we added 0.5 μL of 300 μM Nanogold solution and 400 μL H_2O to the DNA origami solution, mixed it with a Vortex Genie 2 (Scientific Industries, Inc., USA) and spun the solution in the same Amicon Ultra filter again at 16 000 rcf for another 5 min. Subsequently, four times a volume of 400 μL H_2O was added to the Amicon Ultra filter and spun each time at 16 000 rcf. To recover the sample, we placed the Amicon Ultra filter upside down in a new centrifuge tube and spun at 900 rcf for 3 min. The solution of seeded DNA objects was applied for two minutes on hydrophylic formvar-carbon grids. The grids were washed with H_2O and ready for the gold enhancement process.

Two-Step Metallization with Seeding and Electroless Deposition on EM Grids: We applied 1.5 μL DNA origami objects (2 nM) for 2 min on hydrophylic formvar–carbon grids. Grids were washed with H_2O and placed bottom up on a drop of 1.4 nm positively charged Nanogold solution (150 nM, Nanoprobes, USA) for 1 min. Excess of Au nanoclusters were sucked off with Whatman filterpaper. After washing the grids with H_2O, they were air-dried.

Two Step Metallization with Seeding and Electroless Deposition on Silicon Wafers: We applied 10 μL DNA origami (0.2 nM) for 2 min on passivated silicon wafers. Wafers were washed with H_2O and dried with nitrogen. Subsequently, we covered the silicon wafers with 10 μL of a 1. 4 nm positively charged Nanogold solution (150 nm, Nanoprobes, USA) for 1 min. After washing the grids with H_2O, they were dried with nitrogen.

Gold Enhancement: In the second step we enhanced Au nanoclusters with Gold Enhancement for EM (Nanoprobes, USA) following the instructions of the supplier. The developing time for optimal particle size was 30 s.

Supporting Information

Supporting Information is available from the Wiley Online Library or from the author.

Acknowledgements

We thank David M. Smith, Björn Högberg, Deborah K. Fygenson and Theobald Lohmueller for helpful discussions, Friedrich C. Simmel for reading the manuscript and Christoph Schaffer for the preparation of the silicon wafers. The financial support of the Volkswagen Foundation and NIM are gratefully acknowledged.

[1] N. C. Seeman, *J. Theor. Biol.* **1982**, *99*, 237.
[2] N. C. Seeman, *Ann. Rev. Biochem.* **2010**, *79*, 65
[3] D. Zanchet, C. M. Micheel, W. J. Parak, D. Gerion, A. P. Alivisatos, *Nano Lett.* **2001**, *1*, 32.
[4] W. U. Dittmer, F. C. Simmel, *Appl. Phys. Lett.* **2004**, *85*, 633.
[5] S. Beyer, P. Nickels, F. C. Simmel, *Nano Lett.* **2005**, *5*, 719.

[6] S. A. Claridge, H. W. Liang, S. R. Basu, J. M. J. Fréchet, A. P. Alivisatos, *Nano Lett.* **2008**, *8*, 1202.
[7] K. Keren, M. Krueger, R. Gilad, G. Ben-Yoseph, U. Sivan, E. Braun, *Science* **2002**, *72*, 297.
[8] M. Mertig, L. C. Ciacchi, R. Seidel, W. Pompe, A. De Vita, *Nano. Lett.* **2002**, *2*, 841.
[9] S. H. Park, R. Barish, H. Li, J. H. Reif, G. Finkelstein, H. Yan, T. H. LaBean, *Nano Lett.* **2005**, *5*, 693.
[10] K. Keren, R. S. Berman, E. Braun, *Nano Lett.* **2004**, *4*, 323.
[11] Y. Liu, W. Meyer-Zaika, S. Franzka, G. Schmid, M. Tsoli, H. Kuhn, *Angew. Chem. Int. Ed.* **2003**, *42*, 2853.
[12] H. J. Kim, Y. Roh, B. Hong, *Langmuir* **2010**, *26*, 18315.
[13] P. Nickels, W. U. Dittmer, S. Beyer, J. P. Kotthaus, F. C. Simmel, *Nanotechnology* **2004**, *15*, 1524.
[14] P. W. K. Rothemund, *Nature* **2006**, *440*, 297.
[15] S. M. Douglas, H. Dietz, T. Liedl, B. Högberg, F. Graf, W. M. Shih, *Nature* **2009**, *459*, 414.
[16] H. Gu, J. Chao, S. J. Xiao, N. C. Seeman, *Nature* **2010**, *465*, 202.
[17] B. Ding, Z. Deng, H. Yan, S. Cabrini, R. Z. Zuckermann, J. Bokor, *J. Am. Chem. Soc.* **2010**, *132*, 3248.
[18] S. Pal, Z. Deng, B. Ding, H. Yan, Y. Liu, *Angew. Chem. Int. Ed.* **2010**, *122*, 2760.
[19] J. Liu, Y. Geng, E. Pound, S. Gyawali, J. R. Ashton, J. Hickey, A. T. Woolley, J. N. Harb, *ACS Nano* **2011**, *5*, 2240.
[20] I. Stein, V. Schüller, P. Böhm, P. Tinnefeld, T. Liedl, *ChemPhysChem* **2011**, *12*, 689.
[21] H. Dietz, S. M. Douglas, W. M. Shih, *Science* **2009**, *325*, 725.
[22] W. Liu, H. Zhong, R. Wang, N. C. Seeman, *Angew. Chem. Int. Ed.* **2010**, *50*, 264.
[23] S. M. Douglas, J. J. Chou, W. M. Shih, *Proc. Natl. Acad. Sci. USA* **2007**, *104*, 6645.
[24] T. Liedl, B. Hogberg, J. Tytell, D. E. Ingber, W. M. Shih, *Nat. Nanotechnol.* **2010**, *5*, 520.
[25] D. R. Han, S. Pal, Y. Liu, H. Yan, *Nat. Nanotechnol.* **2010**, *5*, 712.
[26] E. S. Andersen, M. Dong, M. M. Nielsen, K. Jahn, R. Subramani, W. Mamdouh, M. M. Golas, B. Sander, H. Stark, C. L. P. Oliveira, J. S. Pedersen, V. Birkedal, F. Besenbacher, K. V. Gothelf, J. Kjems, *Nature* **2009**, *459*, 73.
[27] M. Fischler, U. Simon, H. Nir, Y. Eichen, G. A. Burley, J. Gierlich, P. M. E. Gramlich, T. Carell, *Small* **2007**, *3*, 1049.
[28] S. Pal, R. Varghese, Z. Deng, Z. Zhao, A. Kumar, H. Yan, Y. Liu, *Angew. Chem. Int. Ed.* **2011**, *50*, 4176.
[29] C. Steinhauer, R. Jungmann, T. L. Sobey, F. C. Simmel, P. Tinnefeld, *Angew. Chem. Int. Ed.* **2009**, *48*, 8870.

Received: March 11, 2011
Revised: April 1, 2011
Published online: May 24, 2011

4 DNA-Based Self-Assembly of Chiral Plasmonic Nanostructures with Tailored Optical Response

A challenge in the field of self-assembly is the generation of materials, which are programmable and flexible in design, functional and suitable for large-scale fabrications. Furthermore, it is necessary for optical applications that the material has an isotropic response in the visible range of light with spectral control. To influence the properties of light in the visible range with plasmonic structures it is necessary to create structures with a smaller size than the wavenlength of the incident light (~1% of the wavelength) (cf., chapter 2). Therefore, for visible light it is required to create structures at the nanometer scale with arrangements of metallic or dielectric elements with nanometer precision. On the one side there have already been many sophisticated studies from lithography for arrange plasmonic elements, but most of these are showing two-dimensional nanostructures, or three-dimensional structures, which are inherently difficult to build and all of structures are close to the micrometer scale [74,75].

On the other side there are bottom-up approaches with natural molecules which have already demonstrated that plasmonic nanoparticles can be arranged with sub 10 nm precision [46,47,76]. However, all of these approaches are lacking in possibility to arrange the nanoparticles in arbitrary conformations as required. In particular, neither the helical pitch and diameter, nor the distance between the particles, nor the wavelength of the response was controlled. All of the them are using molecules predesigned by mother nature as well as chiral hierarchical assemblies of such molecules.

The associated publication P2 was the first study showing that distinct optical properties could be achieved from arranging plasmonic elements with the help of DNA nanotechnology. In the associated publication we used the DNA origami method to produce plasmonic nanostructures which display a collective optical behavior. For this, we chose a chiral assembly of the metal nanoparticles into a helix structure (**Figure 4.1**). As previously explained in chapter 2, such chiral plasmonic structures show a strong plasmonic circular dichroism (CD) in the visible range of light. The plasmonic CD signal is easy to detect with a standard UV-Vis CD spectrometer. Opposite chiralities of plasmonic helices show an inverted CD signal. It is therefore possible to clearly distinguish between both chiralities from solution measurements. The CD signal of a plasmonic helix illuminated from all sides shows a bisignated (dip-peak) shape (**Figure 4.1**). With the created chiral structures we were able to demonstrate macroscopic polarization rotation effects depending on the chirality of the helices.

In addition, the influence of the nanohelices on the refractive index was investigated. The theory indicates that a change of the refractive index is predicted if the material shows a strong chirality [77,78]. It has not been possible yet to measure any change in the refractive index which might be due to the high resistance for currents in such small plasmonic structures.

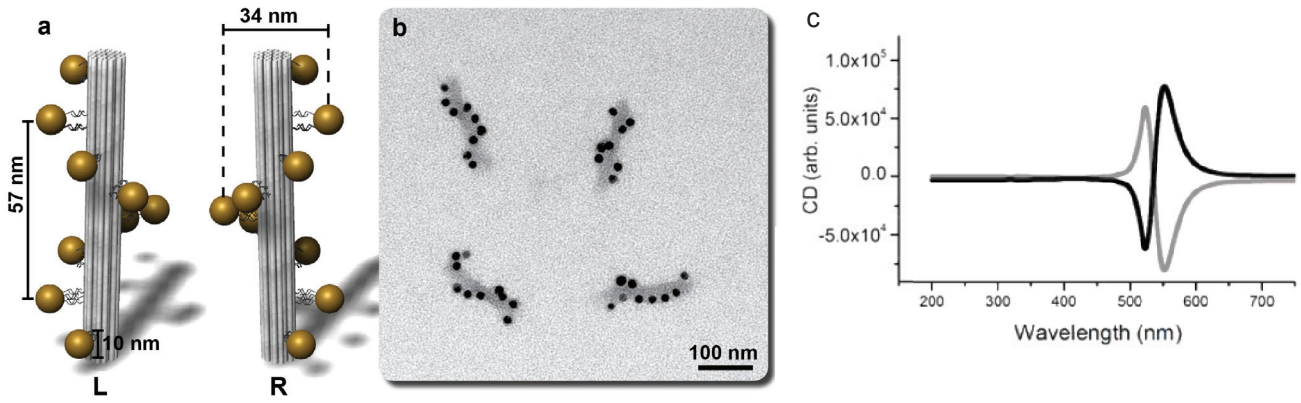

Figure: a, Schematic drawing of a left- and right-handed gold nanohelix. **b**, Transmission electron micrograph of left-handed nanohelices. **c**, Theoretical circular dichroism signal of left-handed (grey) and right-handed (black) gold nanohelices.

To summarize, we were able to generate artificial plasmonic nanostructures that were customized to the optical theories of A. O. Govorov [61]. Thus we successfully showed that the DNA origami method is a promising tool to create plasmonic structures with precisely designed optical properties. It can be envisioned that the nanohelices from associated publication P2 can be even more sensitive bio-sensors in the surrounding areas of chiral bio-molecules (e.g. BSA, flavin or sugar) than non-chiral plasmonic particles (cf., chapter 2: chiral bio-molecules can couple to non-chiral plasmonic nanoparticles to generate a CD signal at the plasmonic resonance [48-50] (see also chapter 7)). It is expected that chiral bio-molecules of the same chiralitiy as the nanohelices result in an observeable change in the plasmonic CD signal. Until now it was not possible to observe significant and reliable changes in the plasmonic CD spectra even at high concentration of the surrounding chiral bio-molecules. This can be due to the size difference of nearly two magnitudes of the nanohelices compared to the chiral bio-molecules.

Furthermore, nanohelices were used as a chiral standard for cryo electron microscopy in a following project with the group of Grant J. Jensen (CalTech) [79]. A small start-up company was established from this cooperation which now sells nanohelices as chiral standards for cryo electron microscopes.

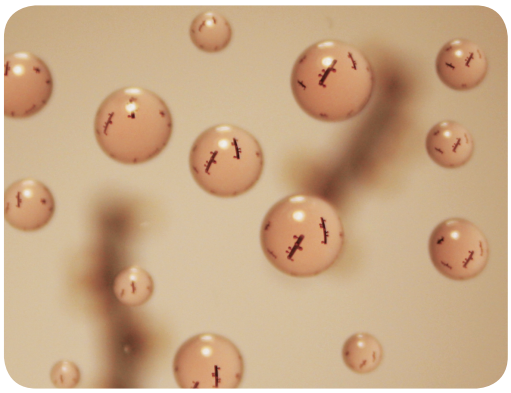

Figure 4.2: Artistic photograph of nanohelices in small droplets. Idea by Anton Kuzyk, Tim Liedl and Robert Schreiber. © Photo by Christoph Hohmann, Nanosystems Initiative Munich (NIM)

4.2 Associated publication P2

DNA-Based Self-Assembly of Chiral Plasmonic Nanostructures with Tailored Optical Response

by

Anton Kuzyk,* Robert Schreiber,* Zhiyuan Fan, Günther Pardatscher, Eva-Maria Roller, Alexander Högele, Friedrich C. Simmel, Alexander O. Govorov and Tim Liedl

*equal contribution

published in

Nature 2012, 483, 311-314

LETTER

doi:10.1038/nature10889

DNA-based self-assembly of chiral plasmonic nanostructures with tailored optical response

Anton Kuzyk[1]*†, Robert Schreiber[2]*, Zhiyuan Fan[3], Günther Pardatscher[1], Eva-Maria Roller[2], Alexander Högele[2], Friedrich C. Simmel[1], Alexander O. Govorov[3] & Tim Liedl[2]

Matter structured on a length scale comparable to or smaller than the wavelength of light can exhibit unusual optical properties[1]. Particularly promising components for such materials are metal nanostructures, where structural alterations provide a straightforward means of tailoring their surface plasmon resonances and hence their interaction with light[2,3]. But the top-down fabrication of plasmonic materials with controlled optical responses in the visible spectral range remains challenging, because lithographic methods are limited in resolution and in their ability to generate genuinely three-dimensional architectures[4,5]. Molecular self-assembly[6,7] provides an alternative bottom-up fabrication route not restricted by these limitations, and DNA- and peptide-directed assembly have proved to be viable methods for the controlled arrangement of metal nanoparticles in complex and also chiral geometries[8–14]. Here we show that DNA origami[15,16] enables the high-yield production of plasmonic structures that contain nanoparticles arranged in nanometre-scale helices. We find, in agreement with theoretical predictions[17], that the structures in solution exhibit defined circular dichroism and optical rotatory dispersion effects at visible wavelengths that originate from the collective plasmon–plasmon interactions of the nanoparticles positioned with an accuracy better than two nanometres. Circular dichroism effects in the visible part of the spectrum have been achieved by exploiting the chiral morphology of organic molecules and the plasmonic properties of nanoparticles[18–20], or even without precise control over the spatial configuration of the nanoparticles[12,21,22]. In contrast, the optical response of our nanoparticle assemblies is rationally designed and tunable in handedness, colour and intensity—in accordance with our theoretical model.

To demonstrate the potential of DNA origami for the programmable and nanometre-precise design of plasmonic nanostructures, we targeted an optical response that emerges as a collective effect from spatially precisely arranged multiple nanoparticles in close proximity, and that requires genuinely three-dimensional structures. The response of helically arranged metallic nanocrystals to an electromagnetic field meets both criteria. Much like the circular dichroism (CD, the differential absorption of left and right circularly polarized light) effect seen with 'optically active' chiral molecules such as DNA and proteins that exhibit CD in the ultraviolet and infrared ranges owing to the electronic and vibronic excitations of their chiral secondary structure[23], strong CD signals in the visible spectrum have been predicted to occur through collective Coulomb interaction of plasmonic dipoles in chiral assemblies of metal nanoparticles[17]. (See Supplementary Information notes 1 and 2 for information on naturally occurring CD, and on the theoretical framework of plasmon-induced CD.)

To create helical nanoparticle assemblies, we used the DNA origami[15,16] approach where hundreds of rationally designed 'staple' oligonucleotides are hybridized to a long single-stranded DNA scaffold to force it into a specific two- or three-dimensional shape. The resulting objects are fully addressable by their DNA sequence, enabling further decoration and functionalization in a unique, sequence-specific manner[24]. Geometrical and material parameters can be tailored by simple adjustments of the design and fabrication protocols, which should make it feasible to quantitatively tune the optical activity of such nanostructures dispersed in solution.

Figure 1a illustrates the nanostructure design (design details and DNA sequences are given in Supplementary Information note 3). It is based on DNA origami 24-helix bundles that offer nine helically arranged attachment sites for plasmonic particles coated with single-stranded DNA, here gold nanoparticles with a diameter of 10 nm. By using nanoparticles covered with multiple linker strands, we can avoid yield-lowering purification procedures and instead add an excess of modified gold particles for hybridization to the DNA structures; unconjugated gold particles are simply removed for re-use in later experiments. The quality of the assemblies was assessed by transmission electron microscopy (TEM) (Fig. 1b) (experimental details and additional TEM images can be found in Supplementary Information note 4). The strength of the optical activity critically depends on the quality of the assembled structures[25], so we improved our experimental protocol to achieve a nanoparticle attachment yield of 96% and 98% per site and an overall yield of 77% and 86% of perfect assemblies of right- and left-handed helices with nine nanoparticles, respectively (Supplementary Information note 5). Most of the imperfect structures exhibited only a single defect within an otherwise well-formed helix. Helices stored for three months at 4 °C were still intact (Supplementary Information note 6). As illustrated in Fig. 1c, CD measurements were then carried out on solutions containing left- or right-handed nanohelices.

Left-handed helical arrangements of plasmonic particles are expected to produce a CD signal with a characteristic bisignate peak–dip shape, with the peak centred around the plasmon resonance frequency. Right-handed helices should produce a vertically mirrored dip–peak signal. Indeed, CD spectra measured on samples with gold nanoparticle assemblies of both helicities exhibited the anticipated signatures (Fig. 2a). These responses arise because the helical arrangement of the gold nanoparticles results in coupled plasmon waves propagating along a helical path and causing increased absorption of those components of the incident light that are in accord with the handedness of the helices. The bisignate appearance of the CD signals results from the isotropic nature of our samples, in which the nanohelices are randomly oriented with respect to the direction of the incident light. The interactions between the individual gold particles within each helix create a splitting between the longitudinal and transverse modes of the electromagnetic wave, and these modes typically have opposite chirality. As a result, the plasmonic CD spectrum acquires the characteristic dip–peak shape (Supplementary Information note 2).

[1]Physik Department and ZNN/WSI, Technische Universität München, Am Coulombwall 4a, 85748 Garching, Germany. [2]Fakultät für Physik and Center for Nanoscience, Ludwig-Maximilians-Universität, Geschwister-Scholl-Platz 1, 80539 München, Germany. [3]Department of Physics and Astronomy, Ohio University, Athens, Ohio 45701, USA. †Present address: Department of Applied Physics, Aalto University School of Science, FI-00076 Aalto, Finland.
*These authors contributed equally to this work.

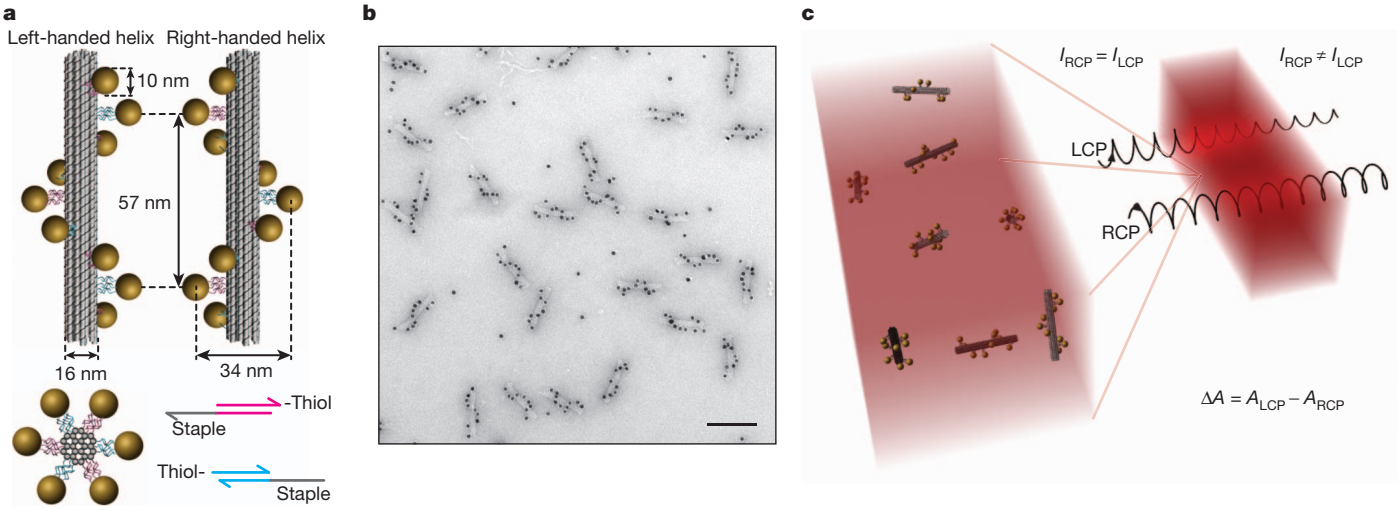

Figure 1 | Assembly of DNA origami gold nanoparticle helices and principle of circular dichroism. **a**, Left- and right-handed nanohelices (diameter 34 nm, helical pitch 57 nm) are formed by nine gold nanoparticles each of diameter 10 nm that are attached to the surface of DNA origami 24-helix bundles (each of diameter 16 nm). Each attachment site consists of three 15-nucleotide-long single-stranded extensions of staple oligonucleotides. Gold nanoparticles carry multiple thiol-modified DNA strands, which are complementary to these staple extensions. Nanoparticles and 24-helix bundles are mixed for assembly and the resulting constructs are gel-purified. **b**, TEM image of assembled left-handed gold nanohelices (scale bar, 100 nm). Analysis of the TEM data yields a 98% success rate for directed attachment of nanoparticles. **c**, Circular dichroism is measured as the difference in absorbance $\Delta A = A_{LCP} - A_{RCP}$ of left-hand-circularly polarized (LCP) and right-hand-circularly polarized (RCP) light as a function of wavelength. CD measurements were performed with a CD spectrometer on samples in cuvettes of optical path length 3 mm.

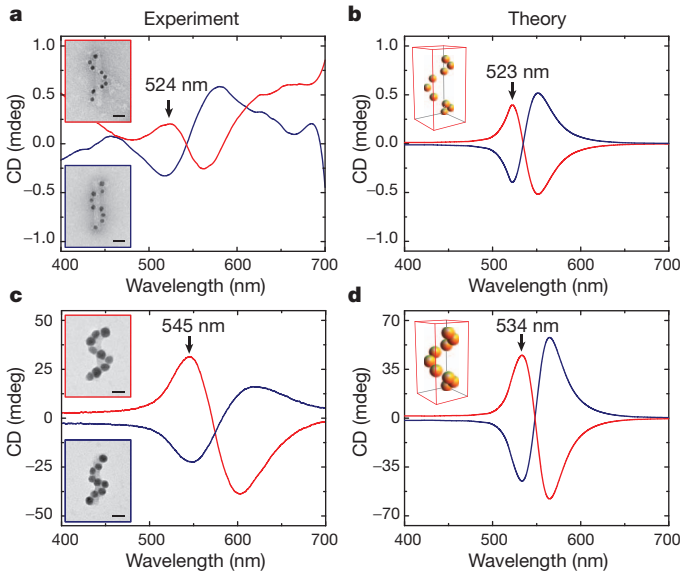

Figure 2 | Circular dichroism of self-assembled gold nanohelices. Experimental (**a** and **c**) and theoretical (**b** and **d**) CD spectra of left-handed (red lines) and right-handed (blue lines) helices of nine gold nanoparticles show characteristic bisignate signatures in the visible. **a**, CD spectra of nanohelices composed of 10-nm gold particles. The peak position in the spectra of left-handed helices (indicated by the arrow) coincides with the plasmon absorption resonance maximum. **b**, The theoretically predicted CDs for the geometries in **a** exhibit the same features; the peak positions and amplitudes are in remarkable agreement with the experiment. **c**, The CD signal increases owing to collective plasmonic enhancement by a factor of 400 for assemblies of nanoparticles with 16-nm diameter, rendering the noise in the spectra invisible (as in **a**). The peak position for left-handed helices exhibits a red-shift from 524 nm to 545 nm. **d**, The corresponding theoretical calculation predicts a 500-fold enhancement of the signal and a peak shift from 523 nm to 534 nm. The CD spectra were recorded at concentrations of nanohelices of 1.5 nM in **a** and 0.4 nM in **c**. The insets in **a** and **c** show TEM images of left-handed (red frame) and right-handed (blue frame) nanohelices (scale bars, 20 nm); the respective left-handed model geometries are depicted in the insets to **b** and **d**.

The experimental spectra agree well with theoretical calculations based on classical electrodynamics (Fig. 2b). The strongest absorption of circularly polarized light is predicted in the vicinity of the surface plasmon frequency of the metal nanoparticles, as experimentally seen with our assemblies. Strikingly, even the strength of the measured signals closely matches the magnitude predicted by the calculations. We further confirmed theoretically that the CD signal remains robust to positional perturbations of the individual particles (see Supplementary Information note 2).

The dipole theory[17] predicts that the CD signal becomes stronger when the particles are either larger or arranged in a tighter helix:

$$\mathrm{CD}_{\mathrm{plasmon}} \approx \frac{a_{\mathrm{NP}}^{12}}{R_0^8} \qquad (1)$$

where a_{NP} and R_0 are the nanoparticle and helix radii, respectively. We quantified the influence of particle size on the CD signal by using electroless deposition of metal from solution[26,27] onto 10-nm seeding particles that were already assembled into the helical geometry described in Fig. 1 (see Supplementary Information note 7 for experimental details and additional TEM images). CD measurements of these 'enhanced' samples showed two notable effects (Fig. 2c): the signal strength increased up to 400-fold for nanoparticle diameters of 16 ± 2 nm, and the absorption as well as the CD peak shifted to longer wavelengths. These results are consistent with theoretical predictions for the plasmonic CD effect. A simple estimate for the CD signal increase based on equation (1) and assuming a particle size of 16 nm yields an enhancement of about 280, and quantitative numerical calculations predict an enhancement of about 500. As in the experiments, the calculated CD for larger particles and the same helix radius is also red-shifted (Fig. 2d), which is typical for strongly interacting plasmonic nanocrystals[28]. Taken together, these observations illustrate that desired optical behaviour can be designed and realized by exploiting the collective interactions between plasmonic particles attached with close to 100% yield and positioned with nanometre-scale precision.

To generate CD at other wavelengths, we plated silver onto pre-assembled 10-nm gold particle helices and thereby produced a silver shell of about 3 nm around each of the gold nanoparticles. Plasmon resonances in silver occur at a shorter wavelength than in gold, so the

recorded CD spectra were shifted into the blue spectral region (Fig. 3a). To fine-tune the optical response to intermediate wavelengths, we used mixtures of gold and silver ions in the plating solution to grow alloy shells around the seed particles. Figure 3a presents a TEM image (upper inset) with the corresponding CD spectrum of an alloy-coated structure. As expected, the CD signal for the alloy helices appears at an intermediate wavelength (absorption spectra and additional CD spectra are presented in Supplementary Information note 8). Mixing of solutions containing different types of structures resulted in a linear superposition of the corresponding spectra (Fig. 3a). These experiments indicate the potential of our assembly method for the fabrication of optically active materials with customized spectral response.

To visualize the collective optical activity of our self-assembled nanohelices in a macroscopic optical experiment, we exposed gold nanoparticle helices to excessive amounts of silver ions during electroless metal deposition and thereby achieved a giant molar CD of around $10^8\,M^{-1}\,cm^{-1}$. The corresponding spectra are presented in Fig. 3b. Droplets of samples containing left-handed or right-handed helices and a non-helical control droplet were placed onto a glass slide between two linear polarizers. As demonstrated in Fig. 4 with polarization-resolved transmission images, the droplets with gold helices rotate the polarization angle of the linearly polarized light. Although our set-up is insensitive to polarization below 550 nm, rotation of the polarization axis of the linearly polarized light was detected for both right- and left-handed helices in the red band of the visible spectrum. The observation is in accordance with the effect of optical rotatory dispersion, which is characteristic of chiral materials exhibiting CD. In the case of our right-handed "metafluid"[29], the polarization axis is rotated clockwise (or counter-clockwise) at wavelengths above (or below) 560 nm; the opposite effect is seen with the left-handed nanohelices. The control sample containing isotropically dispersed 10-nm gold nanoparticles exhibited no such optical activity. Further details on the materials characteristics (anisotropy factor and specific rotation) can be found in Supplementary Information notes 8 and 9.

In future experiments we will explore the possibility of realizing materials with a negative refractive index without the requirement of either ε or μ being negative[30], using fluids with oriented or densely packed plasmonic helices, which should lead to a further increase of the chiral optical response. But irrespective of whether this goal can be realized, the present findings clearly establish DNA origami as a valuable addition to the existing tools at the material engineer's disposal for precisely arranging nanoparticles into assemblies with desired electric or magnetic properties.

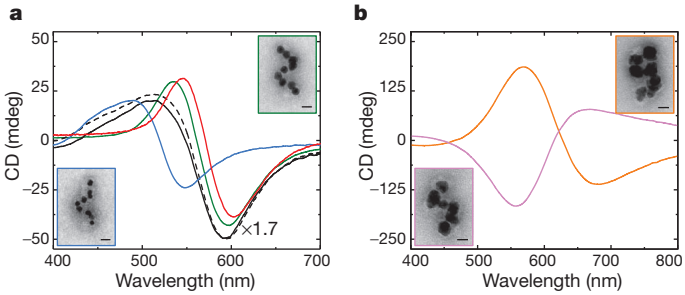

Figure 3 | Spectral tuning of circular dichroism by metal composition. **a**, A pronounced blueshift of the peak position in the CD response was achieved by depositing several nanometres of silver on gold nanoparticles of diameter 10 nm (blue spectrum of left-handed gold-core/silver-shell nanohelices; red spectrum from Fig. 2c is shown for reference). Growth of silver+gold alloy shells gives rise to an intermediate blueshift (green spectrum of left-handed gold-core/silver+gold-shell helices). Mixing of solutions that contain nanohelices of various metal compositions results in a superposition of individual CD responses (black spectrum): a 2:3 mixture of gold-core/silver-shell (blue spectrum) and gold-core/silver+gold-shell (green spectrum) exhibits CD close to the predicted superposition (dashed black line; black curves were rescaled by a factor of 1.7 for presentation purposes). **b**, Excessive metal deposition leads to the merging of nanoparticles and further enhancement of the CD signal for the left-handed (orange spectrum) and right-handed (purple spectrum) gold-core/silver-shell helices. The corresponding molar CD in the visible spectrum is huge with a strength of about $10^8\,M^{-1}\,cm^{-1}$. The CD spectra were recorded at concentrations of nanohelices of 0.4 nM in **a** and 40 pM in **b**. The insets in **a** and **b** show TEM images of left-handed (blue, green and orange frames) and right-handed (purple frame) nanohelices (scale bars, 20 nm).

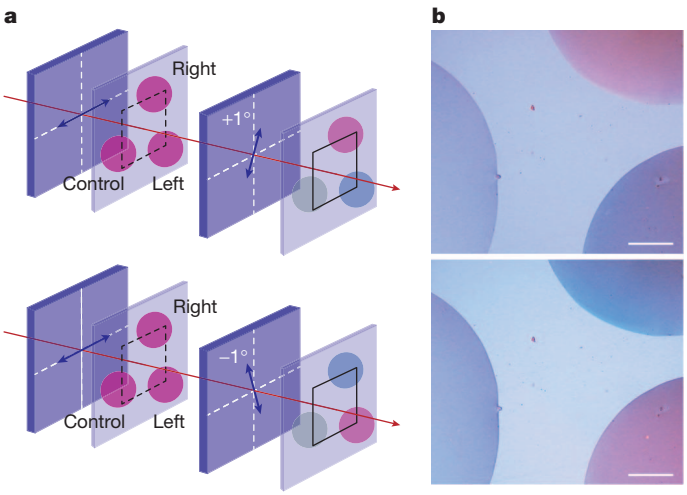

Figure 4 | Optical rotatory dispersion of self-assembled gold nanohelices. **a**, The macroscopic optical activity of the metafluid is demonstrated in polarization-resolved transmission by placing droplets of left-handed and right-handed nanohelices as well as a control droplet with isotropically dispersed gold nanoparticles between two linear polarizers. The components of the transmission set-up are ordered along the propagation path of white light as follows: linear polarizer, sample, linear analyser, screen (charge-coupled-device camera). The extinction characteristics of the linear polarizers render the set-up polarization-insensitive for wavelengths below 550 nm. **b**, Real-colour transmission images (scale bar, 1 mm) of the droplets for clockwise (top) and counter-clockwise (bottom) rotation of the analyser by one degree out of the orthogonal configuration. The droplets of right-handed and left-handed helices appear red in the top and bottom images, respectively, as a result of optical rotatory dispersion. Right- (or left-) handed nanohelices rotate the polarization axis of the transmitted light in positive (or negative) and negative (or positive) directions in the red and blue spectral bands, respectively. The rotation of the polarization in the red band is sensitively detected by the set-up, but green and blue components of white light illumination (below 550 nm) are not polarization-resolved and contribute only to the bluish background.

Received 12 September 2011; accepted 17 January 2012.

1. Liu, Y. & Zhang, X. Metamaterials: a new frontier of science and technology. *Chem. Soc. Rev.* **40,** 2494–2507 (2011).
2. Barnes, W. L., Dereux, A. & Ebbesen, T. W. Surface plasmon subwavelength optics. *Nature* **424,** 824–830 (2003).
3. Polman, A. Plasmonics applied. *Science* **322,** 868–869 (2008).
4. Soukoulis, C. M. & Wegener, M. Past achievements and future challenges in the development of three-dimensional photonic metamaterials. *Nature Photon.* **5,** 523–530 (2011).
5. Gansel, J. K. *et al.* Gold helix photonic metamaterial as broadband circular polarizer. *Science* **325,** 1513–1515 (2009).
6. Jones, M. R., Osberg, K. D., Macfarlane, R. J., Langille, M. R. & Mirkin, C. A. Templated techniques for the synthesis and assembly of plasmonic nanostructures. *Chem. Rev.* **111,** 3736–3827 (2011).
7. Fan, J. A. *et al.* Self-assembled plasmonic nanoparticle clusters. *Science* **328,** 1135–1138 (2010).
8. Seeman, N. C. Nanomaterials based on DNA. *Annu. Rev. Biochem.* **79,** 65–87 (2010).
9. Tan, S. J., Campolongo, M. J., Luo, D. & Cheng, W. Building plasmonic nanostructures with DNA. *Nature Nanotechnol.* **6,** 268–276 (2011).
10. Ding, B. *et al.* Gold nanoparticle self-similar chain structure organized by DNA origami. *J. Am. Chem. Soc.* **132,** 3248–3249 (2010).
11. Mastroianni, A. J., Claridge, S. A. & Alivisatos, A. P. Pyramidal and chiral groupings of gold nanocrystals assembled using DNA scaffolds. *J. Am. Chem. Soc.* **131,** 8455–8459 (2009).
12. Chen, W. *et al.* Nanoparticle superstructures made by polymerase chain reaction: collective interactions of nanoparticles and a new principle for chiral materials. *Nano Lett.* **9,** 2153–2159 (2009).

13. Sharma, J. *et al.* Control of self-assembly of DNA tubules through integration of gold nanoparticles. *Science* **323,** 112–116 (2009).
14. Chen, C.-L. & Rosi, N. L. Preparation of unique 1-D nanoparticle superstructures and tailoring their structural features. *J. Am. Chem. Soc.* **132,** 6902–6903 (2010).
15. Rothemund, P. W. K. Folding DNA to create nanoscale shapes and patterns. *Nature* **440,** 297–302 (2006).
16. Douglas, S. M. *et al.* Self-assembly of DNA into nanoscale three-dimensional shapes. *Nature* **459,** 414–418 (2009).
17. Fan, Z. & Govorov, A. O. Plasmonic circular dichroism of chiral metal nanoparticle assemblies. *Nano Lett.* **10,** 2580–2587 (2010).
18. Schaaff, T. G. & Whetten, R. L. Giant gold–glutathione cluster compounds: intense optical activity in metal-based transitions. *J. Phys. Chem. B* **104,** 2630–2641 (2000).
19. Shemer, G. *et al.* Chirality of silver nanoparticles synthesized on DNA. *J. Am. Chem. Soc.* **128,** 11006–11007 (2006).
20. George, J. & Thomas, K. G. Surface plasmon coupled circular dichroism of Au nanoparticles on peptide nanotubes. *J. Am. Chem. Soc.* **132,** 2502–2503 (2010).
21. Guerrero-Martínez, A. *et al.* Intense optical activity from three-dimensional chiral ordering of plasmonic nanoantennas. *Angew. Chem. Int. Edn Engl.* **50,** 5499–5503 (2011).
22. Guerrero-Martínez, A., Alonso-Gómez, J. L., Auguié, B., Cid, M. M. & Liz-Marzán, L. M. From individual to collective chirality in metal nanoparticles. *NanoToday* **6,** 381–400 (2011).
23. Berova, N., Nakanishi, K. & Woody, R. W. *Circular Dichroism: Principles and Applications* 2nd edn (Wiley-VCH, 2000).
24. Tørring, T., Voigt, N. V., Nangreave, J., Yan, H. & Gothelf, K. V. DNA origami: a quantum leap for self-assembly of complex structures. *Chem. Soc. Rev.* **40,** 5636–5646 (2011).
25. Fan, Z. & Govorov, A. O. Helical metal nanoparticle assemblies with defects: plasmonic chirality and circular dichroism. *J. Phys. Chem. C* **115,** 13254–13261 (2011).
26. Schreiber, R. *et al.* DNA origami-templated growth of arbitrarily shaped metal nanoparticles. *Small* **7,** 1795–1799 (2011).
27. Pilo-Pais, M., Goldberg, S., Samano, E., LaBean, T. H. & Finkelstein, G. Connecting the nanodots: programmable nanofabrication of fused metal shapes on DNA templates. *Nano Lett.* **11,** 3489–3492 (2011).
28. Halas, N. J., Lal, S., Chang, W.-S., Link, S. & Nordlander, P. Plasmons in strongly coupled metallic nanostructures. *Chem. Rev.* **111,** 3913–3961 (2011).
29. Urzhumov, Y. A. *et al.* Plasmonic nanoclusters: a path towards negative-index metafluids. *Opt. Express* **15,** 14129–14145 (2007).
30. Pendry, J. B. A chiral route to negative refraction. *Science* **306,** 1353–1355 (2004).

Supplementary Information is linked to the online version of the paper at www.nature.com/nature.

Acknowledgements We thank H. Dietz and G. Acuna for experimental advice and B. Yurke, E. Graugnard, J. O. Rädler and J. P. Kotthaus for discussions. We acknowledge J. Buchner and M. Rief for giving us access to their CD spectrometers, E. Herold for help with the CD measurements, and T. Martin and S. Kempter for assistance. We also thank D. M. Smith for carefully reading the manuscript. This work was funded by the Volkswagen Foundation, the DFG Cluster of Excellence NIM (Nanosystems Initiative Munich) and the NSF (USA).

Author Contributions A.K., R.S., A.H., F.C.S., A.O.G. and T.L. designed the research. A.K., R.S. and E.-M.R. designed the nanostructures and performed CD measurements. G.P. produced and purified gold samples. A.H. and T.L. investigated ORD effects. Z.F. and A.O.G. performed theoretical calculations. A.K., R.S. and A.O.G. prepared the figures and A.K., R.S., A.H., F.C.S., A.O.G. and T.L. wrote the manuscript.

Author Information Reprints and permissions information is available at www.nature.com/reprints. The authors declare no competing financial interests. Readers are welcome to comment on the online version of this article at www.nature.com/nature. Correspondence and requests for materials should be addressed to T.L. (tim.liedl@lmu.de).

5 Chiral Plasmonic Material with Switchable Circular Dichroism

Studies on conformationally changing plasmonic structures are rare, because so far most plasmonic devices have been static. However, such dynamic plasmonic structures are a key necessity for future switchable metamaterials which can be used to dynamically control the refractive index of matter or are envisioned as devices for data storage. Switchable metamaterials have been created which use electric and magnetic properties of the material itself or are influenced by the change of the refractive index or the temperature [81-86]. Most of the structures are optically active in the infrared wavelength of light [82-84].

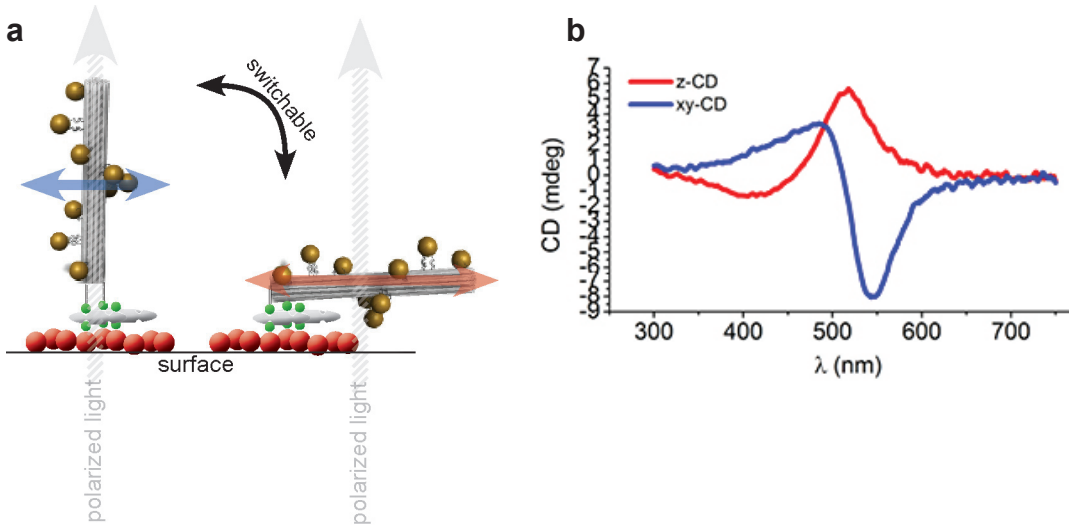

Figure 5.1: a, Schematic drawing of left-handed switchable nanohelices attached to a BSA-Biotin-Neutravidin coated surface. **b**, Typical circular dichroism signal from each plasmonic state of the nanohelices.

In the associated publication P3 we showed that we were able to produce a switchable metamaterial showing plasmonic activity in the visible range of light. In a simplified picture, for isotropically orientated helices, collective plasmonic excitation in a helix can be divided into plasmons parallel to the helix axis (z-CD) and plasmons perpendicular to the helix axis (xy-CD). These two plasmonic modes have an inverted CD signal to each other with small shifts of the excitation wavelength. By orientating our nanostructures orthogonal or parallel to the incidence of light, we demonstrated the excitation of either one of its plasmonic states. We were able to show the externally triggered reversible switching of a chiral plasmonic structure between its two plasmonic states (**Figure 5.1**). The plasmonic states are inverted to each other which enables the distinction between the two states.

Additionally to the alignment of nanohelices on surfaces as shown in associated publication P3, together with Bernard Yurke (BSU) the alignment of nanohelices was also performed in liquid crystals

of herring DNA. The long double-stranded herring DNA pieces align at high concentrations in the liquid crystal phase. By stressing the liquid crystal with pressure the direction of alignment could be controlled.

Currently, the alignment of the nanohelices in strong magnetic fields (>5 Tesla) is investigated by Alexander Högele's group (LMU). The alignment of nanohelices in solution might also be realized by attaching magnetic beads to one end of the nanostructures.

5.2 Associated publication P3

Chiral plasmonic material with switchable circular dichroism

by

Robert Schreiber, Ngoc Luong, Zhiyuan Fan, Anton Kuzyk, Tao Zhang, Philipp Nickels, David M. Smith, Bernard Yurke, Wan Kuang, Alexander O. Govorov, Tim Liedl

submitted to

Nature Communications

Chiral plasmonic material with switchable circular dichroism

Robert Schreiber[1], Ngoc Luong[2], Zhiyuan Fan[3], Anton Kuzyk[4,5], Philipp Nickels[1], Tao Zhang[1], David M. Smith[1], Bernard Yurke[2], Wan Kuang[2], Alexander O. Govorov[3,*], Tim Liedl[1,*]

[1]*Fakultät für Physik and Center for Nanoscience, Ludwig-Maximilians-Universität, 80539 München, Germany*

[2]*Department of Electrical and Computer Engineering, Boise State University, Boise, Idaho 83725, USA*

[3]*Department of Physics and Astronomy, Ohio University, Athens, Ohio 45701, USA*

[4]*Max-Planck-Institute for Intelligent Systems, 70569 Stuttgart, Germany*

[5]*Department of Applied Physics, Aalto University School of Science, FI-00076 Aalto, Finland*

** govorov@phy.ohiou.edu, tim.liedl@lmu.de*

Circular dichroism (CD) of an optically active material is a measure for the differential absorption of left- and right-handed circularly polarized light. The characteristic shape of the CD spectra recorded from proteins or DNA – usually apparent in the UV range – reflects their chiral geometry and originates from the superposition of CD signals of many randomly oriented molecules. Surface plasmon resonances in chiral assemblies of metal nanoparticles can give rise to strong and characteristic CD responses at visible wavelengths[1,2,3,4,5]. Here we show that by first aligning and then toggling the orientation of nanoparticle helices attached to a substrate, we were able to reversibly switch the optical response between two distinct spectra corresponding to either perpendicular or parallel helix orientation in respect to the light beam. The observed directional CD of our switchable plasmonic material is in good agreement with predictions based on dipole approximation theory. Such dynamic metamaterials introduce functionality into soft matter-based optical devices and may enable novel data storage schemes or signal modulators.

Manufacturing dynamic plasmonic materials that interact with visible light in a controllable fashion is challenging for a number of reasons: First, a metallic or dielectric substrate must be structured on a length-scale smaller than the wavelength of the exciting electromagnetic field. For the visible range this implies a characteristic scale of tens of nanometers, while for infrared (IR) wavelengths this requirement is relaxed to hundreds of nanometers[6,7]. Top-down fabrication methods are readily available for the latter length scale, and therefore remarkable progress has been already achieved for switchable plasmonic materials functioning in the IR and longer wavelengths[8,9,10]. Further, to dynamically alter optical responses of metamaterials, generally three approaches can be pursued: i) The electromagnetic properties of the meta-atoms are altered, which can be achieved, e.g., by controlling electric currents[11,12,13]. ii) The electromagnetic properties of the surrounding material are altered. This is equivalent to observing changes in the environment, which is an approach that is successfully applied[14], in particular in sensing applications[15,16,17,18]. iii) Changes in the material's geometry are enabled. This has been shown successfully for micrometer-scale geometries[19], however, the control of nanoscale geometries is only possible in a limited

way in lithographically produced structures. By using molecular linkers, it is possible to detect shifts of plasmonic resonances in absorption or scattering spectra upon aggregation or spatial reorganization of nanoparticles[20,21]. And while absorption and scattering measurements are certainly suitable methods for the detection of frequency shifts, controlled switching of CD spectra of chiral interacting plasmonic objects that are assembled with soft matter templates enables entirely new detection schemes and introduces mobility into metamaterial research. For example, recent studies observed the induced emergence of CD signals in solutions during the formation of nanorod aggregates[4] or the self-assembly of nanorod dimers of left- and right-handed chirality[5].

With the aim to create a dynamic two-state plasmonic material and to overcome the above-mentioned obstacles, we mounted switchable chiral nanostructures that are assembled by the DNA origami method on a glass substrate. The DNA origami method allows the assembly of complex two- and three-dimensional shapes by annealing hundreds of short ssDNA oligonucleotides with a long single-stranded DNA (ssDNA) during a thermo-controlled process[22,23,24,25,26] (**Fig. 1**). DNA nanostructures can be precisely decorated with metal particles with nanometer precision[27,28,29,30,31] and others and us recently demonstrated the assembly of gold particles into left- and right-handed nanohelices with perfectly controlled chirality[2,32]. Notably, these particle helices exhibit strong optical activity, which can be tuned by particle-directed metal deposition[2,33,34] through a wide range of the optical spectrum.

For our experiments, left-handed nanohelices (L-NHs) are attached via bio-linkers to a substrate in a way that they are switchable in orientation. For the L-NHs, 10 nm gold particles are attached to the surface of a rigid DNA origami 24-helix bundle to form a secondary helix with a diameter of 34 nm, a helical pitch of 57 nm and a total length of 79 nm. Each particle attachment site on the 24-helix bundle consists of three 15 nt long single-stranded extensions protruding from the DNA origami surface. Previous to assembly, the gold nanoparticles were functionalized with multiple thiol-modified DNA strands (**Fig. 1a**), which are complementary to the staple extensions. These particles were mixed with the assembled 24-helix bundles followed by gel-purification to remove unbound nanoparticles. Electron microscopy reveals the formation of the particle helices (**Fig. 1b**). The face at one end of the 24-helix bundle was modified with 10

biotin molecules to attach the L-NHs on a BSA-biotin-neutravidin coated quartz glass surface. Due to the multiple attachment sites and the large area of the DNA structure's face, the gold helices stand upright as it has also been shown previously with four- and six-helix bundles with thickened ends[34,35] (experimental details can be found in Supplementary Information Note S1). We performed single-molecule measurements to confirm the upright orientation of the gold nanohelices in solution as discussed later. Quartz surfaces coated with nanohelices were placed in a test tube for a step of additional silver growth on the nanoparticles surfaces (metal enhancement). It is worth mentioning that it is also possible to assemble the gold particles on the origami structures after they have been attached to the surface. For this procedure, surface-bound 24-helix bundles with bare attachment sites are placed in a solution containing the gold particles functionalized with the sequences complementary to the attachment sites (see Supplementary Information Note S2). The gold particle helices assemble within one hour, no further purification is required and the unbound gold particles can simply be removed with a pipette and later be reused for further assemblies. Another advantage of this method is that only nanohelices, which are actually standing upright, will offer all their attachment sites for gold nanoparticle binding.

For the CD measurements the NHs-covered quartz glass is placed perpendicular to the measurement light beam inside a buffer-filled cuvette. The NHs standing upright on the substrate are hence aligned parallel to the beam (**Fig. 2**). Due to the floppiness of the linkers and the roughness of the protein substrate, we did no expect to achieve perfect alignment, i.e., all helices standing exactly perpendicular to the surface. Nonetheless, we observed a dominant plasmonic CD signal of left-handed helices when the circularly polarized light passes through the samples along the helical z-axis (CD_z). Instead of the peak-dip (bisignated) CD of the L-NHs isotropically dispersed in solution (**Fig. 2a**) an inverted dip-peak spectrum with a dominant peak at the plasmon resonance is expected from theory (**Fig. 2b**, see Supplementary Information Note S3 for other geometries) and becomes apparent in the experiment at 528 ± 4 nm (**Fig. 2c**). In the next step the quartz glass was blow-dried and placed again into the emptied cuvette. This resulted in the alignment of the L-NHs parallel to the glass surface and therefore perpendicular to the light beam. As expected, the recorded CD spectrum shows a peak-dip signal with a dominant dip at 552 ± 4 nm (CD_{xy}). The CD_{xy} spectrum is flipped along the horizontal

axis and slightly red shifted (24 ± 8 nm) compared to the CD_z. The wavelength shift between CD_{xy} and CD_z agrees with the calculations for nanohelices in a uniform media. However it should be noted that the refractive index around the gold nanoparticles could also affect the wavelength shift to some extent (see Supplementary Information Note S4). To show the reversibility of the CD switching, the cuvette is filled again with buffer and a new CD spectrum is recorded. Judging from the recovered CD_z signal it can be concluded that the L-NHs stand up again and align parallel to the light beam, although some of the helices or individual nanoparticles may have been washed away and some helices may have stuck permanently to the substrate during the flushing and drying process, respectively (see also Supplementary Information Note S5). Another drying step switches the orientation and the CD signal once more. It is hence possible to reversibly switch between two alignment states and subsequently gather the signals of CD_z and CD_{xy} without changing the orientation of the substrate (see Supplementary Information Note S6 for switching CD spectra of right-handed nanohelices).

Our results agree well with theoretical models: The nanohelices dispersed in solution show the aforementioned peak-dip (bisignate) CD spectra in the visible[1,2]. This shape can be explained by a splitting between the plasmonic modes in a nanoparticle helix. On the opposite sides of the plasmon peak, the plasmon modes have opposite chiralities and therefore a CD spectrum receives its bisignate appearance (**Fig. 3a**). In addition to the slight frequency shift, the calculation shows that CD of transversely oriented helices results in a peak in the spectrum (for left-handed nanohelices) while the signal of longitudinally oriented helices results in a dip (**Fig. 3b**). Since the frequency shift is small, the total CD strength of non-oriented helices is significantly weakened due to the cancellation of CDs from all possible helix orientations. Consequently, an increase of the signal for aligned helices is expected. This increase, however, is strongly dependent upon the variation of orientation – recall the incomplete orientation due to surface roughness and floppiness of the linker molecules – of the nanohelices with respect to the incoming light beam. To account for this effect, we calculated the influence of the angle variation of the standing helices on the CD_z (**Fig. 3c**) (see Supplementary Information

Note S7). The given angle describes the opening angle of a cone that accommodates all helix orientations. Interestingly, even an opening angle of 70° still allows a dominant CD_z to occur. The comparison of these calculations with our experimentally obtained CD spectra in combination with evaluating the density of the aligned L-NHs on a quartz surface by scanning electron microscopy suggests that the cone opening angle might be as large as 60° for our standing helices. Importantly, we find an increase of the CD signal of three- to eight-fold for aligned L-NHs over randomly oriented L-NHs in solution (see Supplementary Information Note S8).

To finally illustrate the formation of the commonly observed bisignate CD shapes, the CD spectrum of L-NHs dispersed randomly in solution is recomposed if two subsequently recorded CD_z and CD_{xy} spectra are superimposed, giving a weight of one third to helices oriented parallel to the light beam (CD_z) and two thirds to perpendicularly aligned helices (CD_{xy}) (**Fig. 3d**). This result is in very good agreement with our theoretical model.

In addition to ensemble measurements on oriented helices, also single molecule measurements were performed to determine the orientation of nanohelices using darkfield scattering spectroscopy. Our calculations for the scattering show excitation of the transverse plasmon modes for the nanohelices aligned parallel to the light beam and excitation of both the transverse and longitudinal plasmon modes for the nanohelices aligned orthogonal to the light beam (**Fig. 4a**). For our experiments we expected the frequency shift between these plasmon resonances to be 20.5 nm (**Fig. 4b**). The panels in **Fig. 4c** and **d** show the darkfield images and scattering spectra of surface-attached L-NHs in solution and dry on a BSA-biotin-neutravidin functionalized glass slide. For polarization-dependent spectral measurements, the scattered light passes through a linear polarizer before it is fed to a spectrometer (the details of the sample preparation, the measurement setup and additional experimental data can be found in the Supplementary Information Note S9). The spectral measurements before and after drying are performed in the same areas and spectra of identical helices are compared. As shown in **Fig. 4c**, the darkfield image of L-NHs in solution (top) correlates well with that of the same L-NHs after drying (bottom), except for a few unspecifically bound nanohelices that were removed by vigorous rinsing before the nanohelices were dried.

For dried L-NHs on glass, the scattering spectra changes with respect to the polarization orientation, as the peak scattering wavelength of the L-NHs depends on the excitable plasmon modes. Here, the peaks for two orthogonal polarizer orientations are separated by 22 ± 4 nm, as shown in **Fig. 4d** (bottom), consistent with the behavior of longitudinal and transverse plasmon modes. In contrast, the scattering spectra of L-NHs in solution do not show clear polarization dependency (top). These experimental results show convincing agreement with the theoretical predictions.

To summarize, we created a dynamic plasmonic material operating in the visible range by switching of plasmonic chiral nanostructures, which show inverted CD spectra after each switching step. The alignment process leads to a multi-fold increased CD signal over signals resulting from randomly oriented samples at equal concentrations. Switchable chiral nanostructures may be applied as sensors for the detection of molecules, their chirality and their orientation, systems for data storage and materials with switchable (negative) refractive index.

References

1. Fan, Z & Govorov, A. O. Plasmonic Circular Dichroism of Chiral Metal Nanoparticle Assemblies. *Nano Lett.* **10**, 2580-2587 (2010).

2. Kuzyk, A. *et al*. DNA-based self-assembly of chiral plasmonic nanostructures with tailored optical response. *Nature* **483,** 311-314 (2012).

3. Shen, X. B., Asenjo-Garcia, A., Liu, Q., Jiang, Q., García de Abajo, J., Liu, N. & Ding, B. 3D Plasmonic Chiral Tetramers Assembled by DNA Origami *Nano Lett.* **13**, 2128 (2013).

4. Li, Z. et al. Reversible Plasmonic Circular Dichroism of Au Nanorod and DNA Assemblies. *J. Am. Chem. Soc.* **134**, 3322–3325 (2012).

5. Ma, W. et al. Chiral plasmonics of self-assembled nanorod dimers. *Scientific Reports* **3**, 1934 (2013).

6. Soukoulis, C. M. & Wegener, M. Past achievements and future challenges in the development of three-dimensional photonic metamaterials. *Nature Photonics* **5**, 523-530 (2011).

7. Liu, Y. & Zhang, X. Metamaterials: a new frontier of science and technology. *Chem. Soc. Rev*. **40**, 2494-2507 (2011).

8. Chen, H. T. et al. Active terahertz metamaterial devices. *Nature* **444**, 597-600 (2006).

9. Zhang, F. et al. Magnetically tunable left handed metamaterials by liquid crystal orientation. *Optics Express* **17**, 4360-4366 (2009).

10. Zhu, W. M. et al. Switchable Magnetic Metamaterials Using Micromachining Processes. *Adv. Materials* **23**, 1792-1796 (2011).

11. Bo, Z. et al. Switchable metamaterial reflector/absorber for different polarized electromagnetic waves. *Appl. Phys. Lett.* **97**, 51906 (2010).

12. Ou, J. Y., Plum, E., Zhang, J. & Zheludev, N. I. An electromechanically reconfigurable plasmonic metamaterial operating in the near-infrared. *Nature Nanotechnology* **8**,252–255 (2013).

13. Chang, W. S. et al. A plasmonic fano switch. *Nano Lett.* **12**, 4977-4982 (2012).

14. Gu, Y., Li, Q., Xiao, J., Wu, K. & Wang, G. P. Plasmonic metamaterials for ultrasensitive refractive index sensing at near infrared. *J. Appl. Phys.* **109**, 23104 (2011).

15. Anker, J. N., Hall, W. P., Lyandres, O., Shah, N. C., Zhao J. & Van Duyne, R. P. Biosensing with plasmonic nanosensors. *Nature Materials* **7**, 442 - 453 (2008).

16. Kabashin, A. V. et al. Plasmonic nanorod metamaterials for biosensing. *Nature Materials* **8**, 867 - 871 (2009).

17. Hendry, E. et al. Ultrasensitive detection and characterization of biomolecules using superchiral fields. *Nature Nanotechnology* **5**, 783-787 (2010).

18. Liu, N., Tang, M. L., Hentschel, M., Giessen, H. & Alivisatos, A. P. Nanoantenna-enhanced Hydrogen gas sensing in a single tailored nanofocus. *Nature Materials* **10**, 631-636 (2011).

19. Zhang, S. et al. Photoinduced handedness switching in terahertz chiral metamolecules. *Nature Communications* **3**, 942 (2012).

20. Raschke, G., Kowarik, S., Franzl, T., Sönnichsen, C., Klar, T. A., Feldmann, J. Biomolecular Recognition Based on Single Gold Nanoparticle Light Scattering. *Nano Lett.* **3**, 935 (2003).

21. Elbaz, J., Cecconello, A., Fan, Z., Govorov, A. O. & Willner, I. Powering the programmed nanostructure and function of gold nanoparticles with catenated DNA machines. *Nature Communications* **4**, 2000 (2013).

22. Rothemund, P.W.K. Folding DNA to create nanoscale shapes and patterns. *Nature* **440**, 297-302 (2006).

23. Douglas, S.M. et al. Self-assembly of DNA into nanoscale three dimensional shapes. *Nature* **459**, 414-418 (2009).

24. Douglas, S. M., Marblestone, A. H., Teerapittayanon, S., Vazquez, A., Church, G. M., Shih, W. M. Rapid Prototyping of Three-Dimensional DNA-Origami Shapes With caDNAno. *Nucleic Acids Res.* **37**, 5001–6 (2009).

25. Seeman, N.C. Nanomaterials based on DNA. *Annu. Rev. Biochem.* **79**, 65-87 (2010).

26. Liedl, T., Högberg, B., Tytell, J., Ingber, D. E. & Shih, W. M. Self-assembly of 3D prestressed tensegrity structures from DNA. *Nature Nanotechnology* **5**, 520–524 (2010).

27. Zhang, J., Liu, Y., Ke, Y. & Yan, H. Periodic Square-like Gold Nanoparticle Arrays Templated by a DNA Nanogrids on a Surface. *Nano Lett.* **6**, 248-251 (2006).

28. Zheng, J. et al. Two-dimensional nanoparticle arrays show the organizational power of robust DNA motifs. *Nano Lett.* **6**, 1502-1504 (2006).

29. Sharma, J. et al. Control of self-assembly of DNA tubules through integration of gold nanoparticles. *Science* **323**, 112 -116 (2009).

30. Ding, B. et al. Gold nanoparticle self-similar chain structure organized by DNA origami. *J. Am. Chem. Soc.* **132**, 3248-3249 (2010).

31. Pal, S., Deng, Z., Wang, H., Zou, S., Liu, Y. & Yan, H. DNA directed self-assembly of anisotropic plasmonic nanostructures. *J. Am. Chem. Soc.* **133**, 17606-17609 (2011).

32. Shen, X., Song, C., Wang, J., Shi, D., Wang, Z., Liu, N. & Ding, B. Rolling Up Gold Nanoparticle-Dressed DNA Origami into Three-Dimensional Plasmonic Chiral Nanostructures. *J. Am. Chem. Soc.* **134**, 146–149 (2012).

33. Pilo-Pais, M., Goldberg, S., Samano, E., LaBean, T.H. & Finkelstein, G. Connecting the nanodots: programmable nanofabrication of fused metal shapes on DNA templates. *Nano Lett.* **11**, 3489-3492 (2011).

34. Schreiber, R. *et al.* DNA origami-templated growth of arbitrarily shaped metal nanoparticles. *Small* **7**, 1795-1799 (2011).

35. Kauert, D. J., Kurth, T., Liedl, T. & Seidel, R. Direct mechanical measurements reveal the material properties of three-dimensional DNA origami. *Nano Lett.* **11**, 5558-5563 (2011).

36. Acuna, G. P., Möller, F. M., Holzmeister, P., Beater, S., Lalkens, B. & Tinnefeld, P. Fluorescence Enhancement at Docking Sites of DNA-Directed Self-Assembled Nanoantennas. *Science* **338**, 506-510 (2012).

Supplementary Information containing additional data, protocols and details on calculations is linked to the online version of the paper.

Acknowledgements: We thank Susanne Kempter and Philip Altpeter for assistance with the TEM and SEM, and Guillermo Acuna and Jaekwon Do for the helpful discussions. We gratefully acknowledge Mathias Rief for giving us access to his CD spectrometers. This work was funded by the Volkswagen Foundation (Germany), the DFG Cluster of Excellence NIM (Nanoinitiative Munich) (Germany), the NSF (USA), the U. S. Army Research Office under contract number W911NF-12-1-0407, IDR No. 1014922 (USA), CAREER No. 0846415 (USA) and the Emil Aaltonen foundation (Finland).

Author Contributions: RS, BY, AK, WK, AOG and TL designed the research, RS and TL designed the nanostructures (NHs), RS, PN, AK, TZ and DMS produced the NHs and RS performed CD measurements, NL and WK performed darkfield measurements and RS and AK performed electron microscopy. ZF and AOG performed theoretical calculations. RS, AK, PN, NL, ZF, WK and AOG prepared the figures and RS, WK, BY, AOG and TL wrote the manuscript.

Author Information: Reprints and permissions information is available. The authors declare no competing financial interests. Correspondence and requests for materials should be addressed to AOG or TL (govorov@phy.ohio.edu, tim.liedl@lmu.de).

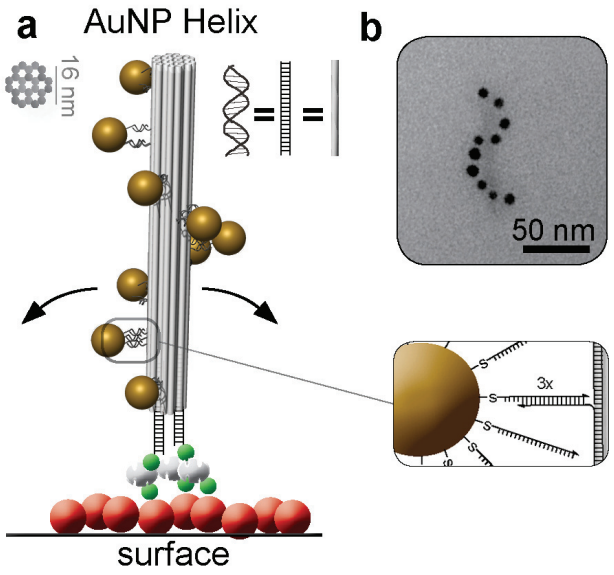

Figure 1 | Chiral plasmonic nanostructure aligned on a surface. a, A DNA origami 24-helix bundle composed of one long scaffolding DNA strand that is folded into shape by short DNA strands. Gold nanoparticles are arranged in a left-handed helix on the DNA origami structure. Zoom in: 10 nm gold nanoparticle functionalized with thiolated ssDNA hybridized to the DNA origami 24-helix bundle. The origami structure is functionalized with biotin groups on one end for the attachment to a BSA-biotin-neutravidin coated surface. After the attachment of the nanohelix on the surface, additional deposition of silver atoms on the gold particles was performed to create a silver shell around each gold nanoparticle (not shown). **b**, Transmission electron microscopy image of a nanohelix.

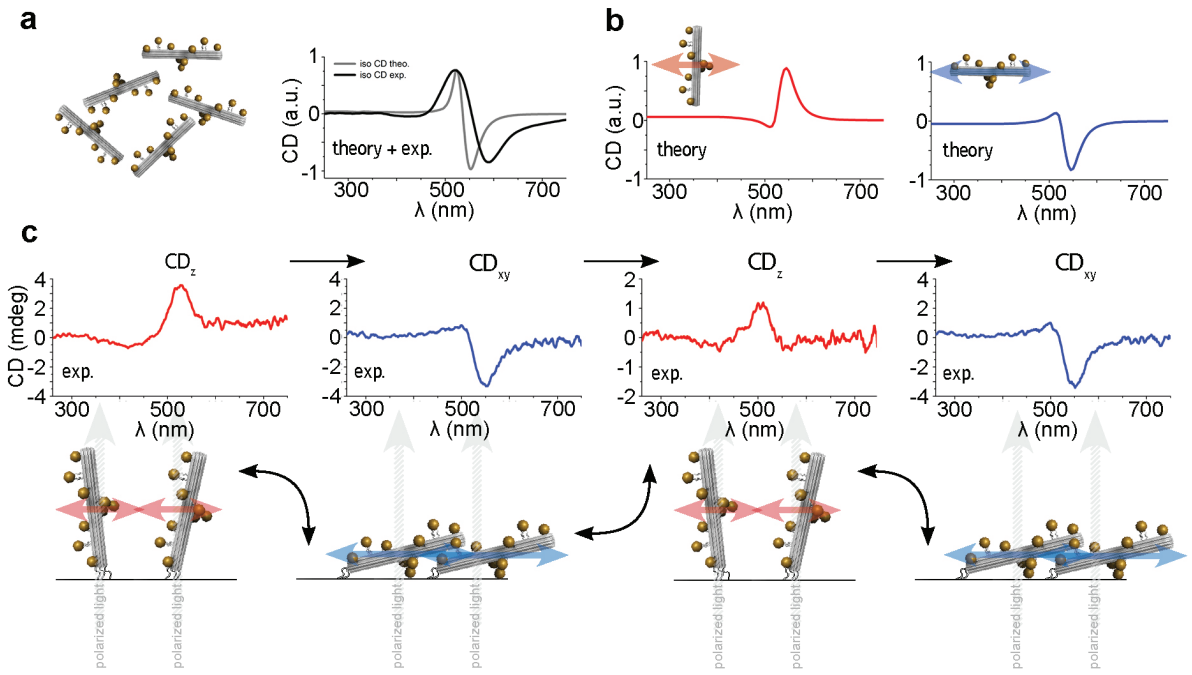

Figure 2 | Dynamic material with switchable circular dichroism. a, Theoretical (grey curve) and experimental (black curve) CD spectra for L-NHs dispersed in solution. **b,** Theoretical CD spectra of L-NHs oriented parallel (red curve) and perpendicular (blue curve) to the incident beam. **c,** Experimental CD spectra (top) and scheme of orientation state (bottom) of the L-NHs. The light beam penetrates the quartz substrate perpendicular to its surface plane. Measurements shown were performed with the same ensemble of L-NHs and in the displayed order. L-NHs stood upright if dispersed in solution and were hence aligned parallel to the incoming light beam. The expected transverse CD_z was observed in this case. After removal of the buffer and air-drying of the surface, the L-NHs laid flat on the substrate and were thus oriented perpendicular to the incoming light beam. Here, the expected longitudinal CD_{xy} was measured. The cuvette was re-filled with buffer, which lead to re-alignment of the L-NHs parallel to the light beam. Again the transverse CD_z was obtained. The sample was air-dried again and the longitudinal CD_{xy} was measured.

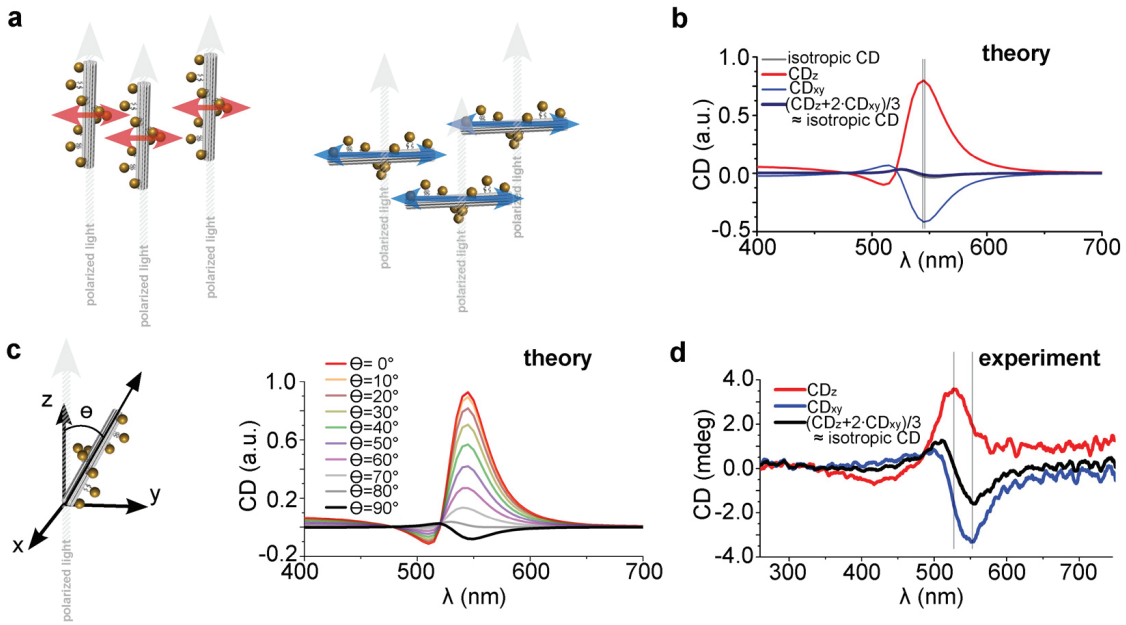

Figure 3 | CD splitting theory and comparison to the experimental results. **a,** Scheme of L-NHs aligned orthogonal and parallel to a polarized light beam. The possible CD excitation modes are indicated with double arrows (red: CD_z, blue: CD_{xy}). **b,** The simulated peak-dip CD signal of randomly oriented L-NHs can be composed by the superposition of weighted transverse CD_z and longitudinal CD_{xy} signals. The directional CD signal (CD_z or CD_{xy}) is much stronger than the signal originating from randomly dispersed helices since averaging over the orientation of the chiral objects typically strongly reduces the CD signal. **c**, Simulated CD spectra for helices oriented at angles restricted to a cone with a given opening angle Θ. **d,** The CD_z (red curve) and the CD_{xy} (blue curve) were measured from the same ensemble of L-NHs by switching the orientation of the L-NHs (cf. Figure 2). The black curve shows the calculated superposition of weighted CD_z and CD_{xy}. Importantly, this curve resembles the CD signal of nanohelices dispersed randomly in solution. Note that the shift between the inverted modes is larger than expected. This can be attributed to differences of the refractive indices of the particle-surrounding media in dry and wet samples.

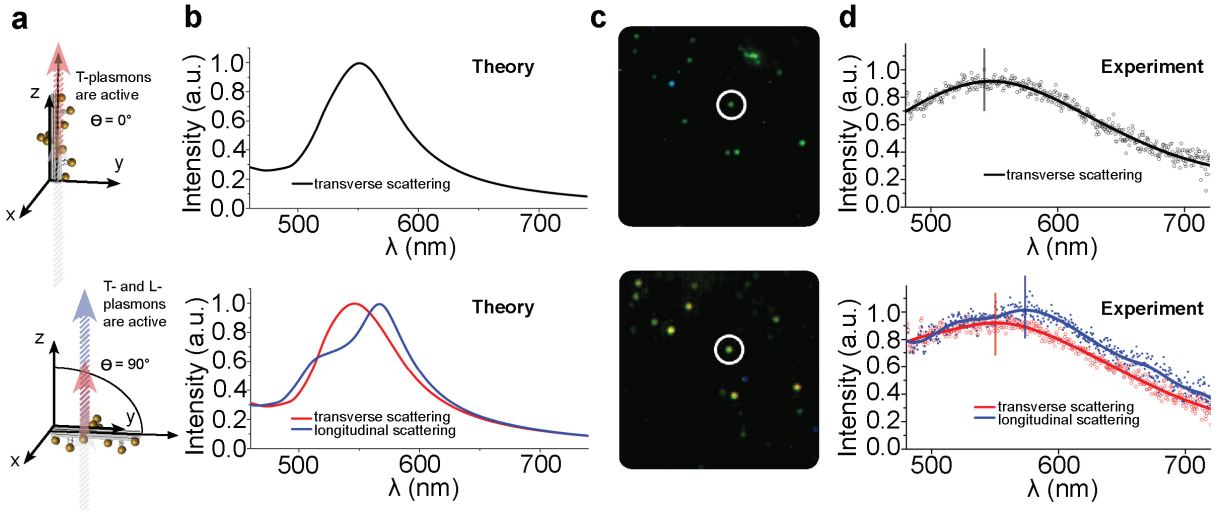

Figure 4 | Darkfield scattering spectroscopy of surface-bound nanohelices. Aligned nanohelices orthogonal to a surface in solution (top row) and aligned nanohelices parallel to a surface dry on glass (bottom row) were studied. **a**, Schemes of nanohelices aligned orthogonal or parallel to a light beam. **b**, Theoretical calculations. Top: only transverse plasmons are excited if the nanohelices are aligned parallel to the light beam. Bottom: longitudinal and transverse plasmons are excited if the nanohelices are aligned orthogonal to the light beam. The expected shift of the plasmon resonance is 20.5 nm. **c**, Darkfield images of aligned nanohelices in the same area are shown in colour. An ozone-free Xe lamp is used as a light source. **d**, The interpolated scattering spectra of a typical nanohelix as highlighted in **c** (circle). Top**:** the scattering spectrum of a surface-bound nanohelix in solution shows no clear polarization dependency. Only transverse plasmon excitation is obtained. Bottom: a dried nanohelix exhibits polarization dependent scattering spectra consistent with xy orientation of the nanohelix. Longitudinal and transverse plasmon excitation is obtained. The observed shift of the plasmon resonance is 22 ± 4 nm.

6 Hierarchical assembly of metal nanoparticles, quantum dots and organic dyes using DNA origami scaffolds

Creating modular three-dimensional networks and hierarchical assemblies with metal nanoparticles, semi-conducting nanoparticles and organic dyes is challenging and can be useful for the creation of complex systems such as plasmonic nanolenses and light-harvesting complexes. Bottom-up approaches have demonstrated the creation of spatial arrangements of metal and semi-conducting nanoparticles and organic dyes around a center nanoparticle [88-90]. These spatial arrangements around a structuring nanoparticle showed a lack of the ability to design the distance between the components (only short ranges). It was also not possible to arrange complex multi-nanoparticle geometries around the center nanoparticle (e.g. chiral assemblies of metal nanoparticle or dyes around a structuring element). In contrast, DNA nanotechnology allows to spatially arrange metal nanoparticles, semi-conducting nanoparticles and organic dyes [32,36,87].

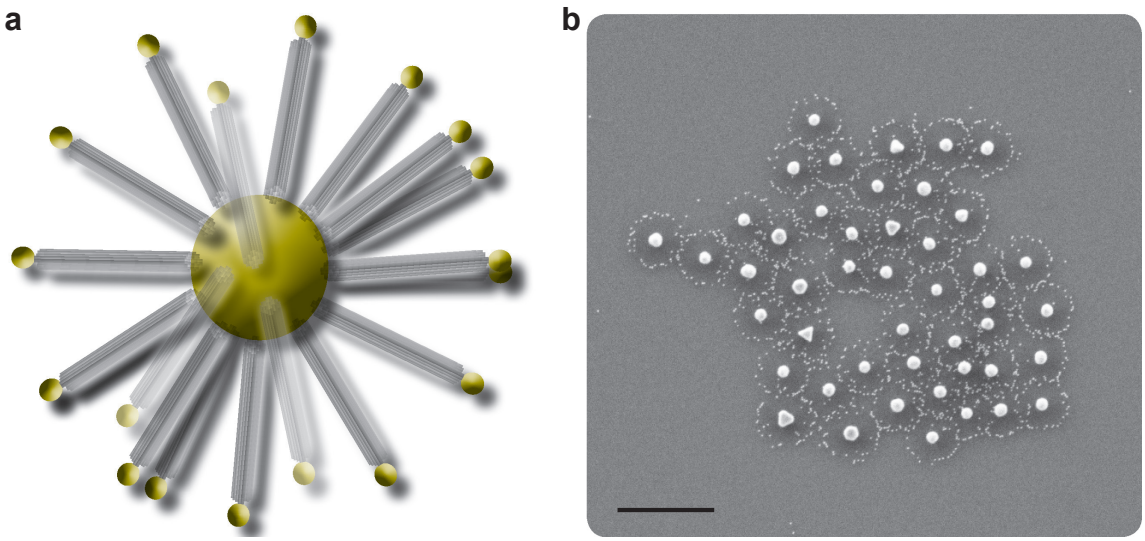

Figure 6.1: a, Schematic drawing of a planet-satellite nanocluster with a 60 nm gold particle as a planet, DNA origami structures (here: 24-helix bundles) as distance control and 10 nm gold particle as satellites. **b**, Scanning electron microscopy image of such planet-satellite nanoclusters. Scale bar, 500 nm.

In the associated publication P4 we used metal nanoparticles, semi-conducting nanoparticles and soft-matter particles as structuring elements to arrange DNA origami structures (**Figure 6.1**). Furthermore, the DNA origami structures were modified with metal nanoparticles or organic dyes, which were organized in specific geometries and at defined distances from the structuring planet-element. All parameters like distance, size, stoichiometry and material composition were controlled by the choice of the planet, its satellites and the design of the DNA origami structure which includes the

choice for the attachment sites of the satellites. This enabled us to create hierarchical assemblies (up to 500 nm diameter) with yet unprecedented complexity, precise control of the spatially arranged components and mono-dispersity in solution. With these assemblies we were able to arrange helices of metal nanoparticles around a plasmonic planet and to investigate the influence of the center metal nanoparticle on the circular dichroism of the attached chiral nanostructures. Furthermore, we were capable to investigate light harvesting-like constructs with organic dyes arranged around a quantum dot. We realized that these structures were not able to prove an energy transfer from the dyes around an acceptor quantum dot. This is possibly due to the fact that the quantum dot gets excited alongside the organic dyes [91]. Moreover we investigated long-range dye quenching effects of organic dyes in the surrounding area of a metal nanoparticle. This confirms the results of recent studies on long-range quenching effects from other groups [92,93].

In addition, cooperations to study these specific planet-satellite systems are already in progress with Joshua B. Edel (ICL) for Raman spectroscopy on liquid boundaries and with Na Liu (MPI, Stuttgart) for cross-talks between chiral and non-chiral plasmonic nanostructures.

6.2 Associated publication P4

Hierarchical assembly of metal nanoparticles, quantum dots and organic dyes using DNA origami scaffolds

by

Robert Schreiber*, Jaekwon Do*, Eva-Maria Roller, Tao Zhang, Verena J. Schüller, Philipp C. Nickels, Jochen Feldmann, Tim Liedl

*equal contribution

accepted for publication in

Nature Nanotechnology

Hierarchical assembly of metal nanoparticles, quantum dots and organic dyes using DNA origami scaffolds

Robert Schreiber[1,*], Jaekwon Do[2,*], Eva-Maria Roller[1], Tao Zhang[1], Verena J. Schüller[1], Philipp C. Nickels[1], Jochen Feldmann[2], Tim Liedl[1,†]

[1]*Molecular Self-Assembly and Nanoengineering Group, Physics Department and CeNS, Ludwig-Maximilians-Universität München, Geschwister-Scholl-Platz 1, 80539 Munich, Germany*

[2]*Photonics and Optoelectronics Group, Physics Department and CeNS, Ludwig-Maximilians-Universität München, Amalienstr. 54, 80799 Munich, Germany*

**These authors contributed equally to this work*

[†]tim.liedl@lmu.de

ONE-SENTENCE SUMMARY: DNA nanotechnology: Rigid DNA origami scaffolds can be used to hierarchically organize metal nanoparticles, quantum dots and organic dyes into functional nanoclusters that have a planet-satellite type structure.

KEY WORDS: DNA nanotechnology, quantum dots, nanoparticles, DNA origami, hierarchical self-assembly

The self-assembly of nanoscale elements into three-dimensional structures with precise shapes and sizes is important in fields such as nanophotonics, metamaterials and biotechnology[1,2]. Short molecular linkers have previously been used to create assemblies of nanoparticles[3,4,5,6,7,8,9], but the approach is limited to small interparticle distances, typically less than 10 nm. Alternatively, DNA origami[10,11] can precisely organize nanoscale objects over much larger length scales. Here we show that rigid DNA origami scaffolds can be used to assemble metal nanoparticles, quantum dots and organic dyes into hierarchical nanoclusters that have a planet-satellite type structure. The nanoclusters have a tuneable stoichiometry, defined distances of 5 to 200 nm between components, and controllable overall sizes of up to 500 nm. We also show that the nanoscale components can be positioned along the radial DNA spacers of the nanostructures, which allows short- and long-range interactions between nanoparticles and dyes to be studied in solution. The approach could, in the future, be used to construct efficient energy funnels, complex plasmonic architectures, and porous, nano-engineered scaffolds for catalysis.

DNA-based self-assembly offers the possibility to fabricate trillions of identical objects at once while achieving nanometre-precise positioning of objects in all three dimensions[12,13]. The early applications of DNA to connect nanoparticles into discrete dimers and trimers[3] led over the years to the fabrication of complex, polypod-like dynamic and hybrid nanoparticle assemblies[5,14,15]. In these assemblies, where individual DNA double-strands (dsDNA) were used as scaffolds, the achievable control over size and shape is limited by the flexibility of dsDNA and the stability of the single chemical bonds between the DNA and the nanoparticles. In recent years, various more sophisticated assemblies of metal nanoparticles based on DNA scaffolding have been realized[16, 17,18,19]. Most of these studies used the metal nanoparticles as exemplary objects to visualize the assembly power of DNA and only very recently function was added by the design of optically active materials[13,15] and geometries that enable fluorescence enhancement of individual dye molecules[20]. Besides DNA, other molecular cross-linkers can be used to arrange plasmonic nanoparticles into planet-

satellite assemblies[6,9] but none of these methods offer control over distances greater than a couple of nanometres nor simple combinatorial freedom in the choice of materials. To overcome these fundamental limitations, we used DNA origami structures as spacers to arrange nanoparticles and organic dyes in three-dimensions. We were able to build and employ a new class of hybrid planet-satellite nanoclusters that are monodisperse, tunable in size and stochiometry and whose structural integrity is provided by the rigidity of DNA origami constructs and the stability of DNA-origami-enabled connection schemes.

DNA origami structures are usually composed of a long (7-8 kb) scaffolding DNA single strand and roughly 200 short "staple" oligonucleotides. The folded objects are comprised of multiple double-helices that can be arranged in an (anti-)parallel[10], crossed[11], twisted, curved[21,22] and pre-stressed manner[23]. To create the planet-satellite nanoclusters, we fabricated chemically asymmetric DNA origami structures of varying length and thickness that offer specific types of attachment sites (**Figure 1a**). Each attachment site consists of 1 to 12 copies of a specific single-stranded DNA sequence protruding from the DNA origami surface. Nanoparticles or organic dyes functionalized with complementary sequences were hybridized to these sites with high fidelity[18,19] (**Figure 1b and c**).

In the first step of the assembly procedure, the DNA origami structures together with the staple strands containing the sequences used for particle attachment were annealed. Next, the DNA origami objects were purified via gel electrophoresis from the molar excess of staple strands and subsequently hybridized (12 hours at 25 °C) with DNA-functionalized dyes or nanoparticles, which later constitute the satellites of the nanoclusters (DNA functionalization protocols for all nanoparticles can be found in Supplementary Note S1). During a second gel electrophoresis step, the origami structures with the attached satellites were purified from the excess of dyes or nanoparticles (Supplementary Note S2) and afterwards hybridized with the planet gold nanoparticles, which serve as solid supports for the origami structures. As planets, DNA-functionalized gold and semiconductor nanoparticles of various sizes (10 nm to 80 nm) were employed. For the planet-satellite hybridization step (12 hours at 25 °C),

an excess of satellite-functionalized DNA origami structures over planet particles was used. To account for the available surface area of the nanoparticle planets, the molar excess was varied for each planet size (Supplementary Note S3). The final super-nanoclusters consisting of nanoparticle planets, DNA origami structures and dye or nanoparticle satellites are in the following called origami nanoclusters (**Figure 1d-h**). origami nanoclusters only tend to aggregate at high concentrations and are stable for long periods of time (8 months) if stored at -18°C (Supplementary Note S4 and S5). By modifying the DNA structures with gold nanoparticles along the radial spokes (**Figure 1f**) we demonstrate the potential of our approach to create chiral assemblies of high complexity. These origami nanoclusters give rise to strong circular dichroism (CD) in the visible range and we find that our chiral structures[13] not only preserve their specific optical activity in this assembly, but also experience an increase of their plasmonic CD due to field enhancement effects in the vicinity of large (80 nm) planet particles (Supplementary Note S6 and S7). We further created hetero-structures featuring quantum dots[24,25] as central planets and gold nanoparticles (**Figure 1g**) or fluorescent dyes (**Figure 1h**) as satellites. We studied potential feeding of fluorescent energy from multiple dyes[26] along the spokes to the central quantum dot, but only a non-significant increase of acceptor fluorescence could be observed (Supplementary Note S8). We attribute this to the fundamental difficulties that arise when using quantum dots as acceptors of fluorescence energy from organic donor molecules[27].

Also by varying the shape and accordingly the extensions of the origami structures, the distance between satellite and planet could be controlled. We used a three-layer origami block for a short planet-satellite distance of 10 nm (**Figure 2a**), a 24-helix bundle for an intermediate distance of 100 nm (**Figure 2b**), and a 14-helix bundle for the longest distance of 200 nm (**Figure 2c**). The actual distances between satellites and planets were determined experimentally by analyzing transmission electron microscopy images of Uranyl-acetate-stained origami nanoclusters. As the nanoclusters adsorbed to the surface of the transmission electron microscopy grid and were further dried after the staining process, they appear in a flattened, two-dimensional manner. The DNA origami structures which are attached to the central sphere from all directions are thus pointing

outwards radially in only one plane. This leads to a systematic error in the distance measurements resulting from origami structures that are attached anywhere between the equator and the poles of the planet. Note that by slowly drying the origami nanoclusters on a substrate it is possible to preserve the 3D structure, which can be proven by transmission electron tomography (Supplementary Note S9). Importantly, these origami nanoclusters represent to our knowledge the largest three-dimensional DNA-based assemblies of defined size (DLS measurements can be found in Supplementary Information Note S10-12).

The stochiometry of the origami nanocluster assembly was effectively controlled by changing the size of the central gold nanoparticle planet from 10 nm to 80 nm (**Figure 3a-d**). If the concentration of satellite-bearing origami structures was excessive during the assembly process, the planet size determines the number of attached satellites. Interestingly, the standard deviation for the number of satellites was very low for each given planet size: 17 % for 10 nm, 10 % for 40 nm, 12 % for 60 nm and 6 % for 80 nm planet particles. In a first estimation, we expected that the absolute number should be directly proportional to the surface area of the central particle. This not being the case can be directly derived from the data shown in **Figure 3e**, where a graph showing the number of satellites as a function of surface area is plotted. It can be observed that with increasing particle size and hence decreasing surface curvature, less origami structures than expected attach to the planets. We attribute this to the increasing electrostatic and steric repulsions that occur between neighbouring DNA structures at a distance from the particles' surfaces when the curvature of the planet surface decreases with increasing size. In accordance with this consideration, we found that performing the assembly at elevated NaCl concentrations leads to higher satellite attachment yields but also to more aggregated clusters (Supplementary Note S11 and S12). For the largest planets (80 nm gold nanoparticle, lowest surface curvature) the average surface coverage with DNA origami structures was 41 % at 0 mM NaCl and 11 mM $MgCl_2$. The maximum coverage of a flat gold surface with our satellite-bearing origami structures under such conditions is therefore expected to be less than this value. Also origami nanoclusters with a soft matter planet were created. To this end we used hollow origami tubes as central

particles and thus demonstrated the realization of origami-structure-guided arrangement of satellites (Supplementary Note S13).

Electroless deposition of gold or silver ions from solution was used to increase the size of planets and satellites of fully assembled origami nanoclusters [13,28]. Gold deposition was performed after the clusters had attached to a solid substrate (**Figure 4a-c**) (Supplementary Note S14). For the silver deposition process, the clusters were kept in solution and gold-silver core-shell satellites and planets were formed (Supplementary Note S14). By controlling the metal deposition time or metal ion concentration, the size of the satellites could be controlled in a step-less manner until the satellites were fusing into a ring (surface-based deposition) or a shell (solution-based deposition) around the planet. While we were not able to demonstrate seamless closing of the shells with transmission or scanning electron microscopy, these origami nanoclusters could be seen as small dots with simple bright field microscopy (Supplementary Note S15). Interestingly, it was possible to conjugate the DNA origami structures carrying gold nanoparticle satellites with the gold planets even after the silver-enhancement process of the satellites. This way hybrids with gold-silver (core-shell) satellites and gold-only planets were formed, however with low assembly yields (Supplementary Note S16).

We further observed that the origami nanoclusters assemble into close-packed lattices when deposited at concentrations of 10 pM and being left to slowly dry on various surfaces (silicon oxide and carbon-coated transmission electron microscopy grids) (**Figure 4d-f**). In the different nanocluster lattices that were formed from samples with 100 nm long 24-helix bundles and varying planet sizes, we found slightly smaller average planet-planet distances than expected (5 - 17 %). This together with careful inspection of, e.g., **Figure 4e** allows us to conclude, that the ends of the satellite-bearing DNA structures interpenetrate slightly during the deposition process without sharing satellite particles. We also interpret the formation of close-packed lattices as a further proof of the uniformity of the nanoclusters.

To demonstrate the simple applicability of this well-controlled scaffolding material, we observed quenching behaviour of the dye molecule Cy5 in the vicinity of gold

nanoparticles (20 nm) in solution-based ensemble measurements. In accordance with other studies we find that gold nanoparticles exhibit measurable quenching effects over a wide range of distances[29,30,31,32,33]. **Figure 5a** shows the design of the photo-functional origami nanoclusters. The modularity of the design allowed us to place dyes at virtually any distance between 5 nm and 100 nm of which we chose 5 nm, 9 nm, 16 nm, 22 nm, and 58 nm. For each measurement the assembled DNA spokes contained dyes at only one of these distances and were conjugated with the 20 nm gold nanoparticle planets (**Figure 5b**). Our experiments (**Figure 5c**) show quenching over a distance of up to 22 nm and when fitting the data to a simplified $1/d^4$ model[33], we obtain an averaged d_0 value – the distance at which the energy transfer efficiency is 50% – of 12 ± 2 nm, which is in very good agreement with calculated values[30] (Supplementary Note S17).

To conclude, we created a great variety of planet-satellite nanoclusters with customized material properties and defined sizes by nanoparticle- and DNA-origami-guided self-assembly. We controlled planet-satellite distances reaching from a few to 200 nanometres and demonstrated the possibility to precisely position nanoparticles and organic dyes along the radial spacers, which allowed us to observe field-enhanced plasmonic CD on the one hand and distance-dependent fluorescence quenching of fluorophores on the other hand. To ultimately build efficient energy-funneling nanoconstructs, we propose to position nanorods as antennas around carefully placed colloidal quantum dots or reaction centres. Using this approach the design of plasmon-based nanolenses or SPASERs can be envisioned. Self-assembling arrays of plasmonic particle rings and shells are also of potential interest for the creation of ordered nanoscopic assemblies in metamaterial research. The nanoclusters could find further applications as a framework for Raman spectroscopy and Fano resonance studies, as porous catalytic materials, or in biomedical research where specific arrangements of bioactive molecules are needed.

References

1. Liu, N., Hentschel, M., Weiss, T., Alivisatos, A. P. & Giessen, H. Three-Dimensional Plasmon Rulers. *Science* **332,** 1407-1410 (2011).

2. Soukoulis, C. M. & Wegener, M. Past achievements and future challenges in the development of three-dimensional photonic metamaterials. *Nature Photon.* **5,** 523-530 (2011).

3. Alivisatos, A. P. *et al*. Organization of 'nanocrystal molecules' using DNA. *Nature* **382,** 609-611 (1996).

4. Parak, W. J. *et al.* Conformation of Oligonucleotides Attached to Gold Nanocrystals Probed by Gel Electrophoresis. *Nano Lett.* **3**, 33-36 (2003).

5. Fu, A. *et al*. Discrete Nanostructures of Quantum Dots/Au with DNA. *J. Am. Chem. Soc.* **126,** 10832-10833 (2004).

6. Xu, X., Rosi, N. L., Wang, Y., Huo, F. & Mirkin, C. A. Asymmetric Functionalization of Gold Nanoparticles with Oligonucleotides. *J. Am. Chem. Soc.* **128,** 9286-9287 (2006).

7. Sebba, D. S., Mock, J. J., Smith, D. R., LaBean, T. H. & Lazarides, A. A. Reconfigurable Core-Satellite Nanoassemblies as Molecularly-Driven Plasmonic Switches. *Nano Lett.* **8,** 1803-1808 (2008).

8. Nie, Z., Petukhova, A. & Kumacheva, E. Properties and emerging applications of self-assembled structures made from inorganic nanoparticles. *Nature Nanotech.* **5,** 15-25 (2010).

9. Gandra, N., Abbas, A., Tian, L. & Singamaneni, S. Plasmonic Planet-Satellite Analogues: Hierarchical Self-Assembly of Gold Nanostructures. *Nano Lett.* **12,** 2645-2651 (2012).

10. Rothemund, P. W. K. Folding DNA to create nanoscale shapes and patterns. *Nature* **440,** 297-302 (2006).

11. Douglas, S. M. *et al.* Self-assembly of DNA into nanoscale three-dimensional shapes. *Nature* **459,** 414-418 (2009).

12. Seeman, N. C. Nanomaterials based on DNA. *Annu. Rev. Biochem.* **79,** 65-87 (2010).

13. Kuzyk, A. *et al*. DNA-based self-assembly of chiral plasmonic nanostructures with tailored optical response. *Nature* **483,** 311-314 (2012).

14. Aldaye, F. A. & Sleiman, H. F. Dynamic DNA Templates for Discrete Gold Nanoparticle Assemblies: Control of Geometry, Modularity, Write/Erase and Structural Switching. *J. Am. Chem. Soc.* **129,** 4130-4131 (2007).

15. Yan, W. *et al*. Self-Assembly of Chiral Nanoparticle Pyramids with Strong *R/S* Optical Activity. *J. Am. Chem. Soc.* **134,** 15114-151121 (2012).

16. Zheng, J. *et al*. Two-Dimensional Nanoparticle Arrays Show the Organizational Power of Robust DNA Motifs. *Nano Lett.* **6,** 1502-1504 (2006).

17. Sharma, J. *et al*. Control of Self-Assembly of DNA Tubules Through Integration of Gold Nanoparticles. *Science* **323,** 112 -116 (2009).

18. Ding, B. *et al*. J. Gold Nanoparticle Self-Similar Chain Structure Organized by DNA Origami. *J. Am. Chem. Soc.* **132,** 3248-3249 (2010).

19. Pal, S. Deng, Z. Ding, B. Yan, H. & Liu, Y. DNA-Origami-Directed Self-Assembly of Discrete Silver-Nanoparticle Architectures. *Angew. Chem. Int. Ed.* **49,** 2700-2704 (2010).

20. Acuna, G. P. *et al.* Fluorescence Enhancement at Docking Sites of DNA-Directed Self-Assembled Nanoantennas. *Science* **338**, 506-510 (2012).

21. Dietz, H., Douglas, S. M. & Shih, W. M. Folding DNA into Twisted and Curved Nanoscale Shapes. *Science* **325,** 725-730 (2009).

22. Han, D. *et al*. DNA Origami with Complex Curvatures in Three-Dimensional Space. *Science* **332,** 342–346 (2011).

23. Liedl, T., Högberg, B., Tytell, J., Ingber, D. E. & Shih, W. M. Self-assembly of three-dimensional prestressed tensegrity structure from DNA. *Nature Nanotech.* **5,** 520-524 (2010).

24. Bui, H. *et al.* Programmable Periodicity of Quantum Dot Arrays with DNA Origami Nanotubes. *Nano Lett.* **10**, 3367-3372 (2010).

25. Deng, Z., Samanta, A., Nangreave, J., Yan, H. & Liu, Y. Robust DNA-Functionalized Core/Shell Quantum Dots with Fluorescent Emission Spanning from UV-vis to Near-IR and Compatible with DNA-Directed Self-Assembly. *J. Am. Chem. Soc.* **134**, 17424-17427 (2012).

26. Dutta, P. K. *et al.* DNA-Directed Artificial Light-Harvesting Antenna. *J. Am. Chem. Soc.* **133**, 11985-11993 (2011).

27. Clapp, A. R., Medintz, I. L. & Mattoussi, H. Förster Resonance Energy Transfer Investigations Using Quantum-Dot Fluorophores. *ChemPhysChem* **7**, 47-57 (2006).

28. Pilo-Pais, M., Goldberg, S., Samano, E., LaBean, T. H. & Finkelstein, G. Connecting the Nanodots: Programmable Nanofabrication of Fused Metal Shapes on DNA Templates. *Nano Lett.* **11,** 3489-3492 (2011).

29. Dulkeith, E., Ringler, M., Klar, T. A. & Feldmann, J. Gold Nanoparticles Quench Fluorescence by

Phase Induced Radiative Rate Suppression. *Nano Lett.* **5**, 585-589 (2005).

30. Anger, P., Bharadwaj, P. & Novotny, L. Enhancement and Quenching of Single-Molecule Fluorescence. *Phys. Rev. Lett.* **96**, 113002 (2006).

31. Acuna, G. P. *et al*. Distance Dependence of Single-Fluorophore Quenching by Gold Nanoparticles Studied on DNA Origami. *ACS Nano* **6**, 3189-3195 (2012).

32. Pal, S. et al. Quantum Efficiency Modification of Organic Fluorophores Using Gold Nanoparticles on DNA Origami Scaffolds. *J. Phys. Chem. C* **117**, 12735–12744 (2013).

33. Persson, B. N. J. & Lang, N. D. Electron-hole-pair quenching of excited states near a metal. *Phys. Rev. B.* **26**, 5409-5415 (1982).

Supplementary Information containing additional data and protocols is linked to the online version of the paper.

Acknowledgements: We thank Guillermo Acuna for helpful discussions and Susanne Kempter for experimental advice. This work was funded by the Volkswagen Foundation, the DFG through the Nanosystems Initiative Munich (NIM), the ERC through the Advanced Investigator Grant HYMEM, and the EU commission through the Marie Curie Research Training Network ICARUS.

Author Contributions: RS, JD, JF and TL designed the research. RS, JD, EMR, TZ, VS, PN and TL designed the nanostructures. RS, JD, EMR, TZ and PN performed experiments and RS, JD and TL wrote the manuscript.

Author Information: The authors declare no competing financial interests. Correspondence and requests for materials should be addressed to TL (tim.liedl@lmu.de).

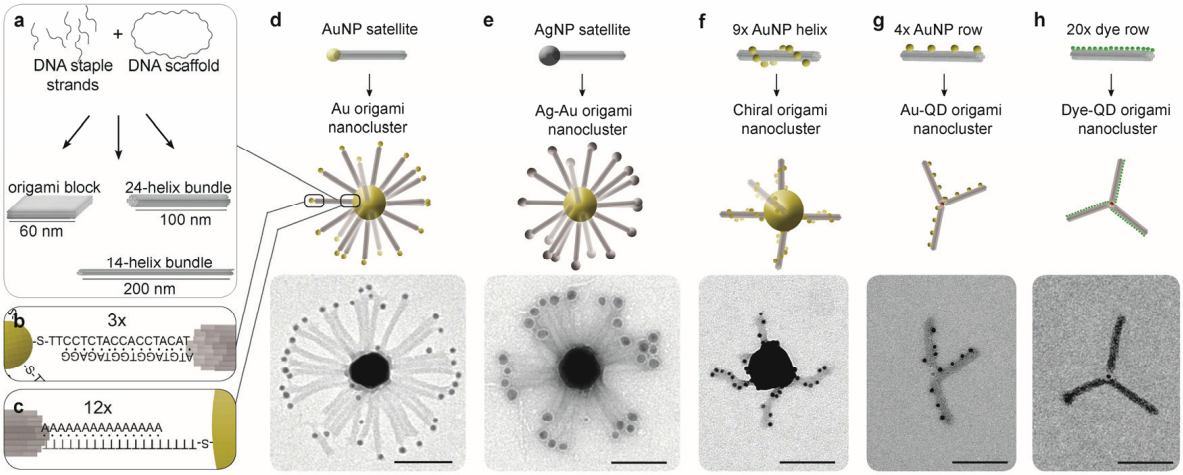

Figure 1 | Planet-satellite nanostructures. **a,** A single-stranded DNA scaffold (~ 8kb) is annealed with ~ 200 synthetic oligonucleotides (staples, each about 40 nucleotides long) to create various DNA origami structures of defined shape and size. **b**, Satellite nanoparticles (NPs) functionalized with multiple thiolated DNA strands are hybridized via handle sequences to the DNA origami structures. **c**, The NP-bearing DNA origami structures are hybridized to NP planets functionalized with a different DNA sequence. **d-h, Top**: Schematic drawings of DNA origami structures carrying various satellites. **d-h**, **Middle**: Schematic drawing of the fully assembled planet-satellite clusters. **d-h, Bottom**: Electron micrographs of Uranyl-acetate-stained structures. Note that the flattened appearance results from the drying process. **d**, Au nanocluster (planet: 60 nm gold nanoparticle (AuNP), satellites: 10 nm AuNPs). **e**, Ag-Au nanocluster (planet: 80 nm AuNP, satellites: 20 nm silver nanoparticles (AgNPs)). **f**, Chiral nanocluster (planet: 80 nm AuNP, satellites: 9 x 10 nm AuNPs in a right-handed helix). **g**, Au-QD nanocluster (planet: quantum dot (QD) CdSeTe 800 nm emission, satellites: 4 x 10 nm AuNPs). **h**, Dye-QD nanocluster (planet: QD CdSeTe 800 nm emission, satellites: 20 x Cy3). Scale bars: 100 nm.

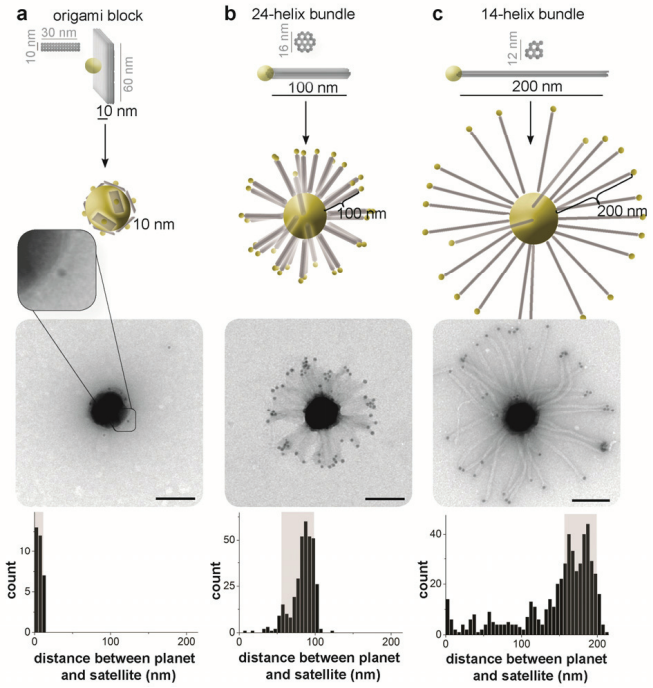

Figure 2 | Planet-satellite distance control. AuNP planets with a diameter of 80 nm were used for all nanoclusters presented in this figure. **Top**: Schemes of DNA structures (spacers) and assembled nanoclusters; **Middle**: Transmission electron microscopy (TEM) images of nanoclusters; **Bottom**: Histograms of distances between planet surface and satellite surface. The grey-shaded areas correspond to a systematic uncertainty resulting from the isotropic attachment of the DNA spacers on the AuNP planets (cf. text). **a**, Three-layered origami block (60 nm x 30 nm x 8 nm) as spacer. Expected distance: 10 nm, measured distance: 6.3 nm ± 3.6 nm (SD). Note that this measurement is severely suffering from imaging in 2D as only satellites that have exactly attached to the equator of the planet exhibit the correct distance in the 2D projection. **b**, 24-helix bundle (length: 100 ㎜, diameter: 16 ㎜) as spacer. Expected distance: 100 ㎜, measured distance: 83 nm ± 15 nm (SD). **c**, 14-helix bundle (length: 200 nm, diameter: 12 nm) as spacer. Expected distance: 180 nm, measured distance: 145 nm ± 53 nm (SD). Scale bars: 100 nm.

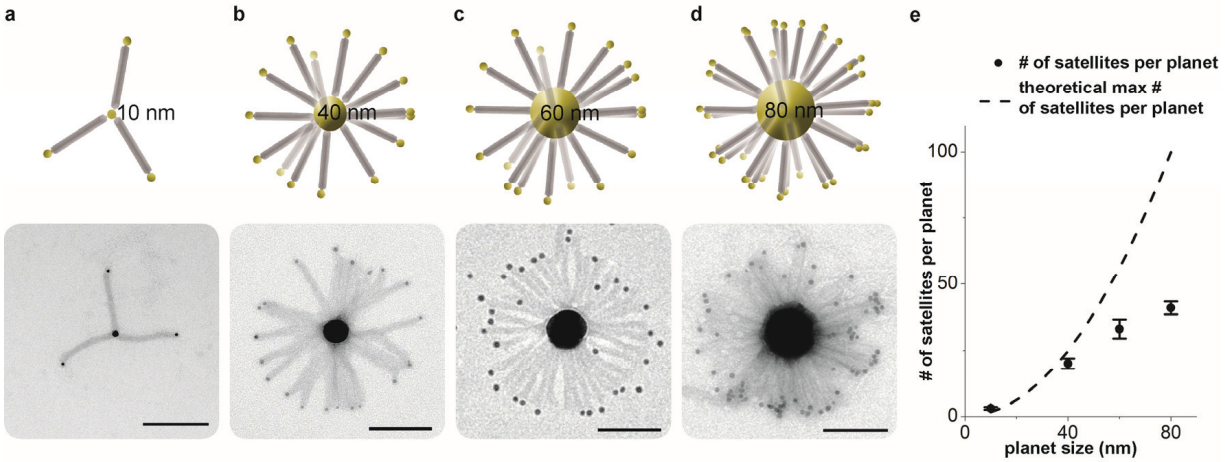

Figure 3 | Planet-satellite stochiometry control. The same DNA origami spacer (24-helix bundle) was used in all experiments presented in this figure. **a-d**, **Top**: Schematic drawings of the nanoclusters; **a-d**, **Bottom**: TEM images of the nanoclusters. On average, **a**, 3 ± 0.5 (SD) satellites per 10 nm AuNP planet, **b**, 20 ± 1.9 (SD) satellites per 40 nm AuNP planet, **c**, 33 ± 3.6 (SD) satellites per 60 nm AuNP planet and **d**, 41 ± 2.5 (SD) satellites per 80 nm AuNP planet are observed. **e**, Number of satellites per planet as a function of the planet size (cf. text). Scale bars: 100 nm.

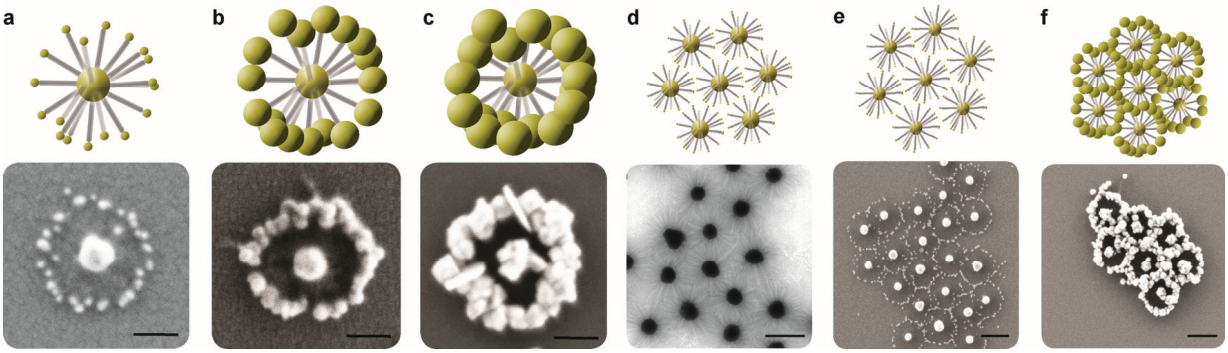

Figure 4 | Gold enhanced origami nanoclusters and close-packed lattices. Top: Schematic drawings; **Bottom**: TEM and SEM images of nanoclusters. **a-c,** nanoclusters consisting of 24-helix bundles, 10 nm AuNP satellites and 60 nm AuNP planets. The clusters were deposited on a Si-surface and exposed to GoldEnhance^{TM} formulation (Nanoprobes.com) for varying enhancement times: **a,** 2 min, **b,** 6 min. **c,** 10 min. Scale bars: 100 nm. **d-f,** Nanoclusters form close-packed lattices if left to slowly dry on solid substrates. Clusters consisting of 24-helix bundles, 10 nm AuNP satellites and 80 nm planet in **d** and 60 nm planets in **e** and **f** were used. The sample in **f** was additionally exposed to GoldEnhance^{TM} formulation. Scale bars: 200 nm.

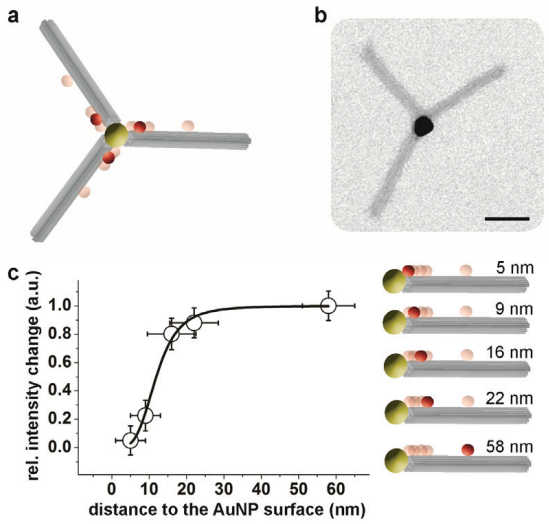

Figure 5 | Fluorescence quenching studied with origami nanoclusters. a, Schematic drawing of a nanocluster consisting of a 20 nm AuNP planet and 24-helix bundles that carry organic dyes (Cy5) at one of five distances to the AuNP surface: (5 nm, 9 nm, 16 nm, 22 nm or 58 nm). **b,** TEM image. Scale bar: 50 nm. **c,** Normalised and threshold-corrected fluorescence intensity measurements (black circles) of Cy5 dyes at varying positions and corresponding fit ($1/d^4$, cf. text) (black curve)[33].

7 Current Progress and Outlook

Previously, we could show in cooperation with Theobald Lohmüller's group (LMU) that the assembly of a DNA origami block between two 40 nm gold nanoparticles (**Figure 7.1**) can be used for surface enhanced Raman spectroscopy. It was possible to analyze fluorescent dyes which intercalated into the DNA origami structure. The project was initiated with Frank Jäckel's group (LMU).

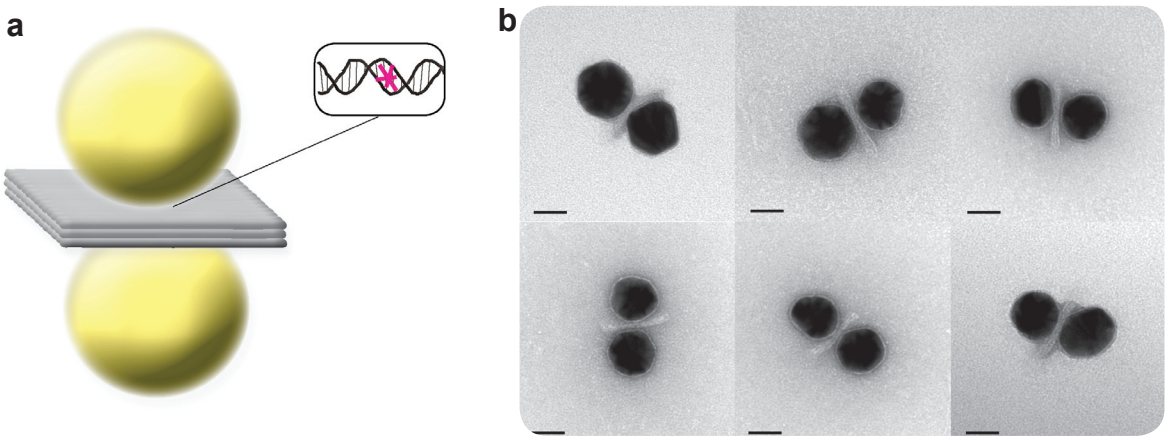

Figure 7.1: a, Schematic drawing and, **b**, transmission electron microscopy images of origami blocks between two 40 nm gold nanoparticles with dyes intercalated in the DNA structure. Scale bars, 20 nm.

A similar assembly of a DNA origami block between two gold nanoparticles is used to create a plasmonic CD signal from chiral molecules in the plasmonic focus point between the nanoparticles. The appearance of the plasmonic CD was predicted by A.O. Govorov in a recent publication [94] and has already been demonstrated [81]. We were able to prove the theory of A. O. Govorov by using a compact DNA origami structure in the plasmonic focus of two metal nanoparticles thereby detecting the chirality of double-stranded DNA from the origami structure in the plasmonic resonance of the metal nanoparticle (**Figure 7.2**). To achieve a sufficiently strong plasmonic lensing a silver shell of 10-20 nm around the 10 nm gold nanoparticles has been grown by electroless deposition of silver ions. A next step will be the incorporation of B-DNA into the DNA origami structure. B-DNA has left-handed chirality. At high salt concentrations B-DNA can be flipped to Z-DNA which has a right-handed chirality [95]. The chirality flip can then be analyzed with CD spectroscopy. Furthermore it is interesting to investigate the possibility of the detection of low amounts of chiral drugs (e.g. Ibuprofen) which can be incorporated into the origami structure.

As a outlook, creating dynamic plasmonic materials with distinct optical properties will certainly be a milestone in the field of plasmonics. It is still demanding to create dynamic plasmonic devices at nanoscale. Currently the groups of Tim Liedl and Na Liu (MPI, Stuttgart) are creating such advanced

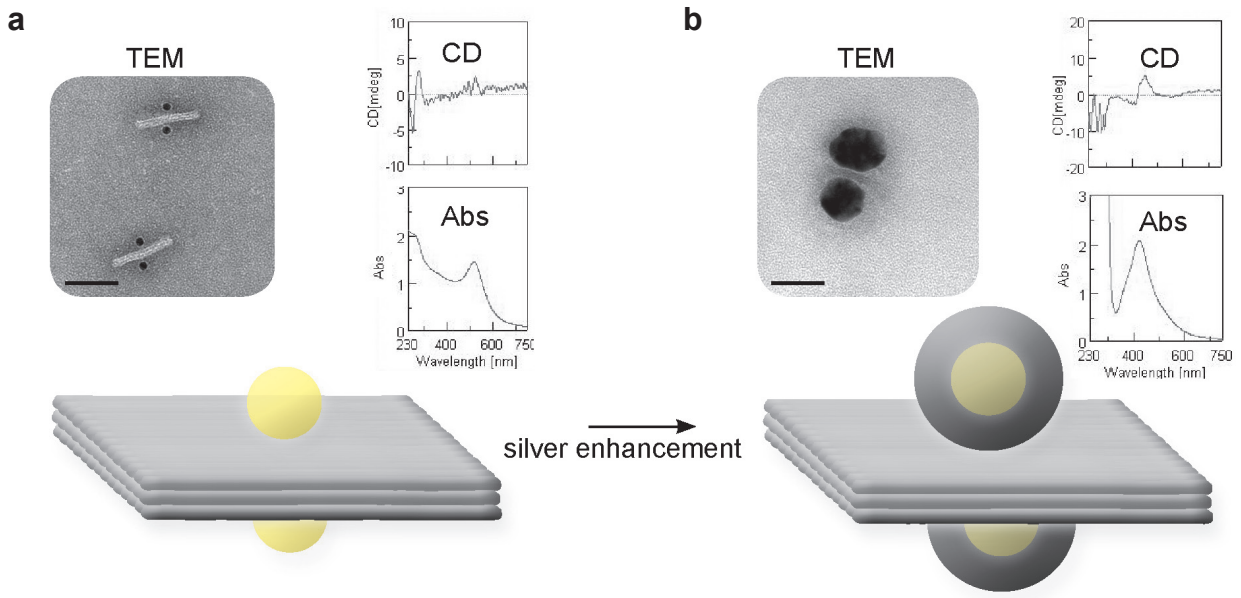

Figure 7.2: a, DNA origami block between two 10 nm gold particles and **b**, after silver enhancement of the gold nanoparticles. **Top,** Transmission electron microscopy (TEM) images, circular dichroism and absorption spectra and **bottom**, schematic drawing of the assembled nanostructures. Scale bars, 50 nm.

devices were plasmonic properties can be controlled by small triggers. Such dynamic plasmonic materials might be envisioned as bio-senors, where the presence of a specific bio-molecule triggers an optical feedback of the nanodevice. This work follows the associated publication P2.

Also initiated by associated publication P2, the following project is currently in progress: The uptake of nanohelices into cells is studied by Susanne Kempter from Tim Liedl's group. The objectives are to investigate in which regions of the cell the origami structures are transported and if they survive their time in cells. This study will be a base for the further use of cell-invasive DNA origami structures. It is also worthwhile to understand whether such plasmonic nanostructures in cells have the ability to be used as bio-sensors. Such sensors might change their plasmonic and optical properties (e.g. their response to circular polarized light) when coupling to specific (chiral) bio-molecules or getting digested.

Initiated by publication P3, the following studies are currently in progress: In cooperation with Na Liu (MPI, Stuttgart) aligned nanohelices will be placed between lithographic nanorods to verify plasmonic coupling and induced CD in the resonance of the nanorods. Following the associated publication P3 it is also envisioned that the alignment of nanohelices might be achieved using strong light sources with polarized light. Jaekwon Do from Jochen Feldmann's group (LMU) was able to show the trapping and printing of origami structures with the help of an optical trap [96]. The next step will be to combine the printing and the simultaneous alignment of nanohelices with the polarization of light. Jaekwon Do has already demonstrated this technique using gold nanorods in one of his recent publications [97].

Initiated by associated publication P4 the following projects are progressing: The creation of extensively complex planet-satellite nanostructures will be done by Luisa Kneer from Tim Liedl's lab to

fabricate catalysis and field enhancement hot spots with gold nanorods.

In conclusion, the impact of DNA nanotechnology is evidently increasing. This thesis shows only a small part of its high potential and amazing properties of controlling the nanoscale. The combination of a robust method with nearly unlimited control over the design, the advantages of self-assembly, its modularity, the nanometer-precise arrangements and compatibility with nearly all kinds of nanoparticles and bio-molecules with high yields pushes DNA nanotechnology to the position of being a all-purpose tool for the nanoscientist.

8 References

[1] http://www.unisci.com/nano_seeman.jsp. accessed Nov 1 (2013)

[2] http://scienceline.org/wp-content/uploads/2009/12/IMG_0023-640x480.jpg. accessed Nov 1 (2013)

[3] V. Linko and H. Dietz. The enabled state of DNA nanotechnology. Curr Opin Biotechnol, doi: 10.1016/j.copbio.2013.02.001 (2013)

[4] N. R. Kallenach, R.-I. Ma and N. C. Seeman. An immobile nucleic acid junction constructed from oligonucleotides. Nature 305, 829 (2013)

[5] J. Chen and N. C. Seeman. Synthesis from DNA of a molecule with the connectivity of a cube. Nature 350, 631-633 (1991)

[6] Y. Zhang and N C Seeman. Construction of a DNA-truncated octahedron. Journal American Chemical Society 116, 1661 (1994)

[7] Y. He, T. Ye, M. Su, C. Zhang, A. E. Ribbe,W. Jiang, and C. Mao. Hierarchical selfassembly of DNA into symmetric supramolecular polyhedra. Nature 452, 718 (2008)

[8] R. P. Goodman. Rapid Chiral Assembly of Rigid DNA Building Blocks for Molecular Nanofabrication. Science 310, 1661 (2005)

[9] W. M. Shih, J. D. Quispe, and G. F Joyce. A 1.7-kilobase single-stranded DNA that folds into a nanoscale octahedron. Nature 427, 618 (2004)

[10] X. Li, X. Yang, J. Qi, and N. C. Seeman. Antiparallel DNA Double Crossover Molecules As Components for Nanoconstruction. Journal of the American Chemical Society 118, 6131 (1996)

[11] T. J. Fu and N. C. Seeman. DNA double-crossover molecules. Biochemistry 32, 3211 (1993)

[12] P. Sa-Ardyen, N. C. Seeman, and A. V. Vologodskii. The Flexibility of DNA Double Crossover Molecules. Biophysical Journal 84, 3829 (2003)

[13] T. H. LaBean, H. Yan, J. Kopatsch, and F. Liu. Construction, Analysis, Ligation, and Self-Assembly of DNA Triple Crossover Complexes). Journal of the American Chemical Society 122, 1848 (2000)

[14] E. Winfree, F. Liu, L. A. Wenzler, and N C Seeman. Design and self-assembly of two-dimensional DNA crystals. Nature 394, 539 (1998)

[15] B. Yurke, A. J. Turbereld, A. P. Mills Jr., F. C. Simmel and J. L. Neumann. A DNA-fuelled molecular machine made of DNA. Nature 406, 605 (2000)

[16] J.-S. Shin and N. A. Pierce. A Synthetic DNA Walker for Molecular Transport. Journal of the American Chemical Society 126, 10834 (2004)

[17] P. Yin, H. M. T. Choi, C. R. Calvert, and N. A. Pierce. Programming biomolecular selfassembly pathways. Nature 451, 318 (2008)

[18] D. Y. Zhang, A. J. Turberfield, B. Yurke, and E Winfree. Engineering Entropy-Driven Reactions and Networks Catalyzed by DNA. Science 318, 1121 (2007)

[19] V. S. Schüller. DNA Origami Structures for Applications in Single Molecule Spectroscopy and Nanomedicine. (2013)

[20] P. W. K. Rothemund. Folding DNA to create nanoscale shapesand patterns. Nature 440, 297-302 (2006)

[21] S. M. Douglas, H. Dietz, T. Liedl, B. Högberg, F. Graf and W. M. Shih. Self-assembly of DNA into nanoscale three-dimensional shapes. Nature 459, 414-418 (2009)

[22] S. M. Douglas, A. H. Marblestone, S. Teerapittayanon, A. Vazquez, G. M. Church and W. M. Shih. Rapid prototyping of 3D DNA-origami shapes with caDNAno. Nucleic Acids Research 37, 5001–5006 (2009)

[23] H. Dietz, S.M. Douglas, and W.M. Shih. Folding DNA into twisted and curved nanoscale shapes. Science 325, 725 (2009)

[24] T. Liedl, B. Högberg, J. Tytell, D. E. Ingber, and W. M. Shih. Self-assembly of 3D prestressed tensegrity structures from DNA. Nature Nanotechnology 5, 520–524 (2010)

[25] D. Han et al. DNA Origami with Complex Curvatures in Three-Dimensional Space. Science 332, 342–346 (2011)

[26] W. Liu, H. Zhong, R. Wang, N.C. Seeman, Crystalline two-dimensional DNA-origami arrays, Angew. Chem. Int. Ed. 50, 264, (2011)

[27] Z. Zhao, Y. Liu, H. Yan. Organizing DNA Origami Tiles Into Larger Structures Using Pre-formed Scaffold Frames. Nano Letters 11, 2997–3002 (2011)

[28] B. Wei, M. Dai, and P. Yin. Complex shapes self-assembled from single-stranded DNA tiles. Nature 485, 623-626 (2012)

[29] Y. Ke, L. Ong, W. Shih, P. Yin. Three-dimensional structures self-assembled from DNA bricks. Science 338, 1177-1183 (2012)

[30] A. P. Alivisatos et al. Organization of 'nanocrystal molecules' using DNA. Nature 382, 609-611 (1996)

[31] J. Zheng, P. E. Constantinou, C. Micheel, A. P. Alivisatos, R. A. Kiehl , and N. C. Seeman. Two-Dimensional Nanoparticle Arrays Show the Organizational Power of Robust DNA Motifs. Nano Letters 6, 1502–1504 (2006)

[32] C. Steinhauer, R. Jungmann, T. L. Sobey, F. C. Simmel and P. Tinnefeld. DNA Origami as a Nanoscopic Ruler for Super-Resolution Microscopy. Angew. Chem. Int. Ed. 48, 2–6 (2009)

[33] B. Ding, Z. Deng, H. Yan, S. Cabrini, R. N. Zuckermann, and J. Bokor. Gold Nanoparticle Self-Similar Chain Structure Organized by DNA Origami. J. Am. Chem. Soc. 132, 3248–3249 (2010)

[34] A. J. Mastroianni, S. A. Claridge, and A. P. Alivisatos. Pyramidal and chiral groupings of gold nanocrystals assembled using DNA scaffolds. J. Am. Chem. Soc. 131, 8455-8459 (2009)

[35] J. Sharma, R. Chhabra, C. S. Andersen, K. V. Gothelf, H. Yan, and Y. Liu. Toward Reliable Gold Nanoparticle Patterning on Self-Assembled DNA Nanoscaffold. J. Am. Chem. Soc. 130, 7820-7821 (2008)

[36] H. Bui, C. Onodera, C. Kidwell, Y. P. Tan, E. Graugnard, W. Kuang, J. Lee, W. B. Knowlton, B. Yurke, and W. L. Hughes. Programmable Periodicity of Quantum Dot Arrays with DNA Origami Nanotubes. Nano Lett. 10, 3367–3372 (2010)

[37] N. Stephanopoulos, M. Liu, G. J. Tong, Z. Li, Y. Liu, H. Yan, and M. B. Francis. Immobilization and One-Dimensional Arrangement of Virus Capsids with Nanoscale Precision Using DNA Origami. Nano Lett. 10, 2714–2720 (2010)

[38] N. V. Voigt et al. Single-molecule chemical reactions on DNA origami. Nature Nanotechnology 5, 200 - 203 (2010)

[39] S.J. Tan, M.J. Campolongo, D. Luo, W. Cheng. Building plasmonic nanostructures with DNA. Nat. Nanotechnol. 6, 268 (2011)

[40] M. Langecker, V. Arnaut, T. G. Martin, J. List, S. Renner, M. Mayer, H. Dietz, F. C. Simmel. Synthetic lipid membrane channels formed by designed DNA nanostructures. Science 338, 932-936 (2012)

[41] G. P. Acuna et al. Distance Dependence of Single-Fluorophore Quenching by Gold Nanoparticles Studied on DNA Origami. ACS Nano 6, 3189-3195 (2012)

[42] X. Shen, C. Song, J. Wang, D. Shi, Z. Wang, N. Liu, and B. Ding. Rolling Up Gold Nanoparticle-Dressed DNA Origami into Three-Dimensional Plasmonic Chiral Nanostructures. J. Am. Chem. Soc. 134, 146–149 (2012)

[43] X. B. Shen, A. Asenjo-Garcia, Q. Liu, Q. Jiang, J. García de Abajo, N. Liu, and B. Q. Ding. 3D plasmonic chiral tetramers assembled by DNA origami. Nano Lett. 13, 2128 (2013)

[44] J. George, K. G. Thomas. Surface plasmon coupled circular dichroism of Au nanoparticles on peptide anotubes. J. Am. Chem. Soc. 132, 2502-2503 (2010)

[45] G. Shemer, O. Krichevski, G. Markovich, T. Molotsky, I. Lubitz, A. B. Kotlyar, Chirality of Silver Nanoparticles Synthesized on DNA, J. Am. Chem. Soc. 128, 11006 (2006)

[46] C.-L. Chen, N. L. Rosi. Preparation of unique 1-D nanoparticle superstructures and tailoring their structural features. J. Am. Chem. Soc. 132, 6902-6903 (2010)

[47] C. Song, M. G. Blaber, G. Zhao, P. Zhang, H. C. Fry, G.C. Schatz, and N. L. Rosi. Tailorable plasmonic circular dichroism properties of helical nanoparticle superstructures. Nano Lett. 13, 3256-3261 (2013)

[48] T.G. Schaaff, and R. L. Whetten. Giant gold−glutathione cluster compounds: intense optical activity in metal-based transitions. J. Phys. Chem. B 104, 2630-2641 (2000)

[49] A. O. Govorov, Z. Fan, P. Hernandez, J. M. Slocik, R. R. Naik, Nano Lett. 10, 1374 (2010)

[50] J. M. Slocik, A. O. Govorov, R. R. Naik. Plasmonic Circular Dichroism of Peptide-Functionalized Gold Nanoparticles. Nano Letters 11, 701 (2011)

[51] http://www.fbs.leeds.ac.uk/facilities/cd/images/1.png. accessed Nov 1 (2013)

[52] B. E. A. Saleh, M. C. Teich. Fundamentals of photonics. John Wiley & Sons Ltd, 2nd. edition, (2007)

[53] A.-P. Eskalinen. Nanoscale assembly using DNA and electromagnetic fields. (2013)

[54] S. V. Gaponenko. Introduction to nanophotonics. Cambridge University Press, 1st. edition (2010)

[55] H. Ehrenreich, H. R. Philipp. Optical properties of Ag and Cu. Phys. Rev. 128, 1622, (1962)

[56] U. Kreipig, M. Vollmer. Optical properties of metal clusters. Springer (1995)

[57] E. Prodan, C. Radloff, N. J. Halas, P. Nordlander. A hybridization model for the plasmon responce of complex nanostructures. Science 302, 5644 (2003)

[58] E. Prodan, P. Nordlander. Plasmon hybridization in spherical nanoparticles. J. Chem. Phys. 120, 5444 (2004)

[59] Weber, W. H., Ford, G.W. Propagation of optical excitations by dipolar interactions in metal nanoparticle chains. Phys. Rev B 70, 125429 (2004)

[60] Y.-R. Zhen, K. H. Fung, C. T. Chan. Collective plasmonic modes in two-dimensional periodic arrays of metal nanoparticles. Phys. Rev. B 78, 35419 (2008)

[61] Z. Fan, A. O. Govorov. Plasmonic Circular Dichroism of Chiral Metal Nanoparticle Assemblies. Nano Lett. 10, 2580 (2010)

[62] J. Yan, S. Gao. Plasmon resonances in linear atomic chains: free-electron behavior and anisotropic screening of d electrons. Phys. Rev. B 78, 235413, (2008)

[63] W. Moffitt, W. Journal of Chemical Physics 25, 467 (1956)

[64] G. D Fasman. Circular dichroism and the conformational analysis of biomolecules, Plenum, New York, (1996)

[65] N. N Berova, K. Nakanishi, R. W. Woody. Circular Dichroism: Principles and Applications, 2nd ed. Wiley-VCH, USA (2000)

[66] K. Keren, M. Krueger, R. Gilad, G. Ben-Yoseph, U. Sivan, E. Braun. Science 72, 297 (2002)

[67] M. Mertig, L. C. Ciacchi, R. Seidel, W. Pompe, A. De Vita. Nano. Lett. 2, 841 (2002)

[68] S. H. Park, R. Barish, H. Li, J. H. Reif, G. Finkelstein, H. Yan, T. H. LaBean. Nano Letters 5, 693 (2005)

[69] K. Keren, R. S. Berman, E. Braun. Nano Lett. 4, 323 (2004)

[70] Y. Liu, W. Meyer-Zaika, S. Franzka, G. Schmid, M. Tsoli, H. Kuhn. Angew. Chem. Int. Ed. 42, 2853 (2009)

[71] H. J. Kim, Y. Roh, B. Hong. Langmuir 26, 18315 (2010)

[72] P. Nickels, W. Dittmer, S. Beyer, J. P. Kotthaus, F. C. Simmel. Nanotechnology 15, 1524 (2004)

[73] R. Schreiber, S. Kempter, S. Holler, V. Schüller, D. Schiffels, S. S. Simmel, P. C. Nickels, and T. Liedl. DNA Origami-Templated Growth of Arbitrarily Shaped Metal Nanoparticles. Small 7, 1795-1799 (2011)

[74] J.K. Gansel et al. Gold Helix Photonic Metamaterial as Broadband Circular Polarizer Science 325, 1513-1515 (2009)

[75] C. M. Soukoulis, and M. Wegener. Past achievements and future challenges in the development of three-dimensional photonic metamaterials. Nature Photonics 5, 523–530 (2011)

[76] J. A. Fan et al. Self-Assembled Plasmonic Nanoparticle Clusters. Science 328, 1135-1138 (2010)

[77] X. Xiong et al. Construction of Chiral Metamaterial with a Helix Array. arXiv.org:1107.4994 (2011)

[78] A. Sonsilphong, and N. Wongkasem. Three-dimensional artificial double helices with high negative refractive index. J. Opt. 14,105103 (2012)

[79] A. Briegel, M. Pilhofer, D. N. Mastronarde, G. J. Jensen. The challenge of determining handedness in electron tomography and the use of DNA origami gold nanoparticle helices as molecular standards. Journal of Structural Biology 183, 95–98 (2013)

[80] A. Kuzyk, R. Schreiber, Z. Fan, G. Pardatscher, E.-M. Roller, A. Högele, F. C. Simmel, A. O. Govorov, and T. Liedl. DNA-Based Self-Assembly of Chiral Plasmonic Nanostructures with Tailored Optical Response. Nature 483, 311-314 (2012)

[81] Z. Li et al. Reversible Plasmonic Circular Dichroism of Au Nanorod and DNA Assemblies. J. Am. Chem. Soc. 134, 3322–3325 (2012)

[82] H. T. Chen et al. Active terahertz metamaterial devices. Nature 444, 597-600 (2006)

[83] F. Zhang et al. Magnetically tunable left handed metamaterials by liquid crystal orientation. Optics Express 17, 4360-4366 (2009)

[84] W. M. Zhu et al. Switchable Magnetic Metamaterials Using Micromachining Processes. Adv. Materials 23, 1792-1796 (2011)

[85] Bo, Z. et al. Switchable metamaterial reflector/absorber for different polarized electromagnetic waves. Appl. Phys. Lett. 97, 51906 (2010)

[86] Ou, J. Y., Plum, E., Zhang, J. & Zheludev, N. I. An electromechanically reconfigurable plasmonic metamaterial operating in the near-infrared. Nature Nanotechnology 8,252–255 (2013)

[87] J. Sharma et al. Control of self-assembly of DNA tubules through integration of gold nanoparticles. Science 323, 112 -116 (2009)

[88] D. S. Sebba, J. J. Mock, D. R. Smith, T. H. LaBean, and A. A. Lazarides, A. A. Reconfigurable Core-Satellite Nanoassemblies as Molecularly-Driven Plasmonic Switches. Nano Lett. 8, 1803-1808 (2008)

[89] Z. Nie, A. Petukhova, and E. Kumacheva. Properties and emerging applications of self-assembled structures made from inorganic nanoparticles. Nature Nanotech. 5, 15-25 (2010)

[90] N. Gandra, A. Abbas, L. Tian, and S. Singamaneni. Plasmonic Planet-Satellite Analogues: Hierarchical Self-Assembly of Gold Nanostructures. Nano Lett. 12, 2645-2651 (2012)

[91] A. R. Clapp, I. L. Medintz, and H. Mattoussi. Förster Resonance Energy Transfer Investigations Using Quantum-Dot Fluorophores. ChemPhysChem 7, 47-57 (2006)

[92] G. P. Acuna et al. Distance Dependence of Single-Fluorophore Quenching by Gold Nanoparticles Studied on DNA Origami. ACS Nano 6, 3189-3195 (2012)

[93] Z. Deng, A. Samanta, J. Nangreave, H. Yan, and Y. Liu. Robust DNA-Functionalized Core/Shell Quantum Dots with Fluorescent Emission Spanning from UV-vis to Near-IR and Compatible with DNA-Directed Self-Assembly. J. Am. Chem. Soc. 134, 17424-17427 (2012)

[94] H. Zhang and A. O. Govorov. Giant circular dichroism of a molecule in a region of strong plasmon resonances between two neighboring gold nanocrystals. Physical Review B 87, 075410 (2013)

[95] C. Mao, W. Sun, Z. Shen, and N. C. Seeman. A nanomechanical device based on the B–Z transition of DNA. Nature 397, 144-146 (1999)

[96] J. Do, R. Schreiber, A. A. Lutich, T. Liedl, J. Rodríguez-Fernández, and J. Feldmann. Design and Optical Trapping of a Biocompatible Propeller-like Nanoscale Hybrid. Nano Lett. 12, 5008-5013 (2012)

[97] J. Do, M. Fedoruk, F. Jäckel, J. Feldmann. Two-Color Laser Printing of Individual Gold Nanorods. Nano letters 9, 4164-4168 (2013)

9 Appendix

Supporting information for associated publication P1

Supporting Information

DNA Origami-Templated Growth of Arbitrarily Shaped Metal Nanoparticles

bya

Robert Schreiber, Susanne Kempter, Stefan Holler, Verena Schüller, Daniel Schiffels, Stephanie S. Simmel, Philipp C. Nickels, and Tim Liedl

published in

Small 2011, 7, 1795-1799

Submitted to small NANO MICRO

Supporting Information for the manuscript:

DNA Origami Templated Growth of Arbitrarily Shaped Metal Nanoparticles

Robert Schreiber, Susanne Kempter, Stefan Holler, Verena Schüller, Daniel Schiffels,

Stephanie S. Simmel, Philipp C. Nickels, Tim Liedl[*]

Department of Physics and Center for Nanoscience, Ludwig-Maximilians-Universität

Geschwister-Scholl-Platz 1, 80539 München (Germany) Fax: (+49)89-2180-3182

[*]tim.liedl@lmu.de

Uranyl Acetate Staining on Electron Microscope Grids: Formvar-carbon coated copper grids (PLANO GmbH, Germany) were made hydrophylic by glow discharge in a plasma cleaner (Diener, Germany) using argon. We applied 1.5 µl DNA origami to the surface of an electron microscope grid for two minutes. Excess of DNA Origami was dabbed off with Whatman filterpaper (Roth, Germany). The grids were washed with a 1 % Uranyl acetate solution (10 µl) and subsequently stained for one minute with additional 10 µl Uranyl acetate solution. Finally, excess of Uranyl acetate solution was dabbed off with Whatman filterpaper and air-dried.

Wafer preparation: We used Silicon wafers (Si-Mat) with a 20 nm silicon oxide layer. First, the wafers were cleaned. All cleaning steps were done in an ultrasonic bath for ten minutes (H_2O, acetone, isopropanol, H_2O). The different cleaning steps were followed by a Piranha solution treatment to get rid of organic residues. Then the wafers were passivated with 3 Aminopropyldimethyl-ethoxysilan (ABCR, Germany) by soaking them for one hour at room temperature in a 1 % 3 Aminopropyldimethyl-ethoxysilan solution in isopropanol. The wafers were washed ten times both with isopropanol and H_2O. Finally, the wafers were dried with nitrogen and incubated for one hour in an oven at 80°C.

TEM Imaging: Samples were imaged with a Transmission Electron Microscope (JEOL JEM-1011, JEOL GmbH) at 100 kV.

SEM Imaging. Samples were imaged with Scanning Electron Microscope (Zeiss, Leo Gemini 982) at 10 kV

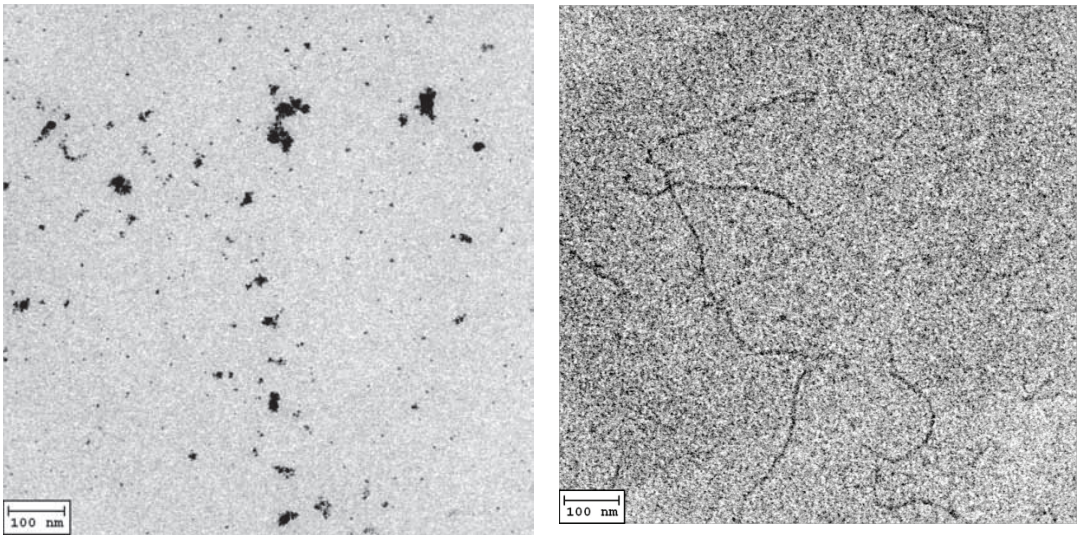

Figure S1. Left: Six-helix bundles were placed on carbon-coated grids and exposed to the electroless gold deposition process without prior Au cluster seeding. Only unspecific growth of shapeless gold particles occurs.
Right: Six-helix bundles were exposed to 1.4 nm Au clusters during the seeding process, but no enhancement process followed. The intact six-helix bundles are visible on the TEM grids without further staining. Individual 1.4 nm clusters could not be resolved in the electron micrographs.

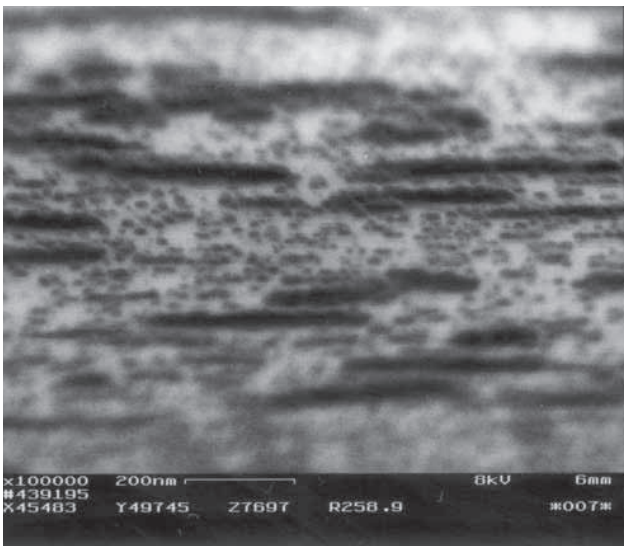

Figure S2. Tilted (80°) Si-wafer with metalized six-helix bundles. The three-dimensional nature of the gold particles is clearly recognizable. Small background particles form half spheres while the large bundles form half cylinders with a height of ~25 nm. Volumes of correctly formed particles were estimated from TEM images, summed up and compared to the sum of estimated volumes of background particles and larger aggregates of undefined size. We conclude that more than 81% of material is converted into particles of correct shape and size.

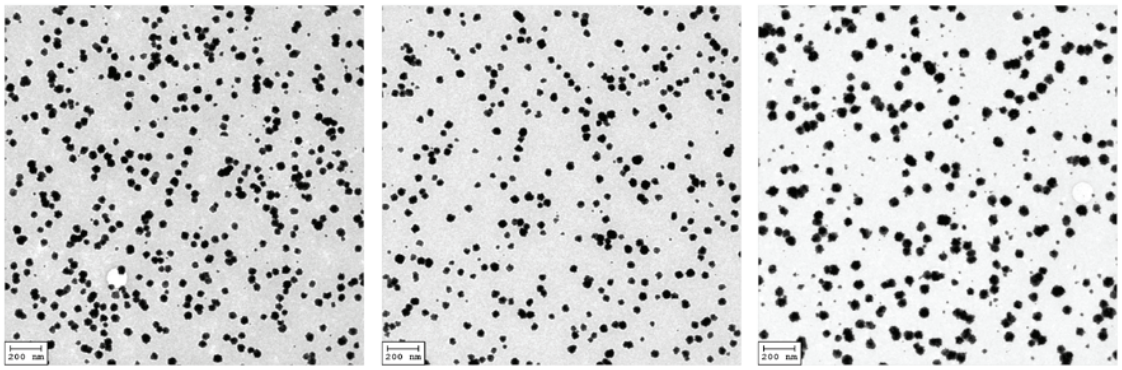

Figure S3. Surface passivation of carbon-coated TEM grids to determine effects on the background formation of Au particles without DNA templates. For all samples we used the previously described process for metallization on carbon-coated grids. Left: Control sample without any passivation. Middle: Passivation with 1% BSA. The 1% BSA solution was incubated for 30 min on the TEM grid. Right: Passivation with Tween. The 0.1% Tween solution was incubated for 30 min on the TEM grid. We found that no significant background reduction could be achieved by treating the carbon-coated grids with BSA or Tween.

Design Schematic of DNA origami six-helix bundle

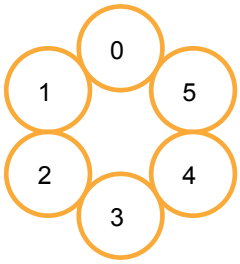

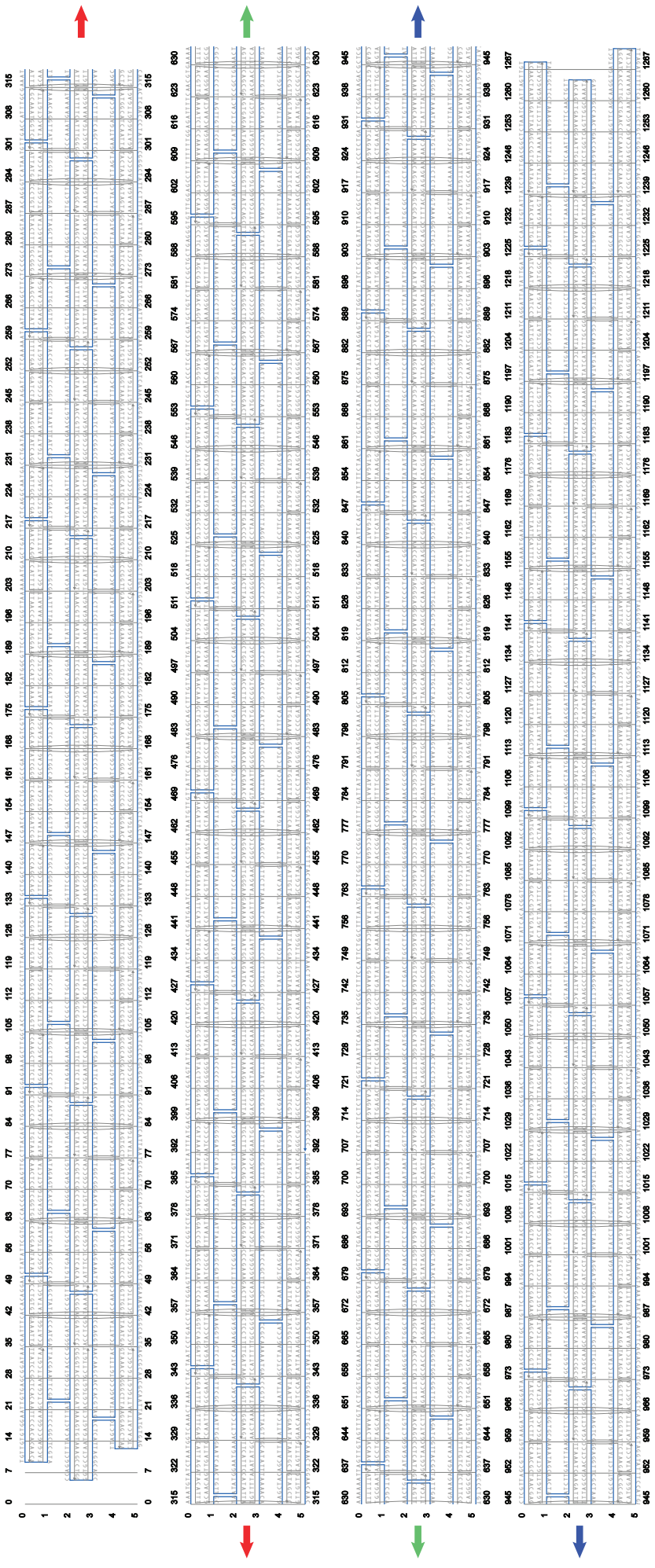

Design Schematic of DNA origami
14-helix bundle

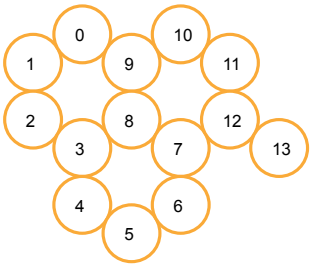

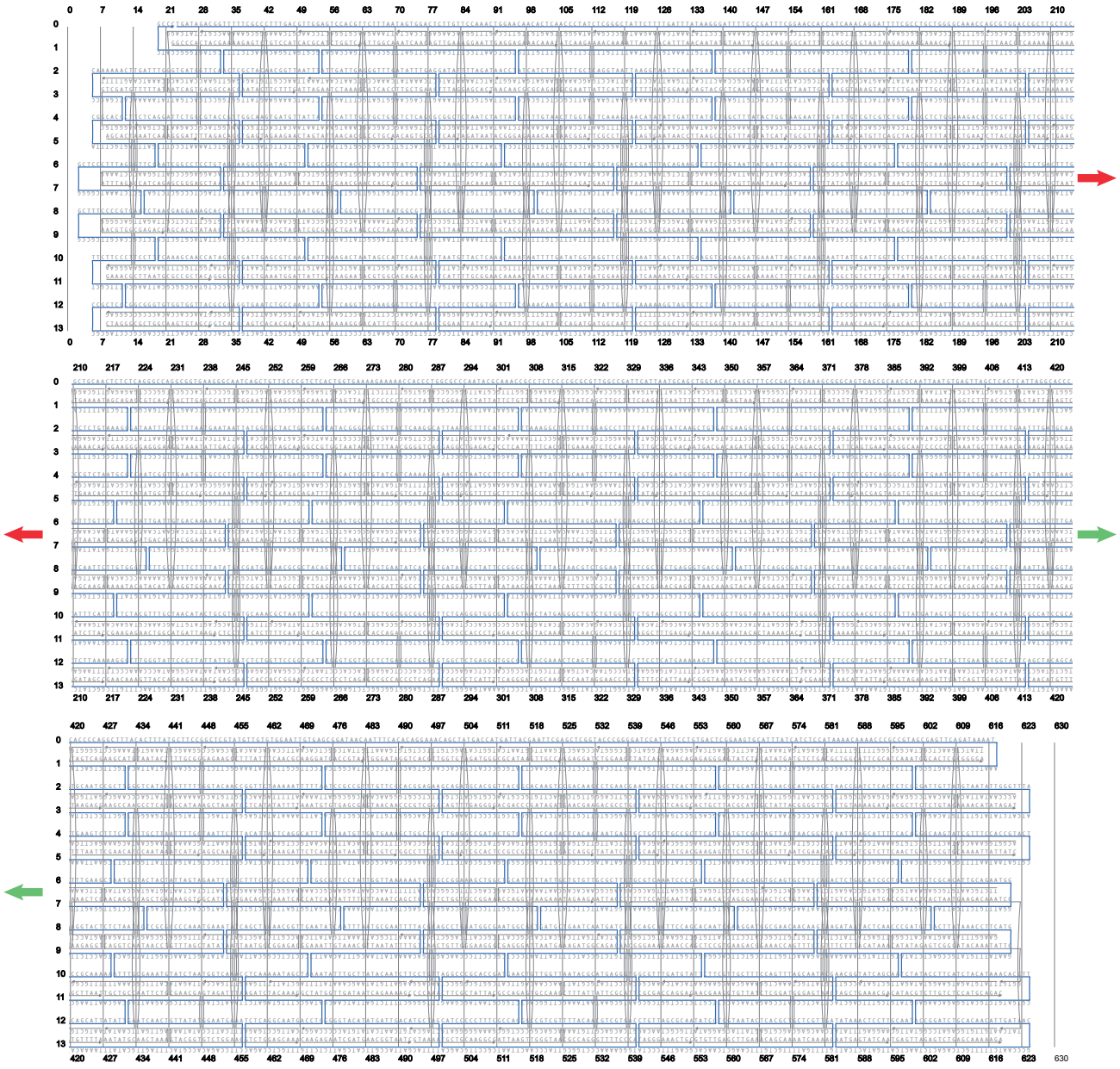

Design Schematic of DNA origami donut implemented by a curved six-helix bundle

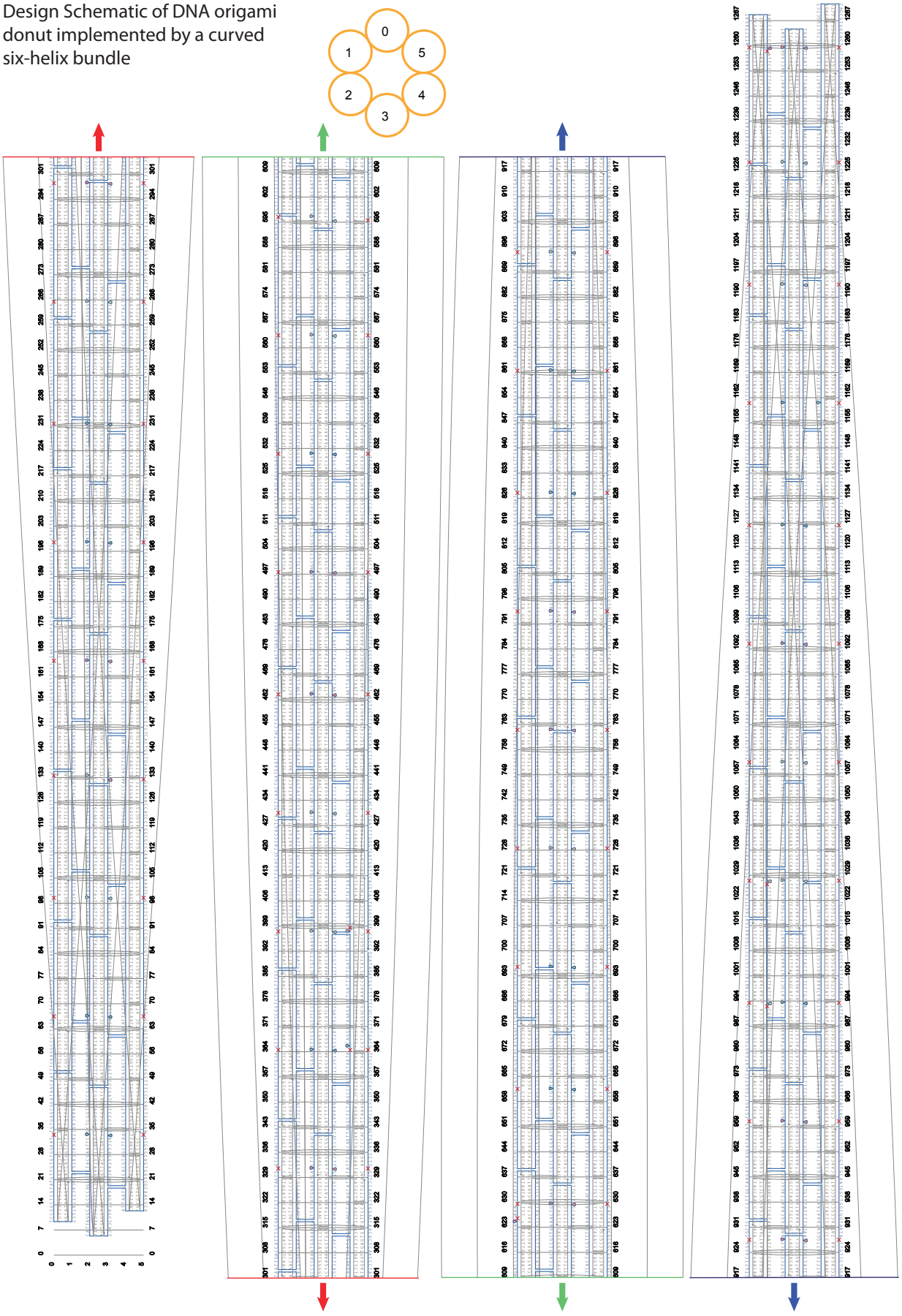

Design Schematic of DNA origami
corner-to-corner polymerized cuboid

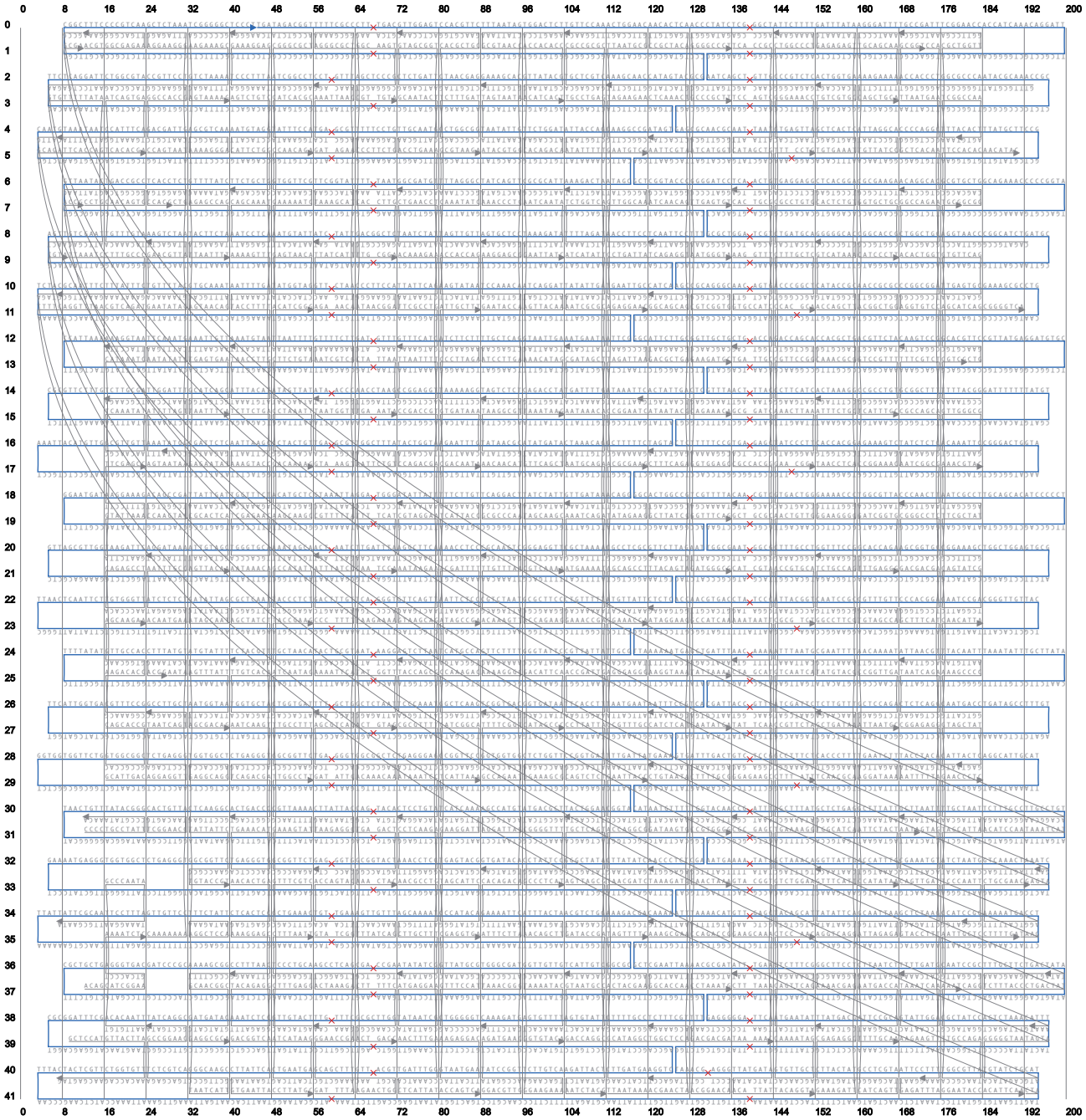

Design Schematic of DNA origami kite

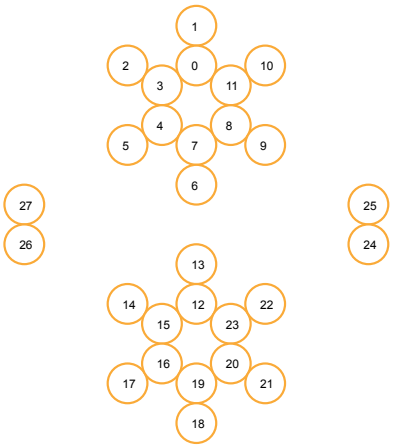

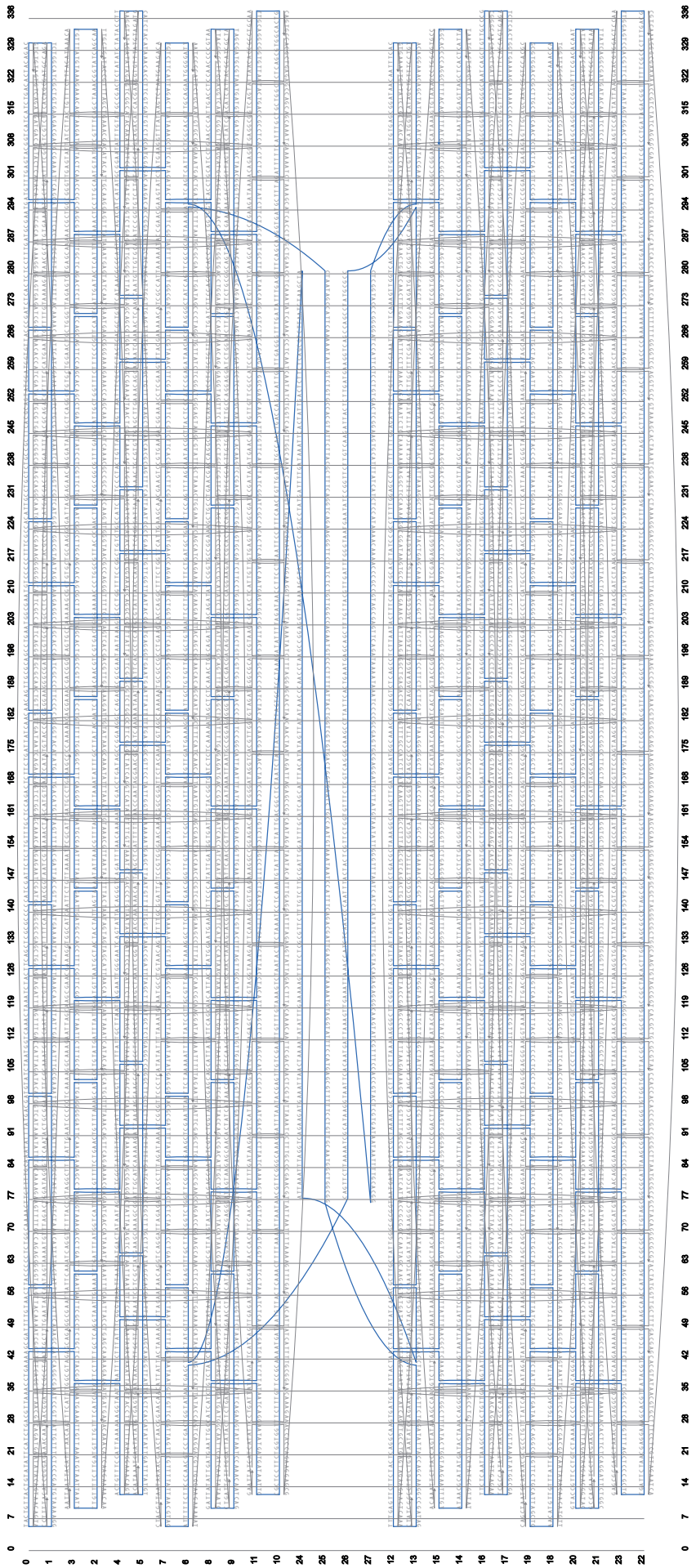

Design Schematic of DNA origami
24-helix bundle

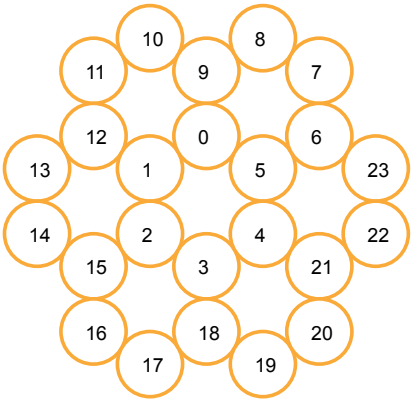

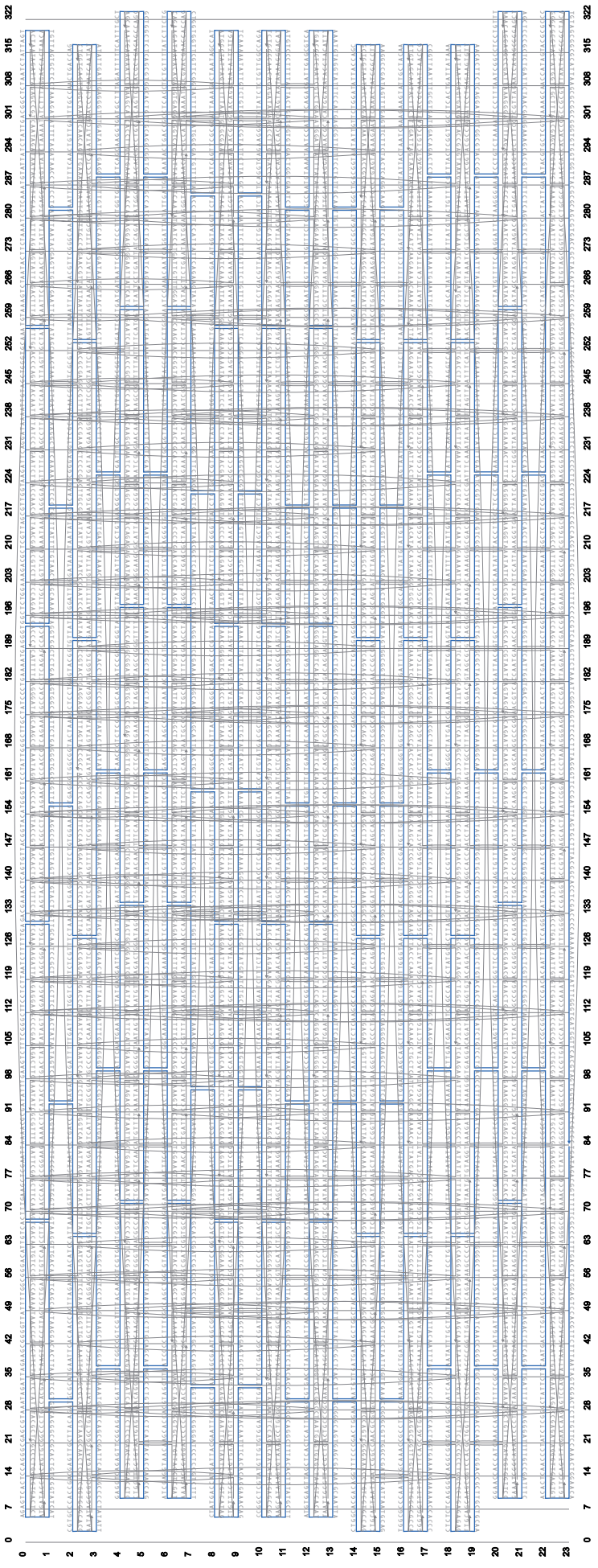

Supporting information for associated publication P2

Supporting Information

DNA-Based Self-Assembly of Chiral Plasmonic Nanostructures with Tailored Optical Response

by

Anton Kuzyk,* Robert Schreiber,* Zhiyuan Fan, Günther Pardatscher, Eva-Maria Roller, Alexander Högele, Friedrich C. Simmel, Alexander O. Govorov and Tim Liedl

*equal contribution

published in

Nature 2012, 483, 311-314

doi:10.1038/nature10889

Supplementary Note S1: Circular dichroism: helical protein and plasmonic helices

In this section we compare optical and chiral properties of bio-molecules and plasmonic nanostructures. Nature is remarkably skilled at creating and tailoring chirality of bio-molecules to achieve specific functions such as chiral recognition in bio-chemical reactions and the majority of bio-molecules and modern drugs are chiral. Their chirality is conveniently tested by measuring circular dichroism (CD) and optical rotatory dispersion (ORD) responses. Interestingly, for most naturally occurring molecules the optical extinction and chiral optical response are predominantly found in the UV spectral interval (Figure S1a and b) and is, e.g., for double-stranded DNA on the order of 5-20 M^{-1} cm^{-1} per base pair. In contrast, most artificial nanoscale objects such as nanocrystals are very strong absorbers in the visible spectrum and do not exhibit CD signals, as they are non-chiral (Figure S1 c and d). The molar extinction of a single metal nanoparticle is many orders of magnitude larger than that of a single molecule. A typical extinction for a molecular dipole is $\varepsilon_{molecule} \sim 10^4 \left(M \cdot cm\right)^{-1}$ whereas, for a gold nanoparticle $\varepsilon_{NP} \sim 10^8 \left(M \cdot cm\right)^{-1}$.

According to the general quantum theory of optical activity, the strength of the CD signal of a molecular dipole is given by[31]

$$CD_0 \sim \mathrm{Im}(\boldsymbol{\mu}_{12} \cdot \mathbf{m}_{21}), \qquad \text{(SEq.1)}$$

where $\boldsymbol{\mu}_{12}$ and $\mathbf{m}_{21}$ are the quantum matrix elements of the electric and magnetic dipole operators, respectively, and the indices 1 and 2 denote the ground and excited states of the molecule. Equation (SEq. 1) shows that a CD signal in a molecular system arises from the joint reaction of electric and magnetic dipoles of a molecule to light. In contrast, optical chirality and CD studied in this paper originate from plasmonic interactions between nanoparticles in an assembly with a chiral geometry (Figure S1e and f). The theory in this case is purely classical[32,33] and is based on Maxwell's equations. However, the classical results (see the Supplementary Note S2) can also be understood in terms of the quantum equation SEq.1. The plasmon-plasmon interactions in a chiral assembly create dynamic magnetic moments which are responsible for the appearance of non-zero CD signals in chiral complexes.

It is instructive to compare qualitatively the mechanisms of formation of the bisignate CD signals in helical proteins and in plasmonic complexes (Figure S1b and f). Obviously, the shapes of the CD spectra are similar but the spectral regions are very different. The protein shows CD in the UV whereas the plasmonic helix has sizeable CD signals only in the visible spectral range. This significant difference is a result of different absorptive properties of the systems. The bisignate CD spectrum of α-helix proteins is well described by the theory of interacting dipoles arranged on a helical line[34,35,36]. In this dipolar theory every residue (building block) in a helical chain of amino acids (see inset in Figure S1a) has one dipole. Dipolar Coulomb interaction gives rise to the formation of a new spectrum of collective excitations. The spectrum of molecular excitons splits due to these collective effects; the corresponding CD signals have opposite signs and their superposition results in a bisignate CD spectrum[34]. The origin of the bisignate CD in the plasmonic helix is a consequence of dynamic Coulomb interaction between dipoles of metal nanoparticles. The spectrum of excitations in this case is more complex since every nanoparticle has three dipoles. In analogy to molecular dipoles, Coulomb interaction creates a splitting between the collective plasmonic modes (Figures S3 and S4). It is noteworthy that even though the handedness of the alpha-helix protein and the plasmonic helix, depicted in Figure S1 a and e, respectively, are the same, the bisignate shape of their CD spectra is inverted. In fact, the sequence of the positive and negative band in the bisignate spectrum of a right-handed plasmonic helix may invert depending on the pitch and on the radius of a helix[33]. Moreover, long-range electromagnetic effects should be taken into account[33,35,36] for long helices (molecular or plasmonic).

For a quantitative comparison of CD from different systems it is convenient to use the asymmetry factor defined as:

$$g = \frac{\Delta\varepsilon_{CD}}{\varepsilon_0}, \qquad \text{(SEq.2)}$$

where $\varepsilon_0 = \left(\varepsilon_+ + \varepsilon_-\right)/2$ is the extinction of a given chiral object. For chiral molecules like proteins, DNA, sugars, etc. this factor is on the order of $\sim 10^{-2} - 10^{-3}$. In particular, for the α-helix, $g_{protein} \sim 30/10^4 \sim 0.003 = 0.3\%$. We can estimate this asymmetry factor for our "super-enhanced" plasmonic helix shown in Figure 3b of the main manuscript. Taking the measured CD and extinction, we obtain a remarkably large number, $g_{plasmonic\ helix} \sim 0.02 = 2\%$. This large number is a signature of strong collective effects arising for large plasmonic dipoles in a tightly-packed chiral assembly.

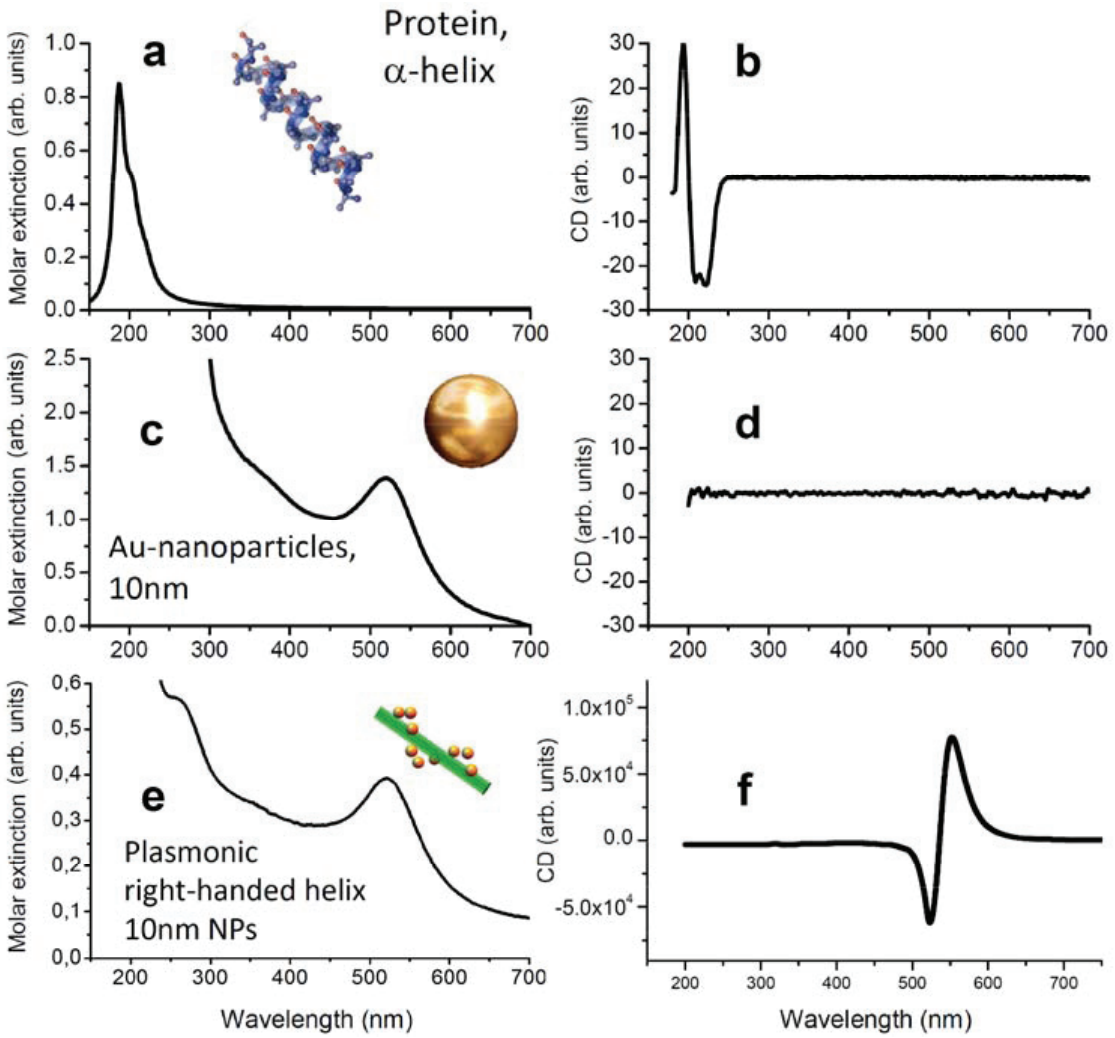

Figure S1 | Chiro-optical properties of α-helix protein, gold nanoparticle and gold nanohelix. a and **b**, Optical extinction and CD signal of solutions containing α-helix peptides (short proteins). **c** and **d**, Optical extinction and CD signal of solutions containing gold nanoparticles. **e** and **f**, Optical extinction and CD signal recorded for solutions with gold nanohelices; the curves **a**, **b**, **c** and **d** are taken from Ref.37.

Supplementary Note S2: Theoretical modelling of plasmonic helices

We describe plasmonic CD spectra of helical assemblies by employing a model of interacting dipoles[32,38]. This approach is valid for large surface-to-surface separation between neighboring particles in an assembly and describes the main properties of CD in nanoparticle systems induced by plasmon-plasmon interactions[32,39]. Since individual particles are non-chiral, the chiral optical property of an assembly emerges from interactions between plasmonic dipoles arranged in a chiral geometry. The experimental CD signal is usually measured as the optical response of randomly-oriented complexes in solution and its theoretical modelling therefore requires averaging over the orientation of all contributing complexes. A detailed description of the related theoretical methods can be found in Ref. 32. Here we recapitulate briefly the main points.

The extinction coefficient of the system is calculated from the general equation:

$$Q_{extinc,\pm} = \frac{1}{2}\mathrm{Re}\int_V \vec{j}^{*}_{\omega,\pm}(\vec{r})\cdot\vec{E}_{ext,\omega,\pm}(\vec{r})\,dV \quad , \qquad \text{(SEq.3)}$$

where $\vec{j}^{*}_{\omega,\pm}$ and $\vec{E}_{ext,\omega,\pm}$ are the complex amplitudes of the induced electric current and the external electric field, respectively. The external electric fields are described by the circularly-polarized electromagnetic wave $\vec{E}_{ext,\omega,\pm} = \vec{e}_{\pm}E_0 e^{i\sqrt{\varepsilon_0}\vec{k}\vec{r}-i\omega t}$ with the polarization vectors $\vec{e}_{\pm}$ and the relative permittivity of the medium $\varepsilon_0 = 1.8$ (water). In the coupled-dipole approach, equation SEq.3 for small particles leads to the following expression for the extinction cross section:

$$\sigma_{extin,\pm} = \sqrt{\varepsilon_0}\,\frac{8\pi}{2\cdot E_0^2\cdot c_0}\,\omega\cdot\mathrm{Im}\left[\left(\sum_{i=1}^{N_{NP}}\vec{E}^{*}_{ext,\omega,i,\pm}\cdot\vec{d}_{i,\pm}\right)\right], \qquad \text{(SEq.4)}$$

where $\vec{d}_{i,\pm}$ are the induced dipoles of the nanoparticles, i is the nanoparticle index, and N_{NP} is the number of particles in an assembly (helix). The dipoles $\vec{d}_{i,\pm}$ are calculated numerically from the system of coupled equations:

$$\vec{d}_i = \alpha_{NP}\left(\vec{E}_{ext,\omega,i} + \sum_{j\neq i}\left[\frac{3(\vec{d}_j\cdot\vec{n}_{ji})\cdot\vec{n}_{ji}-\vec{d}_j}{r_{ij}^3}\left(1-ik\sqrt{\varepsilon_0}r_{ij}\right)+\varepsilon_0 k^2\frac{\vec{d}_j-(\vec{d}_j\cdot\vec{n}_{ji})\cdot\vec{n}_{ji}}{r_{ij}}\right]e^{ik\sqrt{\varepsilon_0}r_{ij}}\right) \quad \text{(SEq.5)}$$

Here, $\vec{r}_{ij} = \vec{r}_i - \vec{r}_j$ are the vectors that interconnect particles along the normal vectors $\vec{n}_{ij} = \vec{r}_{ij} / \left|\vec{r}_{ij}\right|$; $\alpha_{NP}(\omega) = a_{NP}^3\left(\varepsilon_{NP}-\varepsilon_0\right)/\left(\varepsilon_{NP}+2\varepsilon_0\right)$ is the single particle polarizability, where a_{NP} is the particle radius and $\varepsilon_{NP} = \varepsilon_{NP}(\omega)$ is the dielectric function adopted from experimental tables[40].

The total extinction CD is calculated from SEq.4 as

$$\Delta\varepsilon_{CD} = \left(\frac{N_A}{0.23}\right)10^{-4}\cdot\left\langle\sigma_{extin,+}-\sigma_{extin,-}\right\rangle_\Omega, \quad \text{(SEq.4)}$$

where the averaging over the solid angle, $\langle\ldots\rangle_\Omega$, is necessitated by the random orientation of the chiral complexes in solution and N_A is the Avogadro number.

It is constructive to consider individual components of the CD response parallel and perpendicular to the helical axes taken along z. First, we decompose the external electric field:

$$\vec{E}^*_{ext,\omega} = \vec{E}^*_{ext,\omega,\perp} + \vec{E}^*_{ext,\omega,\parallel},$$

where $\vec{E}^*_{ext,\omega,\perp}$ is the electric-field vector in the x-y plane and $\vec{E}^*_{ext,\omega,\parallel}$ is the z-component of the field. An analogous decomposition of the extinction and the CD spectrum yields:

$$\sigma_{extin,\pm} = \sigma_{extin,\pm,\parallel} + \sigma_{extin,\pm,\perp},$$

$$\sigma_{extin,\pm,\parallel} = \sqrt{\varepsilon_0}\frac{8\pi}{2\cdot E_0^2\cdot c_0}\omega\cdot\mathrm{Im}[\left(\sum_{i=1}^{N_{NP}}E^*_{ext,\omega,i,\parallel,\pm}\cdot d_{i,\parallel,\pm}\right)], \quad \text{(SEq.5)}$$

$$\sigma_{extin,\pm,\perp} = \sqrt{\varepsilon_0}\frac{8\pi}{2\cdot E_0^2\cdot c_0}\omega\cdot\mathrm{Im}[\left(\sum_{i=1}^{N_{NP}}\vec{E}^*_{ext,\omega,i,\perp,\pm}\cdot\vec{d}_{i,\perp,\pm}\right)].$$

$$\Delta\varepsilon_{CD} = \Delta\varepsilon_{CD,\parallel} + \Delta\varepsilon_{CD,\perp},$$

$$\Delta\varepsilon_{CD,\parallel} = \left(\frac{N_A}{0.23}\right)10^{-4}\cdot\left\langle\sigma_{extin,+,\parallel}-\sigma_{extin,-,\parallel}\right\rangle_\Omega, \quad \text{(SEq.6)}$$

$$\Delta\varepsilon_{CD,\perp} = \left(\frac{N_A}{0.23}\right)10^{-4}\cdot\left\langle\sigma_{extin,+,\perp}-\sigma_{extin,-,\perp}\right\rangle_\Omega.$$

The above equations define the CD and the extinction contributions induced by the electric-field components that are perpendicular ($\perp$) and parallel ($\|$) to the helical axis. Finally, we define the directional CD signal as:

$$\Delta\varepsilon_{CD}(\theta,\varphi)=\left(\frac{N_A}{0.23}\right)10^{-4}\cdot\left[\sigma_{extin,+}(\theta,\varphi)-\sigma_{extin,-}(\theta,\varphi)\right], \qquad \text{(SEq.7)}$$

that is the CD signal for a particular direction of the incident electric field with the wave vector $\vec{k}$. The direction of vector $\vec{k}$ is given by the two spherical angles, θ and φ (Fig S2).

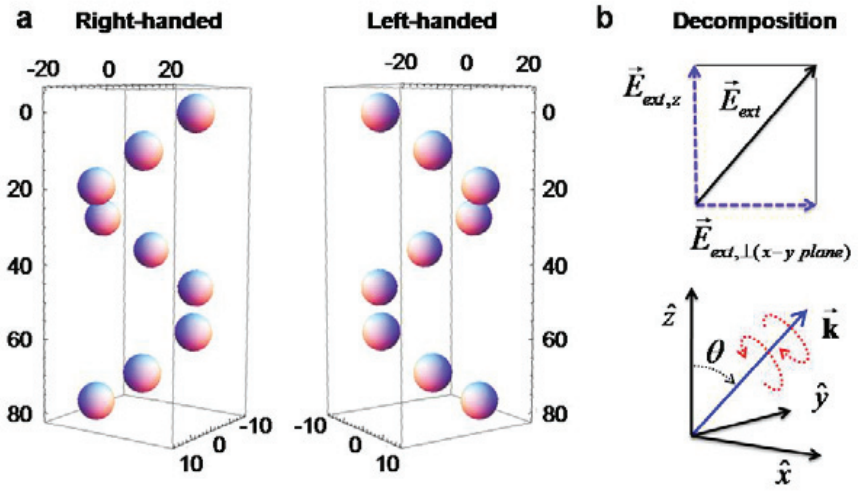

Figure S2 | Models of the helices and the coordinate system. a, Models of right- and left-handed helices (numbers in nm). **b**, The graph also shows the decomposition of the electric field and the coordinate system.

In the main text, Figures 2b and d present calculations based on SEq.3-SEq.9 for helices with the following parameters: N_{NP} = 9 gold nanoparticles, 6 particles per pitch, *pitch* = 9.5 nm and a helical radius of R_0 = 17 nm. The size of the nanoparticles was taken as 10 nm and 16 nm (the radius a_{NP} = 5 nm and a_{NP} = 8 nm) to calculate the CD spectra in Figure 2 b and d (main manuscript), respectively.

Now we will look closely at the CD properties of a plasmonic helix and consider one particular example of particles with a radius a_{NP} = 5 nm (cf. model in Figure S2). The averaged CD spectra for the right- and left-handed helices have the characteristic bisignate shapes that indicate the underlying mechanism of optical chirality. We consider the components of the CD spectra for a right-handed helix shown in Fig. S3a, where we used the following notation: $\Delta\varepsilon_{CD,\|}$ = z-CD and $\Delta\varepsilon_{CD,\perp}$ = xy-CD . We see that the peaks for the z-CD and *xy*-CD are split which is the manifestation of interaction

between plasmonic modes in the helix. In a simplified picture, collective excitations in a helix can be divided into longitudinal (dipoles parallel to the *z*-direction) and transverse (perpendicular dipoles) modes. Due to different longitudinal and transverse coupling strengths among individual NPs, we expect that the energies of the respective collective modes should be different, as shown in Figure S3a. The *z*-modes (dipoles are parallel to the helical axis) are excited mainly by the *z*-component of the incident electric field and they are most active for the incident light with the inclination $\theta \approx \pi / 2$ (Figure S3b, the right graph). These characteristics are seen as the yellow region in the equatorial area in the right panel of Figure S3b and c. These *z*-modes result in a positive signal at $\lambda = 552$ nm and form the positive peak in the total CD at $\lambda = 552$ nm. Interestingly, the *xy*-plasmon oscillations are efficiently excited by the light coming with the inclination angles: $\theta \approx 0$ and π (blue areas in the left panel of Figure S3b and c). In the right-handed helix, the *xy*-modes produce a negative CD signal at $\lambda = 522$ nm (blue colour in the polar areas in graphs b and c on the left). Since the positive *z*-CD peak and the negative *xy*-CD peak are slightly split, the resultant CD spectrum that can be measured experimentally from a solution receives a dip-peak shape (Figure S3a). In the case of the left-handed helix, the spectra become inverted (Figure S4). Some of the above properties of plasmonic helices resemble the features typical for the UV-CD spectra of α-helices of proteins[41].

Finally, we discuss briefly the effects of disorder in our plasmonic structures. The averaged conjugation yield per an attachment site in the experimental structures was 96-98% and, therefore, we can neglect disorder due to missing nanoparticles. A relevant type of disorder can be expected from random fluctuations in the positions of individual nanoparticles. In all our calculations, we found that the bisignate pattern of the CD spectrum is remarkably stable against the spatial disorder in a helix. This result, however, is not surprising if we recall the CD properties of proteins. It is known that proteins exhibit strong CD signals in the UV spectral range even for the random-coil conformational state[41]. Moreover, helical proteins are in general not periodic. Nevertheless, they exhibit remarkably strong UV-CD signals. By analogy one would expect some robustness of CD response from helical arrangement of nanoparticles with respect to the spatial disorder. Figure S5 summarizes the results. The positions of the nanoparticles for non-ideal helices in Figure S5 were obtained using a random-number generator. A particle coordinate was allowed to acquire a random component Δx in one direction. With this displacement, the particle coordinate becomes $x = x_0 + \Delta x$, where x_0 is the position of the particle in the ideal helix. Random numbers for Δx were distributed uniformly in a given interval: $-\Delta x_{\max} < \Delta x < \Delta x_{\max}$. The parameter $\Delta x_{\max}$ was taken as 2, 5, 10nm (Figure S5). A trail was discarded when it gave particle positions that were too close to each other. We found that for the considered helix ($pitch = 9.5$ nm and $R_0 = 17$ nm), a moderate disorder with $\Delta x_{\max} = 2$ nm did not affect significantly the chiral property (Figure S5b, left panel). Only for the largest disorder parameters

($\Delta x_{max} \sim 5-10$ nm), we observed the expected strong reduction of the CD signals. In this case, the CD spectrum starts to fluctuate strongly as a function of the trial number (Figure S5b, right panel). For the helices that were realized experimentally, the disorder parameter is of the order of few nanometres and therefore has only marginal effect on the resulting CD signals. The robustness of the CD of helical geometries against disorder is one of the reasons why our structures consistently exhibited very strong CD signals.

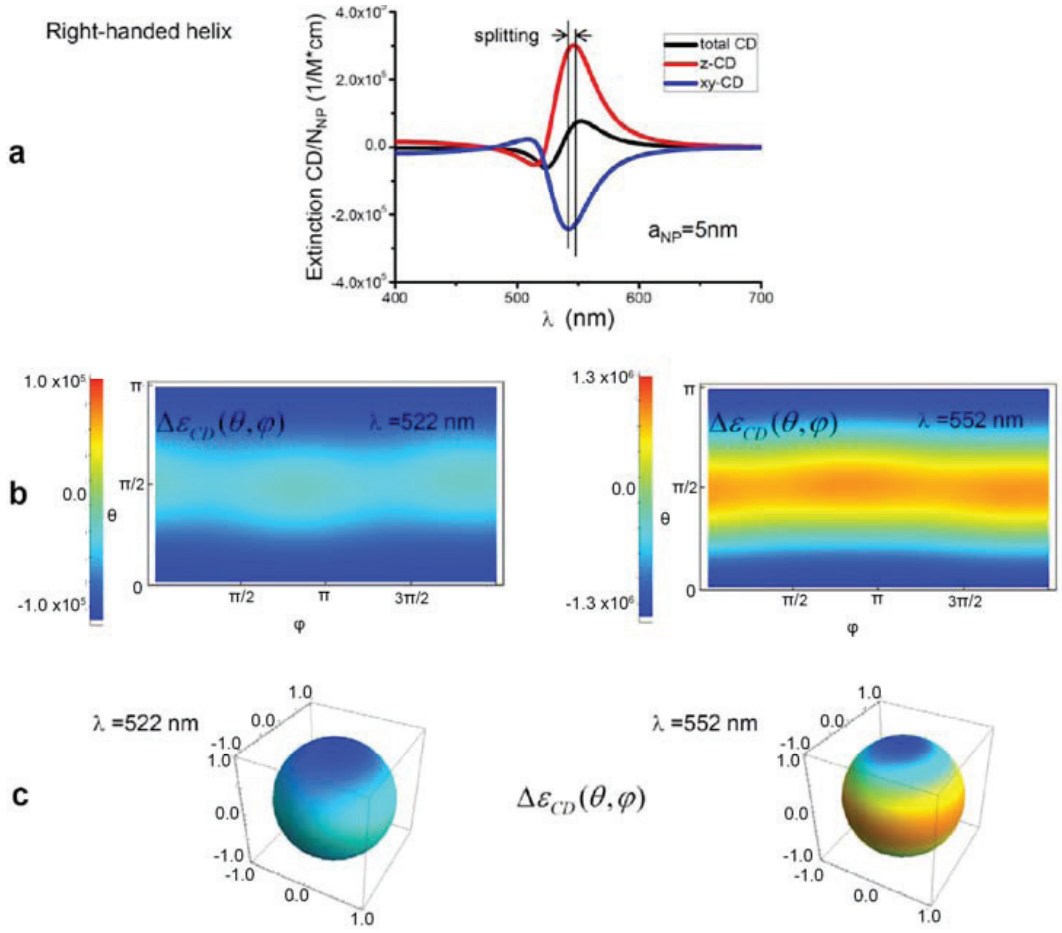

Figure S3 | Calculated CD properties of the right-handed helix composed of 9 nanoparticles. a, Decomposition of the total CD (black spectrum) into parallel *z*-CD (red spectrum) and perpendicular *xy*-CD (blue spectrum) components. **b** and **c**, Calculated directional CD spectra at two wavelengths which correspond to the extremes of the total CD in graph **a**.

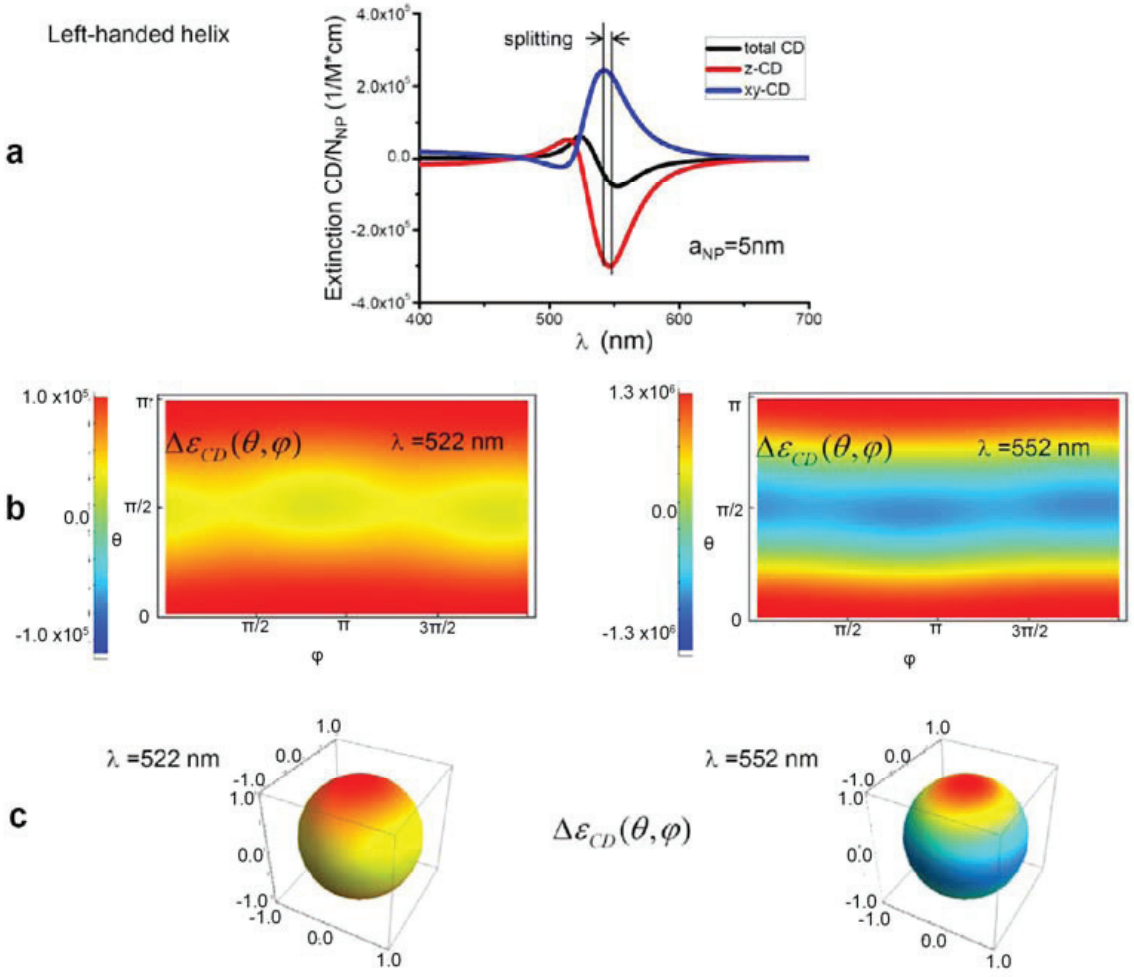

Figure S4 | Plots similar to Figure S3, but for the left-handed helix. The bisignate spectrum of the total CD is reversed.

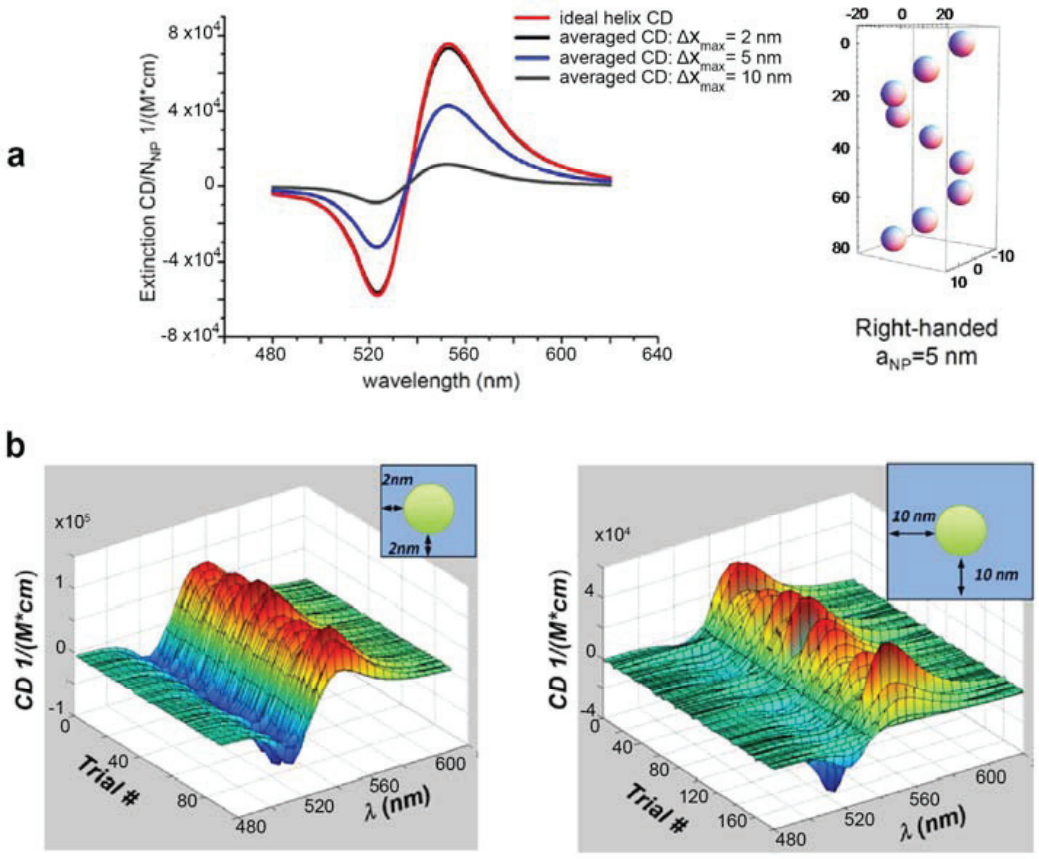

Figure S5 | Effects of disorder on the CD spectra of nine-particle helices. a, Calculated averaged CD spectra for the ideal helix and for three non-ideal helices. For the non-ideal helices, the CD spectra were averaged over a set of trials. Overall, ~80 trials with generating random positions of particles were made. Insert: The model to scale. **b**, Calculated CD spectra for randomized helices as a function of the trail number. Inserts show how the nanoparticle position fluctuations were introduced.

Supplementary Note S3: Design of nanohelices

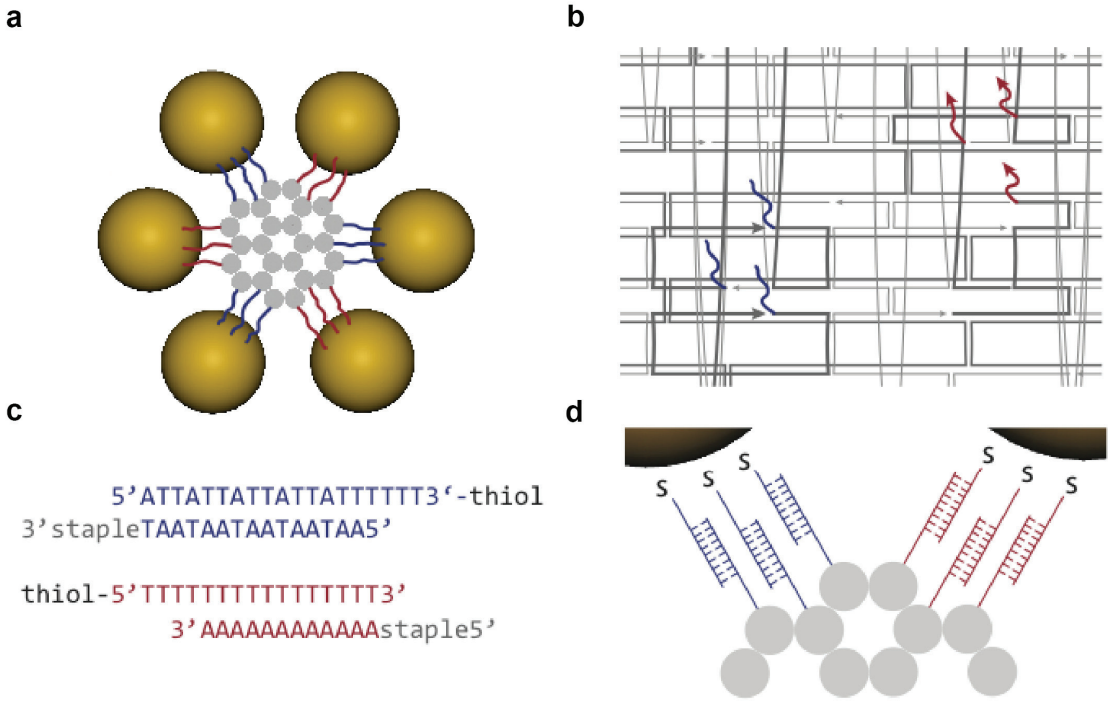

Figure S6 | Details of the attachment sites for AuNPs on the surface of the 24 helix bundle. In order to achieve high binding rates of AuNPs to the DNA origami structures, we proceeded in the following manner: DNA origami 24 helix bundles were designed such that AuNP attachment sites are offered at nine positions on the surface of the DNA structures. Each attachment site consists of three single-stranded 15 nt long extensions of staples whose ends are located on three adjacent helices. **a**, Cross section of the nanohelix (grey: the 24 helix bundle, blue/red: connecting handles, yellow: 10 nm AuNPs). **b**, CaDNAno[42] image of the staple arrangement of two attachment sites. **c**, The specific staple sequences for the hybridization of the AuNPs to the 24 helix bundle. **d**, Cross section close up. The AuNPs are conjugated via a thiol bond to DNA staples which hybridize to the DNA origami structure.

All three attachment strands of neighbouring groups were either extended on the 3' or 5' end and consisted of one of two different sequences. In our experiments, 10 nm AuNPs that were conjugated with multiple copies (> 20) of one of two complements to the attachment strands fixed via thiol modifications of either their 3' or 5' ends were mixed with the assembled 24-helix bundles. The repetitiveness of these sequences facilitates the slippage of the strands along each other thus providing a tight binding of the particles.

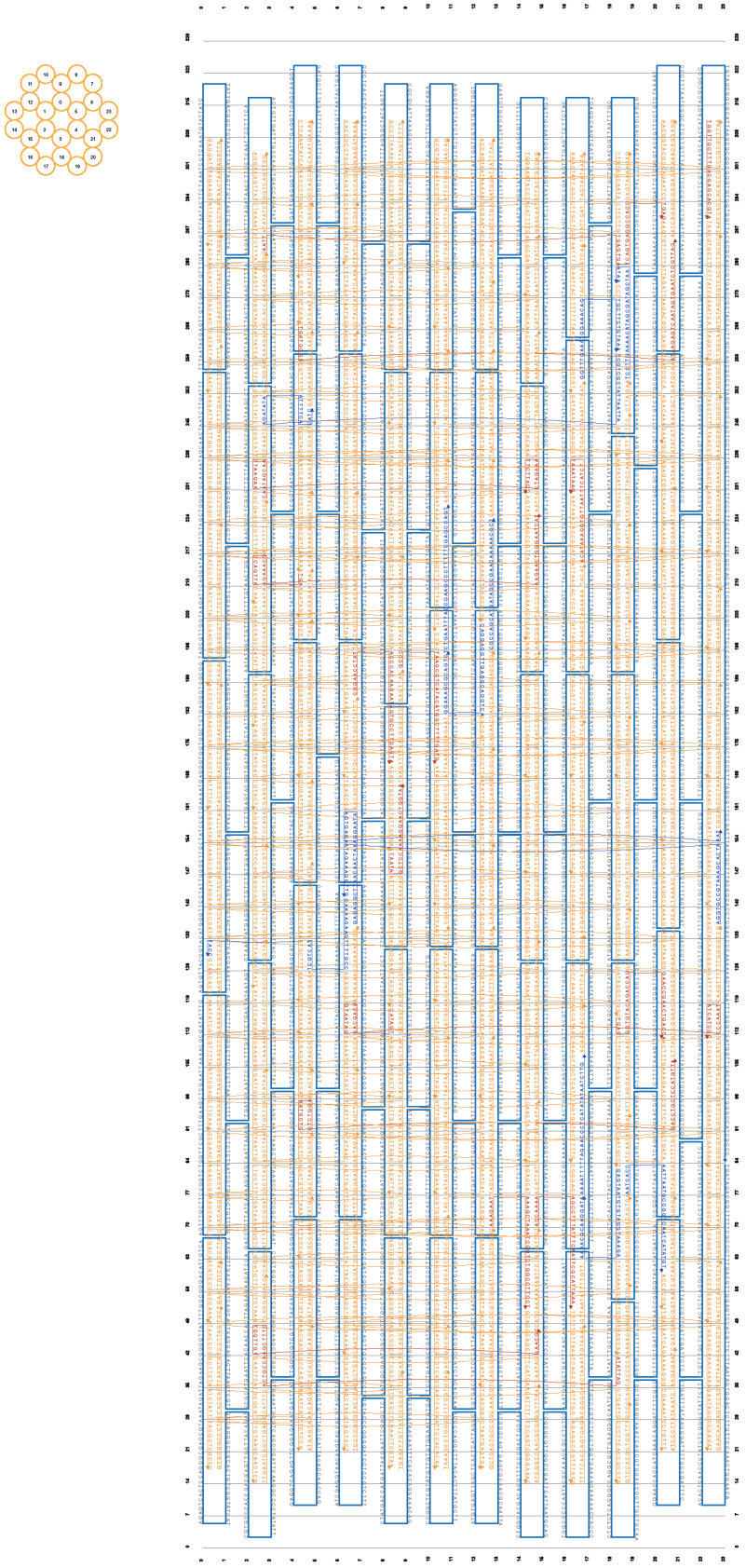

Figure S7 | CaDNAno[42] image of the left-handed 24 helix bundle (incl. sequences). The schematic picture shows the scaffold path (blue), the staple oligonucleotides (orange) and the hybridization sites (blue and red, see also Figure S8).

AATAATAATAATAATCAAAAGAAGTTTTGCCTCGTCATTACC
AATAATAATAATAATGAGAGGCTTAACAACTAAAGGAATAAGTGAGAAAT
AATAATAATAATAATCTGAATTTACCGAAGCCCTTTTTCGAGCCAGT
AATAATAATAATAATCAGGAGGTTGAGGCAGGTCAGGAAAGCGCAGTCT
AATAATAATAATAATCGCCAGCATGATAGCCGAACAAAAACGCT
AATAATAATAATAATAAAATTTTTAGAACCCTCATATATAATCTTG
AATAATAATAATAATGGTTTGAAATGGAAACAGTGCTTCTGTAAA
AATAATAATAATAATGAGTAATGTGTAGGTAAAGAAAAACGCAAGGATA
AATAATAATAATAATTCGTCGCTATTAATTAAGATATAATTTTCACATC
AATAATAATAATAATAATCACCAATTAATGCCGGTCAATCATATGT
AATAATAATAATAATTCCTTGAAAACATAGCGATAGCTAAATAA
AATAATAATAATAATAGGTGCCGTAAAGCACTAATAGAAAGGTTG

CAATAGCAACTAAGAACTAGAAATTCTTACCAAAAAAAAAAAAAAAA
AATTTGAGTGATCAGTGAGGCCACCTGAGAAAAAAAAAAAAAAAA
TGAAGAAACGCCAGTTAAAGAACTGGGAATCATAAAAAAAAAAAAAAA
TGATGGGCATAAGAGTCAATAGTGAATCTCGTTAGAAAAAAAAAAAAAAA
GTCTGGAAATGCTGGACCTGCTCCATGTTAAAAAAAAAAAAAAAA
CGGAACCTATACCCACAAGAATAGTGCCTTGAGTAAAAAAAAAAAAAAAA
CATAGTGACGACGGTAATAGCCCAAATATCATCGCAAAAAAAAAAAAAAA
TAATAGCTCCAAAAGGAACTGGTAAAAAAAAAAAAAAAA
AAAGAATAAAGCTAAATCGGTCTGGCCTTCCTAAAAAAAAAAAAAAA
ACCAAAAAGCCTTTATTTCAATTCGCATTAAAAAAAAAAAAAAAAA
GCCCTAAGCGTCATACATGGCTTTTGATGAAAAAAAAAAAAAAA
ACATAAAGGTGTTAATTTCATCTTAAATAAGAAAAAAAAAAAAAAA
ATATTAGACTGCCAAGCTTTCTGGTTGTGAACGCAAAAAAAAAAAAAAA
TGACGGTGTACAGACCAGGAACCGAACTGACCAAAAAAAAAAAAAAAA
TGGTTGCTTTGACGAGCACGTAAAAAAAAAAAAAAAA

Figure S8 | Handle sequences of the hybridization sites of the left-handed 24 helix bundle for the conjugation of AuNPs (see also Figure S7).

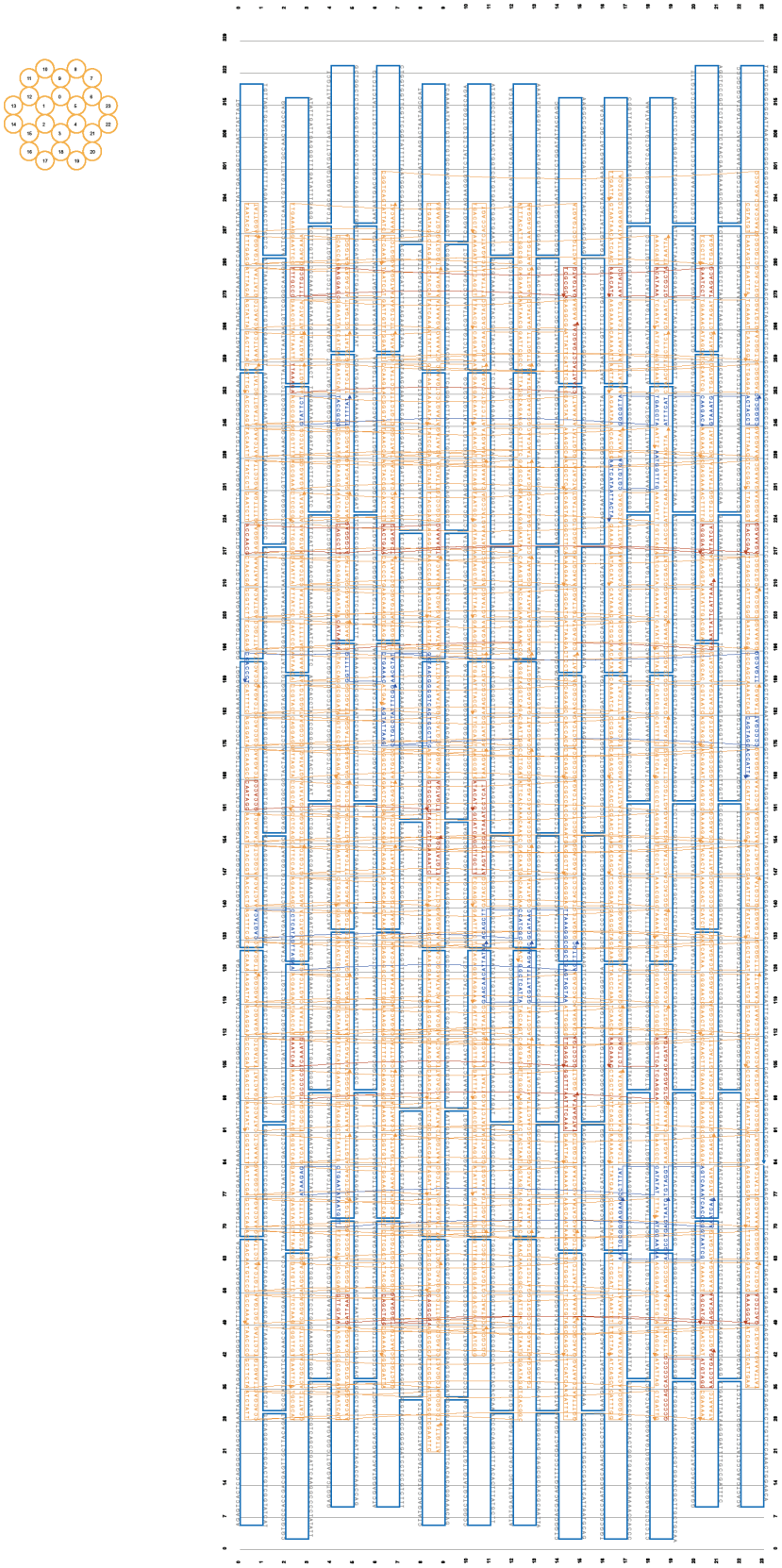

Figure S9 | CaDNAno[42] image of the right-handed 24 helix bundle (incl. sequences). The schematic picture shows the scaffold path (blue), the staple oligonucleotides (orange) and the hybridization sites (blue and red, see also Figure S10).

AATAATAATAATAATAGTATTAAGCCCCGATCAGTAGCACCATTA
AATAATAATAATAATAACCTATGCTAACGGGGTCAGTGCCTTGCCTGCCTATTTCGG
AATAATAATAATAATACAGCTTCCATCGCCAGTACACCTCATAGTTAGAAACTTTGC
AATAATAATAATAATGGCTCATTAGAACAACATTATAA
AATAATAATAATAATGCATAACTTAAAGGCCGCTGAGTAGTAAGCGATTTTAAGAAC
AATAATAATAATAATCCTTTATCATATATATAAGAGCTGAATATAATGTTAAATCAA
AATAATAATAATAATGGCGTTATGACCTAGTATTCTTACCGCGTTTTTAT
AATAATAATAATAATATGCAATAAAATTGCGGGAGAAG
AATAAT AATAATAATAATGGTTTGCGTGTGAAATCATAATTACTA
AATAATAATAATAATTGTAGGTAGTCAAATCACCCGGTAATCGAAGCCTGAGTAATG
AATAATAATAATAATATTTCATCAAGACAGTAAATGACTACCTCGGGCGC
AATAATAATAATAATTTGACGGCTGAAACGGTTTTGCCACCCT

GCCACCCCAATAGGTTGATGAGTGCCCGAAAAAAAAAAAAAAA
TTAAAGACTAATTACCTGAGCAAAAAAAAAAAAAAAAA
CATAACAGAAATTATTCATTAAAAAAAAAAAAAAAAAA
GATTAAGGTTGTAAGAGCAAAAGCATGTAAAAAAAAAAAAAAA
TCAGATGAACTGAAAGAAAGGCACCGACAAAAAAAAAAAAAAA
CAGGCAATGGGAAGCAGCTGGGACTCCAAAAGGCTAAAAAAAAAAAAAAA
TAACGTTGAAAATCTTGTATCGGAAAAAAAAAAAAAAA
TGAAAACACCAACGACGGGAGCAGCCTTATTATCAAGGGAGGAAAAAAAAAAAAAAA
GCATCAGCTTGCTTATAGTTGCGATAAATCCTCATATACATGAAAAAAAAAAAAAAA
GGTTTAATTTCAAATATGAATAAAAAAAAAAAAAAAA
TCAAGAATGCCCCCTCAAATGAAATCAAGCCCTGATTGAGATAAAAAAAAAAAAAAA
GCCCCAGCACCCCGATGTAGGAACCTGAGAAAAAAAAAAAAAAAA
GTGAGGACAGATGAACCTTCATCTTGACAACAAAGAAAAAAAAAAAAAAA
GAATCCTGTCGCTAACATAAAAATTACCAAACATCAAAAAAAAAAAAAAA
TAAGACGAAGGAGCTTTTGCGTTTGCCCGATGATGTCGCGCAAAAAAAAAAAAAAAA

Figure S10 | Handle sequences of the hybridization sites of the right-handed 24 helix bundle for the conjugation of AuNPs (see also Figure S9).

Supplementary Note S4: Methods

To generate nanohelices we first concentrated the gold nanoparticles (AuNPs), then conjugated the AuNPs with ssDNA and finally hybridized the DNA-coated AuNPs to the folded and purified DNA origami structures. As a last step the assembled nanohelices were purified from free AuNPs and agglomerations of AuNPs with DNA origami structures. The protocols of the individual steps are described in the following.

Preparation and concentration of AuNPs. Colloidal AuNP solution (50mL, British Biocell International) of citrated AuNPs of 10 nm size and 10 nM concentration was stirred over night after adding 20 mg of BSPP (Bis(*p*-sulfonatophenyl)phenylphosphine dihydrate dipotassium salt, Sigma-Aldrich). This step is necessary to create a phosphine coating of the AuNPs, which stabilizes the AuNPs at high particle concentrations and in buffers containing magnesium of ~10 mM. To achieve higher concentrations, which are needed for our experiments, the particles are pre-agitated and resuspended in small volumes as follows: Sodium chloride was added until a colour change of the solution from red to blue was observed. Next the AuNPs were sedimented to the bottom of a 50 mL tube by centrifugation of the AuNP solution at 1,600 rcf for 30 min and the clear supernatant was removed with a pipette. The particles were again dissolved in BSPP solution (800 µL, 2.5mM) followed by addition of an equal volume of methanol (800 µL). This mixture was centrifuged (1,600 rcf, 30 min), the supernatant was removed and the particles were once more dissolved in BSPP solution (800 µL, 2.5 mM).

AuNP-DNA conjugation. AuNPs were conjugated with thiolated ssDNA strands (biomers.net) as follows. The procedure was adopted from Ding et al.[43] and adapted where necessary. The concentration of the concentrated AuNPs was determined from the optical absorption at a wavelength of 518 nm using a spectrophotometer (Nanodrop, Thermo Fisher Scientific and Nanophotometer, IMPLEN). For reducing the disulfide bonds of the thiolated ssDNA strands to monothiol, the modified strands were incubated with TCEP (Tris(carboxyethyl) phosphine hydrochloride, Sigma-Aldrich; 20mM) for at least 1/2 h.

AuNPs and thiolated oligonucleotides were mixed in 0.5 x TBE buffer at a ratio of 1:300. The tube containing the mixture was gently shaken for at least 2 days at room temperature. To test the conjugation success, a droplet of the DNA-covered AuNPs was mixed with a droplet of 1 x TAE buffer with 10 mM Mg^{2+} (DNA origami structures are assembled at similar buffer conditions). At this point the DNA-covered AuNPs should not aggregate if transferred to such buffers. If the colour of the mixed droplet changed from red to blue, more thiolated oligonucleotides had to be added to the AuNP-DNA mixture. To remove the unbound thiolated strands, the mixture was spun for 5 min at 14,000 rcf through a 100kDa MWCO centrifugal filter (Amicon Ultra, Millipore) followed by additional 4 spinning steps (5 min, 14,000 rcf) with 400 µl 1 x TAE buffer added to the centrifugal filter before each step. The unbound oligonucleotides should be

removed immediately before adding the AuNPs to the DNA origami structures otherwise eventually newly appearing free oligonucleotides will block the hybridization sites of the DNA origami structure. After the last step the concentration of the AuNPs was determined with a spectrophotometer.

DNA origami folding. For the left-handed and the right-handed design of the 24 helix bundle we used 10 nM of P7560 scaffold[44] and a staple mix containing 100 nM of each staple. The complete folding mixture contained next to the staple and scaffold strands 10 mM Tris, 1 mM EDTA (pH 8) and 14 mM of $MgCl_2$. The folding mixture was then exposed to a thermal annealing ramp, starting with a heating step to 80 °C for 5 min, followed by cooling to 60 °C at a cooling rate of 1 °C / 5 min. The following cooling from 60 °C to 25 °C was performed at 0.5 °C / 45 min.

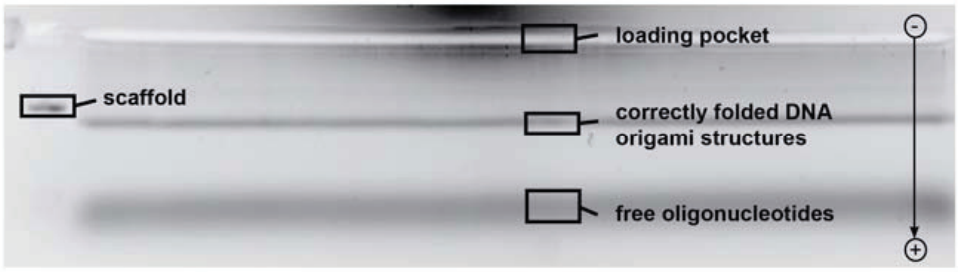

Figure S11 | Purification of the DNA origami structures from staple excess by gel electrophoresis. UV image of the agarose gel. DNA origami structures were purified from excess staples by gel electrophoresis. We ran a 1.5 % agarose gel in 0.5 x TBE buffer with 11 mM $MgCl_2$, soaked in Sybr Gold 5 µM (Invitrogen) and cut out the favoured bands to extract them with Freeze `N Squeeze spin columns (BioRad, Germany).

Conjugation of AuNPs to DNA origami structures. The spin-filtered AuNPs were added to the purified DNA origami structures in an excess of 50 AuNPs per 1 DNA origami structure. The mixture was tumbled over 24 hrs at 23 °C.

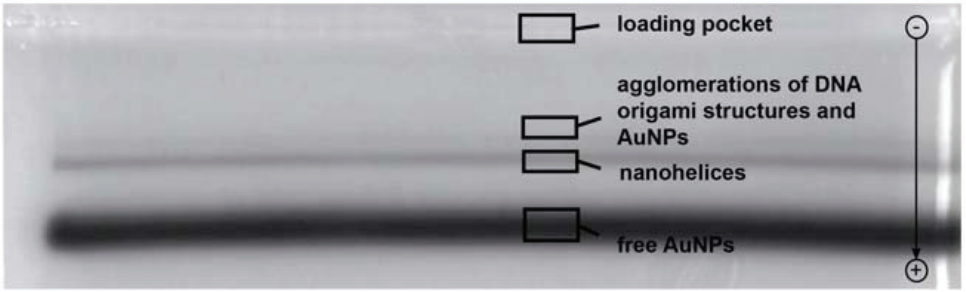

Figure S12 | Purification of the DNA origami structures from free AuNPs by gel electrophoresis. White light image of the agarose gel. To separate the nanohelices from the AuNP excess a second agarose gel purification step was used. We ran a 0.5 % agarose gel in 0.5 x TBE buffer with 11 mM $MgCl_2$. The nanohelices showed a narrow

band in the gel, which runs slower than single AuNPs and faster than aggregates of DNA origami structures and AuNPs. We cut out the favoured bands to extract the nanohelices with Freeze `N Squeeze spin columns from the gel. To concentrate the nanohelices we spun the nanohelices at 10,000 rcf for 10 min and discarded the supernatant.

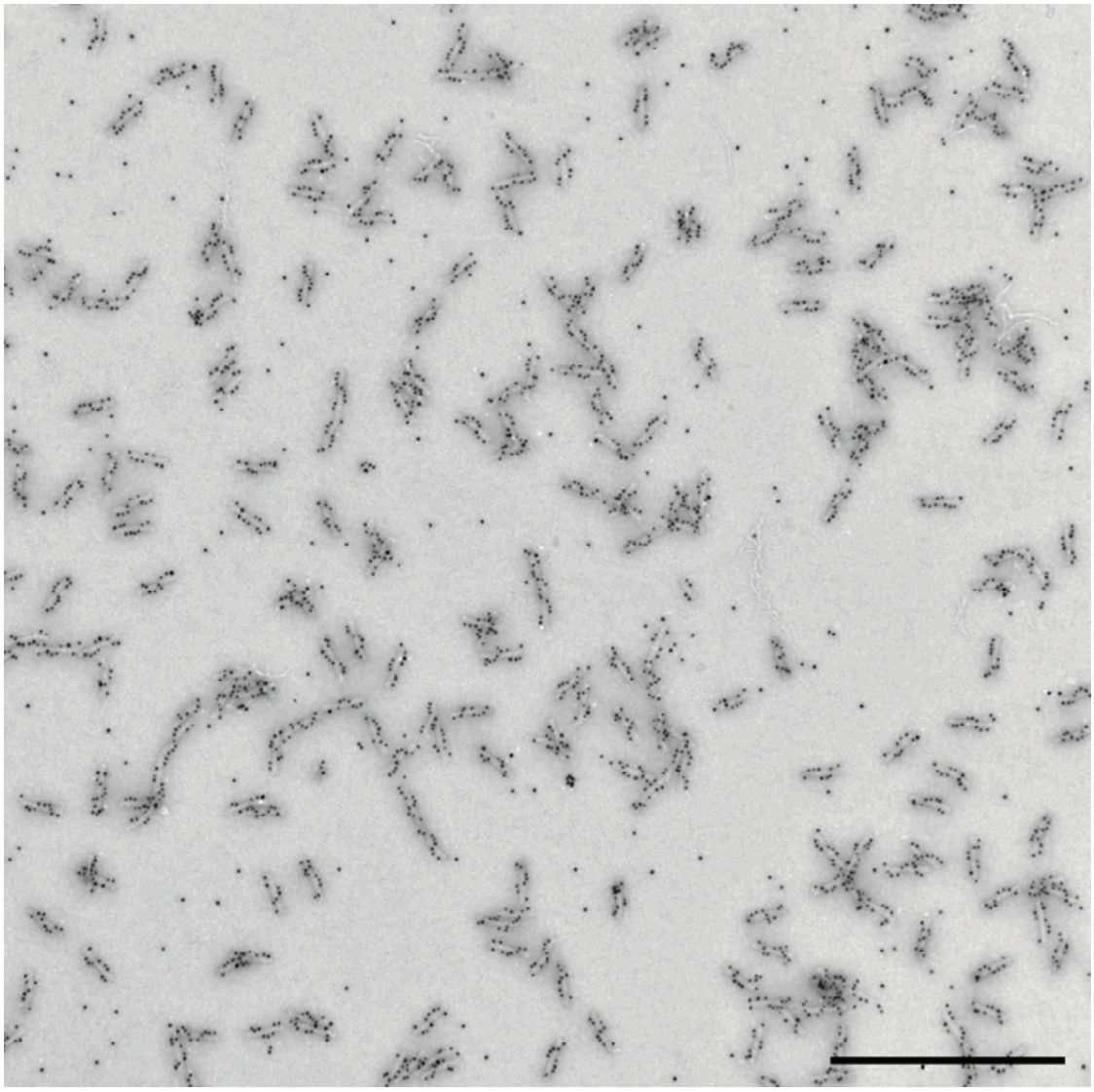

Figure S13 | Wide field transmission electron microscopy (TEM) images of left-handed nanohelices with 10 nm AuNPs. Scale bar 500 nm.

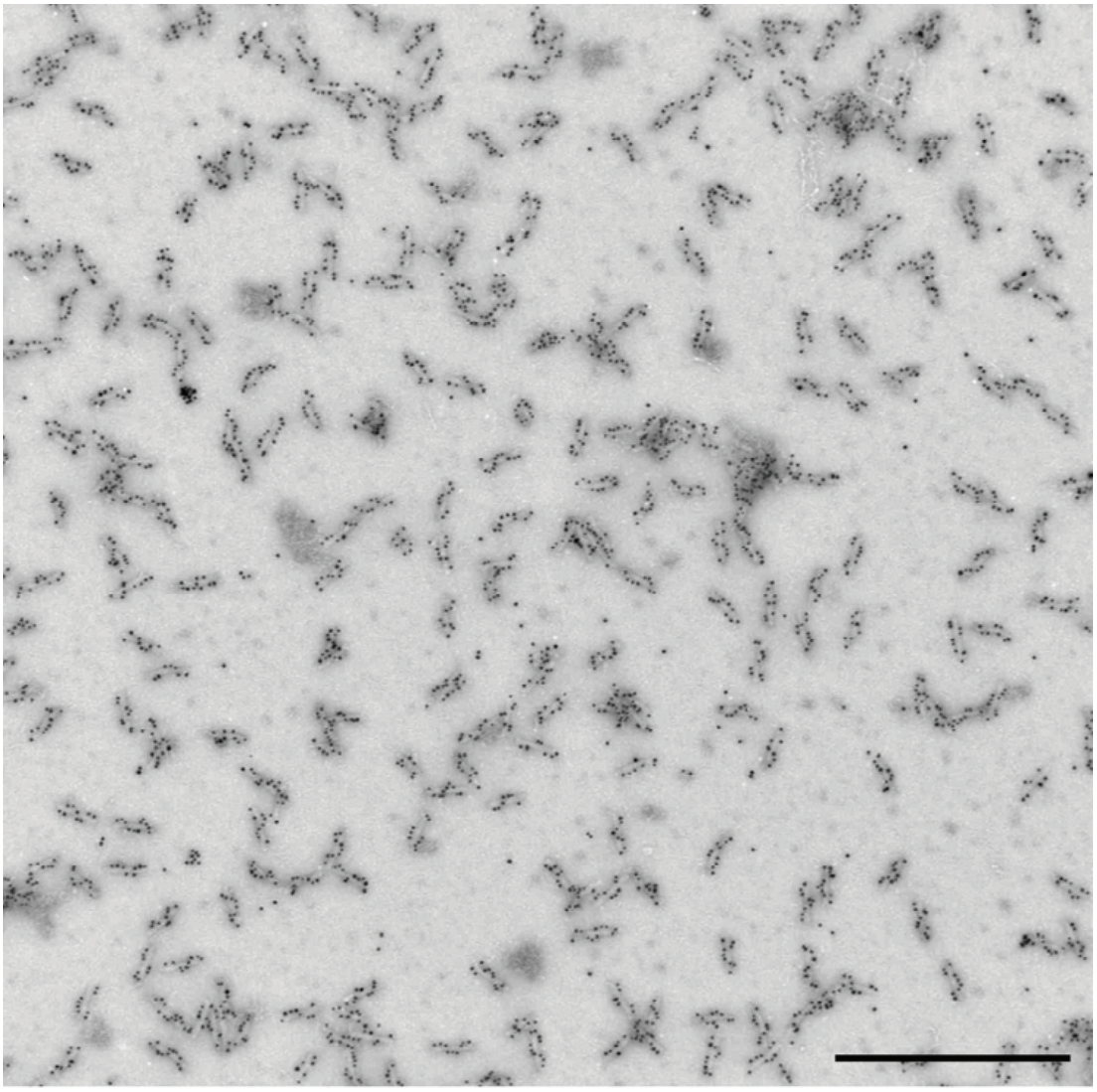

Figure S14 | Wide field TEM images of right-handed nanohelices with 10 nm AuNPs. Scale bar 500 nm.

Supplementary Note S5: Statistics

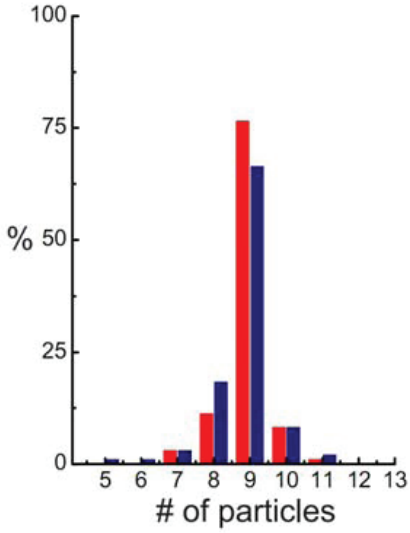

Figure S15 | Statistics of the number of AuNPs per nanohelix. 98 % of the binding sites of the AuNPs of the left-handed nanohelices (red) and 96 % of the binding sites of the AuNPs of the right-handed nanohelices (blue) are occupied. Mathematically, the percentage of correctly assembled helices amounts to 83 % (0.98^9) and 69 % (0.96^9). We counted 77 % and 66 % of helices with exactly nine attached particles. When including assemblies with ten or eleven bound particles (occasionally particles unspecifically bind to the scaffold loops at the ends of the origami helices), 86 % and 77 % of the helices are formed correctly (98 helices were counted for both cases).

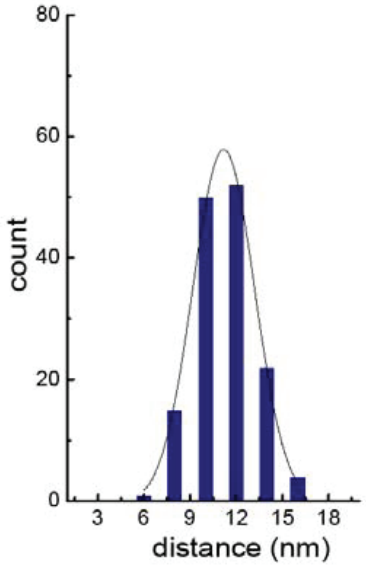

Figure S16 | Centre-to-centre distances of AuNPs. Electron micrographs were analysed to access the accuracy of the NP-helix assemblies. The centre-to-centre distances of 288 neighbouring AuNPs was measured. To minimize the influence of structural distortion due to drying and staining effects on the measurements, we

analysed always those six particles per structure that were resting next to helices and whose positions were not distorted during the adsorption process because they geometrically would lie on top or under the DNA origami structure. We observed an average distance of 11.22 nm (±1.4 nm SD).

Supplementary Note S6: Long-term stability of nanohelices

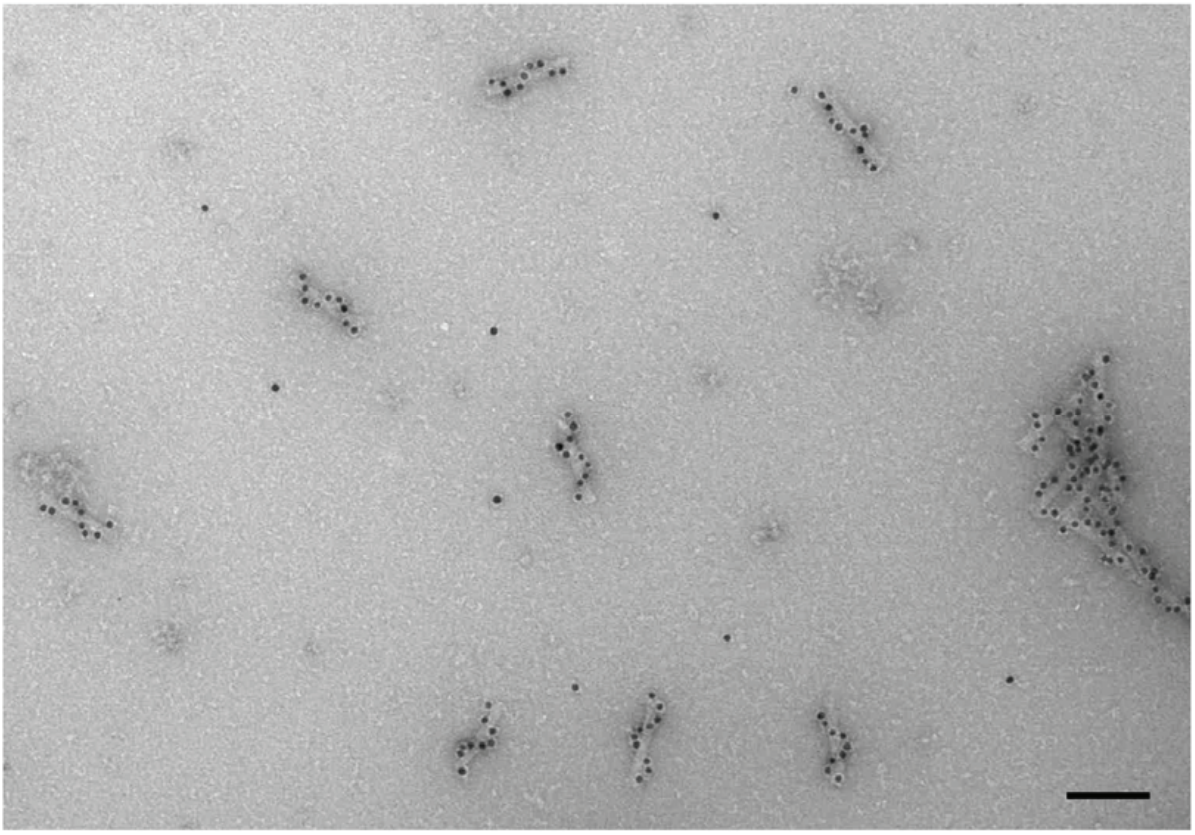

Figure S17 | Long-term stability. TEM images of nanohelices that have been stored for 3 months at 4°C. The nanohelices show high stability over time. Only an increase of clusters of nanohelices could be observed. No increased amounts of unbound particles are observed but helices with unoccupied binding sites show a tendency to aggregate. This can be explained by the fact, that aggregation is mediated by unoccupied binding sites. Interestingly, the remaining non-aggregated helices exhibit 9 attached particles. Scale bar 100 nm.

Supplementary Note S7: Metal growth

Controlled growth of metal on AuNPs conjugated to DNA origami structures was achieved by electroless deposition of gold and silver ions from solution. We used commercially available gold and silver enhancement kits (EM Gold Enhancement and HQ Silver Enhancement, Nanoprobes, USA). To generate the enhancement solutions we followed the supplier's instructions unless specified otherwise.

Gold enhancement. Instead of using all four solutions of the Gold Enhancement kit, we only used solution A ("Enhancer"), solution B ("Activator") and solution C ("Initiator"). Solution D ("Buffer") was omitted to avoid unnecessary dilution of the gold nanohelix samples. To one part of a given sample volume (1.5 nM of nanohelices) we added three parts of the pre-mixed solution A+B+C (i.e. 20 µl of 1.5 nM nanohelices + 60 µl of Gold Enhancement kit pre-mixed solution A+B+C, no D). We let the sample sit for 20 hrs at 23°C and measured the CD spectra without any further treatment. Test series with individual AuNPs showed that most of the particle growth was already finished after 4 min. In the following 20 hrs no significant change of particle size was observed. From this we conclude, that during a CD measurement (which takes ~40 min) no changes in particle size occur.

Silver enhancement. Compared to particles enhanced with the Gold Enhancement kit we observed much faster growth of the metal shells on the seeding AuNPs when the Silver Enhancement kit was employed at the same concentrations as described above. Therefore we reduced the amount of Silver Enhancement solutions added to our samples considerably. To one part of a given sample volume (1.5 nM of nanohelices) we added between 0.035 parts (cf. Ag enhanced helices, Figure 3a, main manuscript) and one part (Super Ag Enhanced Helices, Figure 3b, main manuscript) of the pre-mixed solutions A+B+C of the Silver Enhancement kit (i.e. 20 µl of 1.5nM Nanohelices + 0.7 µl (Ag enhanced helices, Figure 3a, main manuscript) or 20 µl (Super Ag Enhanced Helices, Figure 3b, main manuscript) of HQ Silver Enhancement kit pre-mixed solution A+B+C). Test series with individual AuNPs showed that most of the particle growth was already finished after 4 min. In the following 20 hrs no significant change of particle size was observed. As for the Au enhanced nanohelices in the previous section we conclude, that during a CD measurement no changes in particle size occur.

Alloy enhancement. To generate nanohelices with nanoparticles which consist of a gold and silver alloy shell we used a combination of the EM Gold Enhancement kit and the HQ Silver Enhancement kit (Nanoprobes, USA). To one part of a given sample volume (1.5 nM of nanohelices) we added one and a half parts of the pre-mixed solutions of A+B+C of the EM Gold Enhancement kit and 0.035 parts of the of the pre-

mixed solutions of A+B+C of the HQ Silver Enhancement kit [i.e. 20 µl of 1.5 nM nanohelices + 30 µl of Gold Enhancement kit (pre-mixed solution A+B+C, no D) + 0.7 µl of Silver Enhancement kit (pre-mixed solution A+B+C)].

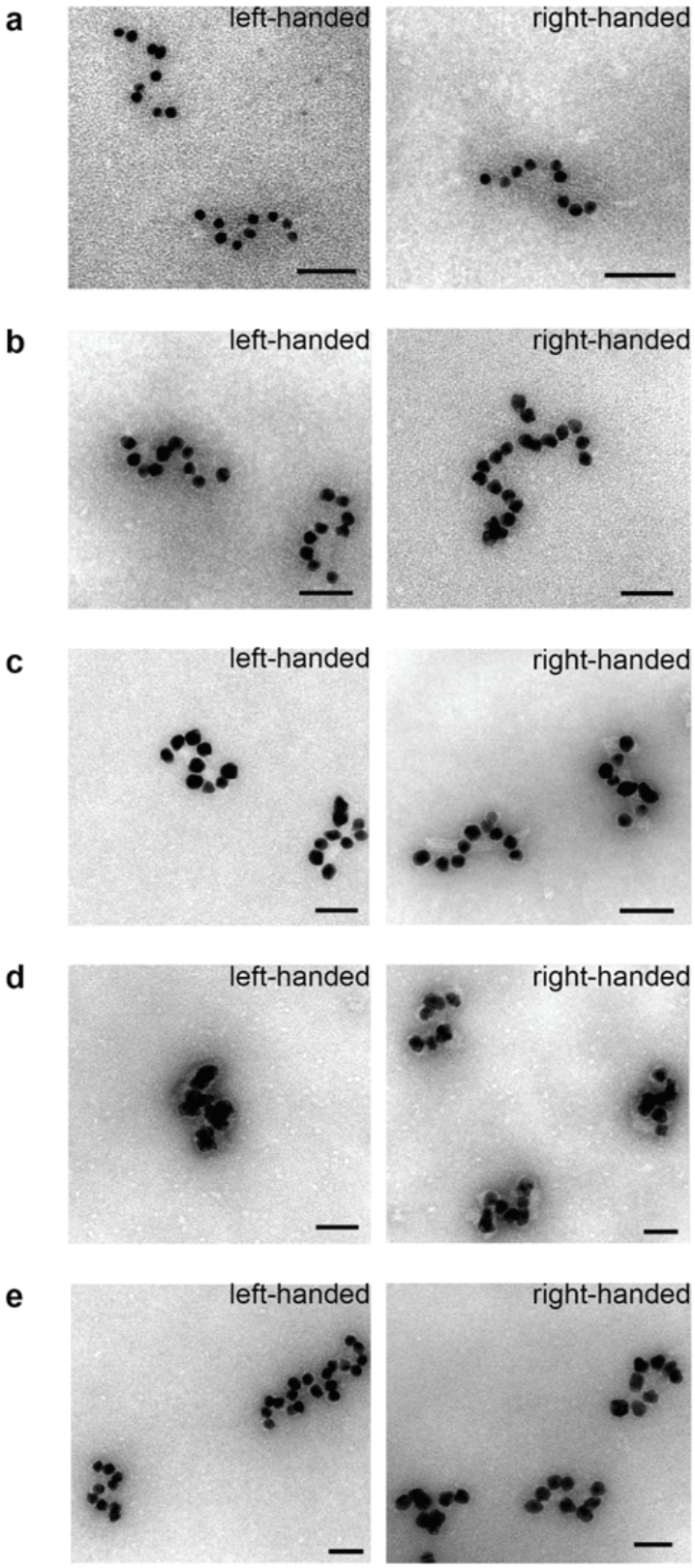

Figure S18 | TEM images of enhanced left-handed and right-handed nanohelices. **a**, Ag enhanced, **b**, Ag/Au enhanced, **c**, Au enhanced, **d**, Super Ag enhanced, **e**, Double Au enhanced. Scale bars 50 nm.

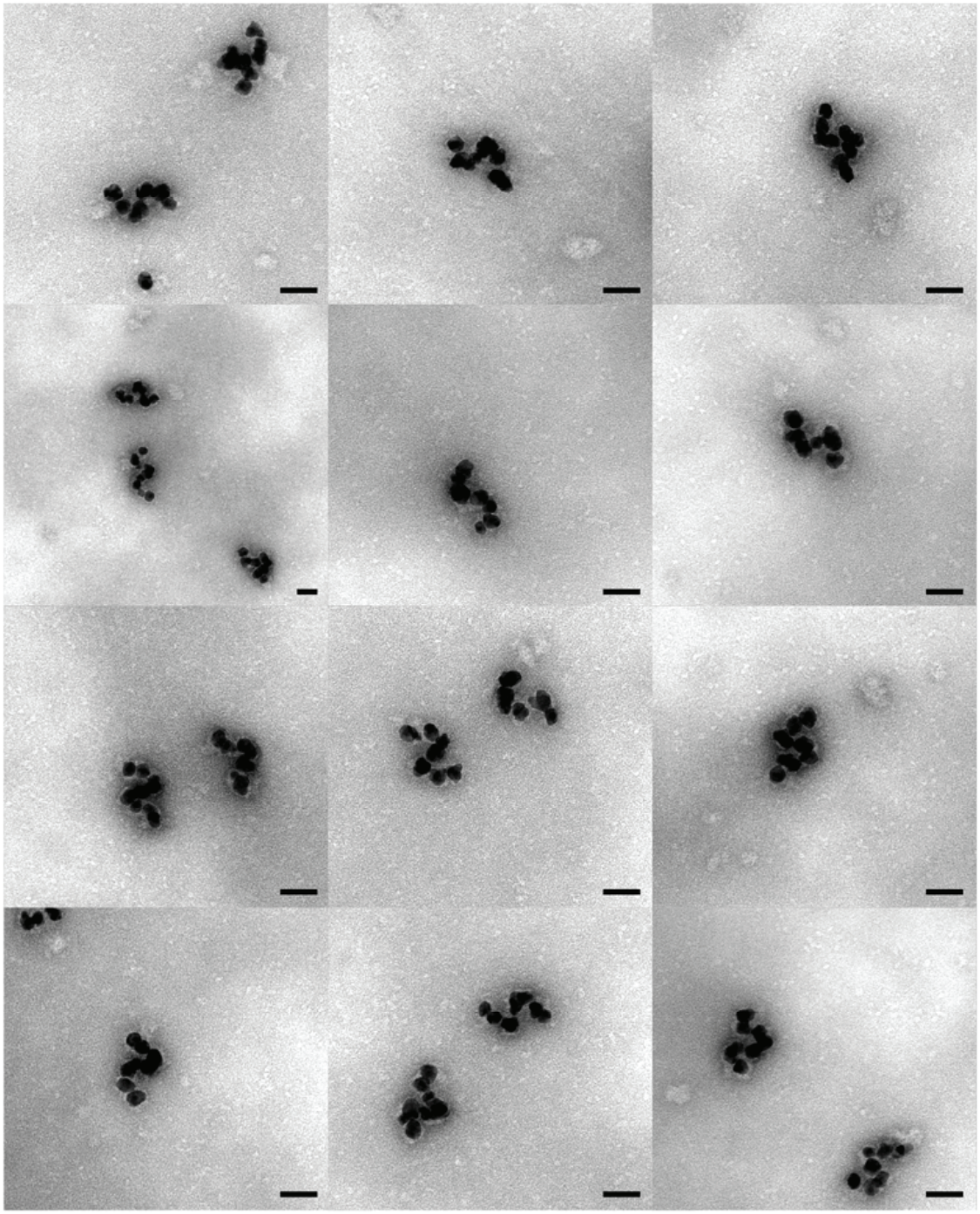

Figure S19 | Super Ag enhanced nanohelices. TEM images of various right-handed super Ag enhanced nanohelices. Scale bars 50 nm.

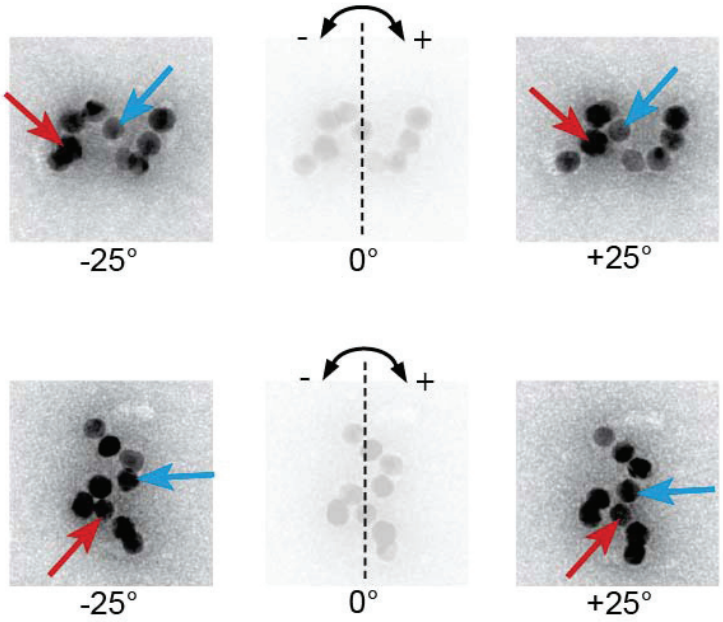

Figure S20 | Three-dimensional structure of enhanced nanohelices revealed by TEM. A carbon-formvar-coated grid covered with nanohelices, is fixed on a holder stage which can be tilted from -25° to +25° while the sample is analysed by TEM (the tilting axis is indicated as a dashed line). By tilting the grid holder stage 50° (from -25° to +25°), identical structures can be examined from different directions. The particle marked with a red arrow moves closer to the particle marked with a blue arrow. This can only be observed if the red marked particle is resting on top and the blue marked particle lying below the origami structure. By comparing the TEM images the three-dimensional structure becomes apparent. Here, left-handed nanohelices are displayed. If the nanohelices were right-handed, the marked particles would move away from each other during rotation.

Supplementary Note S8: CD spetra of enhanced nanohelices

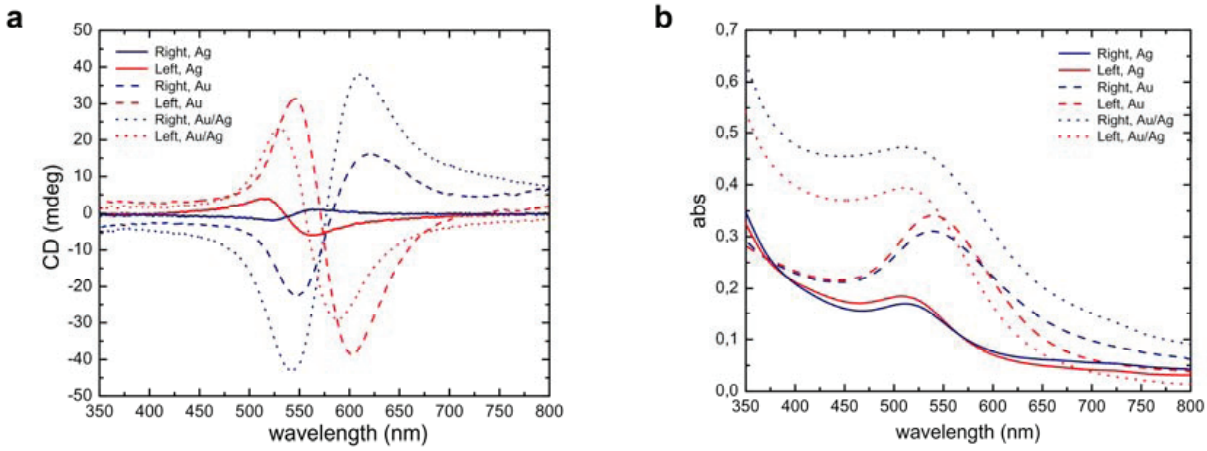

Figure S21 | Additional CD and absorption spectra of enhanced nanohelices. Enhanced left-handed and right-handed nanohelices (Ag enhanced, Ag/Au enhanced, Au enhanced). **a**, CD spectra and **b**, absorption spectra of enhanced nanohelices. The path length of the light is 3 mm.

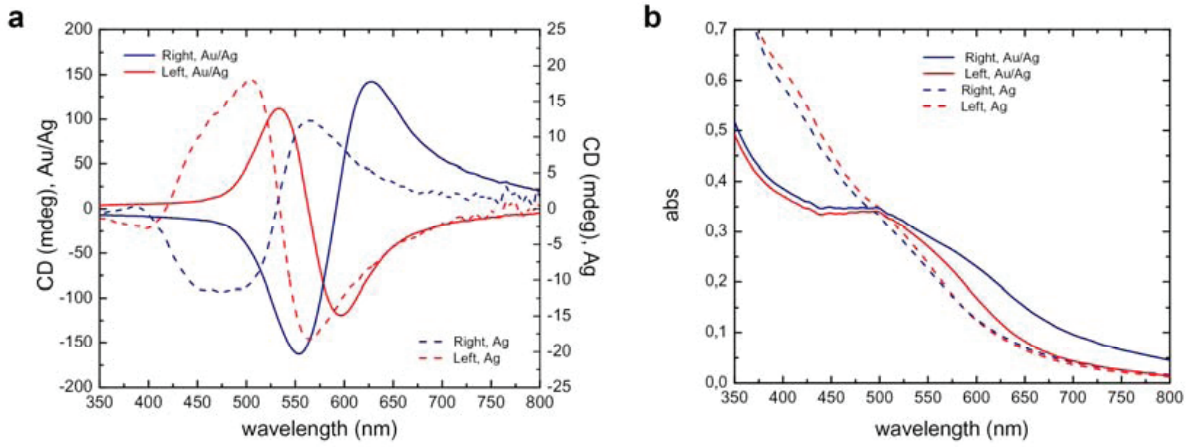

Figure S22 | CD and absorption spectra of double enhanced nanohelices. In order to obtain even stronger CD, we tested the possibility of a second enhancement step. This results in an increase of CD by a factor of 5-10 (graphs are not corrected for dilution effects). **a**, CD spectra and **b**, absorption spectra of enhanced nanohelices. The path length of the light is 3 mm.

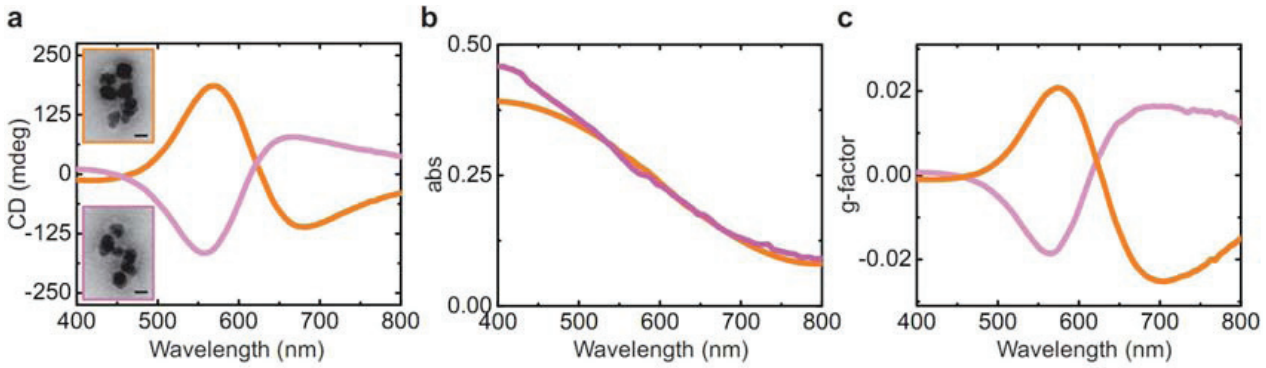

Figure S23 | Anisotropy factor. Another way to characterize chiral materials is through the anisotropy factor g, which is defined as $g = \Delta\varepsilon / \varepsilon$, where $\Delta\varepsilon$ and ε are the molar CD and molar extinction respectively. In our experiments we achieve g factors as high as 0.025 (samples presented in Figure 3b, main manuscript) This value is comparable with the highest g-factors reported for chiroptical metal nanoparticles in solution[45] and other molecules such as protein complexes[46] (0.06) and polyaromatic compounds[47] (0.05). **a**, CD spectra, **b**, absorption spectra, **c**, and anisotropy factor of left- and right-handed super Ag enhanced nanohelices.

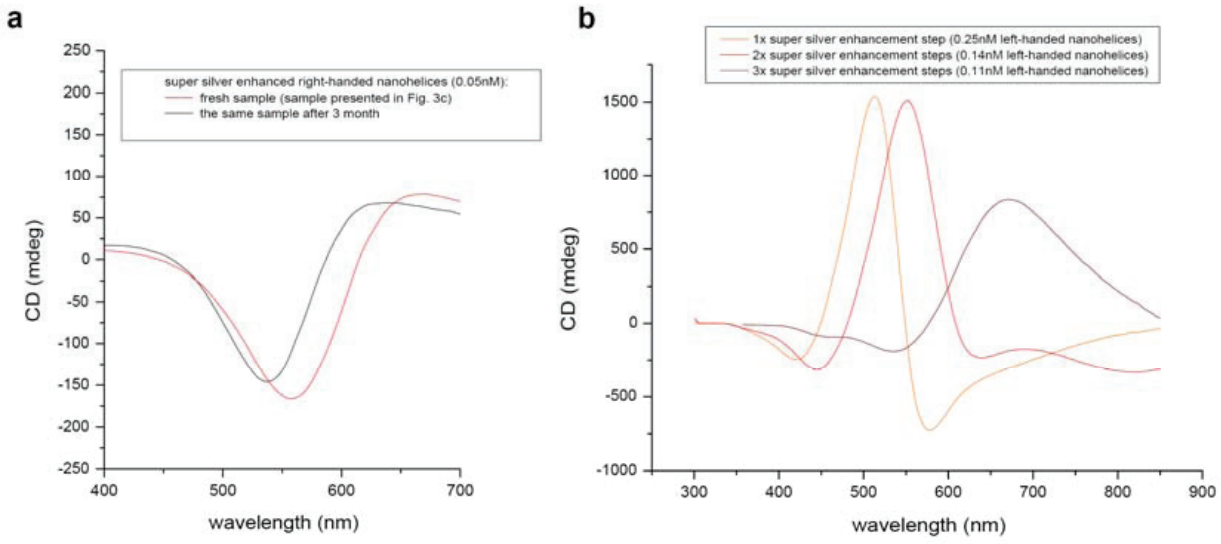

Figure S24 | Long-term stability of enhanced nanohelices and CD spectra of left-handed nanohelices after multiple silver enhancement steps. a, CD spectra of diluted super Ag enhanced right-handed nanohelices (0.05 nM) that have been stored for 3 months at 4 °C. The 3 month old sample shows a slight shift to shorter wavelengths and a decrease in signal by 12 %. **b**, By depositing more silver on the nanohelices, the CD peak shifts to longer wavelengths. The path length of the light is 3 mm in **a** and **b**.

Supplementary Note S9: Specific rotation

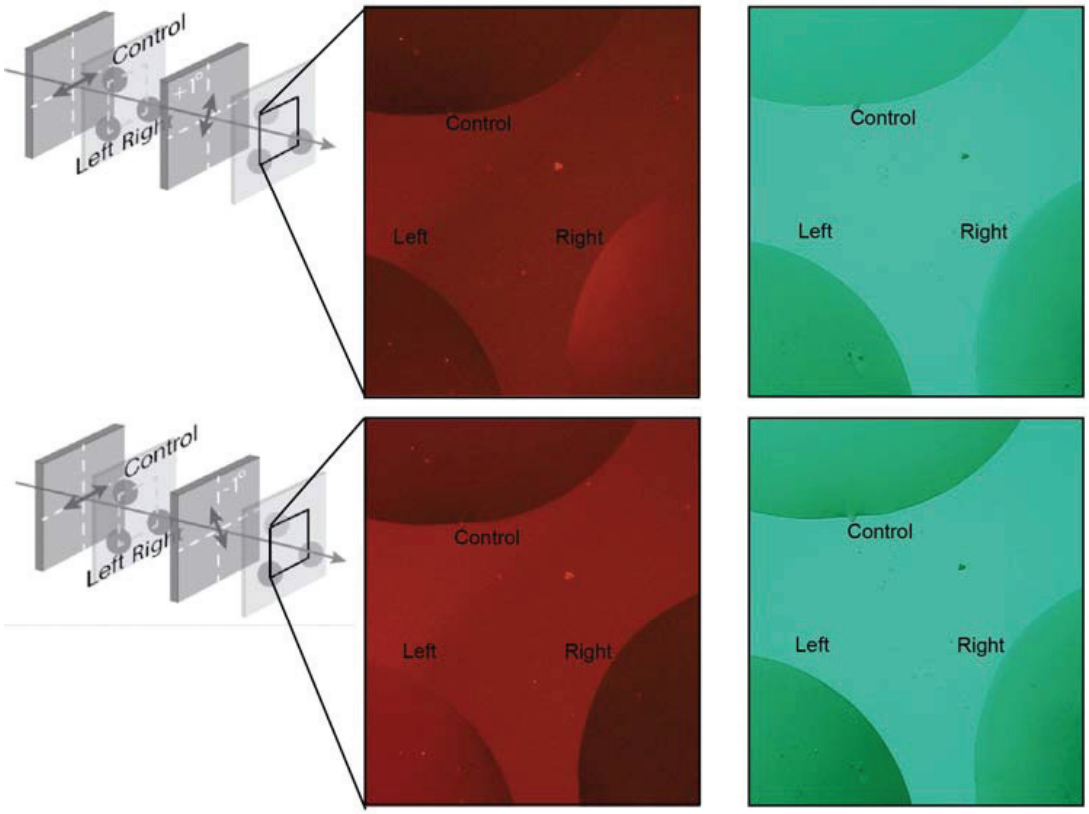

Figure S25 | Optical rotatory dispersion (ORD) of nanohelices in solution. Three 1µl droplets of solutions containing left-handed nanohelices (Super Ag Enhanced Helices, Figure 3b, main manuscript), right-handed nanohelices (Super Ag Enhanced Helices, Figure 3b, main manuscript) or isotropically dispersed AuNPs (approximately equal AuNP concentrations for all samples) were deposited on a glass cover slip. The glass cover slip with the droplets was positioned between two linear polarisation filters as described in Figure 4 of the main manuscript. The images (middle and right) were taken through additional emission filters (middle: 605 nm ± 35 nm, right: 525 nm ± 25 nm) and the analysing polarizer was rotated 1° clockwise (top) or counter clockwise (bottom). At longer wavelengths (middle), the rotation of the polarization results in an opacity change of the droplets depending on their materials properties: right-handed helices rotate the polarization at red frequencies clockwise which results in a brighter appearance of the droplet in the upper and a darker appearance in the lower frame; left-handed helices rotate the polarization at red frequencies counter clockwise which results in a darker appearance of this droplet in the upper and a brighter appearance in the lower frame. The control sample does not change its opacity. At shorter wavelengths (right) the leaking blue light (< 550 nm) dominates the recorded signal.

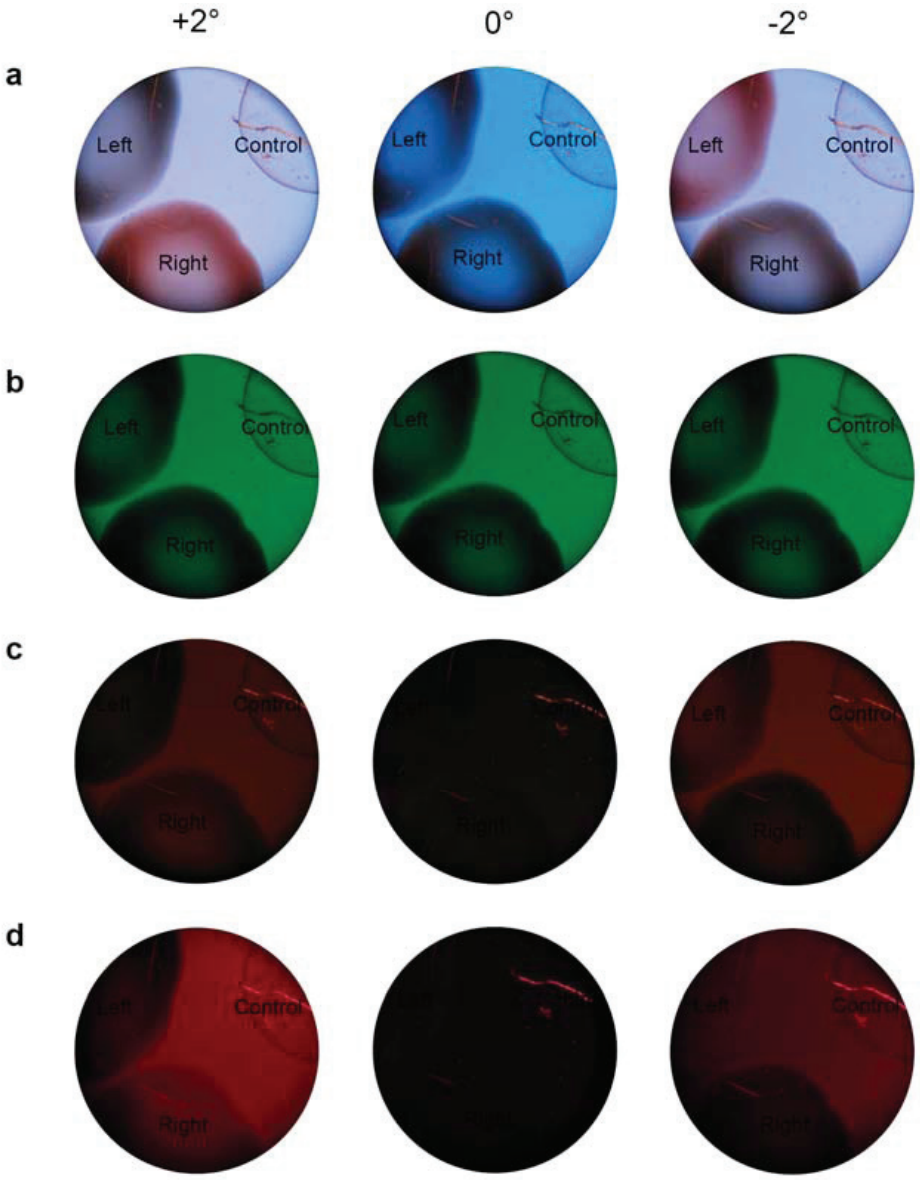

Figure S26 and supplementary video | ORD of dried nanohelices. Interestingly, the optical activity of the samples remains preserved when the nanohelices dry on a glass surface. The same samples and set-up as in Figure 4 of the main manuscript were investigated here, with the only difference being that the droplets were allowed to dry and three more droplets of the same volume and content were deposited on top of the dried spots and allowed to dry again. The middle column depicts images taken with the polarisers crossed at a 90° angle. Here the absorption characteristics of the set-up can be studied: Light of wavelength shorter than 550 nm is not polarization-resolved and dominates the recorded signal (**a** and **b**) while light of longer wavelengths (**c** and **d**) is completely blocked. In this experiment, the analysing polarization filter was rotated 2° clockwise (left) or counter clockwise (right). Qualitatively, the same optical activity as in Figure S25 can be observed while the strength of the effect is increased due to the roughly doubled number of participating nanohelices. Emission filters: **a,** none. **b,** 525 ± 50 nm, **c,** 605 ± 35 nm, **d,** 700 ± 25 nm.

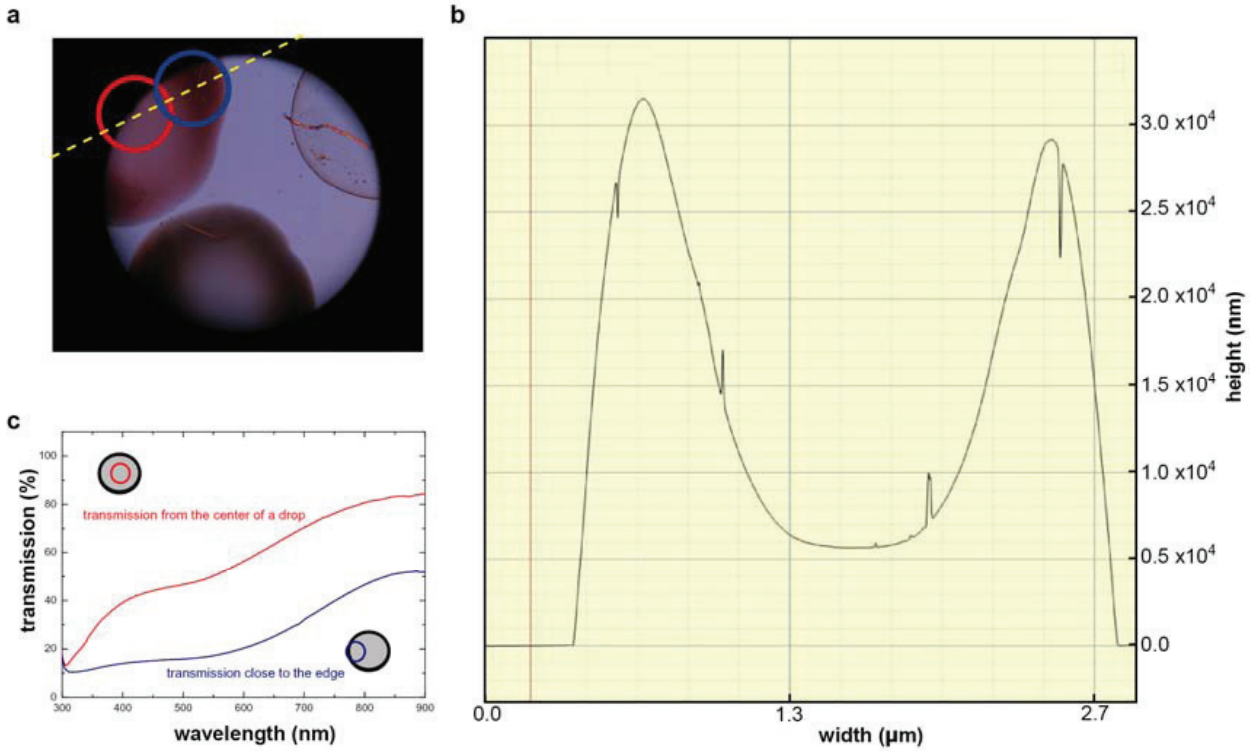

Figure S28 | Specific rotation and absorption losses. The magnitude of optical rotation in our experiment can be compared with other materials using specific rotation of a solid (the optical rotation in degrees produced by a 1 mm thickness of the solid). **a**, Dried nanohelices on a cover slip. **b**, In our experiments we achieve optical rotation of several degrees (Figure S26) for a film thickness of 5 μm (thickness in the centre of the droplet; the film thickness was measured with a Veeco Dektak 150 along the dashed line in panel **a**). This results in a specific rotation on the order of 10^2 [°/mm], which is one order of magnitude higher than the specific rotation of quartz. Specific rotation of chiral molecules in solution is typically lower than 100 deg·dm^{-1}·g^{-1}·cm^3, which leads to rotation of 1 [°/mm] for a typical density of 1 g·cm^{-3}. **c**, The transmission of the films of the dried nanohelix samples is between 45% (@ 500 nm) and 70% (@700 nm). Thus, it is possible to achieve reasonably high optical rotation with relative low absorption/scattering losses.

Supplementary Note S10: Polymerization of nanohelices

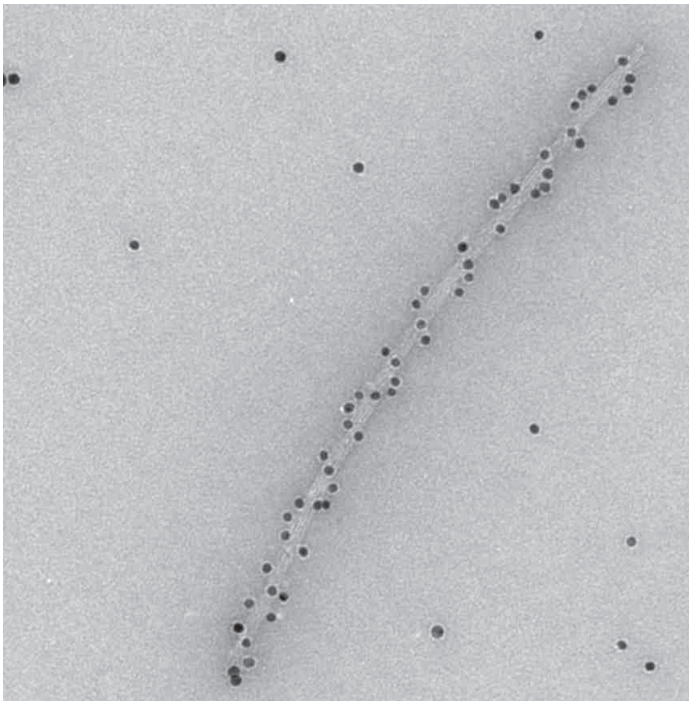

Figure S29 | To realize one-dimensional periodicity of nanohelices, left-handed nanohelices were assembled into polymeric structures. TEM image of a left-handed nanohelix polymer consisting of six monomers. For the polymerization reaction, each polymerization oligonucleotide (see Figure S30) was added at a 10-fold concentration of the left-handed nanohelix monomer concentration. Polymerization proceeded for 12 hrs at 23 °C. The yield analysis of the AuNP DNA origami conjugation for this polymer is 94 % (after 12 hrs polymerization time).

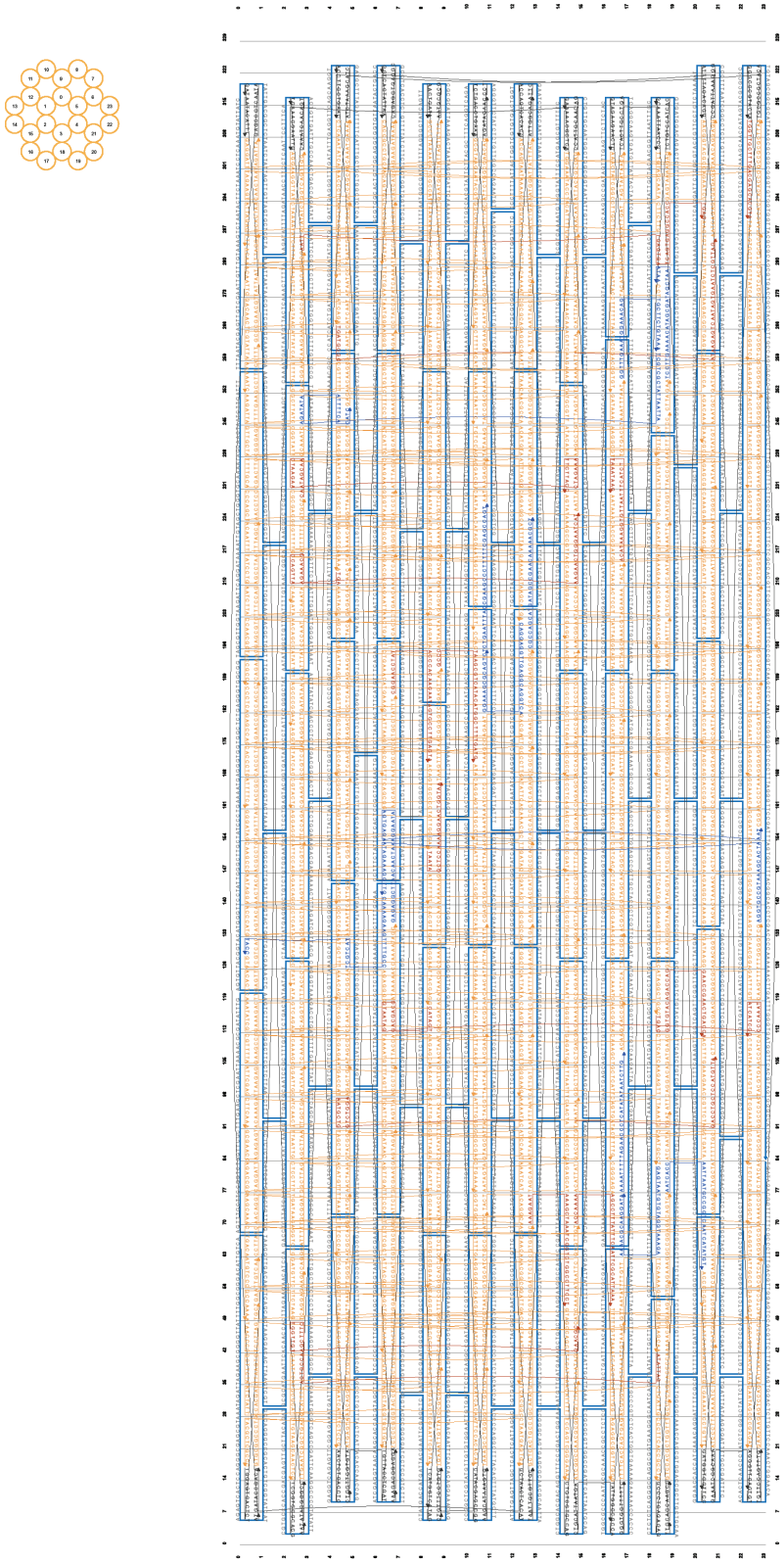

Figure S30 | CaDNAno[42] image of the left-handed 24 helix bundle including polymerization oligonucleotides (black). The schematic picture shows the scaffold path (blue), the staple oligonucleotides (orange) and the hybridization sites (blue and red, see also Figure S8).

SI References

31. Rosenfeld, L. Hadrons and Nuclei. *Zeitschrift für Physik A* 1929, **52**, 161 (1929).
32. Fan, Z., Govorov, A. O. Plasmonic Circular Dichroism of Chiral Metal Nanoparticle Assemblies. *Nano Lett.* 10, 2580 (2010).
33. Fan, Z., A. O. Govorov, A. O. Helical Metal Nanoparticles Assemblies with Defects: Plasmonic Chirality and Circular Dichroism. *The Journal of Physical Chemistry C*, **115**, 13254 (2011).
34. Moffitt, W. Optical Rotatory Dispersion of Helical Polymers. *Journal of Chemical Physics*, **25**, 467 (1956).
35. Fasman, G. D. Circular dichroism and the conformational analysis of biomolecules, Plenum, New York, (1996).
36. Berova, N. N., Nakanishi, K., Woody, R.W. Circular Dichroism: Principles and Applications, 2nd ed. *Wiley-VCH, USA*, (2000).
37. Slocik, J. M., Govorov A. O., Naik, R. R. *Nano Letters*, **11**, 701 (2011).
38. Weber, W. H., Ford, G.W. Propagation of optical excitations by dipolar interactions in metal nanoparticle chains. *Phys. Rev B* 70, 125429 (2004); Zhen, Y.-R., Fung, K.H., Chan, C.T. Collective plasmonic modes in two-dimensional periodic arrays of metal nanoparticles. *Phys. Rev. B* 78, 35419 (2008).
39. Maier, S.A., Kik, P.G., Atwater, H.A. Optical pulse propagation in metal nanoparticle chain waveguides. *Phys. Rev. B* **67**, 205402 (2003).
40. Johnson, P. B., Christy, R. W. Optical Constants of the Noble Metals. *Phys. Rev. B* **6**, 4370-4379 (1972).
41. Woody, W. W. Circular dichroism and the conformational analysis of biomolecules; Fasman, G. D., Ed.; *Plenum: New York*, pp 25-67 (1996).
42. Douglas, S. M., Marblestone, A. H., Teerapittayanon, S., Vazquez, A., Church, G. M. & Shih, W. M. Rapid prototyping of 3D DNA-origami shapes with caDNAno. *Nucleic Acids Research* **37**, 15 (2009).
43. Ding, B., Deng, Z., Yan, H., Cabrini, S., Zuckermann, R. N., Bokor, J. Gold Nanoparticle Self-Similar Chain Structure Organized by DNA Origami. *Journal of the American Chemical Society* **132**, 3248-3249 (2010).
44. Douglas, S. M., Chou, J. J. & Shih, W. M. DNA-nanotube-induced alignment of membrane proteins for NMR structure determination. *PNAS* **104**, 6645 (2007).
45. Guerrero-Martínez, A., Auguié, B., Alonso-Gómez, J. L., Džolić, Z., Gómez-Graña, S., Žinić, M., Cid, M. M., Liz-Marzán, L. M. Intense Optical Activity from Three-Dimensional Chiral Ordering of Plasmonic Nanoantennas. *Angew. Chem. Int. Ed.* 50, 5499 (2011).

46. Pearlstein, R. M., Davis, R. C., Ditson, S. L. Giant circular dichroism of high molecular weight chlorophyllide-apomyoglobin complexes. *Proc. Natl. Acad. Sci.* **79**, 400 (1982).
47. Walters, R. S., Kraml, C. M., Byrne, N., Ho, D. M., Qin, Q., Coughlin, F. J., Bernhard, S., Pascal, R. A., Jr. Configurationally Stable Longitudinally Twisted Polycyclic Aromatic Compounds. *J. Am. Chem. Soc*. **130**, 16435 (2008).

Supporting Information

Chiral plasmonic material with switchable circular dichroism

by

Robert Schreiber, Ngoc Luong, Zhiyuan Fan, Anton Kuzyk, Tao Zhang, Philipp Nickels, David M. Smith, Bernard Yurke, Wan Kuang, Alexander O. Govorov, Tim Liedl

submitted to

Nature Communications

Supplementary Information

Chiral plasmonic material with switchable circular dichroism

Robert Schreiber[1], Ngoc Luong[2], Zhiyuan Fan[3], Anton Kuzyk[4,5], Philipp Nickels[1], Tao Zhang[1], David M. Smith[1], Bernard Yurke[2], Wan Kuang[2], Alexander O. Govorov[3,*], Tim Liedl[1,*]

[1]*Fakultät für Physik and Center for Nanoscience, Ludwig-Maximilians-Universität, 80539 München, Germany*

[2]*Department of Electrical and Computer Engineering, Boise State University, Boise, Idaho 83725, USA*

[3]*Department of Physics and Astronomy, Ohio University, Athens, Ohio 45701, USA*

[4]*Max-Planck-Institute for Intelligent Systems, 70569 Stuttgart, Germany*

[5]*Department of Applied Physics, Aalto University School of Science, FI-00076 Aalto, Finland*

** govorov@phy.ohiou.edu, tim.liedl@lmu.de*

Supplementary Information Note S1: Surface preparation, attachment of the nanohelices to the surface and silver enhancement of the gold particles of nanohelices

Surface preparation for the attachment of the nanohelices on quartz glass

A 1 cm x 1cm quartz slide (CrysTec, Germany) was cut into smaller pieces of ~ 0.5 cm x 0.5 cm that can fit into a cuvette. The pieces were cleaned with Ethanol and placed in a vial (Safe-Lock Tube 2mL, Eppendorf, Germany) for further treatment. 0.8 mg of BSA and 0.2 mg BSA-biotin (Sigma-Aldrich, Germany) were dissolved in 1 mL PBS buffer (pH 7.4). A quartz slide was covered with the BSA-BSA-biotin-PBS solution and incubated overnight at 4°C (the vial with quartz slides was sealed to prevent drying of the surface). After incubation, the quartz slide was flushed 4 times with PBS buffer (pH 7.4) in order to remove free BSA-Biotin (the surface should not get dry to avoid denaturing of the proteins). In the next step, the quartz slide was covered with the Neutravidin solution (0.2 mg of Neutravidin per 1 mL PBS buffer (pH 7.4)) for 30 min at 4°C (Neutravidin binds to the biotin modified BSA on the surface). Finally, the quartz surface was flushed 4 times with PBS buffer (pH 7.4) to get rid of free Neutravidin (the surface should not dry out during this step).

Attachment of the nanohelices to the surface

50 µL of 4 nM of biotin-modified left-handed nanohelices in 0.5xTBE buffer with 11 mM $MgCl_2$ were added to 600 µL of PBS buffer (pH 7.4). The Neutravidin coated quartz slide was covered with the nanohelix solution for 2 hours at 4°C. Next, the surface was flushed with 0.5xTBE + 11 mM $MgCl_2$ buffer in order to remove unbound nanohelices.

Ag deposition on the gold particles of the nanohelices on the quartz surface

Equal amounts of the reaction solutions A (initiator), B (moderator) and C (activator) of the HQ Silver™ Enhancement Kit (nanoprobes.com) were mixed together. 120 µL of the enhancement kit mix were diluted with 600 µL of 0.5xTBE + 11 mM $MgCl_2$ buffer. This step should be performed as fast as possible because the enhancement kit becomes active upon mixing of the reaction solutions. The quartz surface with the attached

nanohelices was covered with the diluted enhancement solution mix for 4 min. Then the surface was flushed with PBS buffer to stop the enhancement reaction.
Efficiency of enhancement depends on the surface density of the nanohelices.

Switching of the orientation of the nanohelices

The switching was performed by simple directed gas flow drying (the drying process should be carried out fast), followed by resuspending the Ag enhanced nanohelices on the quartz slide in PBS.

Supplementary Information Note S2: Direct assembly of nanohelices on the surface and CD spectra of L-NHs assembled on the surface

Gold nanoparticles were directly hybridized to the DNA origami structures on the surface. For this, 24 helix-bundle origami structures with attachment sites for gold nanoparticles were attached to a Neutravidin coated quartz slide (see Supplementary Information Note S1). The 24HB coated quartz surface was washed with 0.5xTBE + 11mM $MgCl_2$. 600 µL of DNA functionalized 10 nm AuNPs (20 nM) in 0.5xTBE + 11mM $MgCl_2$ were added to the quartz surface and incubated for 4 hours at 20°C to allow efficient hybridization of gold nanoparticles to the DNA origami structures. Next, the surface was flushed with 0.5xTBE + 11mM $MgCl_2$. After that, the deposition of silver on the gold nanoparticles was performed (see Supplementary Information Note S1).

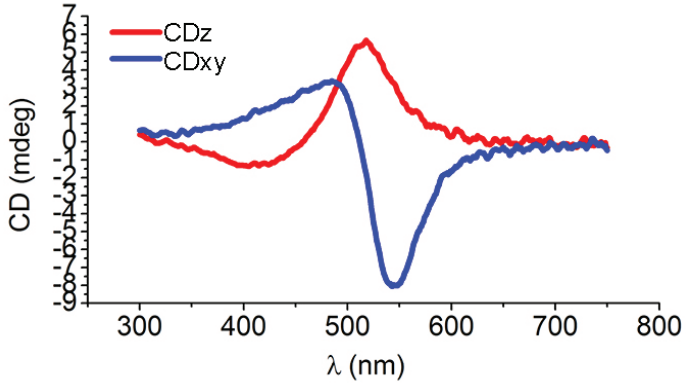

Figure S2 | Switching CD spectra of nanohelices assembled directly on the surface. Measurements were performed with the same ensemble of left-handed nanohelices in solution (red curve) and dried (blue curve)**.**

Supplementary Information Note S3: Circular Dichroism of plasmonic nanocrystal assemblies

It is interesting to compare CD of a plasmonic helix with CD signals of other geometries, such as tetrahedral complexes for example[37,38,39]. In **Figure S3**, we show three chiral geometries of a plasmonic tetramer. We can see that the helical assembly has a clear advantage over the other geometries with tetrahedral arrangements. In a helix, the CD signals are one/two orders of magnitude higher than the CD signals in asymmetric and equilateral tetrahedral complexes. The data were taken from Ref. 39. A chiral plasmonic assembly with an equilateral tetrahedral frame (**Figure S3**) has the smallest CD signals. In fact, the averaged CD for this assembly has a vanishing magnitude for the given geometrical parameters (see **Figure S3 c**). The reason is that such a tetrahedral assembly has no dipolar CD in solution and may have non-vanishing CD signals only due to the multipole interactions between nanoparticles. Simultaneously, a helical assembly has a very strong dipolar CD.

The shapes of CD signals for assemblies of various geometries are typically similar. The reason lies in the physics of the CD signal formation: The CD signal appears due to the Coulomb and electromagnetic interactions between plasmons of single nanoparticles, and these interactions lead to the formation of collective plasmon modes with chiral properties. In an assembly, the integral of the CD spectrum over the frequency should be approximately zero due to the optical sum rule and, therefore, the shape of CD is typically bi-signate (dip-peak or peak-dip). The collective plasmonic spectrum of a chiral assembly has right-handed and left-handed plasmonic excitations on the two opposite sides of the plasmon peak; therefore, this property produces characteristic bi-signate lines in the CD spectra. In **Figure S3**, we also include the data for directional CD. Again we see that the helical assembly demonstrates the strongest signals. Another general property of the plasmonic CD signals can be seen in this figure: the directional CD signals are typically much stronger than the averaged CD in solution.

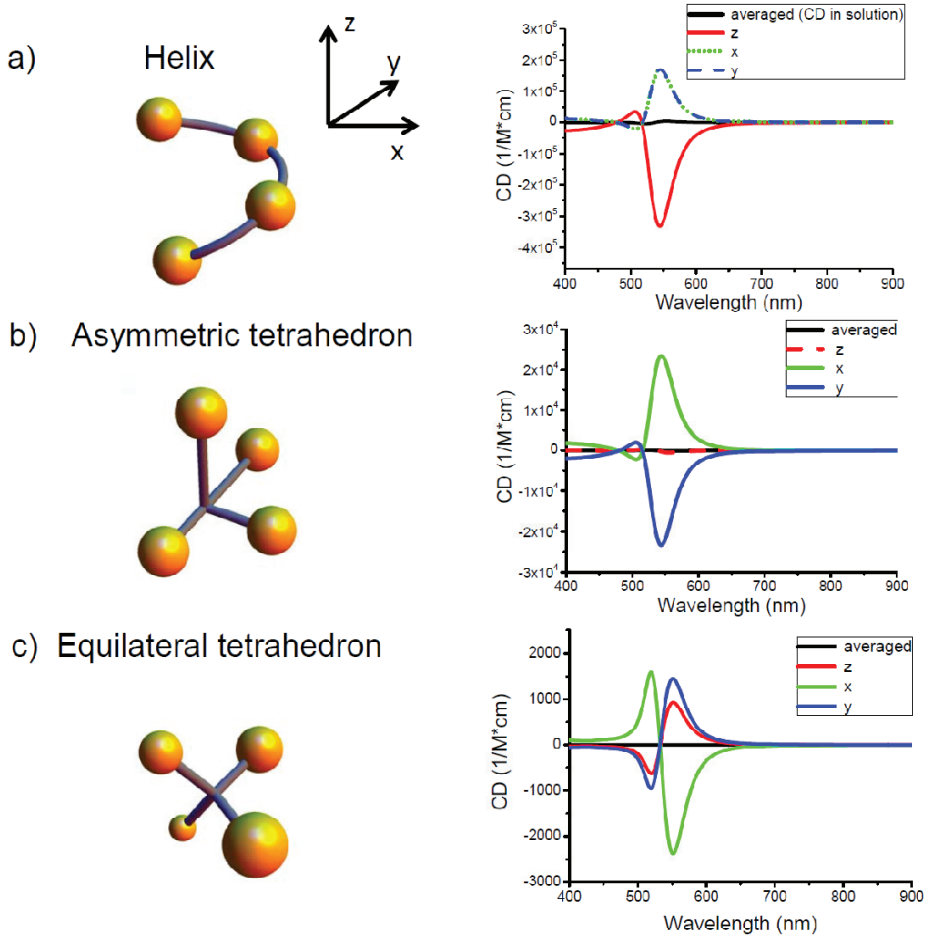

Figure S3 | Calculated CD spectra for three chiral assemblies shown on the left-hand side of the figure. The averaged CD describes the signals coming from a solution; the directional CD spectra are shown for three representative directions, +x, +y, +z. Parameters of the assemblies are given below, in **Table S3**.

Table S3. Coordinates and radii of nanoparticles in the chiral assemblies.

coordinates and radii (nm)	*x*	*y*	*z*	radius
helix	14.376	0	0	5
	0	14.376	8.386	5
	-14.376	0	16.772	5
	0	-14.376	25.158	5
asymmetric tetrahedron	15.56	0	0	5
	0	23.34	0	5
	0	-15.56	0	5
	0	0	23.34	5
equilateral tetrahedron	8.4852	8.4852	8.4852	3
	-8.4852	-8.4852	8.4852	4
	8.4852	-8.4852	-8.4852	5
	-8.4852	8.4852	-8.4852	6

Supplementary Information Note S4: Shift of the CD spectra caused by refractive index change

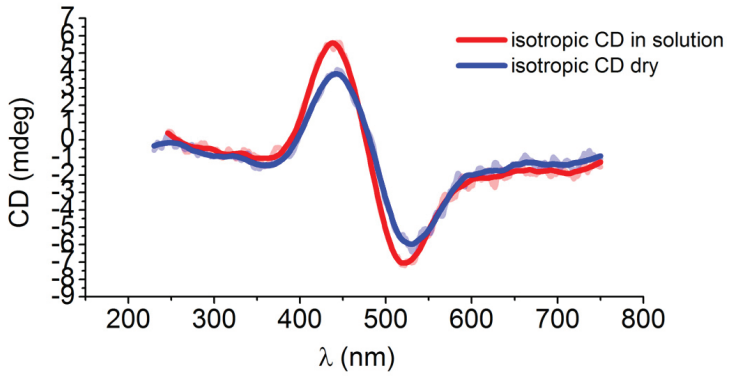

Figure S4 | CD spectra of left-handed nanohelices randomly orientated in solution and on a substrate. These measurements were performed with the same ensemble of left-handed nanohelices, which were isotropically distributed in solution (red curve) and were then simply left to dry on a glass surface (blue curve). In contrast to the other experiments, the structures were not attached to the surface via biotin linkers. Also, no washing step was used to flush away unbound structures. Here, enough material was used to enable the formation of a thin film of dried, but randomly oriented helices. An influence of the change of the refractive index may be observed as a 4 nm shift of the peak and a 10 nm shift of the dip of the CD signal. It is also possible that the helices are not distributed completely isotropically but have a tendency to align parallel to the surface. This effect must be, however, negligible as no significant change in the shape of the CD signal is observed.

Supplementary Information Note S5: Progression of the CD signal during switching

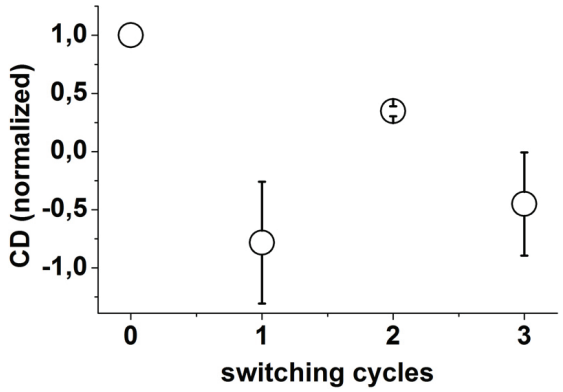

Figure S5 | Progression of the CD signal of L-NHs with switching cycles averaged over 4 experiments. Each data point represents the averaged and normalized maximum peak or dip value of the CD signals of 4 different experiments going through up to 4 switching states. We attribute the decrease of the maximum signals over switching cycle to the following scenarios: at each drying step, some of the nanohelices get trapped in a specific orientation on the surface (most likely lying on the surface) and at each washing step some of the helices (but also individual gold particles) detach from the surface. Any other form of helix destruction or deformation will lead to a loss of signal or the helices.

Supplementary Information Note S6: Switching with right-handed nanohelices (R-NH)

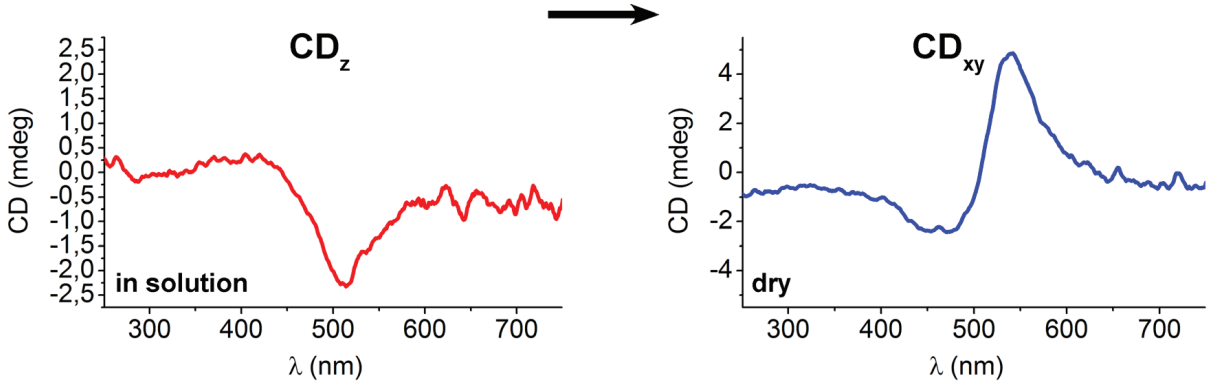

Figure S6 | Switching of R-NH with inverted CD signals. This experiment was performed as described for L-NH in the main text. The recorded CD signal clearly

shows the expected switching behavior. Right-handed nanohelices that are upright in solution (left) show a CD_Z signal that is inverted to the CD_Z signal of L-NHs. After being switched by drying to an orientation parallel to the surface the CD_{xy} signal that is inverted to the CD_{xy} signal of lying L-NHs is recorded.

Supplementary Information Note S7: Dipolar model of nanoparticle helix

Calculations in the manuscript follow the electrodynamics methods used previously in Refs. 37-42. A system of nanoparticles (NPs) is described by a set of dipoles $\vec{p}_i$ induced by the electric fields. The NPs are arranged in a helix (Figures 1 and 3 in the main text). The equation for a dipole of a single NP with index i is

$$\vec{p}_i = \alpha\left(\vec{E}_{ext,i} + \sum_{j\neq i}\vec{E}_{j\to i}\right), \tag{1}$$

where $\vec{E}_{ext,i}$ is the external field, α is the polarizability of a NP, and $\vec{E}_{j\to i}$ is the field due to the neighboring NPs:

$$\vec{E}_{j\to i} = \left\{\left(1-\frac{i\omega\sqrt{\varepsilon_0}r_{ji}}{c}\right)\frac{3\hat{r}_{ji}\cdot\vec{p}_j\hat{r}_{ji}-\vec{p}_j}{r_{ji}^{\,3}} + \varepsilon_0\frac{\omega^2}{c^2}\frac{\vec{p}_j-\hat{r}_{ji}\cdot\vec{p}_j\hat{r}_{ji}}{r_{ji}}\right\}e^{\frac{i\omega\sqrt{\varepsilon_0}r_{ji}}{c}}. \tag{2}$$

The NP polarizability is defined in the usual way: $\alpha(\omega) = R_{NP}^3\left(\varepsilon_{Au}-\varepsilon_0\right)/\left(\varepsilon_{Au}+2\varepsilon_0\right)$, where R_{NP} is the NP radius, $\varepsilon_{Au}(\omega)$ is the Au dielectric function, and ε_0 is the dielectric constant of matrix. The external field varies at different sites by a phase factor $e^{i\vec{k}\cdot\vec{r}_i}$. The set of linear equations (1) can be solved self-consistently for all dipole moments. Then, the total absorption and extinction rates can be calculated using the following equations:

$$Q_{abs} = \frac{1}{2}\omega\cdot\varepsilon_0\sum_i \mathrm{Im}\left(\frac{\vec{p}_i^{\,*}}{\alpha^*}\cdot\vec{p}_i\right), \tag{3}$$

$$Q_{ext} = \frac{1}{2}\omega\cdot\varepsilon_0\sum_i \mathrm{Im}\left(\vec{E}_{ext\_i}^{\,*}\cdot\vec{p}_i\right). \tag{4}$$

The scattering rate calculated is $Q_{scat} = Q_{ext} - Q_{abs}$.

The directional CD for incident light associated with a particular wave vector $\vec{k}$ is given by

$$CD_{\vec{k}} = Q_{ext,+} - Q_{ext,-}, \tag{5}$$

where the symbols $\pm$ are related to the LCP and RCP photons. In colloidal solution systems, the nanostructures are randomly oriented and we need to perform averaging over orientations. Mathematically, averaging can be performed by assuming that the light comes from all directions to a nanostructure with a fixed orientation:

$$\langle CD \rangle = \langle Q_+ - Q_- \rangle_{\Omega_{\vec{k}}} . \tag{6}$$

The calculations of CD and scattering in the main text are based on Eqs.3-6. In Fig. 3d in the main text, we show the data for CD averaged over an interval of the angle of tilting,

$$CD(\theta) = \frac{\int_0^{\theta} CD_{\vec{k}\|-\hat{z}}(\theta') \cdot \sin[\theta'] d\theta'}{\int_0^{\theta} \sin[\theta'] d\theta'}, \tag{7}$$

where θ is the angle giving the tilting of the helix with respect to the normal (see Fig. 3d in the main text). For the medium, we assumed water ($\varepsilon = 1.8$) and for Au dielectric function we used the tables from Ref. 43.

Supplementary Information Note S8: Comparing the CD strength of isotropic and anisotropic L-NHs

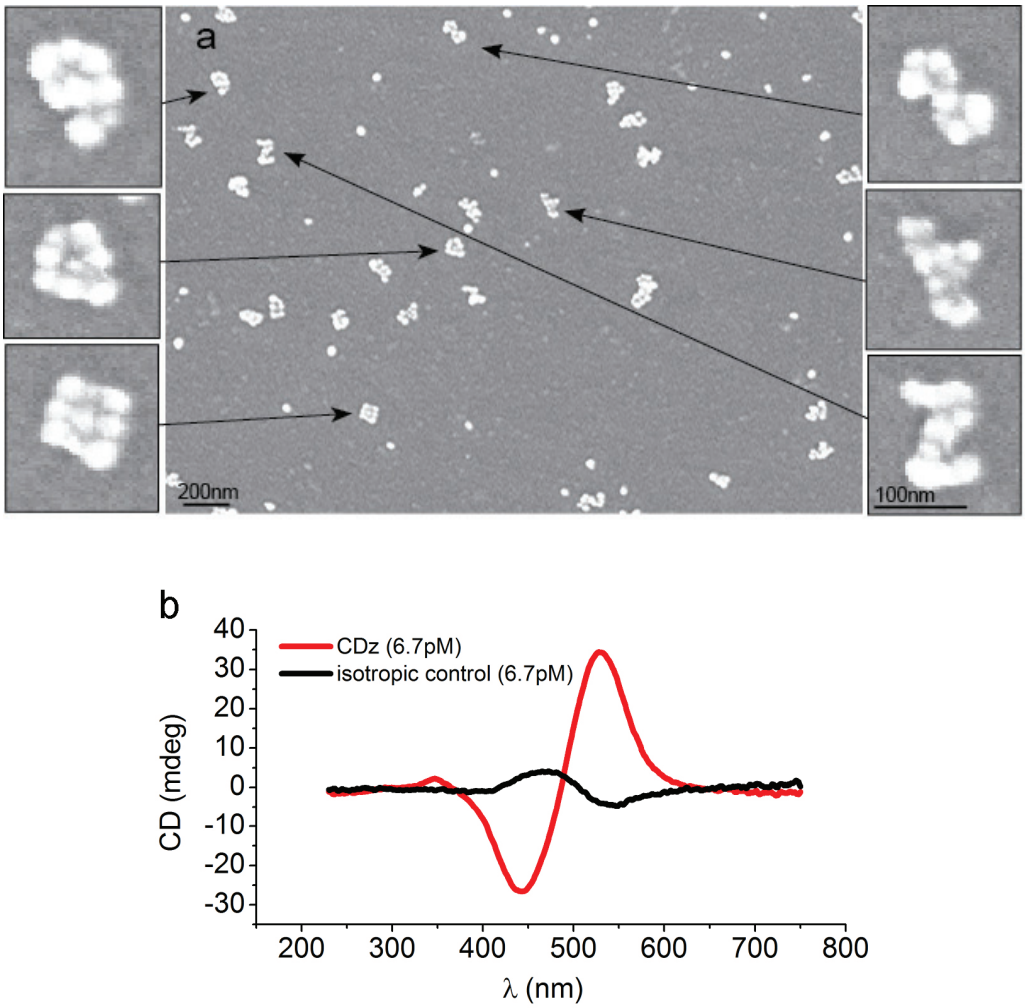

Figure S8 | CD comparison of oriented and randomly distributed helices **a**, Wide field Scanning Electron Microscopy (SEM) image of left-handed Nanohelices attached to a BSA-biotin-neutravidin coated quartz surface. An area density of five left-handed nanohelices per μm^2 was determined. Zoom-in images reveal that super-enhanced helices remain partly upright even after drying. **b**, A CD of 35 mdeg for anisotropic left-handed nanohelices was measured at an area density of five nanohelices per μm^2 (silver enhanced attached helices in buffer, red curve). Silver enhanced helices dispersed in solution at the same area density (area density was converted to volume concentration by mapping the projection of the three-dimensional volume to a two-dimensional plane) result in a CD peak maximum of 4.5 mdeg (black curve). Hence the anisotropic CD is roughly one order of magnitude (~8 times) higher than the isotropic CD of the L-NHs. The shape of the anisotropic CD_z signal presented here differs

slightly from the previous presented CD_z spectra (Fig. 2 and Fig. S2). Such variations may result from different silver enhancement conditions in each set of experiments. Here, a stronger silver enhancement was necessary to enable imaging of the nanohelices with SEM.

Supplementary Information Note S9 and Supplementary Movies: Surface attachment of nanohelices with biotinylated staple strands and details on the darkfield setup

The following two videos provide further evidence that the nanohelices attach to the glass slide via biotinylated staple strands. The glass slide is functionalized with biotin-BSA-neutravidin. In the first video (Solution-Helix-Prior-Biotin-Functionalization.avi), a drop of nanohelices without the biotinylated staple strand in 1x TE buffer with 12 mM Mg^{2+} is place on the glass slide. The darkfield microscopy images of nanohelices under the Xe lamp illumination are taken continuously in color. A linear polarizer is placed just before the imaging camera. It can be seen that few nanohelices bind to the functionalized glass slide without the biotinylated staple strands. The majority of nanohelices move freely in solution. This suggests that the non-specific binding of nanohelices to the glass is very low. Due to the tumbling of nanohelices, their scattering spectra in the orientation of the polarizer changes with time. As a result, the appearing color of the nanohelices changes throughout the video (Movie #1). In the second video (Solution-Helix-Post-Biotin-Functionalization.avi), biotinylated staple strands are added to the solution which hybridize with nanohelices. After 2 hours of incubation at room temperature, the glass slide is thoroughly rinsed with 1x TE buffer with 12 mM Mg^{2+}. The biotin binds to the functionalized glass substrate thus leading to attachment of nanohelices to the glass slide. It shows that most nanohelices in the video are stationary with little change in color (Movie #2). Based on the density of nanohelices in the two videos, we can estimate that roughly 40% of the nanohelices are attached to the glass slide.

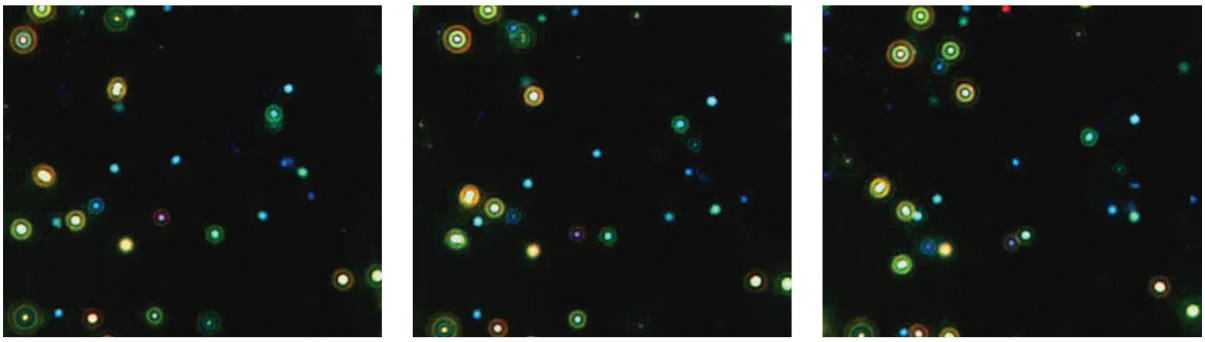

Movie #1: "Solution-Helix-Prior-Biotin-Functionalization.avi"

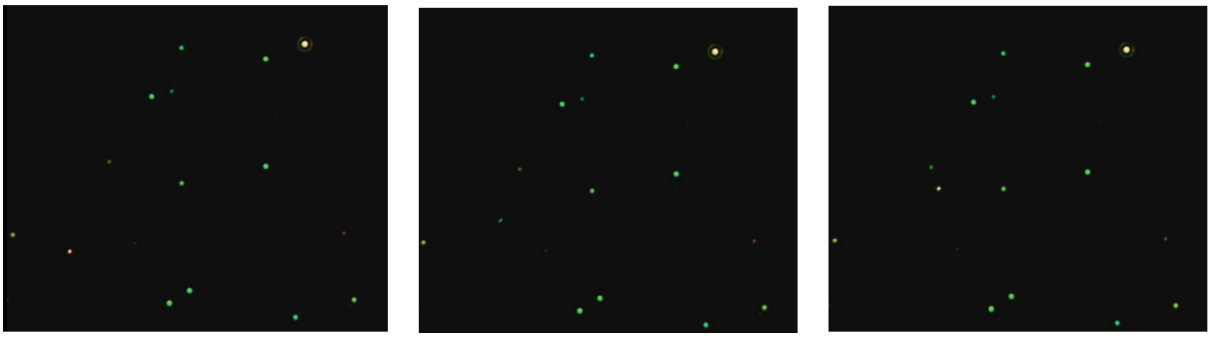

Movie #2: "Solution-Helix-Post-Biotin-Functionalization.avi"

Darkfield scattering spectra measurements

Optical characterization of the nanohelices was performed to investigate the scattering spectra as a function of nanohelices' orientation. The glass slide was functionalized with neutravidin using the protocol described in the manuscript. The nanohelices were deposited inside the silicone gasket previously painted on the slide surface. A coverslip was immediately placed on top the gasket and the edges are sealed. The slide was loaded into an inverted microscope (Nikon, TiU) facing down. A Xe lamp (Shutter Instrument model LB-LS/30) illuminates the slide through a high resolution condenser (Cytoviva). The condenser has a numerical aperture from 1.2 to 1.4, as shown in **Fig. S9.1**. An 100x objective (Nikon, Plan Fluor 100x/0.5-1/3 oil iris) was used to collect the scattering spectra with a 600 lines per mm grating and a CCD camera (Princeton Instruments, ProEM 512). A 480 nm long pass filter (Edmund Optics) was inserted after the lamp to reduce the scattering background generated by the sample substrate. The polarization dependent scattering spectra were collected for individual nanohelices using a custom-made motorized polarizer, which was inserted into the optical path after

the glass slide. The spectrometer's slit width was set to 30 µm and the camera's region of interest (ROI) was set such that only the light emission from the selected nanohelices was collected during the scan from 480 nm to 760 nm. The exposure time for the CCD camera ranged from one to three minutes. To remove background signal that may be present in the scattering spectra, spectra from an adjacent "dark" area containing no sample was subtracted from the scattering spectra. The resulting spectrum was then divided by the spectrum of the Xe lamp. A detailed description of spectral measurements can be found in the supplementary information of reference 44.

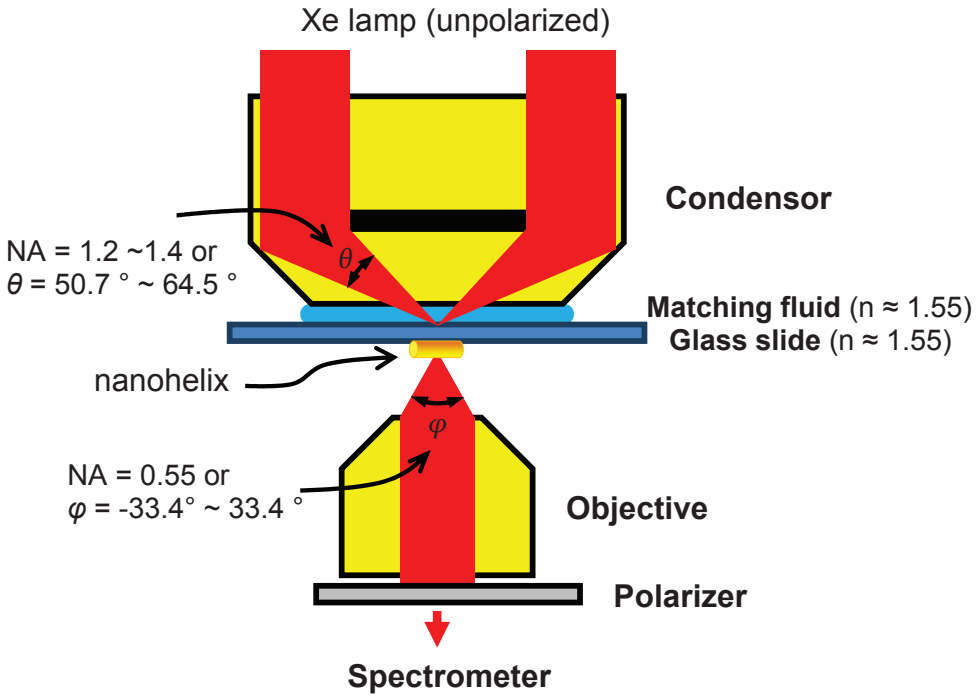

Figure S9.1 | Schematic drawing of the optical setup used to characterize the nanohelices. The glass slide is illuminated by an unpolarised Xe lamp through a high NA condenser (Cytoviva). The light scattered by an individual nanohelix is collected by a 100x objective lens using an adjustable NA of 0.55. The light is fed to a CCD spectrometer (Acton 300i, Princeton Instrument) either directly or via an adjustable linear polarizer.

After the spectra for nanohelices in buffer solution were characterized, the gasket seal is removed. The glass slide is repeatedly rinsed with buffer solution and let dry. It was

then rinsed with milli-Q water to remove salt on the glass surface. The glass slide was loaded back to the microscope. By aligning to the reference marker previously placed on the slide, the same area of the slide where the spectra were taken was located. The reference marker was clearly viewable in the bright field mode on the microscope. **Figure S9.2** shows a colour darkfield image of surface-bound nanohelices in solution (a) and the same area after the drying process (b). The colour change between the two images indicates that the scattering spectra is red shifted, consistent with the change of nanohelices' orientation from up-right in solution to lying-flat in the dry condition. The out-of-focus object in **Fig. S9.2**(a) is most likely an unbound nanostructure floating in solution.

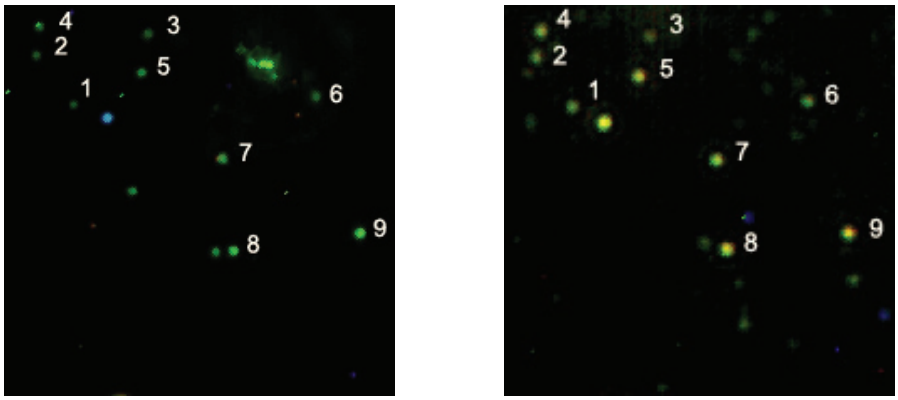

(a) **(b)**

Figure S9.2 | Darkfield colour image of surface-bound nanohelices in solution (a) and after they are dried (b). The nanohelices with a number placed next to it were measured spectroscopically (data shown in **Figure S9.3**).

The spectral shift is further verified in **Fig. S9.3** where darkfield scattering spectra of 9 individual nanohelices (labelled in **Fig. S9.2**) were recorded. The sub-captions for each figure correspond to the numerical labels shown in **Fig. S9.2**. Some variations in the scattering spectra among different nanohelices are observed. In general, the peak scattering wavelength for nanohelices in solution is at 554 ± 8 nm and the peak scattering wavelength for nanohelices after they are dried is at 576 ± 10 nm.

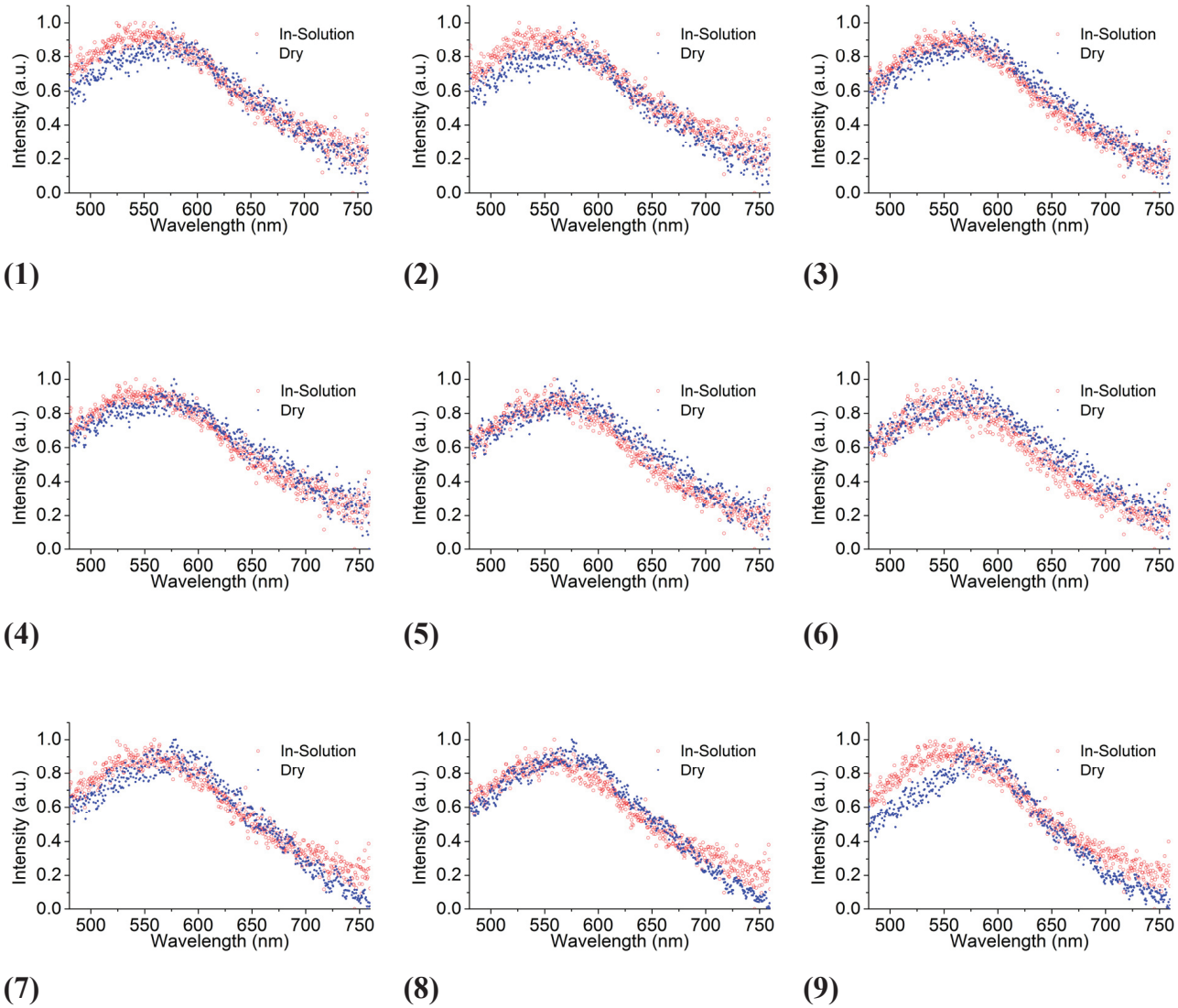

Figure S9.3 | Darkfield colour scattering spectra of 9 surface-bound nanohelices (as labelled in Figure S9.2). Each plot consists of a scattering spectrum of a nanohelix in solution and of a spectrum of the same nanohelix after it was dried. The peak scattering wavelength shows a red shift after the nanohelices were dried.

Figure S9.4 is another example of surface-bound nanohelices and their respective darkfield scattering spectra.

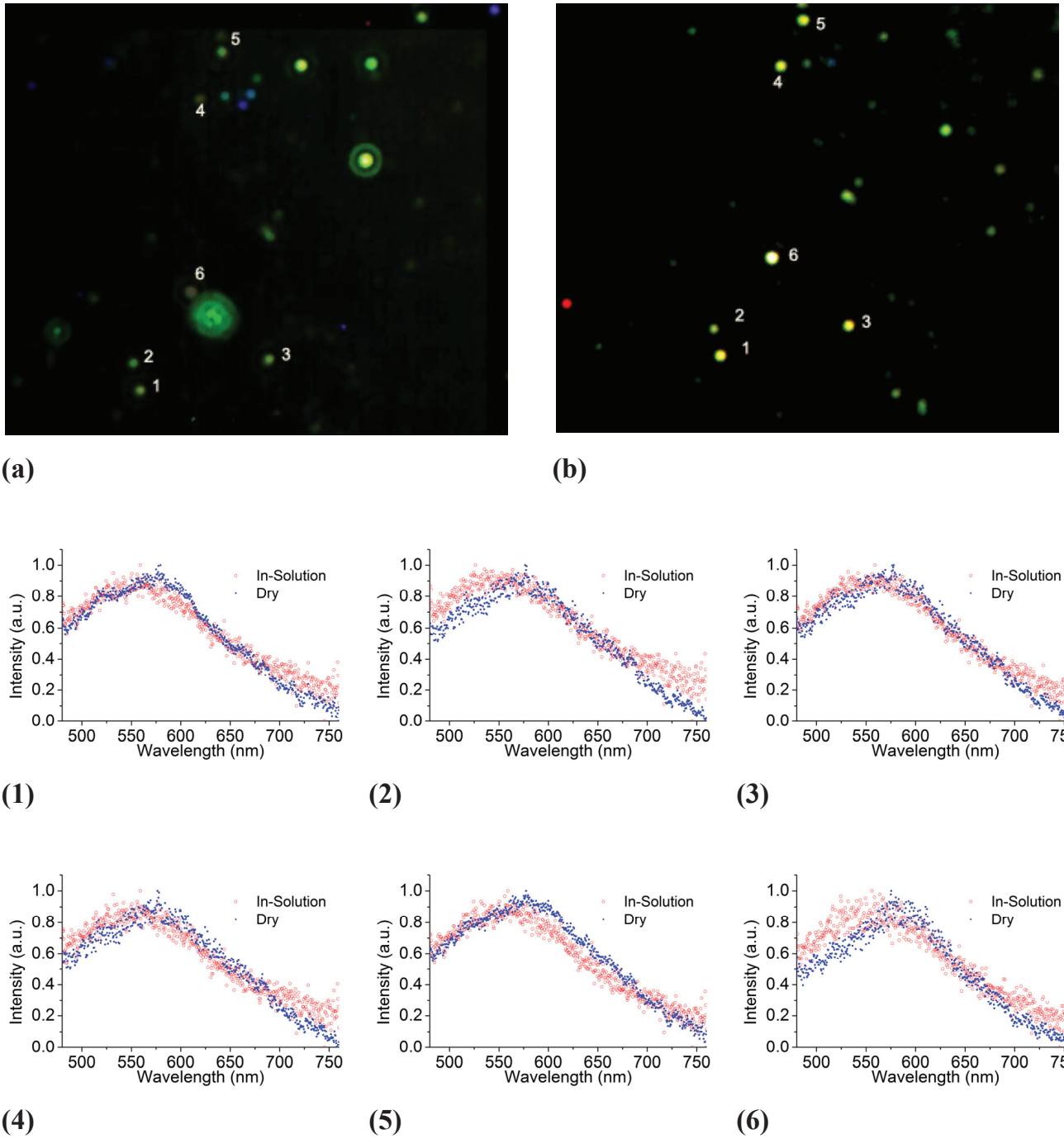

Figure S9.4 | Darkfield image of surface-bound nanohelices in solution (a) and after they are dried (b). (1)-(6) Darkfield scattering spectra of the nanohelices labelled in **(a)** and **(b)**.

It can be observed that the scattering spectra are not polarization dependent for nanohelices in solution. However, the scattering spectra show a considerable

polarization dependency after the nanohelices are dried. **Figure S9.5** shows additional scattering spectra of bound nanohelices for longitudinal and transverse polarizations. During the measurements, a linear polarizer is rotated until a maximum total scattering intensity is observed. The darkfield scattering spectrum for this polarizer angle is considered as the longitudinal scattering. The polarizer is then rotated by 90° to obtain the darkfield spectrum for the transverse scattering.

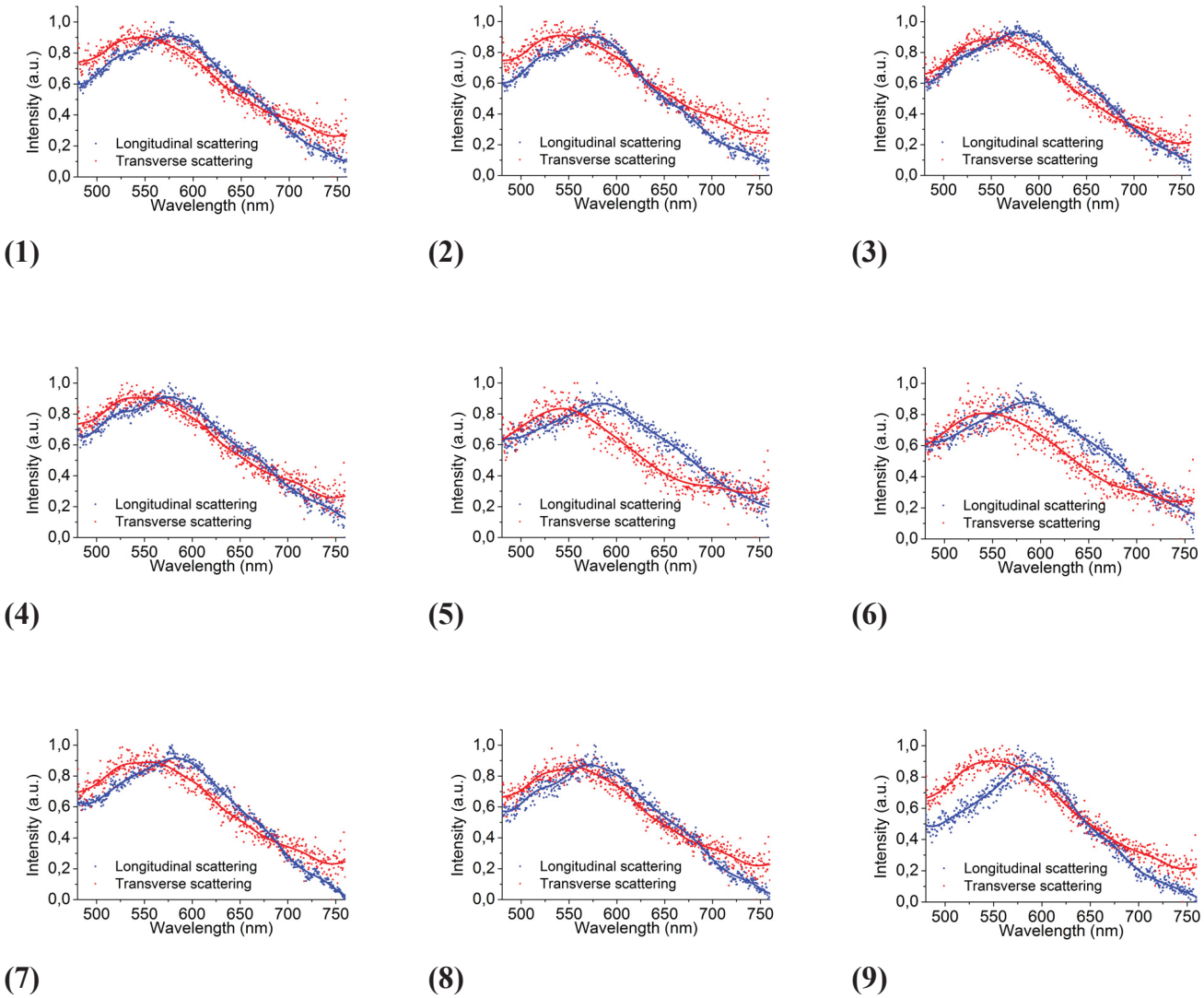

Figure S9.5 | Longitudinal and transverse darkfield scattering spectra for dry, surface-bound nanohelices shown in Fig. S9.3.

In addition to the spectra for longitudinal and transversal scatterings shown in **Fig. S9.5**, the scattering spectra as a function of linear polarizer orientation were measured and a few examples are shown in **Fig. S9.6**. The angle of the linear polarizer is 0º for the transverse scattering and 90º for the longitudinal scattering, respectively.

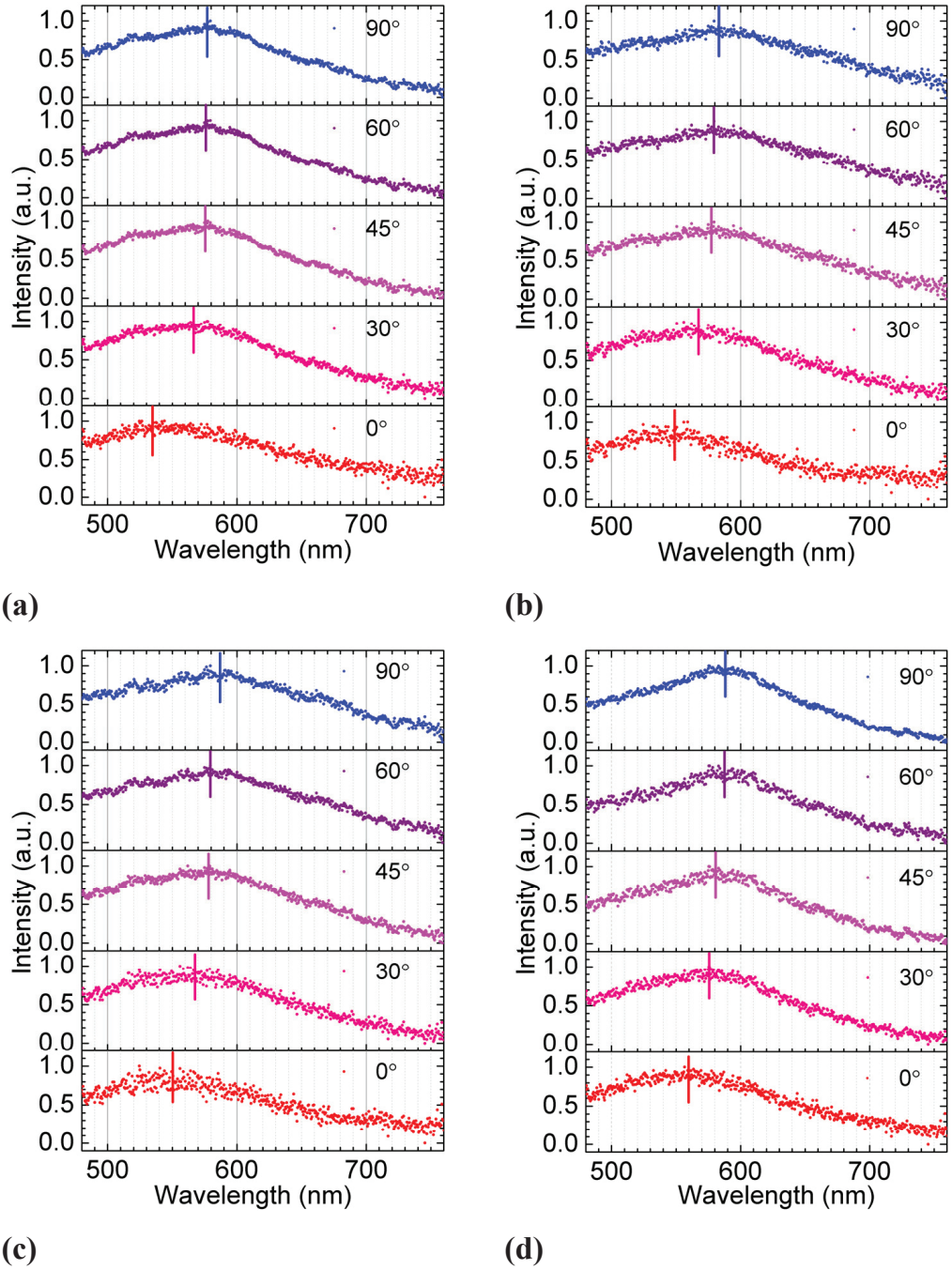

Figure S9.6 | Polarization dependency of darkfield scattering spectra for a surface-bound nanohelix dried on glass.

Supplementary Information Note S10: Additional control experiments of nanohelices on substrates.

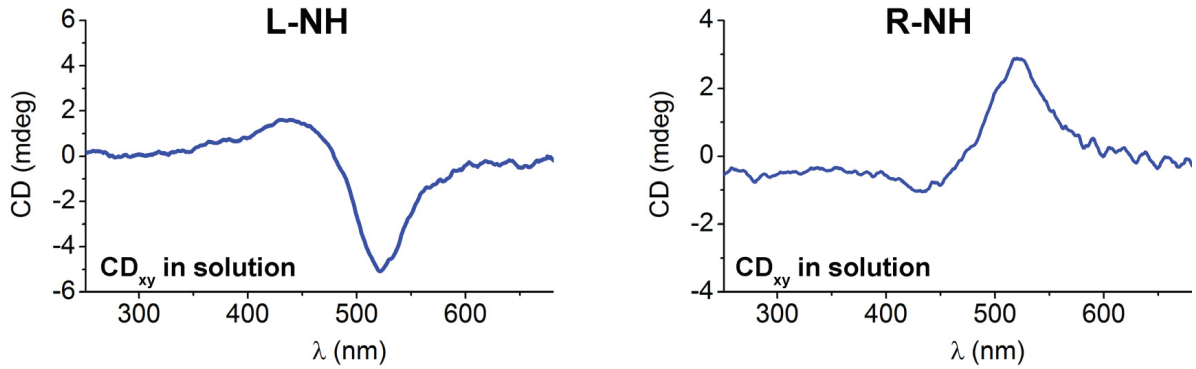

Figure S10.1 | Solution measurement of L- and R-NHs attached parallel to the substrate. A BSA-Neutravidin surface was prepared as describe in Supplementary note S1. Instead of biotinylated nanohelices this time biotynilated poly-A-oligonucleotides (15 nt) were applied to the surface. After washing, nanohelices without biotin were added. As all nine gold nanoparticles of the nanohelices are densely covered with poly-T-oligonucleotides, the helices were tightly coupled via doublestrand formation to the substrate in a parallel fashion. As expected, we recorded clear CD signals of the xy-modes for these samples.

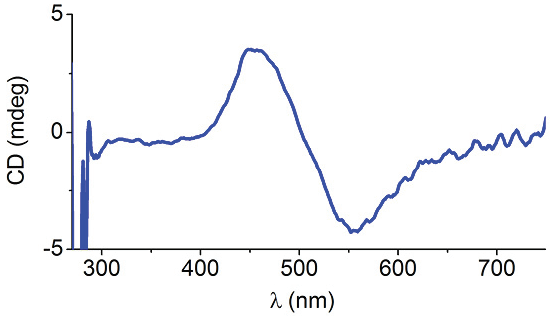

Figure S10.2 | L-NHs on an amine-silane coated glass slide in solution. Assembled nanohelices were deposited on an amine-silane coated glass in 0.5xTBE buffer (pH 6, 11 mM $MgCl_2$) for 2 hrs. The recorded CD signal of this sample is switched compared to the signal from nanohelices standing in solution (see e.g. Figure S2) and differs slightly from dried helices (see e.g. Figure S2). This is in accordance with our expectation as we expect the charge-induced adsorption (DNA is strongly negatively charged) to predominantly result in helices aligned parallel to the surface, but some

helices may also attach upright to the surface as the structures has an aspect ration of only ~ 5:1.

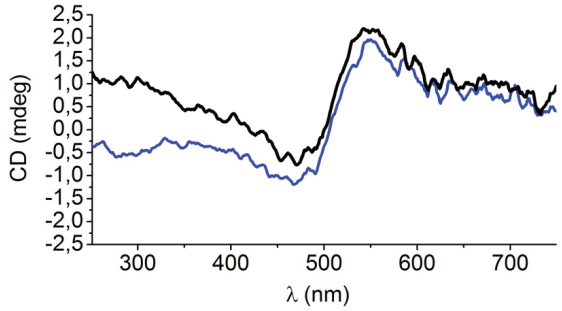

Figure S10.3 | CD signal artifacts by a 90° rotation of the substrate. R-NHs were aligned parallel to the quartz substrate by an airstream. The first spectra (blue) was taken at a given orientation of the substrate in the cuvette (surface pependicular to the probing beam). For the second experiment the substrate was rotated 90° around its normal. As a result we observe a distinct chance of the CD signal in the UV and the blue region of the spectrum. We conclude that substrate-related interferences can weakly influence such measurements and have to be taken into account for quantitative analysis. However, at the plasmonic range (above 500 nm), the effects become negligible.

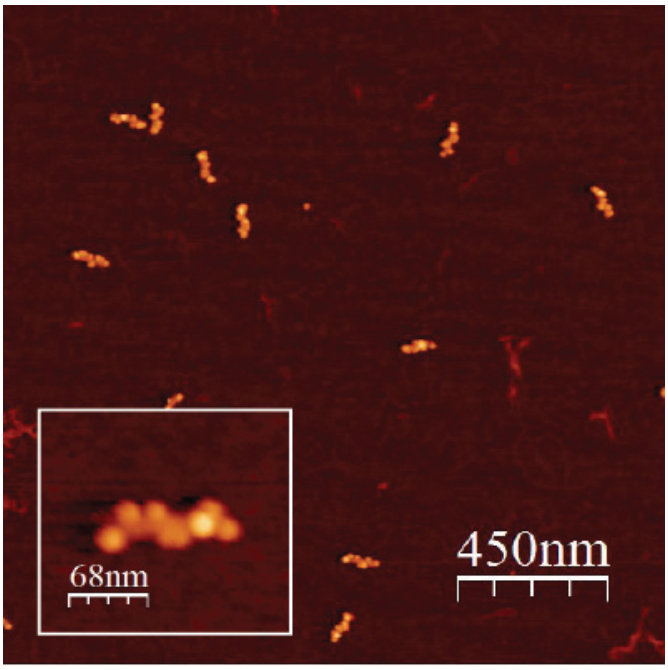

Figure S10.4 | AFM image of left-handed nanohelices on a quartz surface.

SI References

37. Fan, Z. & Govorov, A. O. Plasmonic Circular Dichroism of Chiral Metal Nanoparticle Assemblies. *Nano Lett.* **10**, 2580-2587 (2010).

38. Fan, Z. & Govorov, A. O. Helical Metal Nanoparticle Assemblies with Defects: Plasmonic Chirality and Circular Dichroism. *The Journal of Physical Chemistry C* **115**, 13254-13261 (2011).

39. Fan, Z., Zhang, H. & Govorov, A. O. Optical Properties of Chiral Plasmonic Tetramers: Circular Dichroism and Multipole Effects. *The Journal of Phys. Chem. C* **117**, 14770–14777 (2013).

40. Weber, H. W. & Ford, G. W. Propagation of optical excitations by dipolar interactions in metal nanoparticle chains, *Physical Review B* **70**, 125429 (2004).

41. Zhen, Y. R., Fung, K. H. & Chan, C. T. Collective plasmonic modes in two-dimensional periodic arrays of metal nanoparticles, *Physical Review B* **78**, 035419 (2008).

42. Maier, S. A., Kik, P. G. & Atwater, H. A. Optical pulse propagation in metal nanoparticle chain waveguides, *Physical Review B* **67**, 205402 (2003).

43. Johnson, P. B. & Christy, R.W. Optical Constants of the Noble Metals, *Physical Review B* **6**, 4370-4379 (1972).

44. Klein, W. P. et al. Multi-Scaffold DNA Origami Nanoparticle Waveguides. *Nano Lett.* **13,** 3850–3856 (2013).

Supporting Information

Hierarchical assembly of metal nanoparticles, quantum dots and organic dyes using DNA origami scaffolds

by

Robert Schreiber*, Jaekwon Do*, Eva-Maria Roller, Tao Zhang, Verena J. Schüller, Philipp C. Nickels, Jochen Feldmann, Tim Liedl

*equal contribution

accepted for publication in

Nature Nanotechnology

Supplementary Information

Hierarchical assembly of metal nanoparticles, quantum dots and organic dyes using DNA origami scaffolds

Robert Schreiber[1,*], Jaekwon Do[2,*], Eva-Maria Roller[1], Tao Zhang[1], Verena J. Schüller[1], Philipp C. Nickels[1], Jochen Feldmann[2], Tim Liedl[1,†]

Supplementary Note S1 | Functionalization of AuNP colloids (10 - 80 nm). Concentration of AuNPs. Colloidal AuNPs (100 ml, BBI) of citrated AuNPs of 10 - 80 nm size were stirred for three days at room temperature protected from light after adding 40 mg of BSPP (Bis(*p*-sulfonatophenyl)phenylphosphine dihydrate dipotassium salt, Sigma-Aldrich). To achieve high concentrations of stable nanoparticles in solution, the particles were treated as follows: First, 5 % (v/v) Sodium chloride (5 M) was added to the solution. More sodium chloride was added until a colour change of the solution from red to blue was observed (the charge of the particles is screened by the salt which leads to a decreasing distance between the particles). Next the AuNPs were sedimented to the bottom of a 50 ml tube by centrifugation of the AuNP solution at 1,600 rcf for 30 min at room temperature and the clear supernatant was removed with a pipette immediately (about 1% of the supernatant was left in the tube). The particles were again dissolved in BSPP solution (1.6 ml, 2.5 mM in H_2O) followed by addition of an equal volume of methanol (1.6 ml). This mixture was centrifuged (1,600 rcf, 30 min, room temperature), the supernatant was completely removed and the particles were once more dissolved in BSPP solution (1.6 ml, 2.5 mM in H_2O). The concentration of the AuNPs was estimated by the absorption measured via UV-Vis spectroscopy.

AuNP-DNA conjugation. The AuNPs were conjugated with thiolated ssDNA strands (purchased from biomers.net, HPLC purified) as follows: For reducing the disulfide bonds of the thiolated ssDNA strands (100 µM) to monothiol the modified strands were incubated with TCEP (Tris (carboxyethyl) phosphine hydrochloride, Sigma-Aldrich; 10 mM final concentration) for at least 30 min at room temperature. AuNPs and thiolated oligonucleotides (100 µM, incl. the TCEP) were mixed in 0.5 × TBE buffer at a ratio of 1:300 (AuNPs:DNA) for 10 nm sized AuNPs. We used a higher excess of thiolated DNA for larger AuNPs corresponding to the increased surface of larger AuNPs ($\sim r^2$), e.g. a four times higher excess of DNA over AuNPs (1:1,200) for 20nm sized AuNPs (two times the radius = $2^2 = 4$ times higher excess).

We used the protocol described in reference [1] to avoid 3 days of waiting after mixing the thiol-DNA with AuNPs (as it was previously described in reference [2]) and to achieve higher attachment yields of thiol-DNA to AuNPs. The procedure is the following:

1. add citrate buffer (pH 3) to a final concentration of 20 mM
2. wait 3 minutes
3. add HEPES buffer (pH 7.6) to final concentration of 100 mM

To estimate the yield of the conjugation, a droplet of the DNA-covered AuNPs was mixed with a droplet of 0.5 × TBE buffer with 100 mM $MgCl_2$ (ideally the conjugates should be stable at $MgCl_2$ concentrations of up to 100 mM. We realized that the random sequence CTCTACCACCTACAT is less stable than the 15×T sequence, see comment below). If the colour of the mixed droplet changed from red to blue, more thiolated oligonucleotides had to be added to the AuNP-DNA mixture (this procedure is later called *$MgCl_2$ test*). To remove the unbound thiolated strands and the TCEP, the mixture was centrifuged for 10 min at 10,000 rcf at room temperature in a 100kDa MWCO centrifugal filter (Amicon Ultra, Millipore) followed by 4 additional spinning steps (each 10 min, 10,000 rcf) with 400 µl buffer (0.5 × TBE without $MgCl_2$) added to the centrifugal filter before each centrifugation step. The remaining AuNP-DNA solution was recovered from the Amicon filter with a pipette and transferred to a fresh Amicon filter. This is necessary as we observe decreasing amounts of liquids passing the filters after several centrifugation steps. This might be due to oligonucleotide clusters blocking

the pores of the filter, an effect that we only observe when working with high concentrations of oligonucleotides (~50 μM)). The four filtration steps were repeated once more. In total, the AuNP-DNA solution was centrifuged 8 times. This ensures that as few unbound oligos as possible remain in the solution. Alternatively, agarose gel (0.7 %) purification can be applied to remove remaining unbound oligos (analog to origami structure purification described in reference [2]). The unbound oligonucleotides should be removed immediately before adding the AuNPs to the DNA origami structures. Otherwise newly appearing free oligonucleotides will block the hybridization sites of the DNA origami structure. After the last step the concentration of the AuNPs was determined with a UV-Vis photospectrometer. Ideally, the $MgCl_2$ test as described before should be repeated again at this point to make sure that the conjugation was successful.

Comment on DNA functionalization of AuNPs > 40 nm. We realized that particles which are > 40 nm are only stable for a short time (< 1 day) at the standard $MgCl_2$ concentrations of 10 mM without the surrounding origami structures. The DNA origami structures function as stabilizers for large AuNPs (> 40 nm) and the constructs stayed in solution for many weeks (sedimented constructs can always be re-suspended by gentle shaking).

Functionalization of silver nanoparticle colloids (20 nm). The silver nanoparticle (AgNP) preparation followed with minor changes the protocol described in reference [3]. The 20 nm silver colloid solution (Sigma-Aldrich) was concentrated by using 100 kDa MWCO centrifugal filter (Amicon Ultra, Millipore) (8,000 rcf, 10min, room temperature). Thiolated ssDNA strands (biomers.net, HPLC purified) were added to the concentrated AgNP solution at a ratio of 1:1200 (AgNPs:DNA). Therefore the concentration of the AgNPs had to be estimated via UV-Vis spectroscopy (extinction coefficient 7.1×10^8, typical result was about 90 nM). Next citrate-HCl buffer (pH 3) was added to a concentration of 5 mM. After 5 min more citrate-HCl buffer was added to a final concentration of 10 mM. After incubation for 25 min NaCl was added to a final concentration of 30 mM. Then the pH was raised by adding HEPES buffer (pH 7.6) to a final concentration of 100 mM. The unbound ssDNA strands were removed via centrifuging the solution for 8 min at 6,000 rcf using a 100 kDa MWCO centrifugal filter (Amicon Ultra, Millipore).. This step was repeated 7 times with a filter change after 4 spinning steps. Before each centrifugation step 450 μl of buffer (1 × TBE, 350 mM NaCl) were added to the centrifugal filter. Afterwards the oligonucleotide covered AgNPs were conjugated the DNA origami structure. The ratio of AgNPs per DNA origami structure was 5:1. The solution was left overnight on a shaker for incubation and then the satellite-bearing DNA origami structures were purified from free AgNP as described for AuNPs below in Supplementary Note S2.

Comment on the DNA hybridization yield between DNA functionalized metal nanoparticles and DNA origami structures depending on the DNA sequence. We realized that the hybridization of the multiple T sequence to its complementary sequence is more efficient compared to the hybridization of the random sequence to its complement. This is probably due to two effects: First, the hybridization of the multiple T sequence to its complement allows the bases to slide against each other, which thus allows the strands to catch each other on the very ends of the ssDNA and then zip closer together. Second (as already shown by Storhoff et al. [4]) the A and C bases in the random sequence tend to stick to the gold surface which might cause this ssDNA to not stand that well apart from the surface of the metal nanoparticle as the multiple T

sequence. To achieve high hybridization yields for the random sequence we chose a relative long sequence of 15 bases for our attachment site (note: our attachment sites always consist of minimum 3 ssDNA strands). We observed that for the multiple T sequence and its complement already a sequence of 8 bases is sufficient to ensure the same hybridization yield as for 15 random bases.

Functionalization of QD colloids. Materials: Quantum dots which have emission maxima of ~800 nm (QD800) were purchased from Invitrogen. Phosphorothioate modified DNA (PTO-DNA, sequence: cgg gcg tac TTT TTT TTT, upper case for phosphodiester bases and lower case for PTO bases, HPLC purified) was purchased from MWG Eurofins Operon. Zinc nitrate hydrate, 3-Mercaptopropionic acid (MPA) and Sodium hydroxide were obtained from Sigma Aldrich.

Methods: DNA modified QDs were prepared by attaching PTO-DNA to the freshly grown ZnS shell in the presence of the growing materials including Zn^{2+} and MPA (described in reference [5][6][7]). In a typical experiment, 100 µL QD800 (1 µM) were flocculated from Decane and re-dispersed in chloroform (10 nM, protocol from Invitrogen.com). After a ligand exchange via MPA, 100 µL MPA-QDs (10 nM) were added to 176 µL H_2O followed by adding 20 µL PTO-DNA (100 µM), 2.25 µL Zn^{2+} (50 mM), 4.5 µL MPA (50 mM) and 8 µL NaOH (1 M). The mixture was incubated at 90 °C for 40 min. PTO-DNA modified QD800 were then purified from remaining unbound PTO-DNA by using 100 kDa MWCO centrifugal filters (Amicon Ultra, Millipore) (2x4 centrifugation steps with a filter change after 4 steps, the filter was refilled with 450µl water after each step, 10,000 rcf, 10 min, at room temperature).

Functionalization of streptavidin coated QD colloids. Materials: Streptavidin coated quantum dots with emission maxima of ~800 nm (QD800) were bought from Invitrogen. Biotin modified ssDNA oligos (HPLC purified) were bought from MWG Eurofins Operon.

Methods: The streptavidin coated quantum dots were incubated with biotin modified ssDNA oligos in a ratio of 1:100 (QD:ssDNA) in 1x PBS (pH 7.4) over 12 hours. The DNA modified QD800 were then purified from remaining unbound ssDNA by using 100 kDa MWCO centrifugal filters (Amicon Ultra, Millipore) (2x4 centrifugation steps with a filter change after 4 steps, the filter was refilled with 450µl 1x PBS (pH 7.4) after each step, 10,000 rcf, 10 min, at room temperature).

Supplementary Note S2 | Purification of the satellite-bearing DNA origami structures from free AuNPs by gel electrophoresis. To separate the AuNP-bearing DNA origami structures from the AuNP excess a second agarose gel purification step was applied. The samples were electrophoresed on a 1.0 % agarose gel containing 0.5 × TBE and 11 mM $MgCl_2$ cooled in an ice water bath. The satellite-bearing DNA origami structures showed a narrow band migrating slower than single AuNPs. If the band was too faint to be detected by eye, SYBR® Gold (Invitrogen) staining was used. We cut out the bands of satellite-bearing DNA origami structures and centrifuged the piece of gel at 2,600 rcf for 10 min at 4°C in Freeze`N'Squeeze spin columns (BioRad) and kept the flow through for the further experiments. (cf. text in main manuscript)

Supplementary Note S3 | Excess of satellites (MeNP-bearing origami structures) over planets.

planet	ratio (planet:satellite)
10nm AuNP	1:20
20nm AuNP	1:200
40nm AuNP	1:500
80nm AuNP	1:1,000
tube origami	1:200

Supplementary Note S4 | Low-magnification SEM images of nanoclusters. After assembly, the nanoclusters are well dispersed in solution. Here, SEM wide field images of gold-enhanced nanoclusters exposed to enhancement solution for varying times (as indicated in the bottom left of each image) are shown. "Gold Enhancement" (or electroless ion deposition) protocols are given in SI Note S14.

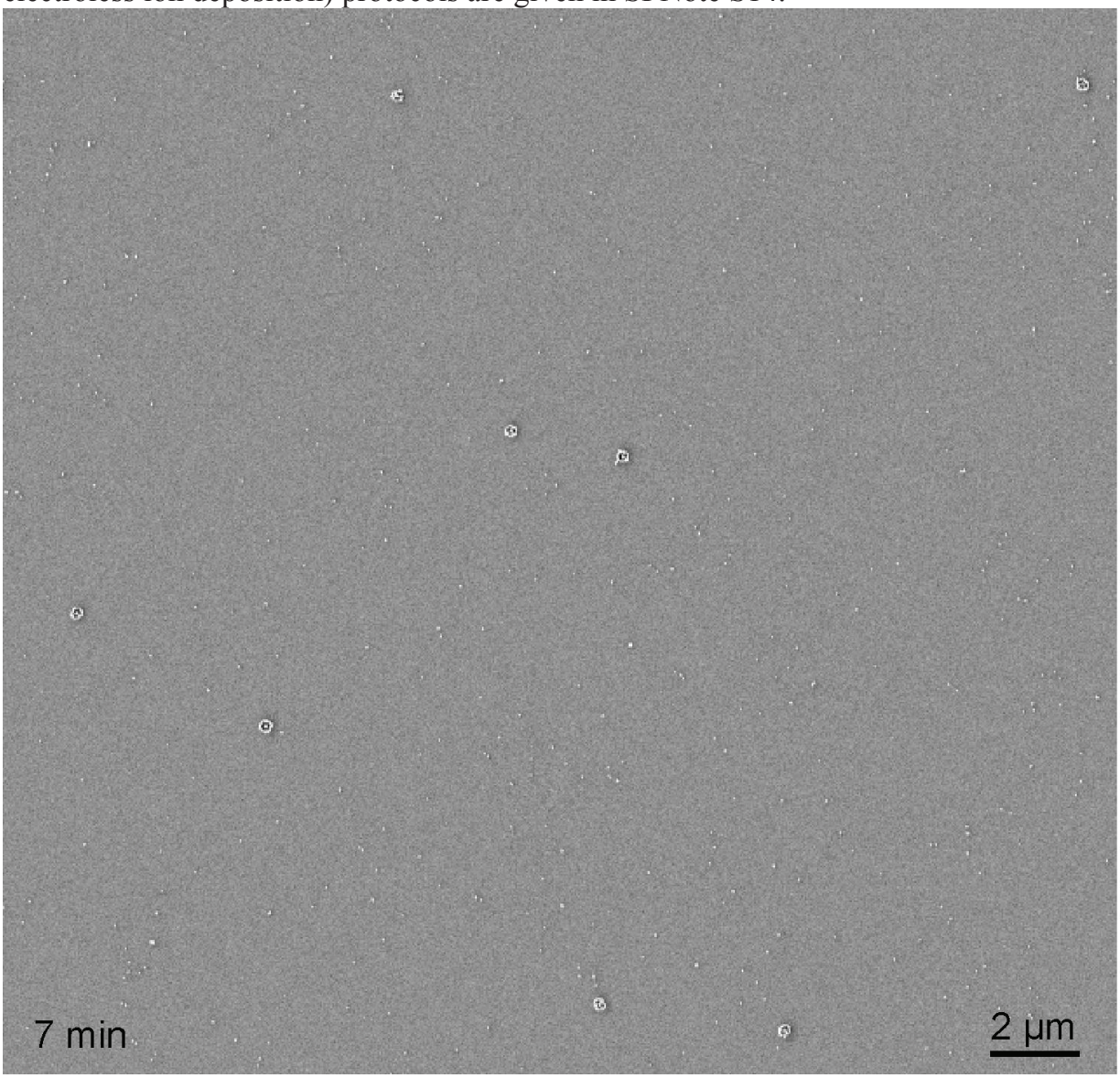

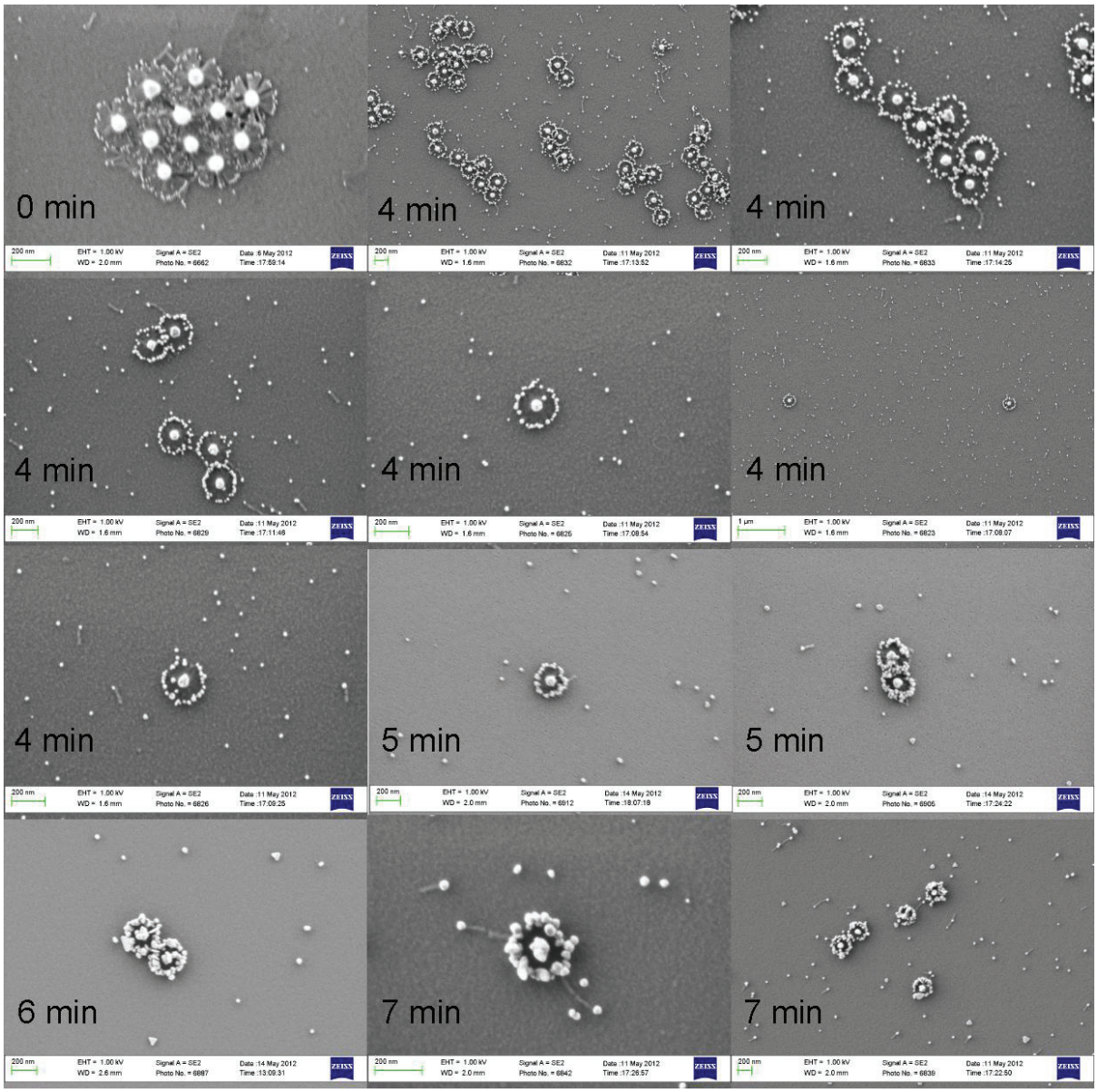
0 min
4 min
4 min
4 min
4 min
4 min
4 min
5 min
5 min
6 min
7 min
7 min

Supplementary Note S5 | Long-term stability. The origami nanoclusters were stored at - 18 °C in the fridge for eight months. Here nanoclusters with 10 nm AuNP satellites, 24 helix-bundle DNA origami structures and 60 nm AuNP planets are shown. The nanoclusters show high stability over time as well as, however, a tendency to aggregate.

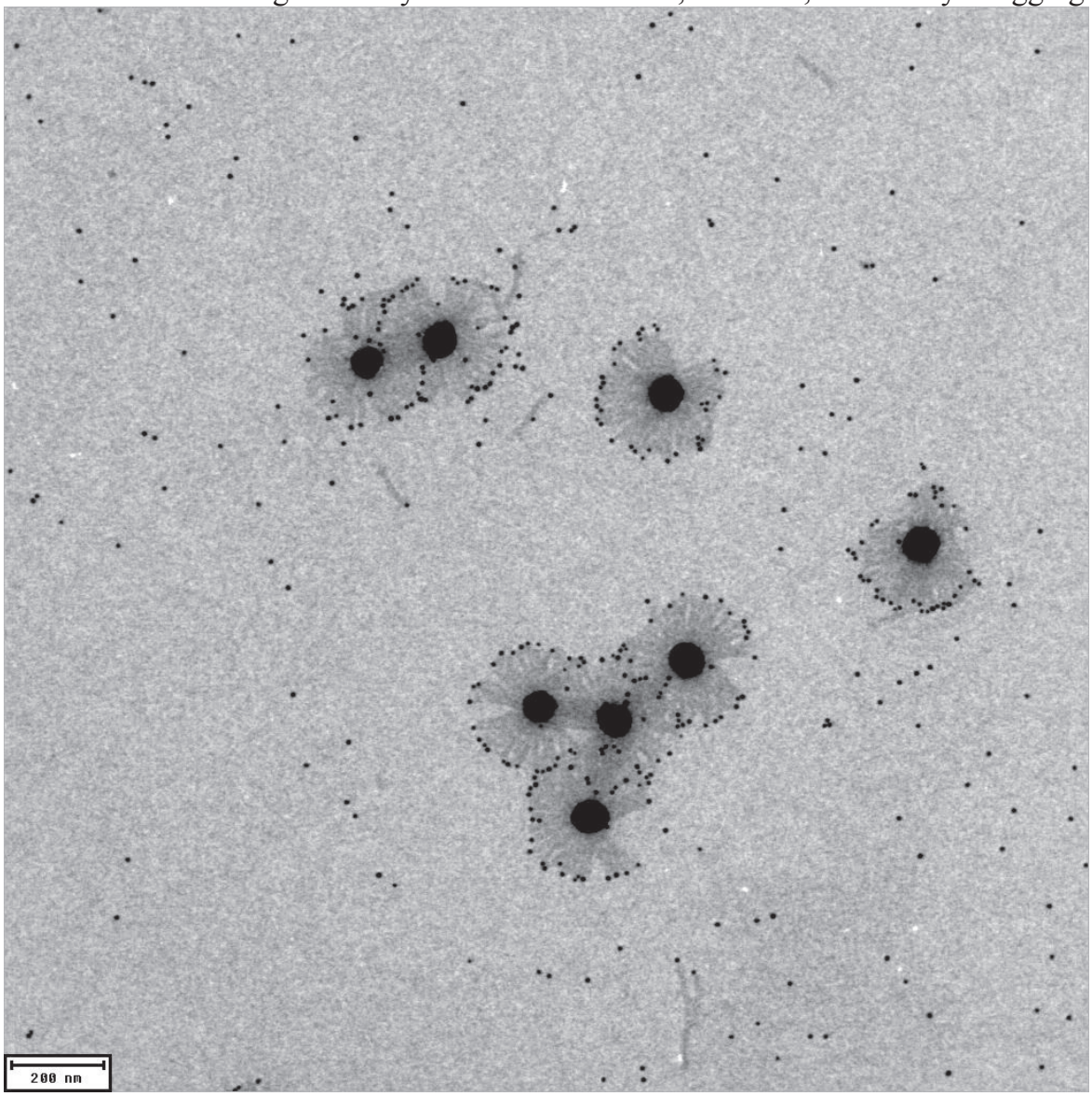

Supplementary Note S6 | Chiral nanocluster assemblies. Right-handed nanohelices (R-NHs) were attached to an 80 nm AuNP planet. Schematic and TEM images of non-enhanced R-NH-Nanoclusters. Left: TEM image of chiral nanocluster with large excess of right handed nanohelices (1:100). Right: TEM image of chiral nanocluster with a low excess of right handed nanohelices (1:10).

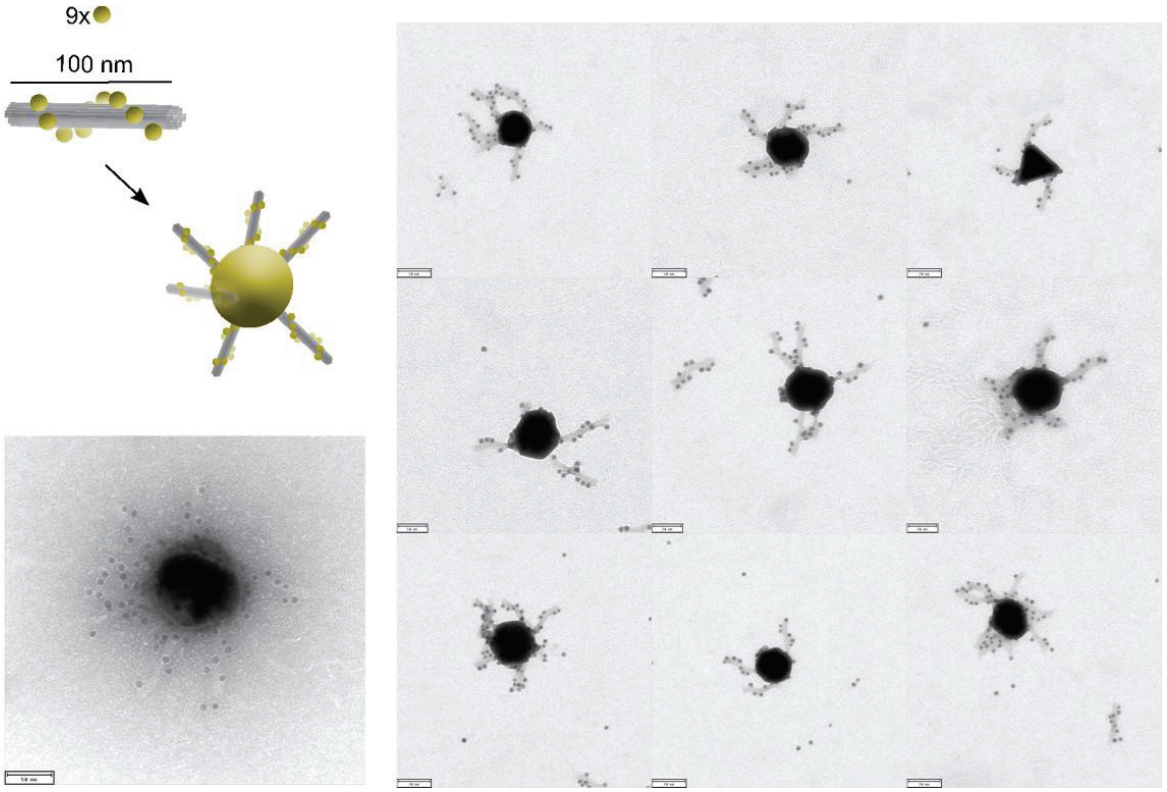

Supplementary Note S7 | Circular dichroism of chiral nanoclusters. The chiral nanoclusters presented in Figure S8 were silver-enhanced in solution. "Silver Enhancement" (or electroless ion deposition) protocols are given in SI Note S14. Top: The structures show strong circular dichroism (CD) in the visible range. Control samples (blue curve, right-handed nanohelices without planet particles) were present at the same concentration as the nanocluster-assembled super-structures (red curve). The chirality of the nanohelices is preserved in the nanocluster assembly and we speculate that the proximity of the helices to the large planet particle is responsible for the increased CD signal. Bottom: TEM images of the silver-enhanced chiral nanoclusters.

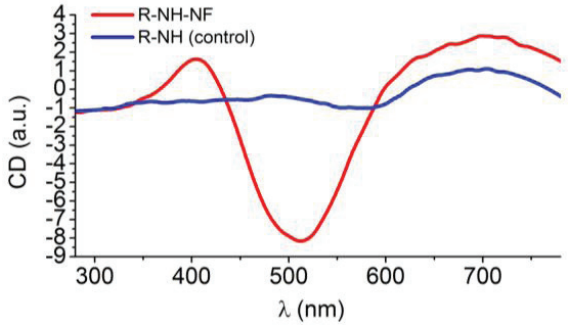

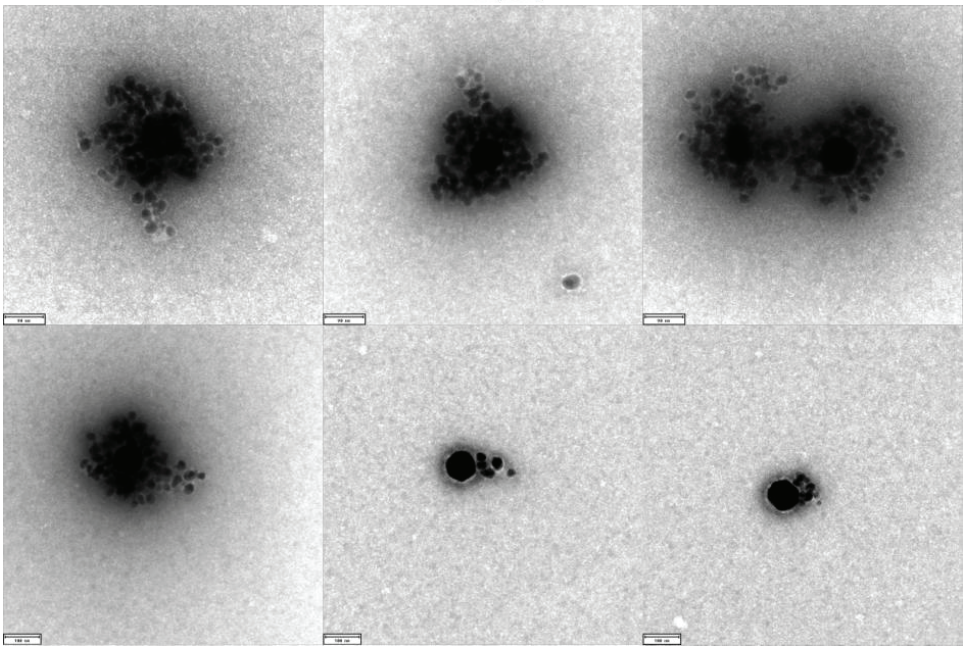

Supplementary Note S8 | Photoluminescence spectroscopy of dye-QD origami nanoclusters. In order to observe feeding of fluorescence energy to a central acceptor, we placed organic dyes (Cy3) along the radial spokes that were attached to a central colloidal quantum dot. Thorough studies on resonance energy transfer through spectral ladders of dye molecules have presented by other groups [8][9]. We therefore decided to test an approach based on QD acceptors. Our results are ambiguous and reflect the principal difficulties that QDs pose as acceptor molecules for photons donated by

organic dyes, which are i) their property to convert light of any wavelength shorter than their emission wavelength into emitted photons and ii) their large absorption cross section compared to organic dye molecules. Taken together, we observe in our experiments increased QD800 luminescence signals over control signals under certain conditions, but the effect becomes marginal when the control experiments are executed extremely careful. Future experiments will include assemblies with donor dyes arranged as a spectral ladder, gold nanorods as field enhancers or QDs as donor elements.

Figure to supplementary Note S8 | Dye-QD origami nanoclusters. a, Schematic and **b**, TEM image of an origami nanocluster consisting of a QD800 planet and 24-helix bundles decorated with 20 dyes (Cy3). **c-e**, QDs with two functionalization methods were tested: Streptavidin-functionalized (**c**) and direct DNA functionalization (**d** and **e**). Photoluminescence spectra were recorded for assembled nanoclusters with QDs and dyes, QDs only (either with Streptavidin-coating or ssDNA-coating, **c** and **d**) and with QDs assembled with 24-helix bundles without attached dyes (**e**).The concentrations were carefully adjusted, however, we noted that the concentration of QDs without attached 24-helix bundles decreased over the course of the experiments (possibly due to adsorption to the walls of the sample container) which probably leads to the relatively lower signals of the control samples in **c** and **d**.

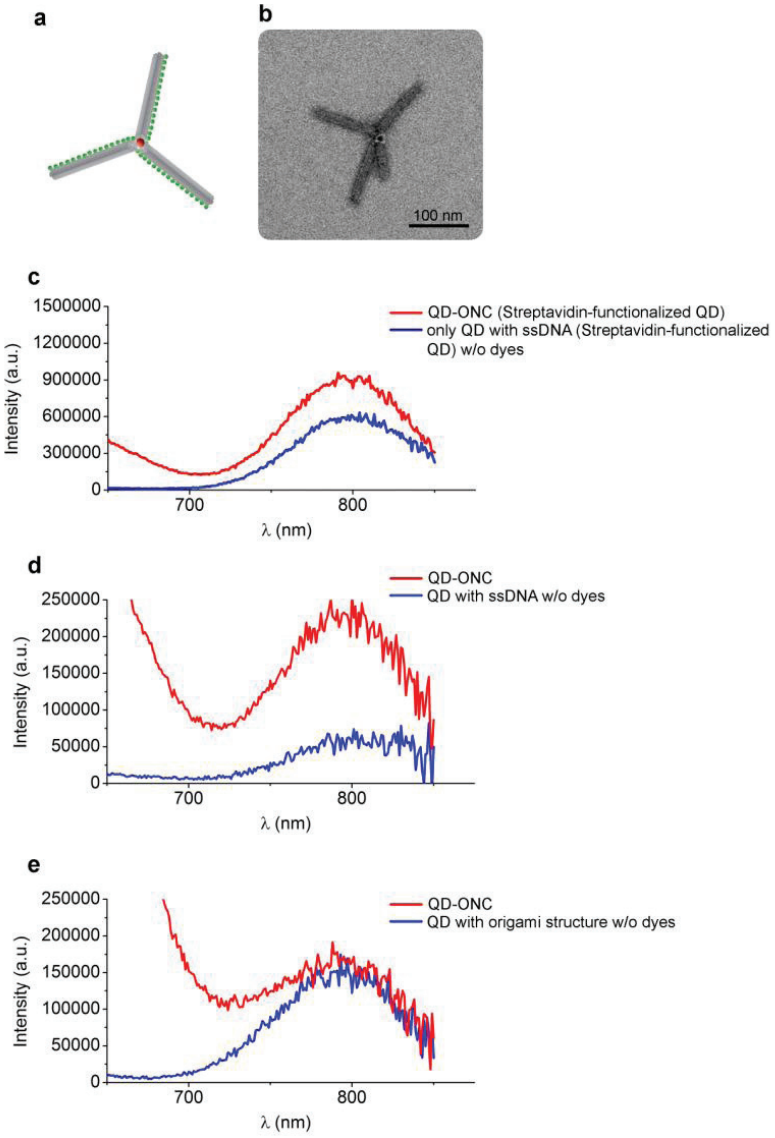

Supplementary Note S9 | Three-dimensional structure of nanoclusters revealed by TEM. 20 µL of gel purified nanoclusters in 0.5 × TBE and 11 mM $MgCl_2$ were deposited on a TEM grid and completely dried via evaporation. We assume that the nanoclusters are embedded in the remaining salt, which supports and stabilizes the three-dimensional structure. The TEM grid was shortly (20s) stained with Uranyl acetate. In the microscope, the TEM specimen stage was tilted over a range of 50° and images were taken every 25°. Two examples are shown in the upper and the lower row. Identical satellites are marked with arrows of the same colour in each image to show the three-dimensional character of nanoclusters.

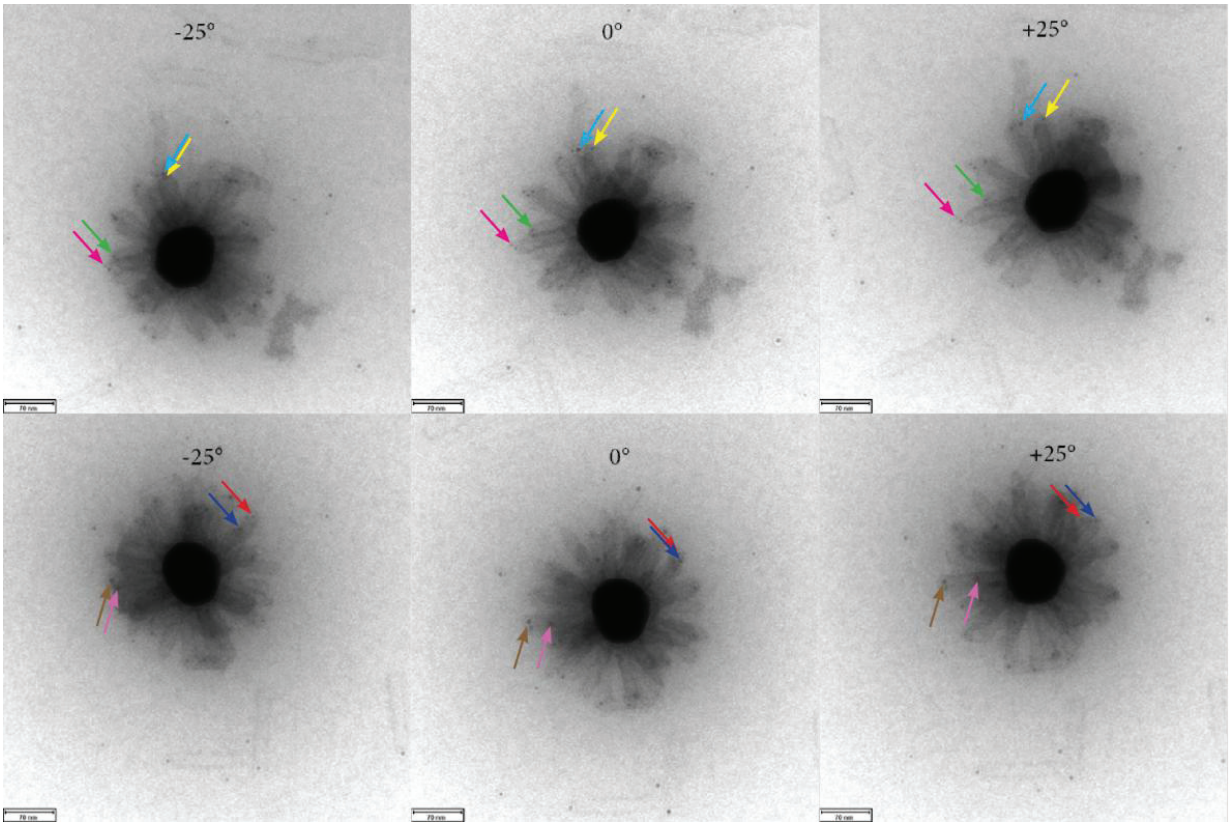

Supplementary Note S10 | Dynamic light scattering (DLS) measurements: Hydrodynamic size of the origami nanocluster as a function of temperature. Origami nanoclusters with 80 nm gold planet and 24-helix bundles assembled in 0.5xTBE+11mM $MgCl_2$. The expected diameter of the nanocluster is ~ 280 nm at room temperature. We observe a diameter of 255 nm at RT (black squares). At temperatures above 55°C the measured diameter drops dramatically to the level of the 80 nm gold particle control (red squares). This nicely indicates the disassembly of the nanoclusters at temperatures above 55°C.

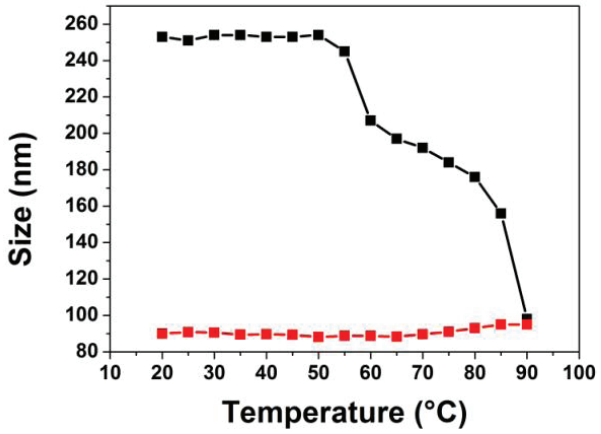

Supplementary Note S11 | DLS measurements: Hydrodynamic size of origami nanocluster as function of NaCl concentration. Origami nanoclusters with 80 nm gold planets and 24 helix bundles assembled in 0.5xTBE+11mM $MgCl_2$ and the following NaCl concentrations: 0 mM, 20 mM, 50 mM, 100 mM and 500 mM. Higher NaCl concentrations permit closer packing of the DNA origami structures on the planet particles, which is reflected in a slightly increased hydrodynamic diameter at higher NaCl concentrations. TEM inspection confirms this assumption (see next comment). Note, that the error bars are of the size of the data point squares.

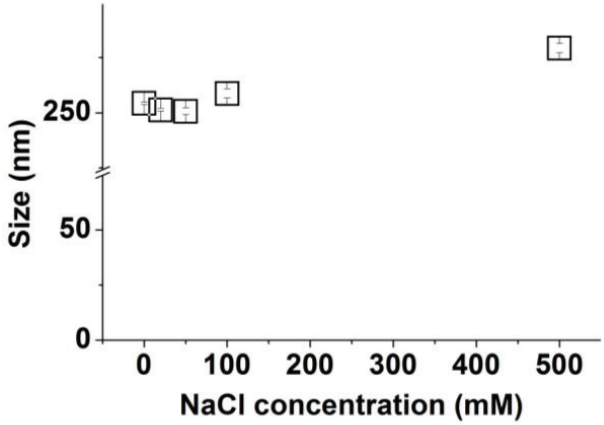

DLS measurements: Hydrodynamic size measurements were performed in a Zetasizer Nano ZS (Malvern Instruments, Malvern UK). Particle diffusion in a small volume cuvette (45 µl) was measured with a 4 mW He-Ne laser operating at 633 nm and at a detection angle of 173°.

Supplementary Note S12 | Planet-satellite stochiometry control by varying NaCl concentration. Origami nanoclusters with 80 nm gold planet and 24-helix bundles assembled in 0.5xTBE+11mM $MgCl_2$+ varying NaCl concentration. Top: Number of satellites per planet as a function of the NaCl concentration. Bottom: Representative TEM images for each salt concentration. A change in salt concentration leads to a change of the electrostatic repulsion between the single DNA origami structures attached to a planet AuNP. Higher salt concentrations also result in higher non-specific attachment of satellite-bearing origami structures. Non-specifically attached structures were not included in the statistics.

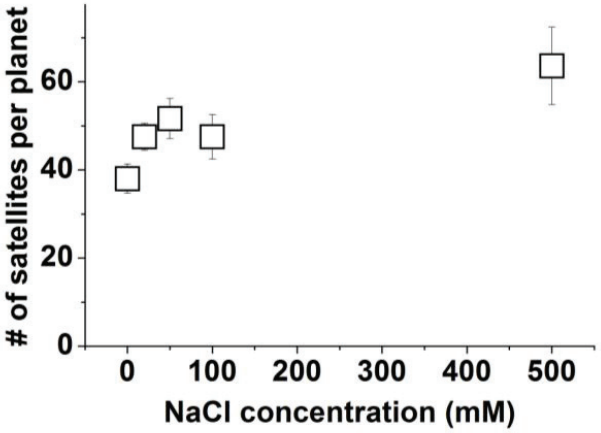

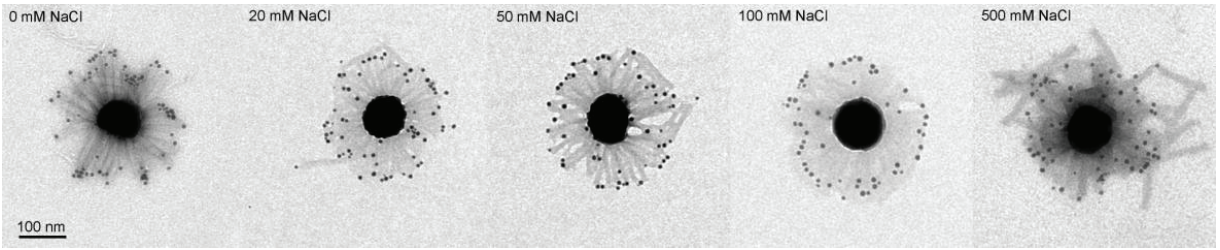

Supplementary Note S13 | Origami-structure-guided arrangement of satellites. The tubular origami structure [10] consists of 30 anti-parallel helices forming a hollow open barrel and offers 62 protruding ssDNA handles (15×T) on its outside for the hybridization of AuNP bearing 24 helix bundle DNA origami structures which offer 12 ssDNA handles (15xA) for the conjugation. **a**, Schematic drawing of the origami-structure-guided arrangement of satellites. **b**, TEM images. **c**, Schematic and **d**, CaDNAno [11] file of the origami planet with handle positions for the attachment of the 24 helix bundle marked in red.

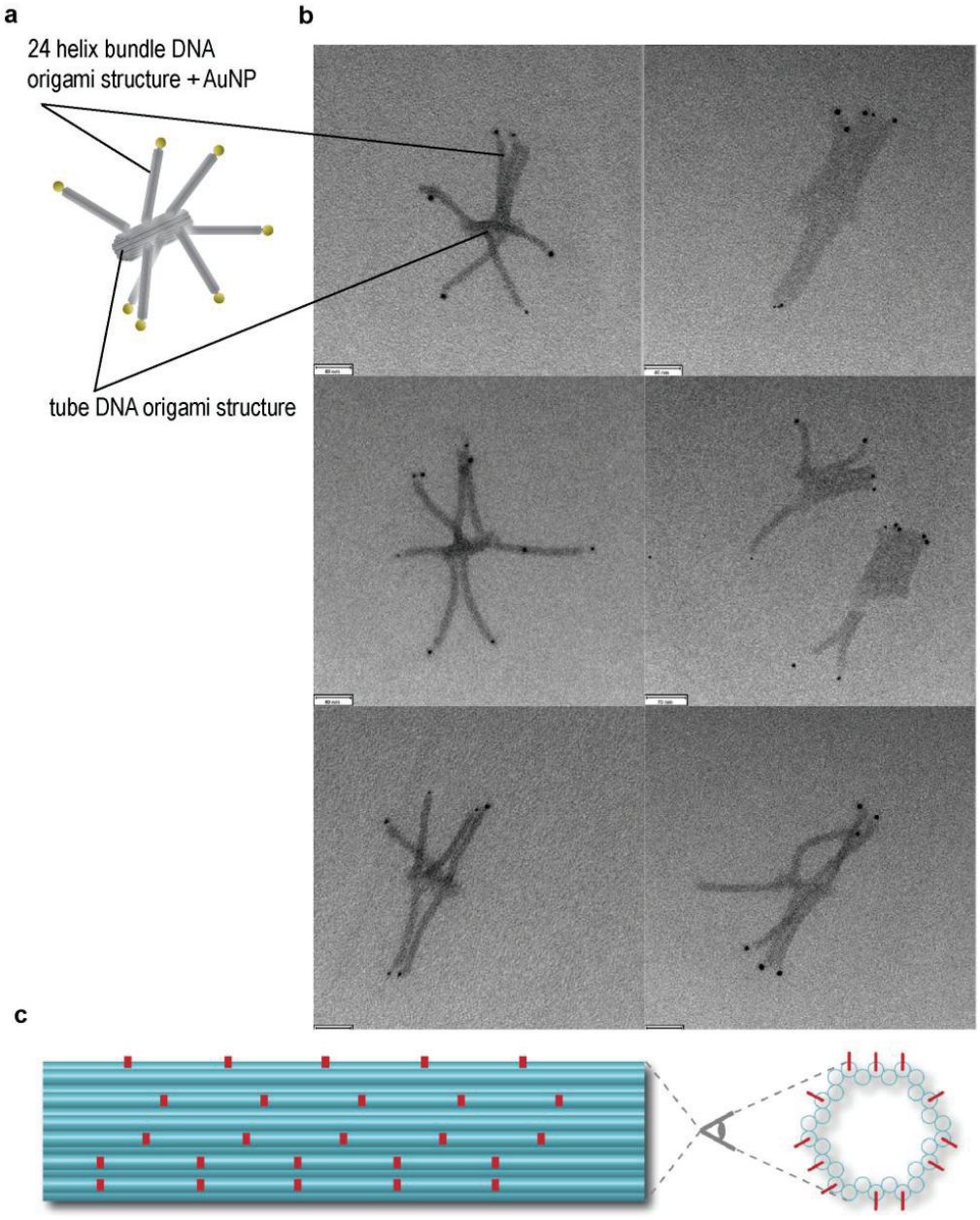

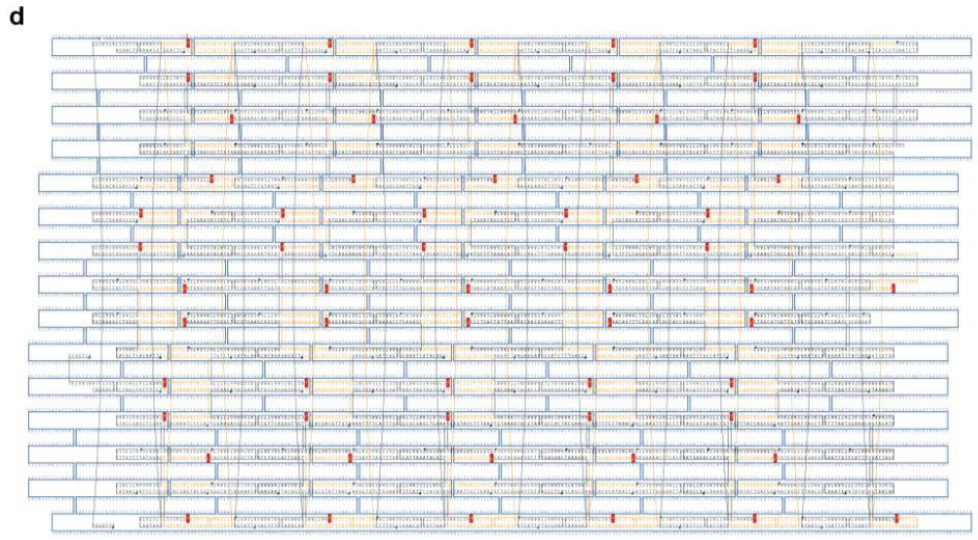

Supplementary Note S14 | Silver and gold deposition on the gold nanoparticles of the planet-satellite nanoclusters. We generally follow the instructions of the supplier (HQ Silver Enhancement Kit and EM Gold Enhancement Kit from nanoprobes.com). The procedure is also described in detail in Kuzyk et al. [2] and Schreiber et al. [12]. In short, equal amounts of the reaction solutions A, B and C of the enhancement kit were mixed together. The planet-satellite nanoclusters were exposed to this mixture either on surfaces or in solution.

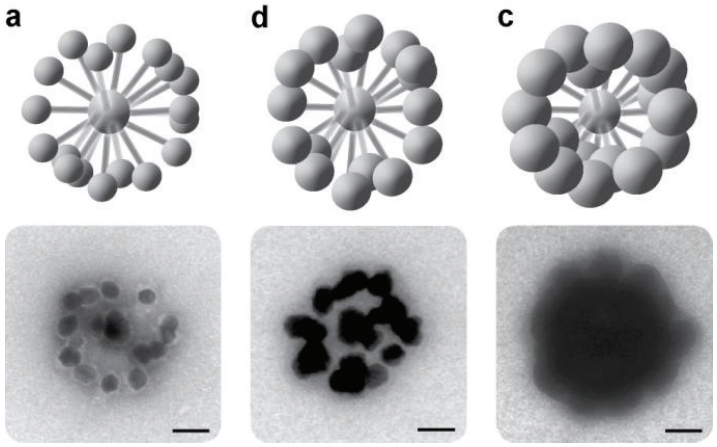

Figure to Supplementary Note S14 | Silver enhancement in solution. Silver enhanced nanoclusters. Nanoclusters consisting of 24 helix-bundles, 10 nm AuNP satellites and 60 nm AuNP planets were used. The nanoclusters were exposed to SilverEnhance^{TM} formulation (Nanoprobes.com) in solution. Top: schematic drawing of the nanoclusters; Bottom: TEM images of the nanoclusters. The silver enhancement was performed in 0.5x TBE + 11 mM $MgCl_2$ buffer containing 30 % in **a**, 40 % in **b** and 50 % in **c** of the enhancement kit. Scale bars: 100 nm.

Supplementary Note S15 | Silver enhanced nanoclusters visualized with bright field microscopy. Far left: Bright field microscopy image of a nanocluster. The nanocluster is visible as a diffraction-limited dot (red arrow). Second left to far right: Zoom-in series of the identical sample area investigated with TEM. It becomes apparent, that only the large nanocluster gives enough contrast to be distinguishable in the bright field image.

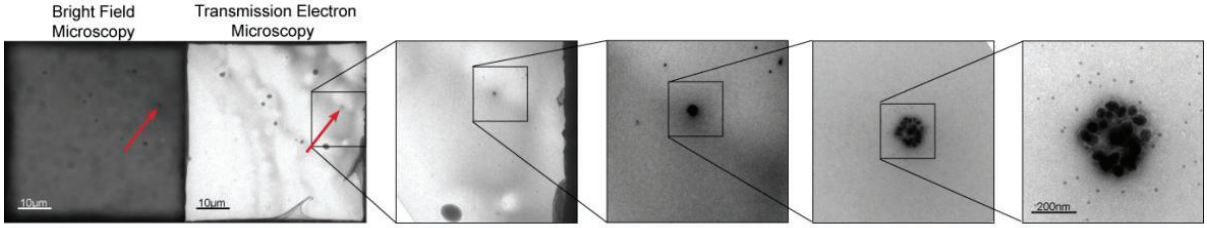

Supplementary Note S16 | DNA hybridization after metal growth in solution. In these experiments, DNA origami structures with AuNP satellites were silver-enhanced in solution before they were mixed with the DNA-covered 80 nm AuNP planet. Although this process only resulted in low yields of hybrid nanoclusters (gold-silver core-shell satellites and gold planets) the experiments demonstrate that hybridization of complementary DNA strands is still possible after the satellite-bearing DNA structures experienced a metallization procedure.

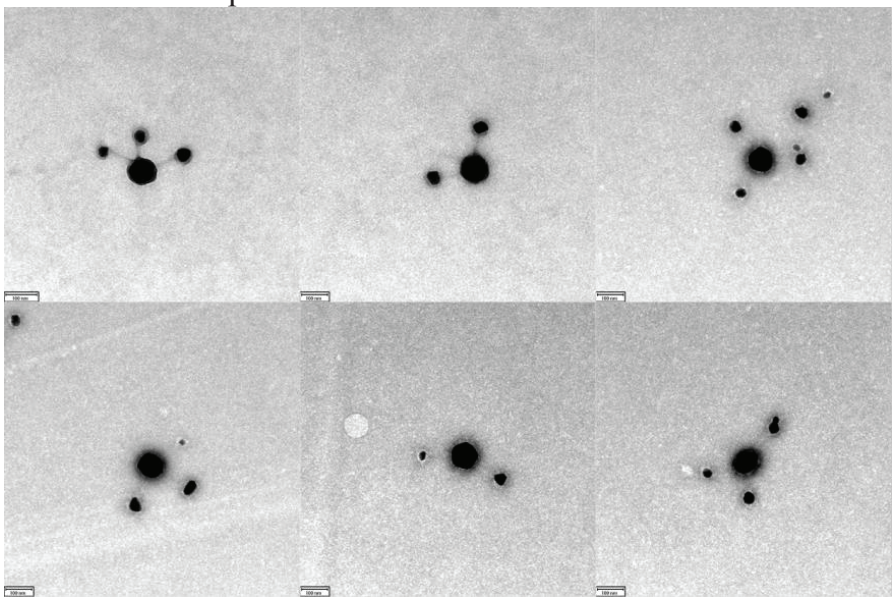

Supplementary Note S17 | AuNP-induced Quenching of Cy5. Cy5 dyes were placed in rings of 4 dyes around the 24-helix bundle as illustrated in the caDNAno [11] diagram below. Note that the distance of the dyes closest to the AuNP surface is already denoted as 5 nm. This results from the fact, that the ssDNA covering the AuNPs is 4 nucleotides longer than the complementary strand sticking out of the origami structure (not shown in the diagram). Additionally, a C6-linker is connecting the thiol groups with the nucleotides. These spacers account for ~ 2 nm distance. Further, the dyes are positioned on the outer helices of the 24-helix bundle, which itself has a diameter of ~ 20 nm. This in turn leads to a geometrically-reasoned additional dye-AuNP distance of ~ 3 nm.

For the fit presented in Figure 5c of the article, we subtracted a threshold of the measured fluorescence values. The intensity of the closest ring of dyes (5 nm distance to the AuNP surface) drops to 62 % of the control value, recorded from 24-helix bundles that are carrying dyes but are not attached to AuNPs. We attribute the incomplete quenching to dye molecules that could have detached from the structures after purification (note that there is always a finite off-rate and that the on-rate is extremely reduced at low concentrations after purification) and are present as background signal. Additionally, we have observed previously that the single-stranded scaffold loops at the ends of DNA origami constructs tend to attract single-stranded DNA unspecifically. These dyes also contribute to the background signal and would not be quenched. In this respect, single-molecule experiments give a distinct advantage as all unquenched dyes can be disregarded. However, it is remarkable that with the simple methods used here (bulk fluorescence detection) meaningful results can be obtained. The versatility of our system further allows in principle the examination of many different dye molecules and central particle sizes at low costs and efforts, as always only the dye molecule of interest with one DNA sequence complementary to the docking sites needs to be purchased.

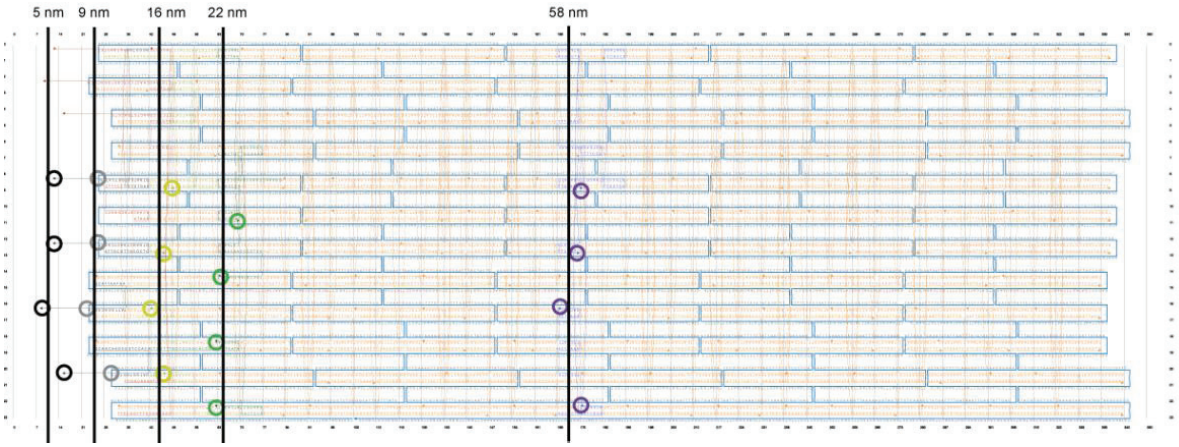

Supplementary Note S18 | Absorption measurements of origami nanoclusters. The absorption measurement of planet-satellite systems with 24-helix bundle as a linker between a 80 nm gold planet and 10 nm satellites shows the DNA absorption peak of the origami structures at 260 nm and the absorption peak of the gold planet at ~550 nm.

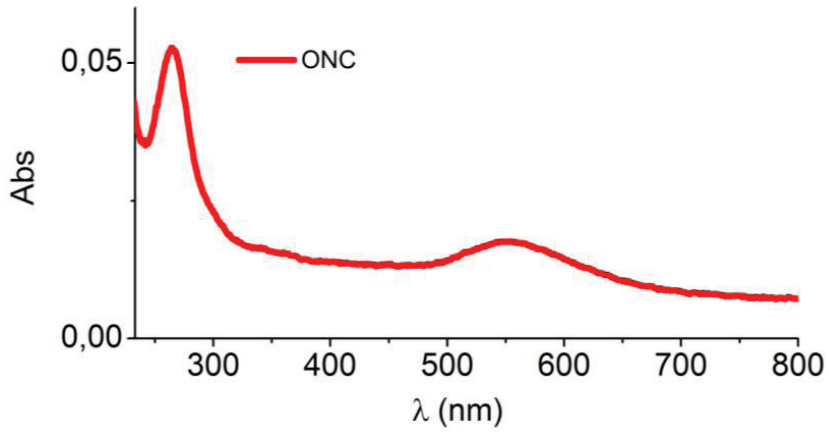

Supplementary Note S19 | Additional TEM images of Au-QD planet origami nanoclusters.

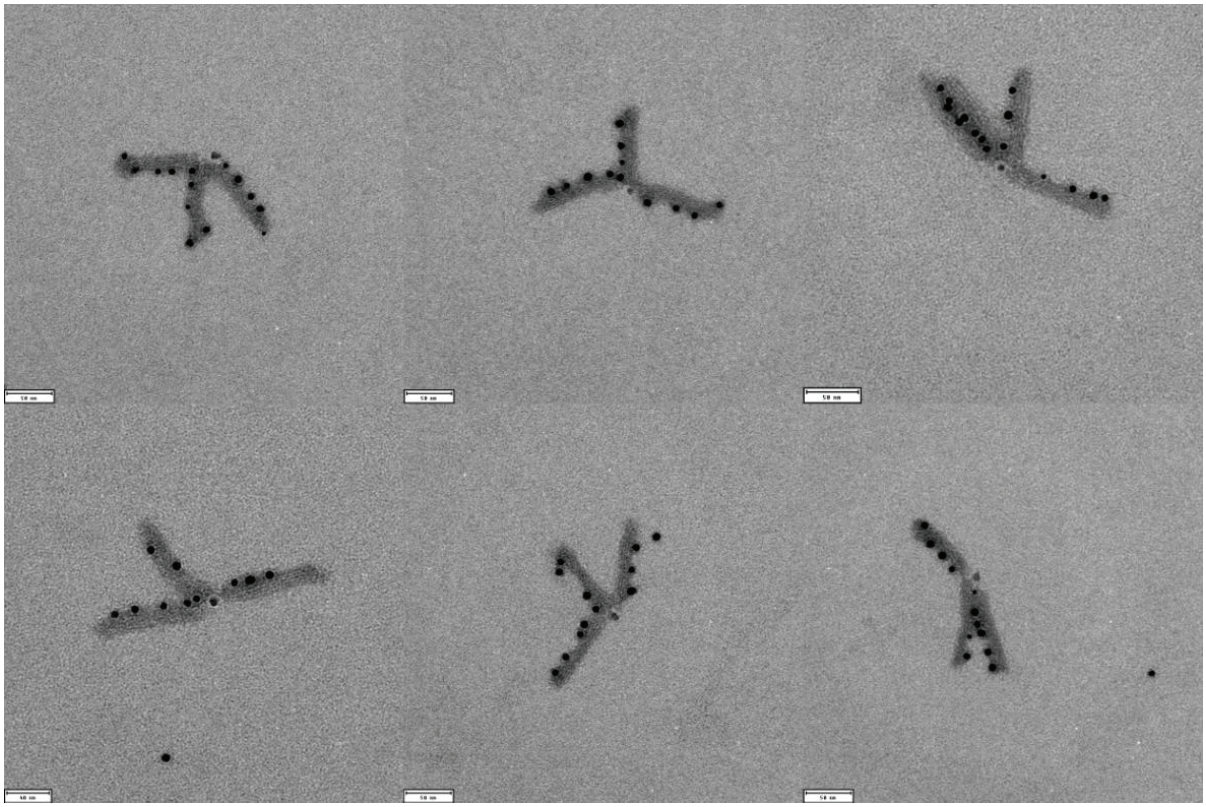

SI References

[1] Zhang, X., Servos, M. R. & Liu, J. Fast pH-assisted functionalization of silver nanoparticles with monothiolated DNA *Chem. Commun.* **48**, 10114 – 10116 (2012).

[2] Kuzyk, A. *et al*. DNA-based self-assembly of chiral plasmonic nanostructures with tailored optical response. *Nature* **483**, 311-314 (2012).

[3] Pal, S. Deng, Z. Ding, B. Yan, H. & Liu, Y. DNA-Origami-Directed Self-Assembly of Discrete Silver-Nanoparticle Architectures. *Angew. Chem. Int. Ed.* **49,** 2700-2704 (2010).

[4] Storhoff, J. J., Elghanian , R., Mirkin , C. A. & Leitsinger, R. L. Sequence Dependent Stability of DNA-Modified Gold Nanoparticles. *Langmuir* **18**, 6666-6670 (2002).

[5] Ma, N., Sargent, E. H. & Kelley, S. O. One-step DNA-programmed growth of luminescent and biofunctionalized nanocrystals. *Nature Nanotech.* **4**, 121-126 (2009).

[6] Ma, N., Tikhomirov, G. & Kelley, S. O. Nucleic Acid-Passivated Semiconductor Nanocrystals: Biomolecular Templating of Form and Function. *Acc. Chem. Res.* **43**, 173-180 (2010).

[7] Deng, Z., Samanta, A., Nangreave, J., Yan, H. & Liu, Y. Robust DNA-Functionalized Core/Shell Quantum Dots with Fluorescent Emission Spannig from UV-vis to Near-IR and Compatible with DNA-Directed Self-Assembly. *J. Am. Chem. Soc.* **134**, 17424-17427 (2012).

[8]Stein, I. H., Steinhauer, C. & Tinnefeld, P. Single-Molecule Four-Color FRET Visualizes Energy-Transfer Paths on DNA Origami. *J. Am. Chem. Soc.* **133**, 4193-4195 (2011).

[9] Dutta, P. K., Varghese, R., Nangreave, J., Lin, S., Yan, H. & Liu, Y. DNA-Directed Artificial Light-Harvesting Antenna. *J. Am. Chem. Soc.* **133**, 11985-11993 (2011).

[10] Schüller, V. J. *et al.* Cellular Immunostimulation by CpG-Sequence-Coated DNA Origami Structures. *ACS Nano* **5**, 9696-9702 (2011).

[11] Douglas, S. M., Marblestone, A. H., Teerapittayanon, S., Vazquez, A., Church,G. M. & Shih, W. M. Rapid prototyping of 3D DNA--origami shapes with caDNAno. *Nucleic Acids Research* **37**, 15 (2009).

[12] Schreiber, R. *et al.* DNA origami-templated growth of arbitrarily shaped metal nanoparticles. *Small* **7**, 1795-1799 (2011).

List of publications (peer-reviewed journals)

P. Kühler, R. Schreiber, E. Roller, T. Liedl[#], T. Lohmüller[#], J. Feldmann.
Plasmonic DNA-Origami Nanoantennas for Surface Enhanced Raman Spectroscopy.
Nature Communications, in review process
[#]Corresponding authors

R. Schreiber, N. Luong, Z. Fan, A. Kuzyk, P. Nickels, D. M. Smith, B. Yurke, W. Kuang, A. O. Govorov, T. Liedl.
Chiral plasmonic material with switchable circular dichroism.
Nature Communications, in revision process

R. Schreiber*, J. Do*, E. Roller, T. Zhang, V. J. Schüller, P. C. Nickels, J. Feldmann, T. Liedl.
Hierarchical assembly of metal nanoparticles, quantum dots and organic dyes using DNA origami scaffolds.
Nature Nanotechnology, accepted
*These authors contributed equally to this work

A. Kuzyk*, R. Schreiber*, Z. Fan, G. Pardatscher, E. Roller, A. Högele, F. C. Simmel, A. O. Govorov, T. Liedl.
DNA-based self-assembly of chiral plasmonic nanostructures with tailored optical response.
Nature 483, 311-314 (2012)
*These authors contributed equally to this work

R. Schreiber, S. Kempter, S. Holler, V. Schüller, D. Schiffels, S. S. Simmel, P. C. Nickels, T. Liedl.
DNA Origami-Templated Growth of Arbitrarily Shaped Metal Nanoparticles.
Small 7, 1795-1799 (2011)

Acknowledgement

I would like to thank the following people for their effort, support and great influence on my thesis:

Prof. Tim Liedl
Prof. Alexander Högele
Prof. Joachim O. Rädler
Prof. Alexander O. Govorov
Prof. Wan Kuang
Prof. Bernard Yurke
Prof. William B. Knowlton
Prof. Friedrich C. Simmel
Prof. Dieter Braun
Dr. Na Liu
Dr. Guillermo Acuna
Dr. Anton Kuzyk
Dr. Susanne Kempter
Dr. Dave M. Smith
Dr. Yongzheng Xing
Dr. Theobald Lohmüller
Dr. Philipp Paulitschke
Verena Schüller
Ingo Stein
Philipp Nickels
Stephanie Simmel
Marc Ablay
Daniel Schiffels
Eva-Maria Roller
Stefan Holler
Philip Böhm
Johanna Schappert
Susanne Rappl
Tao Zhang
Margarete Meixner
Martina Jüttner
Andrea Cooke
Samet Kocabey
Alexander Mario Maier
Luisa Kneer
Timon Funck
Gerlinde Schwanke
Philipp Altpeter
William Klein
Ngoc Luong
Sadao Takabayashi
Mario Hentschel
Jessica Lindlau
Andre Neumann
Jens Repp
Angelika Kardinal
Thomas Nicolaus
Diana Pippig
Michael Fedoruk
Paul Kühler
Zhiyuan Fan
Georg Urtel
and
all the people form the chair of Prof. Rädler

Special thanks to Tim for giving me the chance to do experiments in his lab. I really enjoyed the time in your group! Thanks a lot.